Characterization of Stresses and Strains Involved in the Martensitic Phase Transformations

Thesis

How to cite:

Das, Yadunandan (2017). Characterization of Stresses and Strains Involved in the Martensitic Phase Transformations. PhD thesis The Open University.

Faculty of Science, Technology, Engineering & Mathematics

School of Engineering and Innovation

Materials Engineering Group

CHARACTERIZATION OF STRESSES AND STRAINS INVOLVED IN THE MARTENSITIC PHASE TRANSFORMATIONS

YADUNANDAN DAS

January 2017

A THESIS SUMMITTED TO THE SCHOOL OF ENGINEERING AND INNOVATION OF THE OPEN UNIVERSITY FOR THE DEGREE OF DOCTOR OF PHILOSOPHY

I. Abstract

Transformation-induced plasticity (TRIP) steels are an example of steels used in the automotive industry, where strain-induced martensitic transformations, associated plasticity and work hardening, enhance both the strength and ductility of the material. This has enhanced both the passenger safety (improved crash-performance) and fuel efficiency as less material is consumed (lighter structure). To gain insights into these strain-induced transformations, it is crucial to understand the impact the applied stress/strain on the martensitic transformation and how the resulting strain fields affect the further deformation and transformations.

This PhD dissertation reports a series of experimental measurements on how the applied deformation affects strain-induced transformations, using three techniques, namely: electron backscatter diffraction (EBSD), high-resolution digital image correlation (HRDIC) and in situ neutron diffraction. It is shown here that applied stress favours the formation of strain-induced martensite in certain orientations of austenite. Crystallographic information gathered by EBSD and HRDIC indicates that the formation of martensite is governed by prior slip in the parent austenite. HRDIC measurements showed that strain heterogeneity is found not only between different grains within the microstructure, but even within individual austenite grains, suggesting that input parameters of macro stress strain properties are inadequate for variant selection models. EBSD, HRDIC and neutron diffraction measurements at ambient temperature confirm that the transformation is preceded by plastic deformation of the austenite crystal lattice and subsequent formation of nucleation sites. Here, it was shown that the intensity of those diffraction peaks from austenite grain families most affected by plastic deformation, decreased most due to martensitic transformation. Whereas, at the lower temperature deformation regimes, slip is suppressed, this is not the case. This dissertation illustrates how the above-mentioned techniques may be used to probe material phenomenon at various length scales, stress states and temperature regimes of interest.

II. Acknowledgements

Firstly, let me thank the department of Engineering and Innovation at The Open University for funding my PhD project. The beam time allocated at the ENGIN-X instrument by the ISIS facility is also gratefully acknowledged.

My sincerest gratitude goes to my supervision team comprising of Dr Richard Moat (lead), Dr Salih Gungor and Professor Michael Fitzpatrick without whose encouragement, support and guidance, this work would not be possible. Further, I am very grateful for the insightful discussions, critique and most importantly friendship of Dr Alex Forsey and Dr Thomas Simm (Swansea University). The help, support and guidance of ENGIN-X instrument scientists Dr Joe Kelleher and Dr Saurabh Kabra is greatly appreciated.

I would also like to take this opportunity to appreciate the support of Stan Hiller, Gordon Imlach, Dr Felicity Williams, Peter Ledgard and Damian Flack for their assistance in the experimental and laboratory work.

Special thanks to all my colleagues, Dr Shan Moturu, Dr Jino Mathew, Dr Yeli Traore, Dr Jeferson Oliveira, Dr Jose Rodolpho de Oliveira Leo, Dr Abdul Syed, Rahul Unnikrishnan, Abdullah Mumun, Anas Achouri, Avishek Dey, Safaa Lebjioui, Ellies Muyupa, Zuochao Zhao, John Brokx and others at the department and the university for their friendship and support throughout my time here at Milton Keynes.

Most importantly, I would like to thank my parents and family for their love and support. Finally, my sincerest appreciation is reserved for my wife Ekta Pandya, for her unconditional love. I must acknowledge her for brilliantly managing the birth of our daughter Tulasi, in the final year of my PhD, with such little support.

III. Preface

This thesis is submitted for the degree of Doctor of Philosophy of The Open University, UK. The work described in this thesis was carried out under the supervision of Dr. Richard Moat, Dr. Salih Gungor and Professor Michael Fitzpatrick (now at Coventry University) in the School of Engineering and Innovation, Faculty of Science, Technology, Engineering and Mathematics, between August 2013 and January 2016.

Except for where explicitly mentioned, the work is entirely the author's own work. None of this has been submitted for a degree or other qualification at this or any other university. Some of the work has been published in academic journal and conference presentation as listed below:

Y. B. Das, A. N. Forsey, T. H. Simm, K. M. Perkins, M. E. Fitzpatrick, S. Gungor, and R. J. Moat, "In situ observation of strain and phase transformation in plastically deformed 301 austenitic stainless steel," *Materials and Design*, vol. 112, pp. 107–116, 2016.

IV. Table of contents

Faculty of Science, Technology, Engineering & Mathematics

V. Table of figures

1 Introduction

1.1 Background

The need to improve the crash-performance of automobile structural components, without increasing the overall weight, has led to the development of high-strength steels. This has been achieved in a number of ways [1]. One class of high-strength steels of particular interest are those that derive strength from the formation of solid-state transformation, products in the form of a constituent martensite phase [2]–[5]. In contrast to steels strengthened directly through alloying alterations, these steels also exhibit exceptional ductility [6]. A high strength, high ductility material is ideal for use in applications where energy absorption is key, such as in motor vehicle crumple zones.

Martensitic transformations are solid-state diffusionless transformations and they have been extensively investigated over the past century[3], [7]–[9], yet they still continue to intrigue the research community [2], [10], [11]. Martensite is well known, especially within the undergraduate community, as the iron-carbon phase with poor mechanical properties, however, Zackay *et al.* were the first to exploit martensitic transformations to enhance ductility of steels, coining the now well-known term TRansformation Induced Plasticity (TRIP) steels [12].

In TRIP material the formation of martensite is mechanically induced. Essentially, metastable FCC (face-centred cubic) austenite is transformed into martensite by the addition of strain energy. In commercially interesting alloys such as those reported in [2], small regions of austenitic phase are retained by heat treatment and then transformed mechanically to form a ferrite matrix with small martensite regions. These alloys are far too complex, both in terms of their microstructure and phase makeup, for the purpose of gaining an initial understanding and ultimately predicting the local strains and crystallography of TRIP martensite. Therefore, the material reported in this dissertation is a meta-stable, virtually 100% austenitic, type 301-austenitic stainless steel. This material is known to transform to martensite under room temperature deformation [13], [14] and due to the almost fully austenitic starting microstructure, offers an opportunity to isolate newly forming martensite for analysis.

The local stress state around a single martensite region provides resistance to dislocation motion, *i.e.*, it acts as a localised strengthening mechanism and improves the mechanical performance of the steel. This stress/strain state is influenced by many factors, with those believed to be of most significance being the orientation of the martensite forming and the extent to which the parent grain has slipped [15]. The orientation of the forming martensite directly influences the transformation strain. This dissertation reports an analysis of the local strain occurring during the strain induced martensitic transformations and variant selection based on a theory proposed by Patel and Cohen [16] and as reported in [17].

1.2 Key objectives

The key objective of this PhD project was to improve and develop techniques for assessing stress-strain-material interactions. This was achieved by using the deformation-induced martensitic phase transformation in the 301 austenitic stainless steel as an example. Further, high-resolution digital image correlation (HRDIC) was developed to map these resulting stresses and strains at the microstructural length scales.

In the 301 austenitic stainless steels, the plastic deformation of the parent austenite lattice leads to the creation of nucleation sites for forming strain-induced martensite. The formation of strain-induced martensite further deforms the parent material and plays an important role in the strain-induced nucleation of the subsequent transformation events. Therefore, in this dissertation, a study at the microstructural length scale on a 301 austenitic stainless steel showing the TRIP phenomenon (deformation-induced martensitic transformation) is reported. This is done using electron backscatter diffraction (EBSD), *in situ* high-resolution digital image correlation (HRDIC) and neutron diffraction techniques. The EBSD and HRDIC techniques have been proven in [18]–[23] to be very useful tools to develop an understanding of microstructural length scale deformation. Furthermore, the combination of the HRDIC, EBSD and neutron diffraction give a comprehensive insight into material behaviour at different stages of the deformation process. The EBSD and HRDIC techniques have been used in this study to investigate the strain-induced martensite formation in relation to crystallographic planes within a given grain and how the material constraints within the grain and its surroundings affect the overall transformation mechanisms. Lastly, as EBSD and HRDIC are surface measurement techniques, therefore neutron diffraction measurements were made to compare the surface measurements to bulk transformation and hardening behaviour of the material.

The overall aim of the dissertation was to understand plastic-strain-induced transformation at the microstructural length scale and ultimately, to develop techniques capable of supplying data sets as input data for improving the reliability of existing material models.

1.3 Structure of thesis

This dissertation starts with a literature review *i.e.*, a review of the various strengthening mechanisms in materials, which is followed by notes on TRIP steels and martensitic transformations. The review further explains the fundamental aspects of the various techniques used in this project, such as fundamentals of diffraction and strain mapping at the microscale. The next chapter is the experimental methods chapter, which provides further specific details on the application of the three main experimental techniques, namely EBSD, high resolution DIC and neutron diffraction. Three original results chapters then follow. Chapter 7 contains the main discussion of the entire findings. The dissertation ends with a conclusions and further work chapter, in which the key findings of the PhD project are reiterated. It also includes a few notes on how future projects might further investigate the transformation or continue to develop/improve these measurement techniques.

2 Literature review

Since the material used throughout this project is an austenitic stainless steel, the literature review will start with a review of the iron - carbon phase diagram (the basic building blocks of steels) and the various phases present within it. This is followed by discussion of the various strengthening mechanisms relevant to ferrous material. Thereafter, an introduction to martensite is followed by an introduction to the thermodynamics of the martensitic transformation. This chapter then discusses the conventional heating and quenching technique to harden materials (by forming martensite), as well as the difference between the stress-assisted and strain-induced transformations seen in TRIP steels. It then reviews the crystallographic variant selection for the martensitic phase transformations. This is followed by an introduction to the diffraction theory, which forms the basis of the two results chapters. The chapter also discusses the key principles of digital image correlation.

Following this review of key principals, a review of the current state-of-the-art with regard to HRDIC and the diffraction based phase detection in steels and TRIP steel studies is presented.

2.1 Iron and it’s alloys

2.1.1 The Iron-Carbon Phase diagram

Before proceeding with discussion of the martensitic phase transformation, which is the focus of this dissertation, it is important to understand the various equilibrium and non-equilibrium phase transformations occurring in steels and iron alloys. This project deals with steels that have relatively small amounts of carbon. Therefore, the phase changes of iron-carbon alloy will be discussed to build up the background for the martensitic phase transformation. There are 5 thermodynamically stable phases occurring in the iron–carbon phase diagram below (up to 6.67% carbon) (refer Figure 2-1), namely liquid phase, delta iron (δ), gamma iron (γ), alpha iron (α) and cementite (Fe_3C) [24], [25]. Iron (with trace quantities of carbon present) undergoes various phase transformations in different temperature ranges. The liquid phase is present above 1539 °C. Between 1397-1539 °C delta iron (δ) is present, having a bcc crystal structure. Gamma iron (γ) is present in the temperature range of 910-1396 °C, which has a face-centered cubic crystal structure. The γ–iron, also known as austenite, has a maximum solubility of carbon of about 2 % at 1147 °C. Below 910 °C alpha iron (α) is present and has a bcc crystal structure with maximum carbon solubility of 0.02% at 723 °C. However, at room temperature the solubility of carbon in alpha iron (α) is extremely low (~ 0.0025% C) [24], [25].

The diagram may further be divided into two greater sections: steels and cast iron. Here, up to about 2% carbon steel is obtained, whereas, above 2% carbon concentration cast iron is formed. Steels may be further divided into two sections hypo eutectoid steels having not more than 0.8% carbon and hyper eutectoid steel having carbon in the range 0.8-2% carbon [25]. Steels used in this dissertation only contain traces of carbon having less than 0.01% carbon so fit into the hypo-eutectoid range.

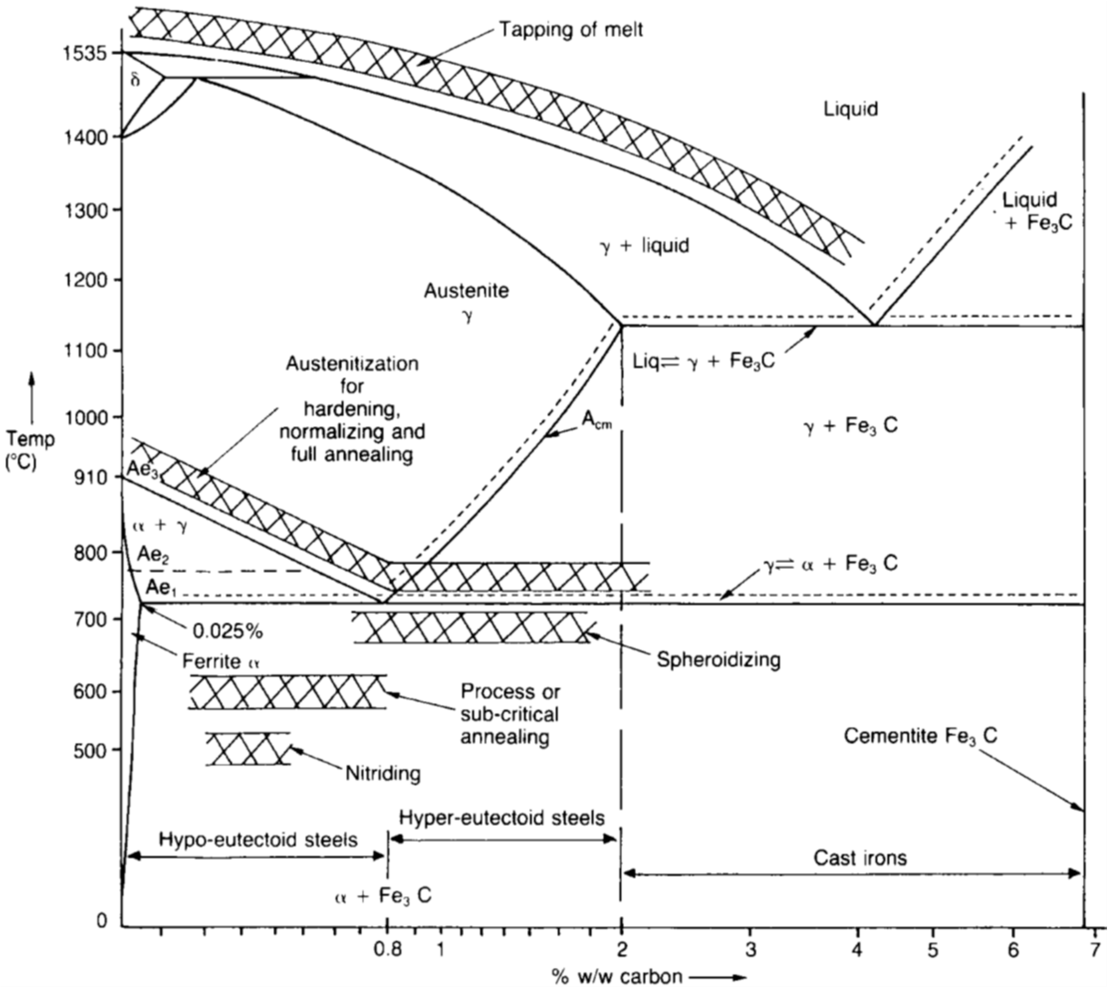

Figure 2-1 Iron carbon phase diagram [25].

For steel, the large difference in solubility of carbon in the austenite and ferrite phases, in addition to the eutectoid reaction (austenite (solid) → ferrite (solid) + cementite (solid)) means that a variety of properties may be obtained by heat treatments [25]. For example on slowly cooling (to below 723 °C), at the eutectoid point (~ 0.8% C), a pearlite micro-constituent is formed. It is a lamellar composite, which comprises of a soft, ductile ferrite phase and a hard, brittle cementite (Fe_3C) phase [25]. However, when the transformation occurs very quickly, *i.e.* no diffusion takes place, the austenite transformations into either bainite/martensite. Both bainite and martensite may be considered as hard phases with carbon trapped within the crystal lattice positions. These transformations are explained in detail below in the Section 2.2.7 and Section 2.3.

2.2 Strengthening mechanisms in metals

Although pure iron may be soft, steels can be manufactured having a wide variety of mechanical properties, with yield stress ranging from lows of about 200 MPa (Nmm^{-2}) to as high as 5500 MPa [26] and commonly up to 1000MPa. The hardness and strength of metals may be defined as its ability to withstand or resist deformation [27].

Strength in steels can be derived from many combinations of mechanisms; those believed to be most important are listed below:

- Refinement of grain size.
- Solid solution strengthening by interstitial atoms.
- Solid solution strengthening by substitutional atoms.
- Work hardening.
- Dispersion strengthening

Brief descriptions of the above processes are given below.

2.2.1 Grain size refinement

Hall and Petch [28], [29] carried out a scientific analysis of the dependence of the strength of a metallic material on its grain size and found a relationship between the yield stress (σ_y) and the grain diameter (d), named the *Hall-Petch* relationship. In any metallic material, the refinement of grain size in accordance with the *Hall-Petch* relationship represents a very important strengthening mechanism, mainly because of the ease at which we, the materials scientist/engineer, can alter the grain size of a metal and therefore influence the material strength. This can be summarised mathematically below.

$$\sigma_y = \sigma_o + Kd^{-1/2} \qquad \textit{Equation 1}$$

Where σ_0 and K are constants. σ_0 is a frictional stress, which includes contributions from particles and solutes but not dislocations (linear lattice imperfections [30]); in other words σ_0 is the flow stress of the un-deformed sample [31]. This relationship holds true for a variety of ferrous and many non-ferrous metals and alloys [26]. From the equation above, it is clear that the yield stress of the material is inversely proportional to the square root of the grain diameter, *i.e.*, smaller the grain diameter greater is the yield strength of the metallic alloy. As the grain size decreases, the grain boundaries increase and with it there is an increase in the barriers for dislocation motion. This leads to the higher mechanical properties in metallic alloys. This suggests that by grain refinement much improvement to strengths of metals and alloys may be achieved [32]. It has been reported in literature that the *Hall-Petch* relationship holds down to a grain size of ~ 20 nm.

2.2.2 Solid solution strengthening

Another mechanism to strengthen and harden pure metals is by the addition of alloying elements, as pure metals are softer and weaker in comparison to metallic alloys [25]. The alloying elements or impurities kept in a solution are classed as either substitutional or interstitial elements, depending on where they sit in the lattice of the parent material. This strengthening mechanism is called solid solution strengthening [27]. The increase in strength arises when the impurity atoms in the solid-solution impose a lattice strain on the surrounding host atoms, *i.e.* if the substitutional atom is smaller than the host it exerts a tensile strain on the surrounding crystal lattice and conversely if it is larger it exerts a compressive strain in its vicinity [27]. Strengthening occurs when these strain fields around the misfitting solutes interact and impede the motion of dislocations [26]. This lattice strain interacts with the stress field of the moving dislocation and thereby creating a barrier for their motion.

2.2.2.1 Carbon and nitrogen as interstitials

Both carbon and nitrogen greatly influence the strength of ferritic steels, however their effect is somewhat limited in austenitic steels. Carbon atoms are ~ 40% smaller than iron atoms and form interstitial compounds by squeezing into the lattice spaces between the iron atoms [33]. When carbon dissolves interstitially in α-iron in this manner, there may be a marked expansion of the crystal lattice which is distorted from cubic to tetragonal [34]. Furthermore, these interstitials interact with the shear component of dislocations and impede their motion [26]. This is why carbon and nitrogen interstitial elements provide a very potent strengthening mechanism in ferrite. The solubility of carbon and nitrogen in ferritic steels is small and there is a tendency for carbon to segregate towards defects. Further, the carbon and nitrogen interstitials may promote heterogeneous deformation of the crystal lattice by making it difficult initiate plastic flow.

2.2.3 Work hardening

Plastic deformation in metallic materials is due to dislocation movement. As the material is deformed, it work hardens as previously present dislocations impede the propagation of newly formed dislocations, *i.e.* some dislocations stuck in the crystal lattice act as sources of internal stress which oppose free movement of other gliding dislocations [25]. Work hardening or strain hardening may be defined as the increase in hardness and strength of a material due to plastic deformation [27], at low temperatures relative its melting point [25], [35]. It is the process of deforming a strain free crystalline material by plastic deformation, *i.e.*, by the generation, accumulation and entanglement of dislocations, which results in resistance to further movement of dislocations. Although, properties such as tensile strength, hardness and yield strength are enhanced on work hardening, there is an associated reduction in ductility and in the ability to deform the material. Work hardening is an important way in which the strength of both plain carbon and alloy steels may be improved, particularly when it comes to increasing the strength in rods and wires. For example on 95% reduction in area owing to the wire drawing process, the tensile strength of a 0.05 weight percentage carbon steel is raised by 550 MPa, whereas steels with a higher carbon content may even be strengthened by twice as much [26]. Changes to the mechanical properties of materials through work hardening have great industrial significance. It can be said that work hardening is the consequence of dislocations interacting with each other. Both internal and external parameters can influence work hardening behaviour: chemical composition, crystal structure, crystal orientation or texture and grain size are some of the internal parameters, whereas previous deformation history, temperature, strain rate and deformation mode are some external parameters influencing the work hardening of materials [35].

However, the extent to which work hardening can strengthen materials is limited by the amount of uniform deformation that can be applied, *i.e.* the amount of deformation that can be applied before the onset of necking, upon which, failure will occur due to the reduction in cross-sectional area.

2.2.4 Dispersion strengthening

Dispersion strengthening is achieved in metallic materials by the formation of oxides, nitrides and carbides [25]. These oxides, nitrides and carbides interact with dislocations and oppose their motion. If particles are too small then the dislocation may cut through it, and if they are too large it may lead to the softening of the matrix. Optimum size of the precipitates is required to maximise their interaction with the motion of dislocations. The size and shape of the particles may be optimised to oppose the propagation of dislocation by an adequate ageing heat treatment. In such a manner, in addition to grain size refinement and solid solution strengthening, the strength may be further enhanced to a considerable extent by controlling the dispersion of other phases in the ferrite or austenite microstructures [26]. The most common phases in steels are carbides, nitrides and intermetallic compounds. Fe_3C (cementite) is an example of one of the most common carbides in plain carbon steels and appears either in coarse lamellar form in pearlite, or as spheroidal precipitates or fine rods in tempered steels [26]. In alloy steels, iron carbides are sometimes replaced with other more stable metallic carbides (often, especially in the case of stainless steels, containing high levels of chromium ($Cr_{23}C_6$)). Although most of the carbides and nitrides lead to strengthening, they may have an adverse effect on the toughness and ductility of the material. Indeed, in most cases the upper limit to strengthening by dispersoids will be when the degradation of other properties becomes limiting, rather than the diminishing effect of dispersion strengthening.

2.2.5 Heat treatments to strengthen steels

In industry heat treatments are widely used to improve the strength of steels. The steel is heated to a single-phase region (fully austenitic), where carbon is in solid solution in γ-iron. Depending on the cooling rate, the decomposition of austenite results in various phases or mixtures of phases being obtained. However, phase diagrams only show the equilibrium phases and cannot predict phases when the cooling rate is above a certain value. This may be represented by the *Time Temperature Transformation* (TTT) diagram or *Isothermal Transformation* (IT) diagrams for a given steel as shown in Figure 2-2 [36], [37]. These diagrams show the austenite transforms into various products, which is a function of time and temperature. This is a convenient way to investigate the decomposition of austenite under both equilibrium and non-equilibrium conditions, e.g. variable cooling rates during quenching and to obtain insights into the transformation of austenite to pearlite, bainite or martensite [24]–[26], [33], [36]–[39]. Alloying elements, such as Cr, Ni and Mo, shift the transformation curves in TTT diagram towards the right, hence more time is required for the austenite to transform to either pearlite or bainite [36]. These transformations can be classed as either diffusive (pearlite or bainite) or displacive transformations (martensite) [33].

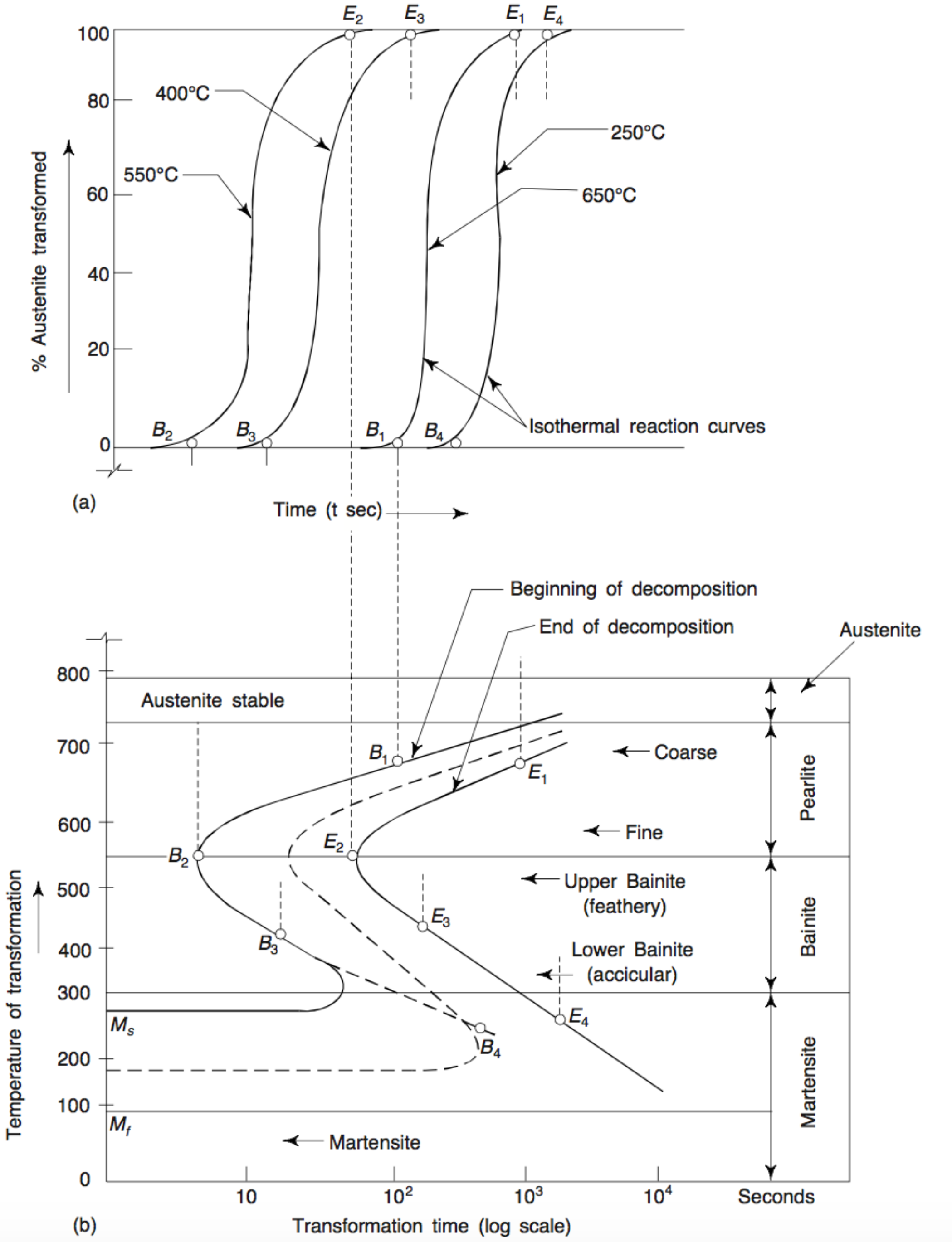

Figure 2-2. Time Temperature Transformation diagram for plane carbon steel (a) isothermal transformation curves and (b) construction of the TTT diagram [36].

2.2.6 Tempered martensite and maraging steels

In order to get complete fcc austenite (γ) → bcc martensite (α′) transformations, a critical cooling rate is employed such that it misses the starting decomposition curve in Figure 2-2. This way austenite at room temperature would be undercooled by ~ 900 °C and there would be a huge driving force available for the γ→α′ transformation to take place. Here the transformation mechanism is a displacive one and the martensite plates nucleate at the austenite grain boundaries and move across the parent grains at a very high speed [33].

The lattice of bcc iron and that of pure iron martensite are identical, however their microstructures are very different. Martensite (as explained below) is shaped like tiny lenses compared to the large equiaxed grains of bcc iron. Grain boundaries get in the way of the dislocation movement in the fine grained martensite plates and hence pure iron martensite is almost twice as hard as the bcc iron [33]. Higher hardness enhances the abrasion and deformation resistance of the martensite [36]. As the carbon percentage increases the strength of martensite increases. This is because the martensitic transformation is rapid and the interstitial carbon atoms freeze in their original positions, causing the martensite (bcc iron has solubility limit of ~ 0.0025% carbon) to become grossly oversaturated with carbon. Space is made for the carbon atoms by expanding the lattice dimensions in one direction to form a body centered cubic (bct) unit cell from the original body centered cubic (bcc) unit cell [26].

Martensite, obtained by rapidly cooling down to below the martensite start (M_S) temperature or simply *quenching (*below *M_S),* is very hard phase, but very brittle at same time [25]. By simply reheating martensite, *i.e. tempering* martensite in between 300-600 °C, the toughness lost may be regained with a small hardness trade-off [33]. On tempering martensite, sufficient thermal energy is available for the carbon atoms to diffuse out from the interstices within the lattice and form small closely spaced cementite precipitates (Fe_3C). This results in the lattice going back to the standard bcc structure and there is a recovery in the ductility and toughness of the steel. There is not much loss in hardness owing to the precipitation hardening, which is due to the formation of Fe_3C precipitates and its continued ability to impede the propagation of dislocations.

In some high alloy steels such as, *maraging steels*, containing 18 – 25 % nickel, secondary hardening may be obtained by the precipitation of intermetallic compounds obtained on the tempering of martensite [26]. Here, the carbide precipitation is almost eliminated by the use of very low carbon compositions and resulting martensite is soft but has a high dislocation density. Tempering the martensite formed at about 400-500 °C, intermetallic formation is accelerated by the presence of the high dislocation density. Other alloying elements present are cobalt, molybdenum and titanium; e.g. an alloy with composition 18-19 Ni, 8.5-9.5 Co, 4.5 Mo and 0.5-0.8 Ti may be tempered to give a yield strength of ~ 2000 Nm^{-2} [26]. In maraging steels, the high strength is accompanied by good toughness and ductility.

2.2.7 Bainitic Steels

In the TTT diagram, at temperatures between 550-720 °C austenite decomposes to pearlite, whereas at relatively lower temperatures below 250 °C austenite transforms to martensite and neither phase occurs within the gap of 250-550 °C

[26]. Within this temperature range *bainite* phase, which are fine aggregates of ferrite plates (or laths) and cementite particles, is formed. On lowering the temperature, the nature of the bainite changes and there are two main types of bainite: *upper* and *lower* bainite as shown in Figure 2-2.

There are two distinct stages in the formation of upper bainite, the first involves the formation of bainitic ferrite, which has very low solubility for carbon, enriching the remaining austenite with carbon, see Figure 2-3. Finally from the remaining austenite, cementite (Fe_3C) precipitates in-between the ferrite sub-units [26] and the amount of cementite depends on the carbon concentration of the steel.

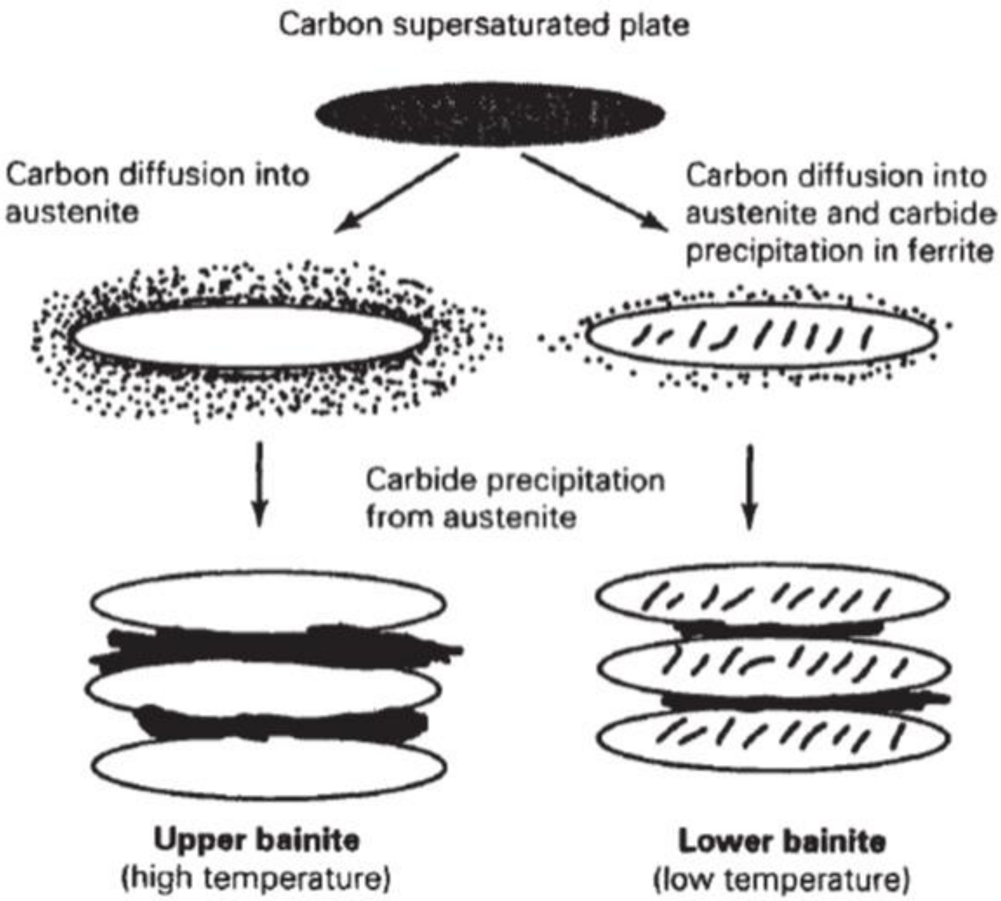

Figure 2-3. Schematic of Upper and Lower Bainite from [26].

The microstructure and crystallographic features of lower bainite are very similar to that of the upper bainite with the major distinction being that the cementite (Fe_3C) may precipitate both within the bainitic ferrite and the carbon rich austenite [25], see Figure 2-3. The cementite precipitates within the bainitic ferrite have a similar orientation relationship to that of 'tempered martensite', found during the heat treatment of martensite [26]. There may be formation of other carbides depending on the chemical composition and transformation temperature of the alloy.

Unlike in martensite, carbon is present mostly as coarse carbides in bainite and the resulting strength improvement is insignificant. Small variations in carbon content have little effect on the tempering of bainite [26]. A secondary hardening phenomenon is observed in bainitic steels during annealing at higher temperatures, in the presence of strong carbide forming elements such as Cr, V, Mo and Nb.

2.3 Martensite crystallography

As mention in Section 2.1.1, pure iron has a *face-centered cubic* (fcc) arrangement of atoms in the temperature region of 910-1382 °C [24], [25], [40]. On lowering of the temperature there is a transformation of this fcc lattice to a *body-centered cubic* (bcc) allotrope of iron. However, when the fcc phase is very rapidly cooled to below the M_s temperature, there may not be sufficient time or atomic mobility for the diffusional transformation to occur. As the degree of under cooling increases, the driving force for the transformation increases, resulting in diffusionless martensitic transformation. This martensitic transformation occurs by displacive or shear deformations that have a systematic and coordinated movement of atoms across the interface [25]. Therefore, martensitic (α′) transformations are also known as 'military' transformations. The concept that the austenite to martensite transformation occurs by shear deformation of austenitic lattice was first introduced by Bain in 1924 [7] and as a consequence the strain induced by the deformation is known as Bain strain.

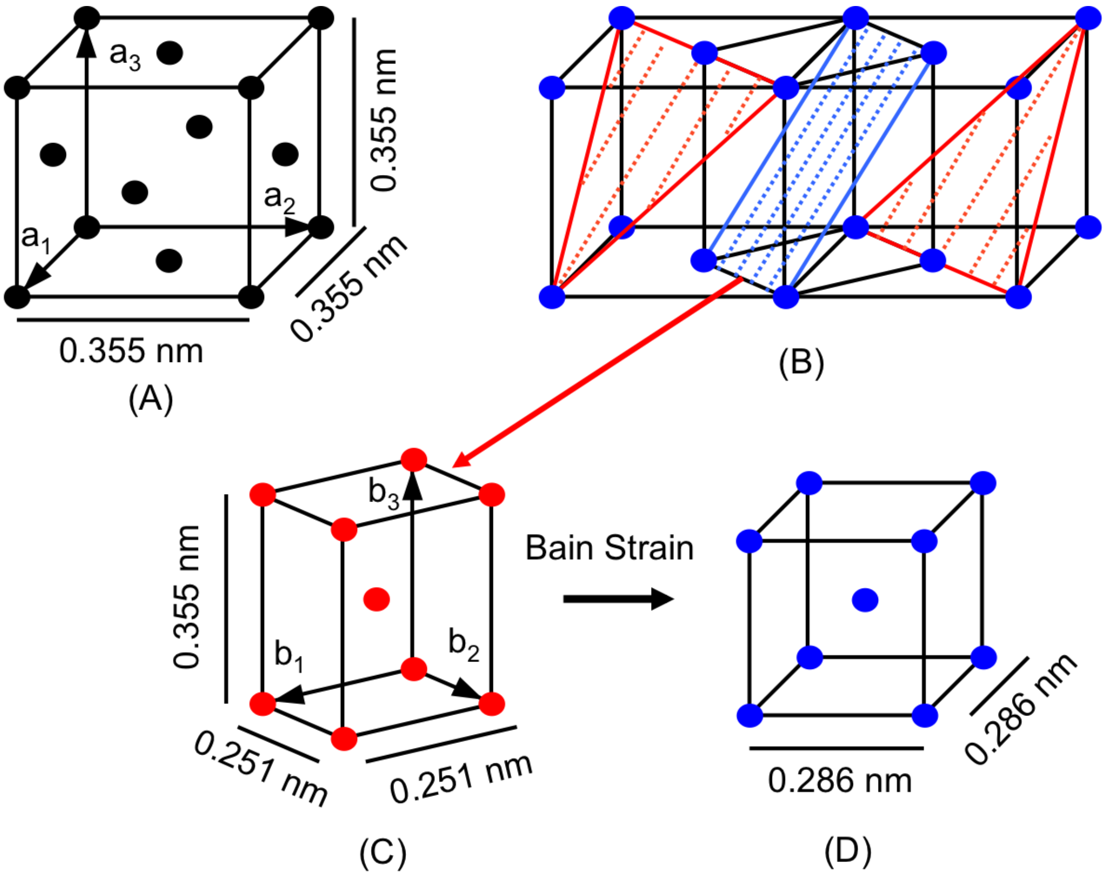

Figure 2-4: (a) Standard fcc unit cell. (b) Relationship between fcc and bct cells of austenite. (c) bct cell of austenite. (d) Bain strain deforming bct austenite lattice into bcc martensite lattice. Figure adapted from [15], [33].

The illustration in Figure 2-4 (A) shows the standard austenite fcc unit cell and Figure 2-4 (B) depicts two standard fcc unit cells arranged next to each other, such that a bct unit cell (shown in red) can be superimposed into the two adjacent fcc unit cells. However, when the displacive or shear transformation occurs, the fcc crystal structure is converted into a bct crystal structure. Now, as the bct structure has c/a ratio ~ 1.4 and is consequently unstable, it tries to transform into a bcc crystal structure. Here, there is a compression along the c axis and elongation in the other two axes and this results in the Bain strain, Figure 2-4 (C) and (D). Moreover, bct crystal has a lower packing efficiency as compared to fcc crystal and thus there is about 3-4 percent volume expansion associated with the α′ transformation.

The orientation relationship between austenite and martensite phases varies within a well-defined range; usually close-packed $\{111\}_{fcc}$ planes (coloured light blue Figure 2-4 (B)) are approximately parallel to the $\{011\}_{bcc}$ (coloured orange Figure 2-4 (B)). The well-known orientation relationships are the Kurdjumov-Sachs relationship [41], in which $<101>_{fcc} \parallel <111>_{bcc}$ and the Nishiyama–Wasserman relation [42], showing the $<101>_{fcc}$ at about 5.3° from $<111>_{bcc}$. Although, it is very difficult to experimentally distinguish between these relationships using ordinary electron diffraction or X-ray techniques, Crosky *et al.* showed a spread of fcc-bcc orientation relationships very similar to those encountered in the Kurdjumov-Sachs and Nishiyama–Wasserman relationships [43]. For most engineering purposes it is reasonable to assume the KS relationship. This is because there are four (111), $(\bar{1}11)$, $(1\bar{1}1)$, $(11\bar{1})$ slip planes in fcc crystal structure and six possible slip <110> directions, *i.e.*, in total 24 {111} [110] slip systems. There are 24 possible variants that can form as per the KS relationships and these can be found listed in the Table 2-1.

Table 2-1. Twenty four variants of K-S relation

Variant Number	Plane parallel $(\gamma)\parallel(\alpha')$	Direction Parallel $[\gamma]\parallel[\alpha']$
1	$(111)\parallel(011)$	$[\bar{1}10]\parallel[\bar{1}\bar{1}1]$
2	$(111)\parallel(011)$	$[\bar{1}10]\parallel[\bar{1}1\bar{1}]$
3	$(111)\parallel(011)$	$[\bar{1}01]\parallel[\bar{1}\bar{1}1]$
4	$(111)\parallel(011)$	$[\bar{1}01]\parallel[\bar{1}1\bar{1}]$
5	$(111)\parallel(011)$	$[0\bar{1}1]\parallel[\bar{1}\bar{1}1]$
6	$(111)\parallel(011)$	$[0\bar{1}1]\parallel[\bar{1}1\bar{1}]$
7	$(\bar{1}11)\parallel(011)$	$[\bar{1}\bar{1}0]\parallel[\bar{1}\bar{1}1]$
8	$(\bar{1}11)\parallel(011)$	$[\bar{1}\bar{1}0]\parallel[\bar{1}1\bar{1}]$
9	$(\bar{1}11)\parallel(011)$	$[0\bar{1}1]\parallel[\bar{1}\bar{1}1]$
10	$(\bar{1}11)\parallel(011)$	$[0\bar{1}1]\parallel[\bar{1}1\bar{1}]$
11	$(\bar{1}11)\parallel(011)$	$[101]\parallel[\bar{1}\bar{1}1]$
12	$(\bar{1}11)\parallel(011)$	$[101]\parallel[\bar{1}1\bar{1}]$
13	$(1\bar{1}1)\parallel(011)$	$[110]\parallel[\bar{1}\bar{1}1]$
14	$(1\bar{1}1)\parallel(011)$	$[110]\parallel[\bar{1}1\bar{1}]$
15	$(1\bar{1}1)\parallel(011)$	$[011]\parallel[\bar{1}\bar{1}1]$
16	$(1\bar{1}1)\parallel(011)$	$[011]\parallel[\bar{1}1\bar{1}]$
17	$(1\bar{1}1)\parallel(011)$	$[\bar{1}01]\parallel[\bar{1}\bar{1}1]$
18	$(1\bar{1}1)\parallel(011)$	$[\bar{1}01]\parallel[\bar{1}1\bar{1}]$
19	$(\bar{1}\bar{1}1)\parallel(011)$	$[1\bar{1}0]\parallel[\bar{1}\bar{1}1]$
20	$(\bar{1}\bar{1}1)\parallel(011)$	$[1\bar{1}0]\parallel[\bar{1}1\bar{1}]$
21	$(\bar{1}\bar{1}1)\parallel(011)$	$[101]\parallel[\bar{1}\bar{1}1]$
22	$(\bar{1}\bar{1}1)\parallel(011)$	$[101]\parallel[\bar{1}1\bar{1}]$
23	$(\bar{1}\bar{1}1)\parallel(011)$	$[011]\parallel[\bar{1}\bar{1}1]$
24	$(\bar{1}\bar{1}1)\parallel(011)$	$[011]\parallel[\bar{1}1\bar{1}]$

As discussed above in Section 2.2.5, the martensitic transformations are diffusionless transformations that may occur at relatively low temperatures where diffusion is either not feasible or is insignificant. At such low temperatures, diffusion of even interstitial atoms is difficult in the given time scale. Even when martensite occurs at high temperatures, the rate of transformation is so high that diffusion does not occur [15]. The M_s (martensite start) temperature is the highest temperature below which martensite forms on cooling of the parent austenite phase.

Further, the shape deformation accompanying the martensitic transformation should be an invariant-plane strain; this is a fundamental requirement of the transformation [15].

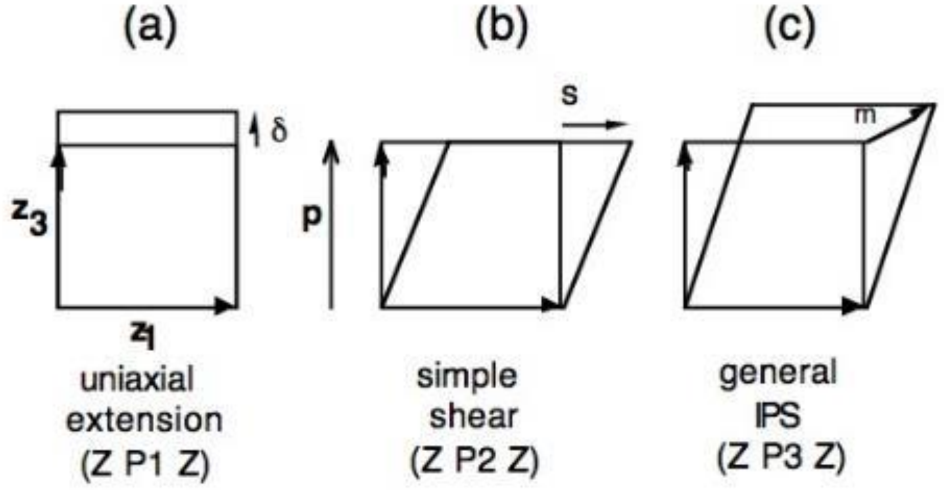

Figure 2-5. The three kinds of invariant-plane strains. Shapes before deformation are indicated by the squares. The terms δ, s and m represent the dilatational strain, shear strain and the general displacement respectively. The unit vector is denoted by term p, the shear strain s is parallel to the z_1 direction and dilatational strain δ is parallel to the z_3 [15].

Figure 2-5 illustrates the concept of invariant plane strain, *i.e.* a plane that is unrotated and undistorted, also known as the habit plane. Figure 2-5 (a) shows invariant plane strain, which is fully dilatational and is expected when the plate shaped precipitate grows and a volume change accompanies this transformation.

In Figure 2-5 (b) the invariant plane strain corresponds to simple shear and no volume change is associated with it. This is similar to the homogeneous transformation of crystals by slip. Here, the shear character (direction of applied shear stress) of the transformation is well reflected in the deformed parent crystal. Figure 2-5 (c) depicts the most general invariant-plane strain that involves both a volume change and a simple shear. Let us assume this displacement vector is *md*, where *d* is the unit vector in the direction of the displacement involved and *m* is the scalar giving the magnitude of the displacement, such that $md=sz_1+\delta z_3$ [15]. Here, s and δ are the shear and dilatational components of the invariant plane strain respectively (refer Figure 2-5). This type of invariant-plane strain is associated with the martensitic transformations, where there is both a shear of the parent crystal lattice and volume change associated with it. Also, the resulting interface between the parent austenite and martensite lattice must be glissile (dislocations must be able to move freely without any hindrance), to minimise the energy required for the transformation [15].

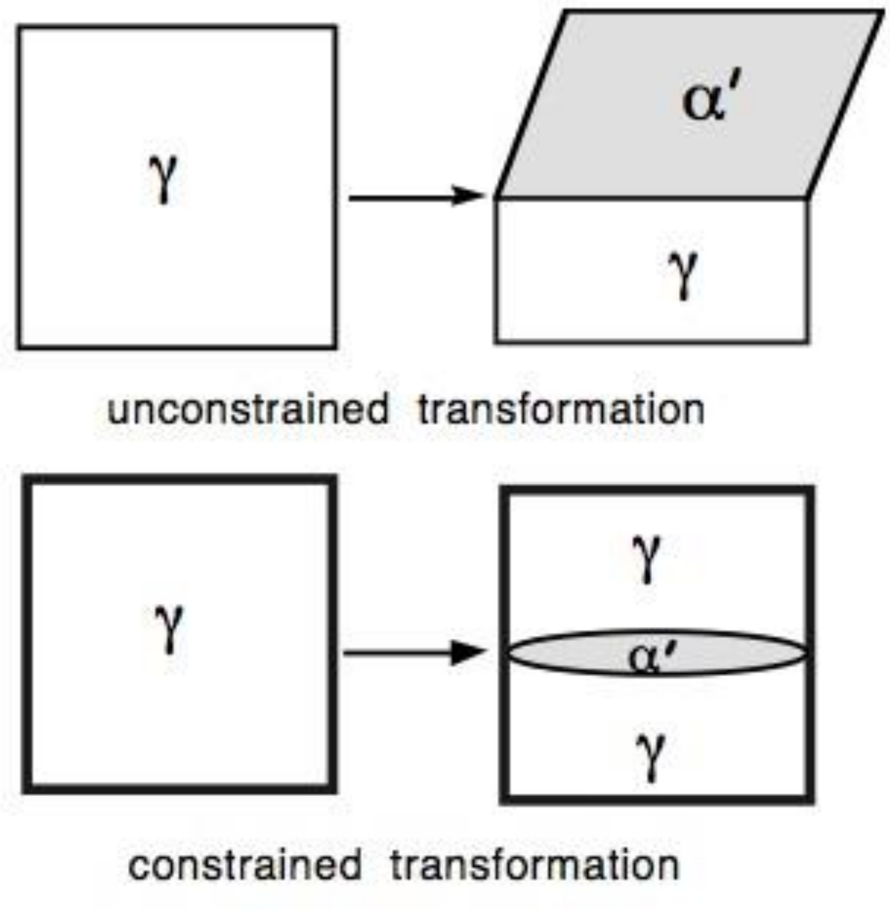

Figure 2-6: Habit planes of martensite (α′) formed during unconstrained and constrained transformations [15].

This interface between the parent austenite and martensite lattice is known as the habit plane. Figure 2-6, illustrates the habit planes when the transformation occurs in a constrained and unconstrained manner. The plane is macroscopically flat when the transformation occurs in an unconstrained manner. However, during the constrained transformation martensite grows into thin lenticular plates or laths. In this case, the habit plane is a little less clear, having a curved interface on a macroscopic scale. The aspect ratio (thickness to length) of these lenticular plates is 0.05 and some examples of habit planes are given in Table 2-2 [15].

Table 2-2. Martensite habit plane for various materials [15].

Composition / wt. %	Approximate habit plane indices
Low-alloy steels, Fe-28Ni	$\{1\ 1\ 1\}_\gamma$
Plate martensite in Fe-1.8C	$\{2\ 9\ 5\}_\gamma$
Fe-30Ni-0.3C	$\{3\ 15\ 10\}_\gamma$
Fe-8Cr-1C	$\{2\ 5\ 2\}_\gamma$
ε-martensite in 18/8 stainless steel	$\{1\ 1\ 1\}_\gamma$

2.3.1 Phenomenological theory of martensite

Bain was the first to propose a γ→α′ transformation strain, known as the Bain strain [7]. However, this explanation was not sufficient to account for the crystallography or shape deformation associated with the α′ transformation. As explained earlier in the Section 2.3, there is both a dilatational and shear strain associated with the martensitic transformation. The problem is correctly solved by the phenomenological theory of martensite crystallography, which correctly predicts both the crystallography and shape deformations [44]–[47]. The formation of martensite in a constrained environment causes distortion to the parent lattice in its vicinity. For every unit volume of martensite formed, the strain energy as a result of this distortion is given by [15], [48], [49]:

$$E = \frac{\mathrm{c}\,\mu}{r}(s^2 + \delta^2) \qquad \textit{Equation 2}$$

Where, μ is shear modulus of austenite lattice, *c/r* is the thickness to length ratio of the lenticular martensite plate and *s* and δ are the shear and dilatational components of shape deformation strain. It should be noted here, that it is in fact this distortion that contributes to the strengthening mechanisms of TRIP steels [15].

As explained earlier, the martensite interface must contain an invariant-plane strain. However, this cannot be achieved by Bain distortion alone. Therefore, an invariant plane is only obtained by the combination of Bain strain with a rigid body rotation (resulting in an invariant line strain *i.e.* an unrotated and undistorted line) coupled with a second shear deformation (explained below).

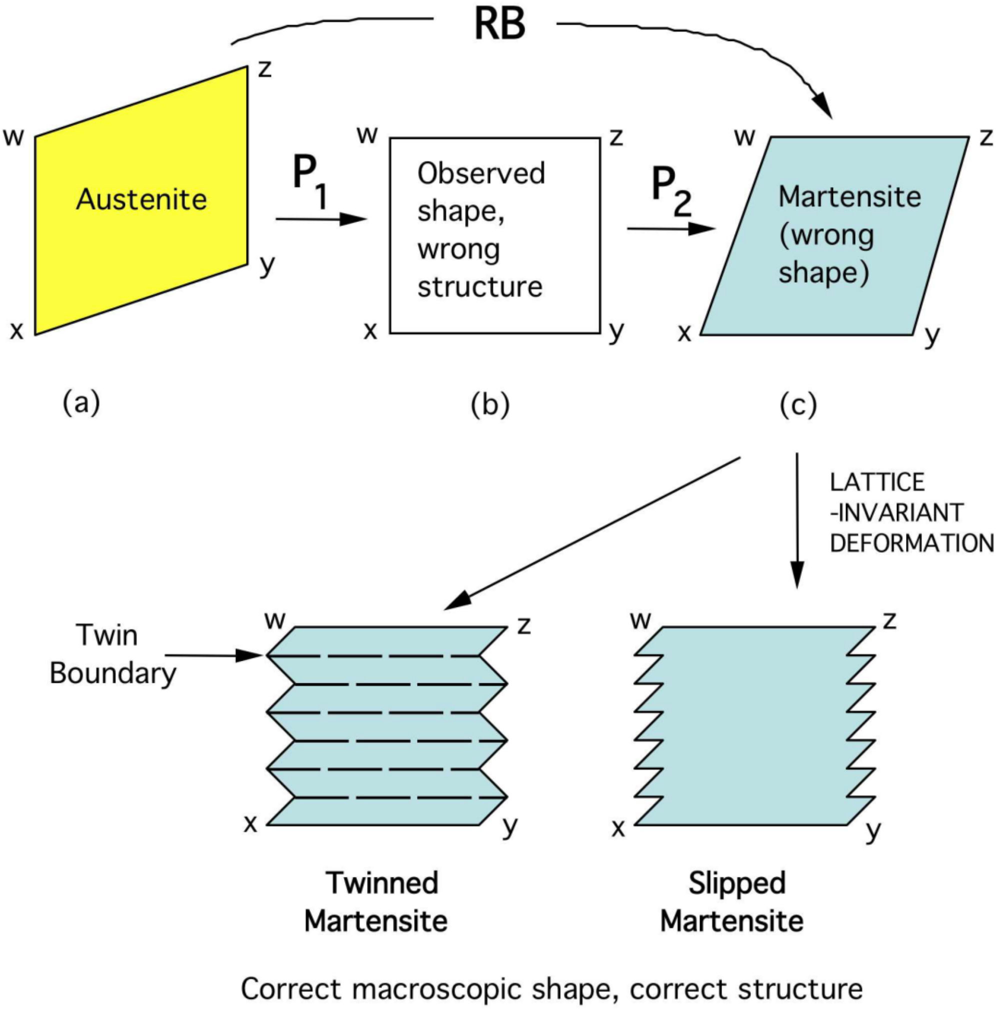

Figure 2-7: Schematic illustration of the phenomenological theory of martensite crystallography [15].

As mentioned above, Bain strain alone is not sufficient for explaining the true irrational orientation relationship between the parent (γ) and the product (α′) phases. The condition is that at least one plane is invariant (unrotated and undistorted) at the γ/α′ interface. This problem is solved by the phenomenological theory of martensite crystallography, schematically represented in Figure 2-7. Figure 2-7 (a) depicts the start of the austenite grain with fcc crystal structure prior to deformation. The Bain strain (B) alters the shape of parent γ into the product α′ phase. When a rigid body rotation (R) is added, the lattice deformation RB becomes an invariant-line strain. This is shown in steps a to c of Figure 2-7. The shape deformation observed as a result of P_1 (invariant-plane strain step a to b) is correct but the crystal structure obtained is wrong. Combining another homogeneous shear P_2 (step b to c) gives the correct crystal structure but the wrong shape. Now, the addition of inhomogeneous lattice-invariant deformations such as slipping or twinning resolves the shape changing effect of P_2 on a macroscopic scale. Thus these shortcomings maybe overcome [15].

2.3.2 Thermodynamics of martensite formation

As mentioned in Section 2.2.5, in the *TTT* diagram, martensite is obtained when the austenite is cooled at a rate greater than or equal to the critical cooling rate to a temperature below the M_S temperature. However, when the temperature is above M_S martensite may still be formed if additional energy is provided to overcome the barrier for spontaneous transformation to occur. Wayman *et al.* [40] represented the thermodynamics of the martensitic transformation in Figure 2-8, which shows the chemical free energies of austenite and martensite as a function of temperature. For a spontaneous martensitic transformation to occur, the chemical driving force needs to attain the critical value of $\Delta G_{M_s}^{\gamma\rightarrow\alpha'}$, which occurs at M_S temperature.

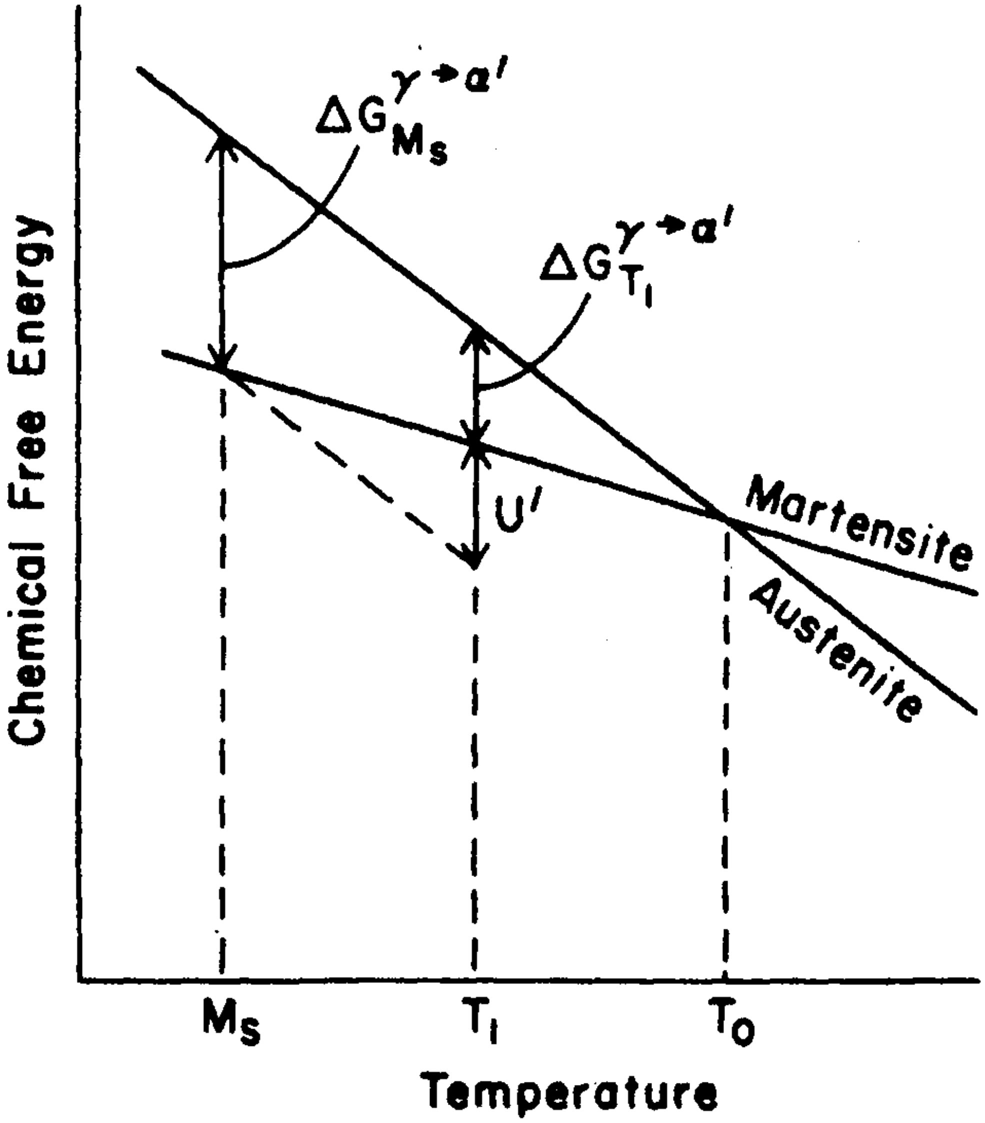

Figure 2-8: Schematic illustration of chemical free energies of austenite and martensite phases as a function of temperature [40]

For transformation to occur at temperatures *T1* above *Ms* with chemical driving force $\Delta G^{\gamma\rightarrow\alpha'}_{T_1}$, a sufficient external applied stress, or a mechanical driving force U' needs to be available. This mechanical driving force is presumed to originate from an applied stress, such that:

$$\Delta G^{\gamma\rightarrow\alpha'}_{T_1} + U' = \Delta G^{\gamma\rightarrow\alpha'}_{M_s}$$ *Equation 3*

Patel and Cohen [16] proposed the following expression for the mechanical driving force as a function of stress and orientation:

$$U' = \tau\gamma_0 + \sigma\varepsilon_0 = \frac{1}{2}\gamma_0\sigma\sin\theta \pm \frac{1}{2}\varepsilon_0\sigma(1 + \cos 2\theta)$$ *Equation 4*

Where, the terms $(\tau\gamma_0)$ and $(\sigma\varepsilon_0)$ are the work done by shear stresses and normal stresses respectively, σ and τ are the absolute value of the applied stress (tension or compression) and shear stress, γ_0 and ε_0 are the transformation shear strain and the normal component of the transformation strain and θ is the angle between the stress axis and the normal to any potential habit plane.

The above theory forms the basis of how TRIP steels are manufactured. Initially these steels start out as a ferrite/bainite matrix with regions of austenite. When TRIP steels are loaded, sufficient mechanical driving force is supplied to cause retained austenite to transform to martensite.

2.4 Stress assisted and strain induced nucleation of martensite

The above discussions make it clear that an externally applied stress alone is sufficient to obtain plastic-deformation-induced martensitic phase transformation in previously stable austenite. However, beyond the yield strength of the material, only strain-induced transformations are possible (explained below). Figure 2-9 is the Olson and Cohen diagram showing the interrelationships between the stress-assisted and strain-induced nucleation of martensite [50].

Investigations on the kinetics of martensitic reactions have largely dealt with spontaneous transformation, unassisted by externally applied stress. Most such transformations, especially in Fe-base alloys, involve autocatalytic nucleation [51]–[53]. Martensitic transformations display macroscopic displacements due to which the surrounding parent lattice is plastically strained and this strained-induced nucleation leads to autocatalysis (the residual stress field may trigger further transformation of the parent lattice). The nucleation sites and corresponding martensite embryos can be identified when strain-induced nucleation is studied systematically through intentionally-imposed plastic deformation, [54]–[56].

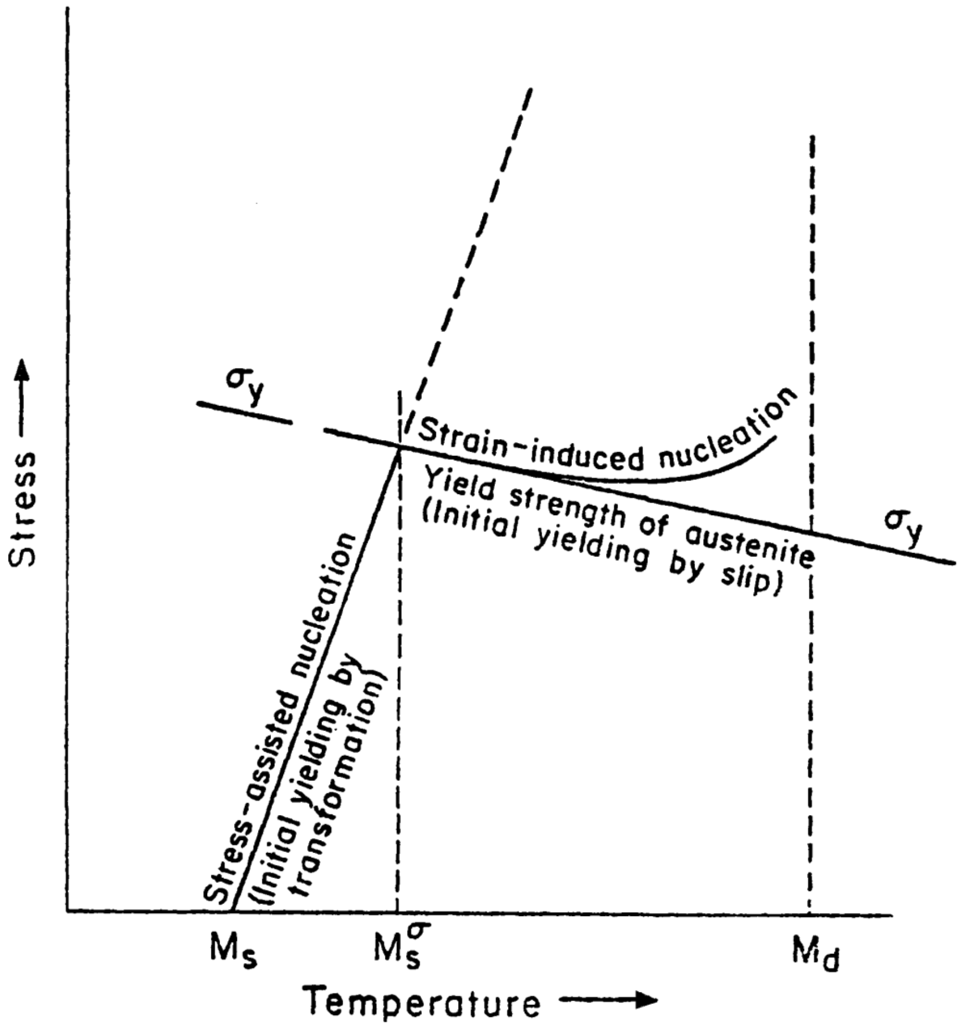

Figure 2-9: Schematic illustration of the interrelationships between stress-assisted and strain-induced nucleation of α′martensitic in Fe-Ni-C alloys [50].

Bolling *et al.* [9], [57]–[59] studied the interrelationships between applied stress, plastic strain and martensitic transformations in Fe-Ni-C and some Fe-Ni-Cr-C alloys. They defined a temperature $M_S{}^{\sigma}$ higher than M_S. At temperatures below $M_S{}^{\sigma}$, on application of stress, plastic deformation of the parent lattice is initiated by martensite formation and the temperature dependence of yield stress is positive. Here, the stress to initiate the martensite transformation approaches zero as temperature nears the M_S temperature. At temperatures above $M_S{}^{\sigma}$, slip processes initiate yielding of parent crystal lattice under applied stress and the temperature dependence of the yield stress is negative (normal) above $M_S{}^{\sigma}$. Olson and Cohen schematically represented these relations in Figure 2-9.

At temperatures under $M_S{}^{\sigma}$, the plastic deformation of the parent crystal lattice occurs due to stress-assisted nucleation of martensite, which is below yield stress (σ_y) of austenite [16], [50]. At temperatures above $M_S{}^{\sigma}$, the applied stress required to add sufficient driving force must exceed the yield stress (σ_y) in order to initiate martensitic transformation and this is considered to be strain-induced nucleation [50]. Furthermore, stress-assisted nucleation depends on the same nucleation sites or embryos responsible for spontaneous nucleation. Whereas, new sites or embryos are required for strain-induced nucleation by plastic deformation, generated predominantly at shear band intersections [3], [5], [50], [60].

However, this is further complicated by variant selection and the crystallography of the martensite formed. It is known that there are 24 possible KS variants of martensite that can form in a given grain of austenite, with the thermodynamic properties of each variant differing from the others. Therefore the applied stress can influence the formation of certain variants differently to others [15], [17]. This causes what is known as variant selection, which will be discussed in the next section on crystallographic variant selection.

2.4.1 Variant selection

Variant selection plays a role in the formation of transformation texture and hence may lead to anisotropy of properties in the resulting material in addition to having a profound effect on the transformation strain[61]. It is well known that according to the Kurdjumov-Sachs orientation relationship, there are 24 variants of martensite existing in steels, as listed in Table 2-1. All these variants should have equal chances of transformation if chemical driving force (a function of temperature and composition) alone accounts for the transformation. However as martensitic transformation may be stress assisted, Kundu *et al.*,[17], [44] showed that under the influence of stress alone, or the cumulative influence of stress and strain, α′ transformation will favour those variants that comply with the direction of applied stress. In other words, the mechanical driving force experienced by some variants will be greater than for others with the same applied stress. Therefore some variants are more likely to form than others and this results in what is known as variant selection. This variant selection follows Patel and Cohen’s theory [16].

There has been a long-standing interest in variant selection during the martensitic transformation, because steels may be designed favourably for the transformation to occur and the TRIP phenomenon (explained in the following section) may be exploited. Various scientists have put forth their theories in this regard; variant selection of α′ phase takes place due to externally applied stress when, nucleation sites are the same as the ones that would occur on spontaneous cooling [16], [17], [62], or strain when new highly potent sites are available due to the plastic deformation of the austenite matrix[17], [63]–[66].

In the bulk texture of polycrystalline austenitic steels, certain groups of variants are absent as proof of variant selection [64], [67]. Kundu [68] showed that transformation texture will be more influenced by the prior austenite texture than variant selection, but this does not rule out the presence of variant selection. Kundu *et al*. [61] studied variant selection at the resolution of an individual austenite grain. Dividing the variants into different groups, they showed how the volume fraction of these groups vary with their cumulative interaction energy [44]. Thus, analysis in articles [17], [61] shows the variant selection phenomenon follows Patel and Cohen's theory [16], when α′ transformation takes place under the application of stress or cumulative influence of stress or strain. When variant selection takes place according to the Patel and Cohen theory, the variants with higher interaction energy form in higher volume fraction and vice-versa [69].

Following [16], the compliance of a particular variant with the applied stress can be expressed in terms of an interaction energy:

$$U = \sigma_N \delta + \tau s \qquad \textit{Equation 5}$$

Where σ_N is the component of stress normal to the habit plane, τ is the shear stress resolved on the habit plane in the direction of shear and δ and s are the respective normal and shear strains associated with transformation. Thus, the interaction energy of individual variants can be calculated. In this project, an attempt has been made to see how the interaction energy of different variants evolves with initial nucleation of α′ variant.

The phenomenological theory of martensite crystallography (PTMC) (Bain strain plus rigid body rotation) describes the crystallography and shape of α′ correctly [45], [47]. However, the mechanistic models [65], [67], [70] developed ignore the PTMC and use the orientation relationships such as Kurdjumov-Sach (KS) [41] or Nishiyama-Wassermann (NW) [42], [71] in the models, which are unable to explain the true irrational orientation relationships between austenite and α′. Detailed experimental data gathered by Nolze [72] showed how orientation relationships deviate from the KS or NW relationships and a precise identification of the variants in a pole figure enables the development of the correct quantitative variant selection model.

Recently, Kundu *et al.* [69] calculated the volume fraction of the individual variants. Defining variant selection as systematic absence of a few variants due to the influence of external stress or strains they introduced the concept of "naturally absent variants". In a single austenite grain, one or more of the 24 variants may be absent as there may not be sufficient space for all of them to form, since nucleation is a stochastic process and some nuclei are able to grow and others are not. They showed that the position of the nuclei and the space constraint in the microstructure might play a role in deciding which variant will form, irrespective of their interaction energy [69]. However, it seems that the above-mentioned theory is quite similar to the variant selection theory in general and is probably a different way of expressing the same concept.

It is quite clear from the above theories that variant selection is due to applied stress. But as seen earlier, the formation of constrained martensite causes distortions of the parent austenite. This will result in local changes in stress and strain and as a consequence the local stress and strain will not be equal to that applied macroscopically. This is not taken into consideration in the transformation variant selection models [17], [44]. Hence, one aim of this project is to study the evolving local strain and consequent stress as a function of this α′ transformation using digital image correlation and to use the generated data to quantitatively determine the shortcomings of current transformation models.

2.5 TRIP steels

Transformation-Induced Plasticity (TRIP) is a phenomenon in which strain-induced transformations (martensite, bainite or Widmanstatten ferrite) promote lattice deformation resulting in enhanced ductility [32], [73]. Zackay *et al.* were the first to exploit martensitic transformations to enhance the ductility of Fe-Cr-Ni alloy steels, coining the now well-known term 'TRIP' steels [12]. TRIP steels are multiphase materials wherein the microstructure contains ferrite, bainite and metastable austenite [74]. In TRIP material the formation of martensite is mechanically induced. Essentially, metastable FCC (face-centred cubic) austenite is transformed into martensite by the addition of strain energy. In commercially interesting alloys such as those reported in [2], small regions of austenite are retained by heat treatment and then transformed under applied stress to form a ferrite matrix with small martensite regions.

The high strength and improved ductility of TRIP steels is due to a combination of the hard martensite phase in the soft austenite matrix, analogous to a hard-particle-reinforced composite [75]. The solid-state solution hardening of carbon in iron and the very high dislocation density obtained from the rapid diffusionless martensitic transformation, are further exploited in the strengthening process. Extensive literature can be found on martensite's influence on the properties of TRIP type steels, such as the correlation between martensite fraction and strength [2], [76], [77], martensite fraction and ductility [11] and deformation and transformation kinetics [60], [78]–[80]. Also, one particular area of conjecture was the origin of the exceptional ductility observed in TRIP type steels, with many authors attributing it to transformation strain [81], a theory mathematically disproven by Bhadeshia in [75] and to some extent experimentally corroborated by Moat *et al*. in [2] and shown to be closely related to composite theory. It is reasonable to assume that for better understanding of the strengthening mechanisms that lead to the exceptional strength and ductility of TRIP steels, there needs to be a thorough investigation of local stresses and strains observed in the vicinity of the transformation product. It is as a result of these stress and strain fields around transformation sites that dislocation movement and localised plasticity are resisted [82], [83].

2.5.1 Transformation strain

The 15-25 % uniform elongation in the TRIP steel cannot be accounted for by the transformation strain due to the martensitic transformation, where the shape deformation associated with the transformation accounts for about 2% tensile strain, as the amount of retained austenite is small in TRIP steel [26]. The transformation strain associated with the martensitic transformation increases the dislocation density in the ferrite and strengthens it [84]. This and the enhanced work hardening due to the deformation-induced martensitic transformation are the major contributors to uniform elongation [26].

During the transformation of TRIP steels the retained austenite plays an important role in providing resistance to necking. Therefore, it is important to delay the transformation of retained austenite to martensite to the later stages when a considerable amount of deformation has accumulated in the steel.

2.6 Diffraction theory

Diffraction techniques are widely used to probe the structure and property relationships in material science and engineering. Some of these diffraction techniques include the use of electrons, neutrons and X-rays to probe materials.

Diffraction is obtained due to certain phase relations between two or more waves [85]. Let us assume the example of wave (visible light), which bends when a portion of the wave front is impeded by an obstacle or barrier. When this barrier has a small aperture or opening, approximately similar to the wavelength of the incident beam, the beam diffracts due to the bending of the wave, *i.e.*, owing to the constructive interference of the waves. When these waves are in phase they creates a diffraction spot. In other words, diffraction occurs due to a large number of in-phase scattering of waves which reinforce each other.

2.6.1 Bragg Law

When an incident beam interferes with a regular array of lattice points it scatters in all directions. In some directions there is constructive interference occurring and for crystalline solids the diffraction maximum occurs when Bragg's condition is satisfied, *i.e.*:

$$n \lambda = 2 d_{hkl} \sin \theta_{hkl} \qquad \textit{Equation 6}$$

Where n is an integer, λ is the wavelength of the incident electron, neutron and X-rays beam, d_{hkl} is the interplanar spacing of the crystallographic lattice planes and θ_{hkl} is the angle of incidence with the lattice planes (see Figure 2-10). For diffraction to occur another required factor is that the wavelength of the incident beam needs to be similar to the dimensions of the lattice plane/spacing.

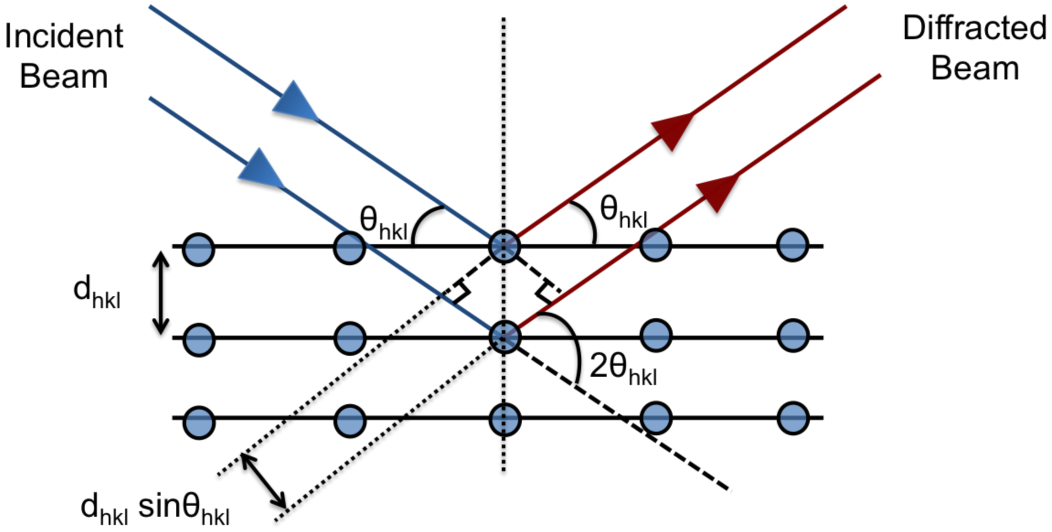

Figure 2-10. Schematic of Bragg's Law

For a cubic material, such as the materials studied in this dissertation, the lattice parameter '*a*' is directly proportional to the d_{hkl} spacing. Using the above-mentioned Bragg's Law, d_{hkl} can be calculated, from which the lattice parameter (a) may be determined. The accurate measurement of d_{hkl} and therefore a, depends on the precision of sin θ_{hkl} (derived quantity) and not on θ_{hkl} (measured quantity) measurement. Luckily the value of sin θ_{hkl} changes very little when $2\theta_{hkl}$ is close to 90° and therefore precise measurements may be made when detectors are at 90°, this is one of the reasons why detectors at many diffractometers, such as in the ENGIN-X beamline that is used in the current study, are kept at 90° (this will be explained in detail later in Section 3.4). A similar result may be obtained by differentiating Bragg's Law with respect to θ_{hkl}.

$$\frac{\Delta d}{d} = -\cot\theta_{hkl}\Delta\theta \qquad \textit{Equation 7}$$

For a cubic system

$$a = d\sqrt{h^2 + k^2 + l^2} \qquad \textit{Equation 8}$$

Therefore

$$\frac{\Delta a}{a} = \frac{\Delta d}{d} = -\cot\theta_{hkl}\Delta\theta \qquad \textit{Equation 9}$$

As θ_{hkl} approaches 90° when cot θ_{hkl} approaches zero, therefore, the fractional error caused in 'a' ($\Delta a/a$) due to the error in θ_{hkl} also approaches zero. Therefore, for accurate measurement of the lattice parameter, the reflected beams should have 2θ values as close to 180° as possible.

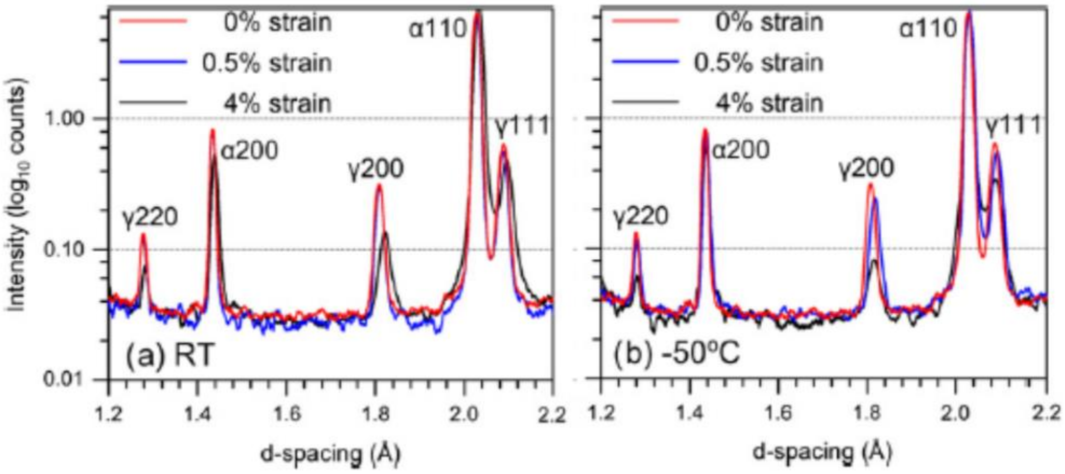

Figure 2-11. Diffraction profiles of a multiphase material [2].

In reality using neutron diffraction, one does not only measure the internal phases, but may also investigate the internal stress state of the materials, by measuring shifts in the interplanar spacing in their crystal lattices (see Figure 2-11). The changes or shifts in crystal lattice spacing give information about elastic strains. In other words, the lattice spacing may be used as a strain gauge to measure the strain in stressed materials. Here if d_0 is the strain free lattice spacing and the corresponding Bragg's angle is θ_0, then the strain may be computed by the following formula:

$$\varepsilon = \frac{\mathrm{d} - \mathrm{d}_0}{\mathrm{d}_0} = -Cot\ \theta_0\ \Delta\theta$$

Equation 10

Diffraction may occur from any plane when its inclination angle to the incident beam θ satisfies the Bragg condition. Furthermore, the size and shape of a unit cell enable the determination of its diffraction directions [85]. In other words, the direction in which a given set of lattice planes diffracts is determined by the crystal system to which it belongs to and its lattice parameter. For e.g. combining

$$n\lambda = 2\mathrm{dSin}\theta$$ *Equation 11*

And,

$$\frac{1}{d^2} = \frac{(h^2 + k^2 + l^2)}{a^2}$$ *Equation 12*

Gives,

$$Sin^2\theta = \frac{\lambda^2}{4}(\frac{h^2 + k^2 + l^2}{a^2})$$ *Equation 13*

Using the above equation, it is possible to predict all the possible Bragg angles at which diffraction occurs, for a particular wavelength (λ) and a particular cubic crystal unit cell [85].

For a tetragonal crystal unit cell, the equation becomes

$$Sin^2\theta = \frac{\lambda^2}{4}(\frac{h^2 + k^2}{a^2} + \frac{l^2}{c^2})$$ *Equation 14*

Similar equations may be derived for other crystal systems. However, these are all ideal cases, where there is a perfect crystal and the incoming beam is perfectly parallel (due to good collimation), consisting of monochromatic radiation. Such conditions are not found in practice and destructive interference occurs in all directions other than those in which the Bragg condition is satisfied.

All real crystals have a mosaic structure, *i.e.* a structure wherein a "single" crystal is broken up into smaller perfect crystals. Here atoms within the lattice positions do not extend in a regular manner from one side of the crystal to the other, instead the crystal lattice is broken into smaller blocks and every block is slightly disoriented with respect to the surrounding blocks [85]. Depending on the crystal, the maximum angle of misorientation varies from a small value up to one degree. If this angle is ω, diffraction resulting from a monochromatic beam occurs from the single crystal, not only at the angle of incidence (θ), but also in-between all θ and $\theta+\omega$ angles [85]. Another effect of mosaicity is that it increases the intensity (relative to the ideal perfect crystal) of the reflected beam. Polycrystalline materials are similar, where individual grains act as the smaller single crystals. For such a polycrystalline material, the scattering intensity vs 2θ is close to zero for all angles, other than certain angles at which the diffracted beams form high sharp maxima.

In materials science, diffraction is used for two main purposes:(i) to determine the phases present in a diffracting volume and (ii) to determine the lattice parameter of those phases. In this dissertation, the main focus of the work using diffraction is for the purpose of phase analysis. Of particular interest is the ability to quantify the fraction of martensite in the microstructure of the steel under investigation with respect to load history.

2.6.2 Scanning electron microscope (SEM)

Unlike traditional metallurgical microscopes that use light to produce an image, a scanning electron microscope (SEM) uses electrons. In the SEM, electrons are bombarded onto the surface of a conductive material, rastering along a pattern of parallel lines. Various signals are obtained as a result of this impact, which are collected to form an image or to analyse the surface of the material. Due to its good depth of field, surface topography may be imaged with high resolution. In a typical SEM, the electron beam is generated by the electron gun above the sample chamber (see Figure 2-12). These electrons are produced by thermal emission sources, which could be a tungsten filament or a field emission gun (as used in the present study at The Open University). A series of electromagnetic lenses in the SEM column are used to focus the electron beam. Deflection coils at the bottom of the column are used to direct and position the beam on the surface of the sample and to produce a raster pattern. The entire system is kept under vacuum.

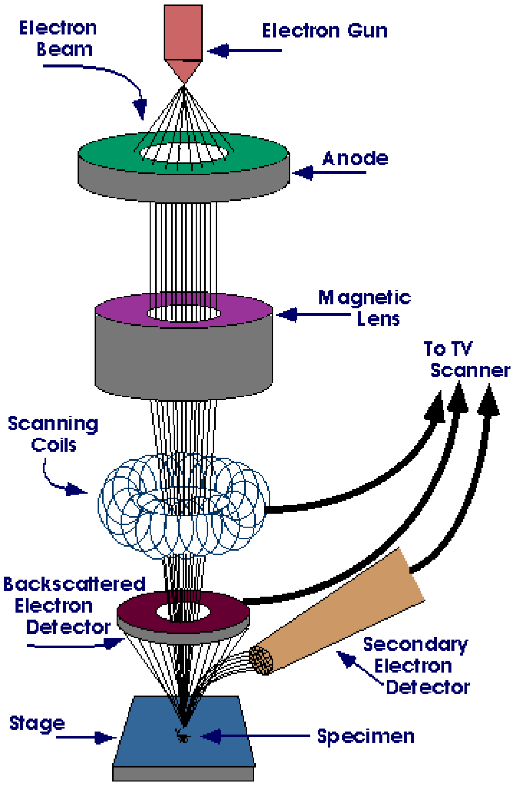

Figure 2-12. Schematic of working principle of scanning electron microscope [86]

As the incident electron beam interacts with the surface, a variety of X-rays, backscattered electrons and secondary electrons are emitted from near-surface material. Using detectors, these signals are measured and interpreted in real time to give an output onto a computer display.

Backscattered electrons are the high-energy electrons ejected as a result of the collision of incident electrons with a sample atom's nucleus and they have energy comparable to that of the incident electron. For the material used in this project, the backscattered mode (atomic number contrast imaging mode), was preferentially used. Backscattered electrons produce better contrast relative to secondary electrons, between the tiny gold markers, which are produced on the sample's surface for DIC analysis and the steel background. As discussed in Section 3.3, this gives excellent images with high contrast (as gold and iron are far away in the periodic table) useful for digital image correlation. Secondary electrons are lower-energy electrons that are also emitted during scattering of the incident beam. An image is created by the detection of re-emitted electrons from the sample surface onto the electron detectors.

2.6.2.1 Working principles for Electron Backscatter Diffraction (EBSD)

Several reviews [87]–[91] have explained the working principle of EBSD in detail. EBSD is a point-by-point probe of the electron diffraction pattern obtained from a sample being measured in the scanning electron microscope (SEM). The schematic representation of the EBSD process is given in Figure 2-13, which covers an explanation of the principal components of EBSD in terms of electron/material interaction, pattern generation, pattern acquisition, pattern recording, pattern detection, background correction and pattern indexing [89]. The entire data acquisition process is automated and is controlled by a central computer. The interpretation and analysis of the acquired data is done through data processing software and may be done afterwards and away from the SEM.

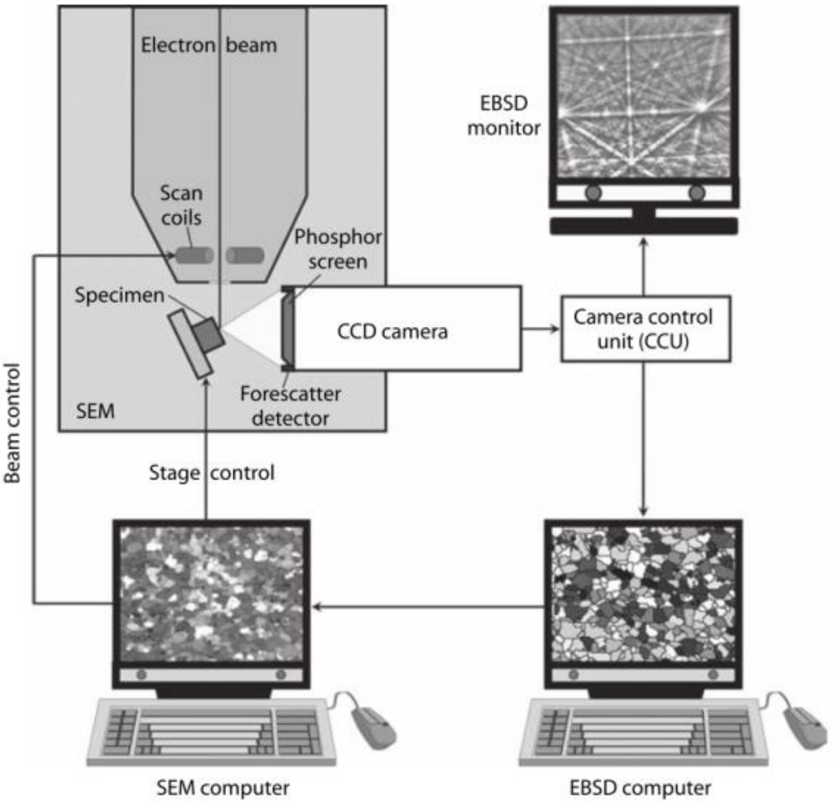

Figure 2-13. Schematic of principal components of electron backscatter diffraction observation [92]

As mentioned above, EBSD maps are point-by-point measurements, which are formed by rastering the electron probe over the surface of a bulk sample, in the SEM. The EBSD data is collected through orientation mapping of an area using uniformly spaced data points in either square or hexagonal grids. The distance between measurement points (known as the step-size or grid-size) defines the resolution of the map. The electron beam entering the crystalline solid will scatter in all directions and therefore at least some electrons will diffract and follow Bragg's Law at every set of lattice planes of spacing d_{hkl}.

$$n\lambda = 2d_{hkl} \sin \theta$$ *Equation 15*

Where, n is an integer, λ is the wavelength of the electrons and θ is the angle of incidence of the electron on the diffracting plane. These electrons may undergo elastic scattering to give a very strongly reinforced beam. The electrons arriving at the Bragg angles give a strong diffracted beam; the diffracted beams form cones of ±θ to the planes. Figure 2-14 shows the two diffracted Kossel cones that represent each family of planes. As the diffraction angles (θ) are very small the Kossel cones are nearly parallel as observed on the phosphor screen [93].

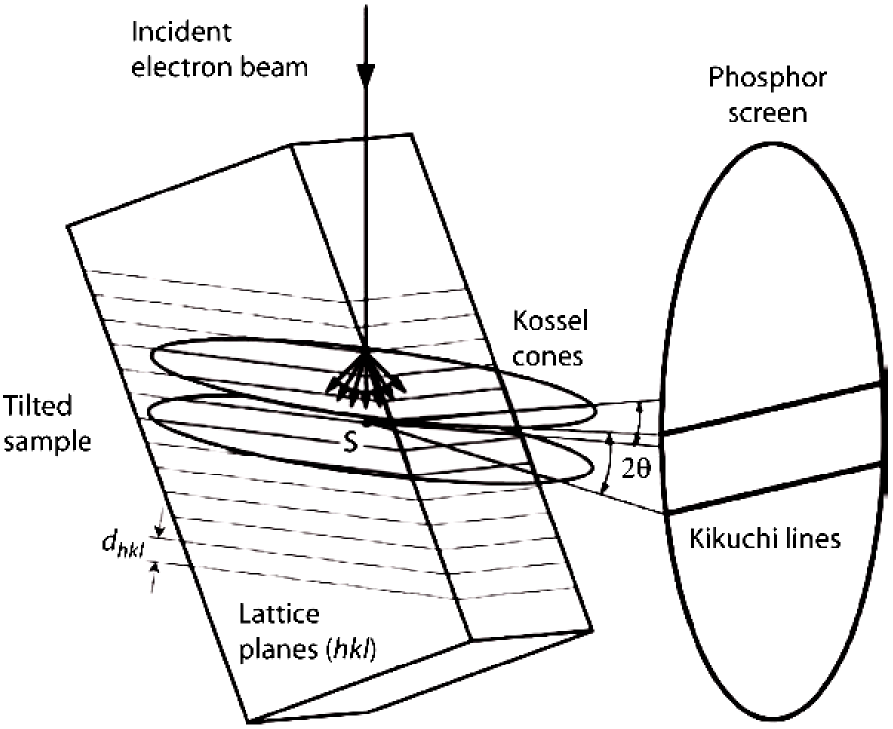

Figure 2-14. Schematic the diffracting plane, the specimen (tilted at 70 °) and the phosphor screen [92].

2.6.3 Kikuchi patterns (electron diffraction)

2.6.3.1 Working principles

A phosphor screen is placed in line with a charge coupled device (CCD) camera (see Figure 2-13) so as to interpret these diffracted beams also known as Kikuchi lines. The Kikuchi pattern is made of parallel lines (bands), which are unique and illustrate various crystallographic planes, as shown in Figure 2-15. The angular separation of two Kikuchi lines (2θ) is proportional to the interplanar spacing and each pair corresponds to a distinct set of crystallographic planes. A zone axis is identified by the intersection of bands, with the major ones corresponding to where a number of bands intersect. Thus all the interplanar and interzonal relationships are illustrated by the Kikuchi bands [94].

With EBSD it is possible to obtain useful information about crystallographic orientations, texture, Schmid factors of grains, as well as obtaining useful information about the volume fraction of individual phases [92]. This crystallographic information may be utilised to gain enhanced understanding the strains resulting from the martensitic phase transformation.

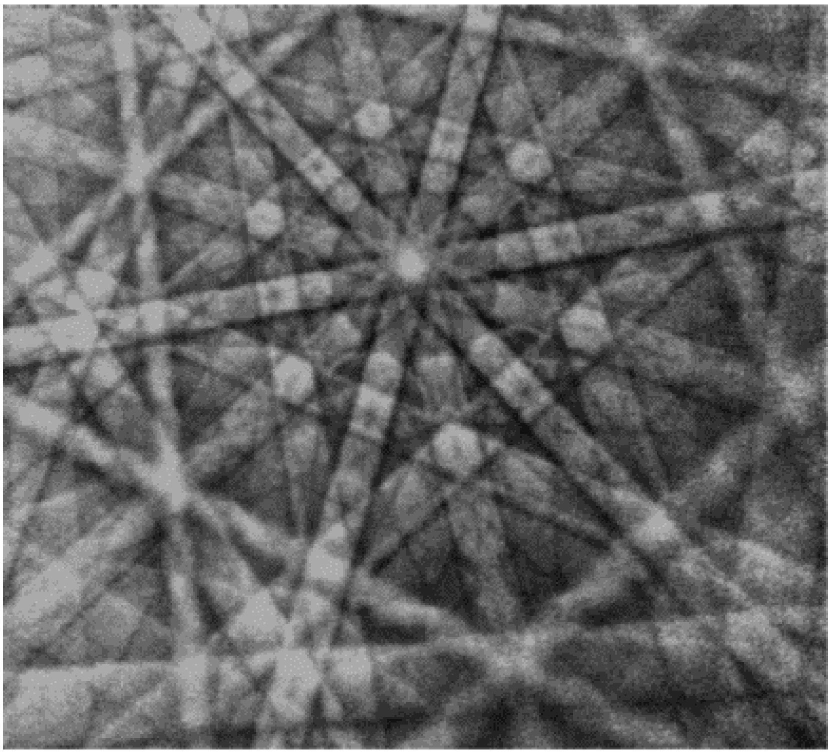

Figure 2-15. Kikuchi bands from cadmium on the phosphor screen 20 kV accelerating voltage [92].

2.6.3.2 Phase fraction analysis with EBSD

The identification of phases using EBSD dates back to work of Baba-Kishi and Dingley [95] in which crystal symmetry, point and space group identities were directly extracted from patterns on a photographic film. However, most modern EBSD systems mainly use the following 4 steps to properly index a phase.

I. Obtaining the kikuchi pattern: As mentioned earlier, an EBSD kikuchi pattern is a pair of goniometric projections of Kossel cones from a point source in the crystal; each cone represents Laue's diffraction in positive and negative *hkl planes* (refer Figure 2-14). The center line between two bands corresponds to the line of projection of the diffracted crystal plane. The point of intersection of these lines corresponds to the zone axis of the crystal. The width of bands corresponds to the diffraction angle. Kikuchi patterns are usually analysed by the width of the bands. Considering the different symmetries in bands found at different zone axes after taking into consideration the distortion in goniometric projection of bands due to sample tilt, the crystal class can be determined. But symmetry may not be clearly visible for all crystals. Hence the unit cell of the lattice has to be determined.

II. Determining the crystal unit cell: This step involves setting one of the vectors of the unit cell to unity, calculating the relative magnitude of the other two vectors from interaxis angles and then identifying the best possible match from the crystal database using measured crystal and chemical parameters. There are already established Houghes algorithms in automated EBSD systems to do the best possible fit with accuracies better than 0.5 degrees. This method works well for phases that are already in the data base.

III. Discovering the lattice symmetry: However, if the phase is not in the data base, Dingley *et al.*, proposed a new method where a triclinic unit cell is constructed by finding at least 3 bands passing through the zone axis in the pattern [96]. The EBSD pattern is indexed as triclinic cell. The relationships between multiple orientations resulting from the symmetry of the crystal can be used to determine the symmetry of the crystal system. Then the crystal parameters can be determined by comparing simulated bands with measured bands.

IV. Re-indexing the pattern: The final stage involves re-indexing the kikuchi pattern according to the discovered crystal class [92].

2.6.4 Phase fraction analysis with Neutron Diffraction

In order to quantify the volume fraction of a particular phase within a sample, diffraction needs to be collected from all the phases present. In order to achieve this, either diffraction using multiple wavelengths or with a single wavelength over a wide angular range is necessary to cover a spread of lattice planes.

If the crystalline phases are randomly oriented, then their peak intensities are proportional to their volume fractions scaled by the theoretical intensity of that particular reflection. Cullity [85] listed the various factors that define the theoretical intensity of a peak as follows:

2.6.4.1 Polarization factor

It is difficult to measure and calculate the absolute intensity of the incident beam, however, for diffraction the relative intensities are sufficient to solve the problem. As the incident beam may not be polarized the term $\frac{1}{2}(1+\cos^2 2\theta)$, called the polarization factor, needs to be used and it is common to all intensity calculations.

2.6.4.2 Structure factor

Structure factor is denoted as '*F*'. It is simply obtained by adding the waves scattered by individual atoms within a unit cell. It is generally a complex number and it represents both the amplitude and phase of the resulting waves. It is defined as the ratio of amplitudes given below

$$|\mathrm{F}| = \frac{\text{amplitude of waves scattered by all atoms in unit cell}}{\text{amplitude of wave scattered by a single electron/neutron}}$$ *Equation 16*

The intensity of the beam diffracted by all the atoms in a unit cell is proportional to the term $|F|^2$, which is obtained by multiplying the structure factor with its complex conjugate [85]. Also, the structure factor is independent of shape and size of the unit cell, *i.e.*, a face-centered cubic cell will have reflections absent if h, k and l are mixed. For body-centered cubic cells reflections will be absent when (h+k+l) is odd. Therefore, the structure factor is very important as it enables the calculation of intensity, based on the knowledge of atomic position within the unit cell.

2.6.4.3 Multiplicity factor

The multiplicity factor (p) represents the number of different (hkl) planes having the same lattice spacing. For example the multiplicity factor of {111} planes in a cubic crystal is 8 while that of the {100} planes is 6. It is different for different crystal systems. Detail can be found in Appendix 9 of reference [85].

2.6.4.4 Lorentz Polarization factor

Certain trigonometrical factors can affect the intensity of the reflected beam [85]. This effect is defined by the Lorentz factor

$$\text{Lorentz factor} = \frac{1}{4\sin^2\theta\cos\theta}$$

Equation 17

Combining it with the polarization factor gives:

$$\text{Lorentz} - \text{Polarization factor} = \frac{1+\cos^2 2\theta}{\sin^2\theta\cos\theta}$$

Equation 18

2.6.4.5 Absorption factor

The amount of beam being absorbed within the material is another factor that needs to be considered. The exact absorption factor is difficult to calculate and this effect is usually neglected while making intensity calculations [85].

2.6.4.6 Temperature factor

In a unit cell, atoms are not stationary but undergo thermal vibrations, even close to absolute zero [85]. The vibrational amplitude of atoms increases with temperature. This thermal vibration leads to a spread in range of the lattice planes and thereby decreases the intensity of the diffracted beam. This means that the atoms do not lie on perfect mathematical planes but rather on plate-like regions of varying thickness. Thermal vibrations do not cause a significant peak broadening of the diffracted peaks.

With the above principles clear, we next move to measuring the intensities of the diffracting peaks. When neutrons are irradiated on a material, each grain family forms a unique diffraction pattern. Each diffraction pattern (peak(s)) represents distinctively the austenite and martensite {hkl} planes present in the material. ASTM E 957-03 standard [97] outlines an expression that can be used for austenite volume fraction determination in steels,

$$I_{\alpha}^{hkl} = \frac{K R_{\alpha}^{hkl} V_{\alpha}}{2\mu} \qquad \textit{Equation 19}$$

Where:

$$K = \left(\frac{I_o^{e^4}}{m^2 c^4}\right)\left(\frac{\lambda^3 A}{32\pi r}\right) \qquad \textit{Equation 20}$$

And

$$R_{\alpha}^{hkl} = \frac{|F|^2 p L P e^{-2M}}{v^2} \qquad \textit{Equation 21}$$

Where:

I_{α}^{hkl} = integrated intensity of the (hkl) diffraction peak in the α phase,

I_o = intensity of the incident beam

μ = linear absorption coefficient of steel

e,m = charge and mass of electron/neutron r = radius of the diffractometer

c = velocity of light

λ = wavelength of incident radiation

A = cross sectional area of the incident beam

ν = volume of the unit cell

$|F|^2$ = Structure factor times its complex conjugate

P = multiplicity factor

θ = Bragg's angle

LP = Lorentz Polarization factor

e^{-2M} = Debye-Waller or temperature factor. This is function of θ, where $M = B(\sin^2\theta)/\lambda^2$, $B = 8\pi^2\mu_s^2$, μ_s^2 is the mean square of displacement in the direction perpendicular to the diffracting plane and V_α = Volume fraction of the α plane.

2.6.4.7 Phase fraction quantification

Moat *et al.* modified the above equation to account for the difference in scattering properties of X-rays compared to neutrons [2]. They used this relative peak intensities approach by comparing each of the diffracting peaks and austenite volume fraction was quantified using the following equation:

$$V_\gamma = [\frac{1}{q}\sum_{j=1}^{q}\frac{I_{\gamma j}}{R_{\gamma j}}/\{\left(\frac{1}{p}\sum_{i=1}^{p}\frac{I_{\alpha j}}{R_{\alpha j}}\right)+\left(\frac{1}{q}\sum_{j=1}^{q}\frac{I_{\gamma j}}{R_{\gamma j}}\right)\}] \qquad \textit{Equation 22}$$

Where I_γ and I_α are the integrated intensities of the austenite and martensite reflections respectively. R_γ and R_α are the Rietveld number for the respective phases. However, this equation does not take into account the hexagonal epsilon martensite phase, which was measured and therefore the equation was further modified as follows:

$$V_{\gamma} = [\frac{1}{q}\sum_{j=1}^{q}\frac{I_{\gamma j}}{R_{\gamma j}} / \{\left(\frac{1}{p}\sum_{i=1}^{p}\frac{I_{\alpha j}}{R_{\alpha j}}\right) + \left(\frac{1}{q}\sum_{j=1}^{q}\frac{I_{\gamma j}}{R_{\gamma j}}\right) + \left(\frac{1}{r}\sum_{j=1}^{r}\frac{I_{\varepsilon j}}{R_{\varepsilon j}}\right)\}] \qquad \textit{Equation 23}$$

Where I_{ε} and R_{ε} are the integrated intensity and Rietveld number of the epsilon martensite reflection. A similar approach was used by Hedstrom *et al*. for volume fraction measurements using high-energy X-ray diffraction [98].

2.7 Diffraction apparatus

In this section, for the purposes of brevity, only diffraction apparatus that is capable of determining the volume fraction of phases in engineering alloys (particularly steel) will be discussed.

2.7.1 Neutron diffraction using a constant wavelength

When a neutron beam impinges on a monochromator crystal, it generates a monochromatic neutron beam that follows the Bragg's equation. This generates a set of diffracting beams, from which a selected monochromatic beam is irradiated on the sample/specimen being measured. The diffracted beam from the specimen follows Bragg's Law and can be recorded by a neutron detector. A detailed description of the process can be found in books by Fitzpatrick & Londini [99] and Hutchings *et al.,* [100]. The use of monochromatic radiation is the most widely used neutron diffraction technique. An example is the SALSA (Strain Analyser for Large and Small scale engineering Applications) instrument at the European Institute Laue Langevin (ILL) [101]. Here the neutrons are produced from nuclear fission using a highly enriched ^{235}U isotope [99].

The SALSA instrument has a continuous high flux neutron beam, it is flexible and is well suited for the study of a broad range of materials science and engineering materials. It can be used to measure very large samples and is optimized for high spatial and strain resolution [101]. Usually, using a constant wavelength source, only one {hkl} lattice plane may be measured at a time, which was not ideal for the measurements required in this research project. For the measurements required in this dissertation, the entire spectrum (number of {hkl} peaks) needs to be analysed simultaneously and this may be done using a time of flight diffractometer.

2.7.2 Neutron diffraction using the time of flight technique

The measurements reported in this dissertation were made on a time of flight neutron diffractometer, at a pulsed neutron source, the ISIS facility at the Rutherford Appleton Laboratory, UK. Here, intense pulses of protons at 50 Hz are accelerated by an 800 MeV Synchrotron accelerator before they collide with a tungsten target, producing neutrons through a spallation process [102]. The tungsten target is bombarded with these high energy protons and approximately 15 neutrons are produced for every incident proton [99]. These neutrons need to be slowed down before they can be used for materials research. They are slowed by hydrogen containing moderators (CH_4, H_2O or H_2) around the target before being directed to the neutron instruments to explore different material properties.

The advantages of using a spallation source are that less heat is produced near the target and the bright neutron pulse has a flux comparable to reactor sources; however, the average flux at the experimental stations is much lower [99]. Most importantly the time of flight technique has the ability to investigate numerous {hkl} lattice planes simultaneously with high precision. In this dissertation this means that diffraction peaks can be obtained from both the austenite and martensite phases simultaneously. Furthermore, the changes in the relative peak intensities of the individual Bragg peaks enable the preferred crystallographic orientation evolution to be investigated, both qualitatively and quantitatively [99].

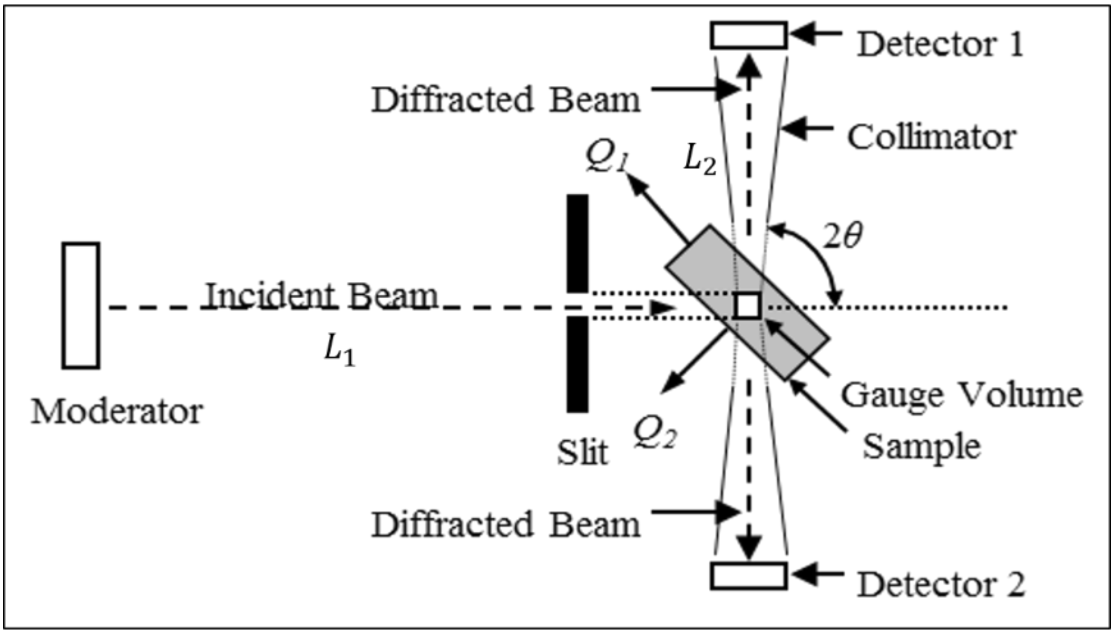

Figure 2-16. Schematic of a time-of-flight neutron strain scanner is illustrated. The elastic strains are measured along the directions Q1 and Q2. The gauge volume explored by the instrument is defined by the intersection of the incident and diffracted neutron beams, which are defined by the slits and the collimators [103].

After being generated at the target, the neutrons travel a distance L along the respective beam lines. The time of flight for each neutron is measured, enabling measurement of its wavelength [99]. The time of flight depends upon its momentum and its wavelength as given by the de Broglie equation:

$$\lambda = \frac{h}{m_n \nu} = \frac{h\,t}{m_n L}$$ *Equation 24*

Where h is the Planck's constant, m_n is the mass, ν is the velocity and t is the time of flight of the neutron. Substituting these values in Bragg's equation

$$t = \frac{2\, d_{hkl}\, L\, m_n\, \sin\theta_{hkl}}{h} \qquad \textit{Equation 25}$$

Now lattice planes d_{hkl} for a particular set of {hkl} lattice planes within the sample may be determined by measuring the time of flight (t) of neutrons from the moderators to the detectors, knowing the diffracting angle (2θ) and the path length L (moderator to sample (L_1) + Sample to detector (L_2)), as shown in Figure 2-16. To measure a large number of {hkl} lattice planes (diffraction peaks), the time-of-flight technique uses a wide wavelength range typically (0.5 – 5 A°) [99]. Figure 2-17 shows a typical diffraction spectrum for an austenitic stainless steel taken at the ENGIN-X instrument (details of which are discussed later in the section), using the time of flight (TOF) principle.

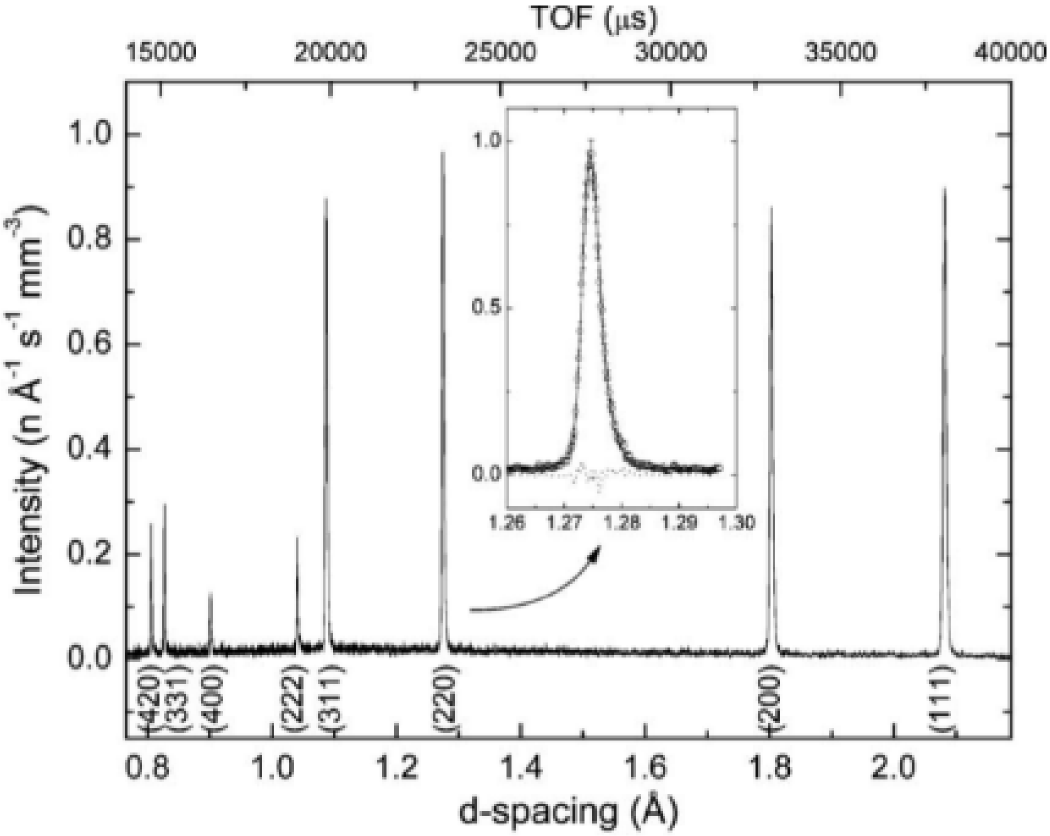

Figure 2-17. Typical diffraction spectrum of austenitic stainless steel at ENGIN-X [103].

Furthermore, in bulk materials the average velocity of neutrons depends on the temperature T. At thermal equilibrium the average kinetic energy of each neutron remains constant. The neutrons can be represented as an ideal mono-atomic gas with three translational degrees of freedom. Applying the Equipartition Theorem gives [104], [105]:

$$E_{avg} = \frac{1}{2} m_n v^2 = \frac{3}{2} k_B T$$

Equation 26

Where k_B is the Boltzmann constant. Now the velocity of neutrons in a bulk material can now be expressed as:

$$v = \sqrt{\frac{3 k_B T}{m_n}}$$

Equation 27

Using the above equations, the velocity and wavelength for different neutron energy ranges were calculated and the results are shown in Table 2-3.

Table 2-3. Velocity and wavelength of different neutrons

Type of Neutron	Energy Range (MeV)	Temperature range (K)	Velocity (ms^{-1})	Wavelength (A°)
Cold	0.1-5	1-60	150-1200	10-80
Thermal	5-100	60-1000	1200-4800	2.5-10
Hot	100-500	1000-6000	4800-12000	1-2.5

The thermal neutrons have wavelengths comparable to the {hkl} lattice spacing in most engineering materials.

For strain measurements, applying the Rietveld refinement technique (a technique that fits a theoretical profile to a measured profile) [106], the information from all the diffraction peaks may be used for establishing the average unit cell parameters a, b and c. At a specific point within the sample, once the lattice parameter 'a' is determined, it is straightforward to calculate the corresponding strain ε using the equation below [99]:

$$\varepsilon = \frac{a - a_0}{a_0} \qquad \textit{Equation 28}$$

Where a_0 is the reference lattice parameter from a stress-free material. At a pulsed source, many diffraction peaks are obtained simultaneously, which produces a wealth of information about the material and its internal stress state.

The volume of material diffracting corresponds to the intersection of the incident and the diffracted neutron beams, which are dependent on the size of the slits and the collimators as shown in the Figure 2-16. However, for measurements reported in this dissertation, the gauge volume was larger than the sample dimensions. It was assumed that the sample stays in place throughout the deformation process, as the instrument and stress rig were well-aligned, *i.e.* no out of plane movement takes place during the straining process. The centroid of the gauge volume was defined as the measurement point [103] and in the experiments made here, it was the centre of the sample. However, the neutrons penetrate deep into the materials, making it possible to measure bulk stresses/phases in thicker samples without damaging the material, or in other words, non-destructively.

It is worth noting that strain measured this way is actually a vector quantity (*i.e.* the strain is measured in either the longitudinal (parallel to loading) or transverse (perpendicular to loading) direction) and measured along the direction Q given by the following equation

$$Q = K_1 + K_2 \qquad \textit{Equation 29}$$

Where K_1 and K_2 are the directions of the incident and scattered neutron beams respectively and having magnitudes $K = 2\pi/\lambda$.

Some of the limitations of the neutron diffraction technique are associated with the fact that they are laboratory-based measurements at national facilities, where access is not always easy and can be expensive. Moreover, the technique is only applicable to crystalline materials. The grain size and texture may affect the measurements, in addition to the size (volume and weight of the test specimen) restrictions. Compared to X-rays, neutrons have low flux (partially compensated as neutrons are less absorbed and have a superior signal to noise ratio)[99].

2.8 Strain Measurement

Strains can be a consequence of deformation, *i.e.* when a body is under applied stress. Engineering strain may be defined as the change in length of a prescribed initial length [107], or simply the change in length over initial length. Whereas, at the microstructural length scales, strains are the mismatches between lattice planes, arising due externally applied stress, presence of defects, or due to phase transformations. There are various methods for strain measurement and they are classified as either mechanical or diffraction methods [108], relaxation [109], diffraction and other techniques [109], destructive, semi-destructive and nondestructive procedures [37].

Classification here is based on the length scale requiring to be measured, which may be further categorized as either bulk or local strain measurement techniques.

2.8.1 Bulk methods

As discussed above, the techniques that are used to measure the strains (and corresponding stresses), that vary over large length scales may be classed as bulk measurement methods. These strains may be measured using contact based (strain gauges, or extensometers), or non-contact based (e.g. digital image correlation (DIC), or diffraction) techniques. Strain gauges or extensometers are attached onto the specimen being measured and they measure the average strain in the gauge section over many thousands of grains in engineering alloys [107].

Some of the diffraction-based techniques may be used to measure strains for the bulk material, in a non-destructive manner. For e.g. in neutron diffraction, this is done by measuring changes in the interplanar spacing (atomic planes), for crystalline or polycrystalline materials [99] and from a large number of diffracting grains.

DIC is a non-contact method to measure strains. It compares images acquired prior to and post deformation and computes the full-field displacement of an object in either tension or compression. DIC can be used to obtain global strain, *i.e.* strains at small length scales, to strains in large engineering structures. Detailed explanation of the process is given in Section 2.8.4.

2.8.2 Local methods

Most of the contact techniques are not suitable for the measurement and characterisation of local variations of strains in materials. In this PhD project, DIC and electron backscatter diffraction (EBSD) were used and developed as effective tools for strain measurements at the microstructural length scales. DIC correlation was done using images acquired before and after deformation process, using the atomic number contrast imaging mode within a scanning electron microscope (SEM). These were then correlated with the crystallographic microstructural features obtained using EBSD. EBSD was also used to quantify the increase in plastic deformation at different increments of global strain. A brief explanation of the various processes used is given in the following sections.

2.8.3 Effect of strain on EBSD pattern

In engineering materials strain localisation/ concentration near microstructural features, such as inclusions, precipitates, secondary phases and grain boundaries needs to be studied in detail to understand the deformation processes or reasons for failure. There is an observed change in the EBSD pattern of a strained material, which may be either elastic or plastic [92], [110].

2.8.3.1 Elastic strain

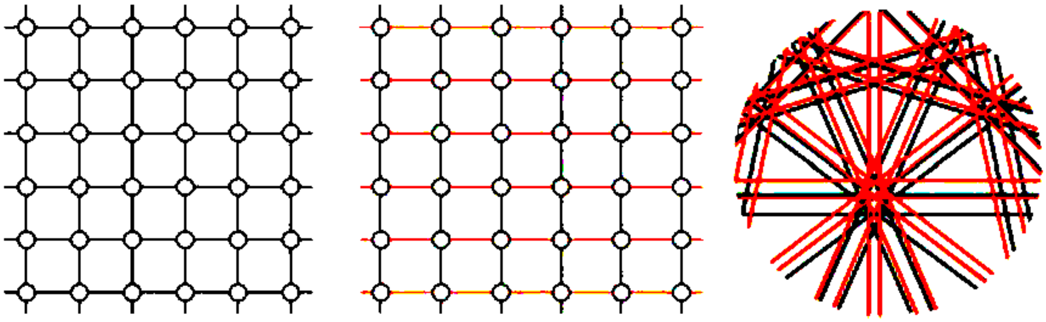

Figure 2-18 A crystal lattice strained 11% uniaxially in the horizontal direction and a schematic overlay of the patterns with (red) and without strains (black) [110].

There is distortion of the crystal lattice due to elastic strains. This distortion may appear in an EBSD pattern as shifts in the zonal axis or change in the widths of some diffracting bands [110]. Figure 2-18 shows these elastic strain exaggerated and typical elastic strains only show changes of just a pixel or two in typical EBSD patterns. On retracting the cameras in an EBSD system, improved pixel resolution can be achieved and thus finer pattern shift maybe measured. However, there is an associated drop in signal and it becomes difficult to measure high quality patterns. Thus, to make meaningful elastic strain measurements, very careful image analysis of patterns needs to be made [110].

2.8.3.2 Plastic strain

Plastic strain degrades the pattern quality of diffraction patterns. This is one of the reasons very careful sample preparation is critical to good EBSD measurement [111]. Care must be taken during the polishing stages to ensure no plastic strain is induced. Dislocations accommodate distortion in crystal lattices when they are plastically deformed [110] and be classified as:

i. Statistically stored dislocations (SSD) are encountered in materials with significant dislocation density, but have a net zero Burgers vector. The diffraction patterns from this volume are degraded due to local perturbations of diffraction lattice planes, leading to incoherent scattering as shown in Figure 2-19. Higher dislocation density leads to greater degradation in pattern quality.

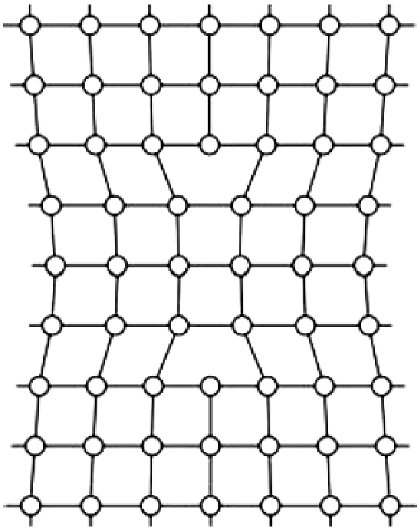

Figure 2-19. Diagram showing the disturbance in the crystal lattice due to two opposing edge dislocations with a net zero Burgers vector[110].

ii. Geometrically necessary dislocations (GND) have a net non-zero Burger’s vector across which crystallographic orientation may vary and arrays of GND can form subgrain boundaries. If a diffracting volume contains GND, then degradation in pattern quality is due to the super-position of individual subgrain over one another as shown in Figure 2-20.

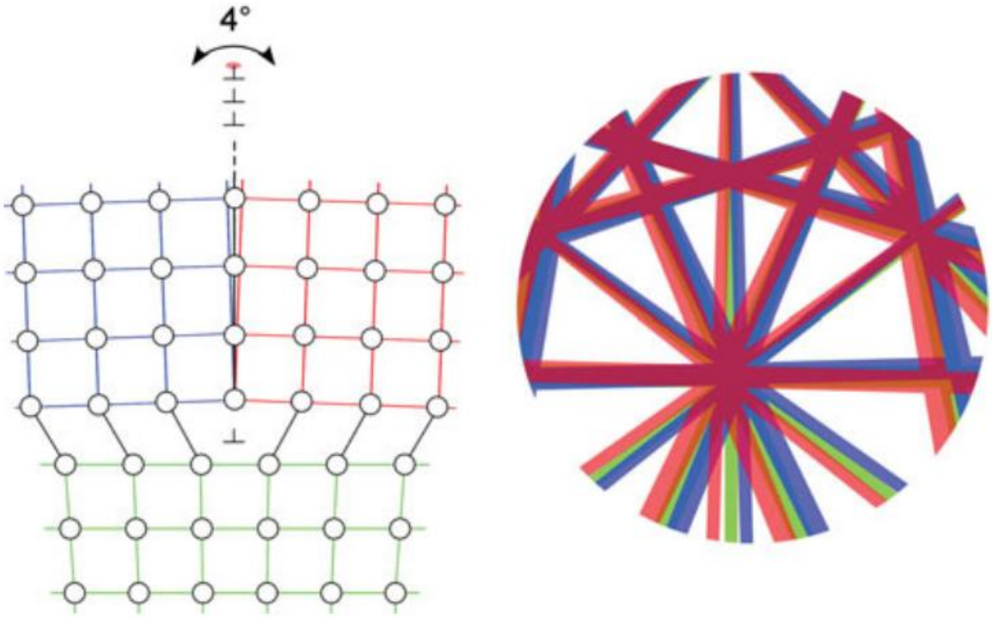

Figure 2-20. Schematic showing the effect of sub-grain boundary on the EBSD pattern [110].

2.8.4 Micro scale strain assessment with Digital Image Correlation

The digital image correlation (DIC) technique was developed by a group of researchers at the University of South Carolina in the 1980s [112]–[115]. The 2D-DIC technique is a non-contact method to measure in-plane deformation of a planar object surface in tension or compression, using images acquired with a camera. DIC has also been successfully applied to measure the out of plane distortion, using a 3D DIC technique [116]. However, the work in this project focusses on 2D DIC, therefore discussions here will be limited to the various aspects associated with only 2D DIC.

2.8.4.1 Theory and background of DIC

For any material investigated, DIC can provide full-field displacements and subsequently full-field strain measurements to sub-pixel accuracy, by correlating images taken before and after deformation process [117]. Thus full-field displacement maps are obtained by comparing small sub-regions within the images, throughout the deformation process [116]. Information (features-variation in grey scale) is needed in each sub-region (subset), in order identify it and to track it throughout the deformation process. These features are also known as speckle patterns and when random, these features enable the unique identification of the subset tracked. These patterns may include lines, grids, dots and arrays [116]. DIC is also known as the digital speckle correlation method (DSCM), texture correlation, computer aided speckle interferometry (CASI) and electronic speckle photography [117].

The following sections outline the various requirements that need to be considered for full field strain measurements using DIC.

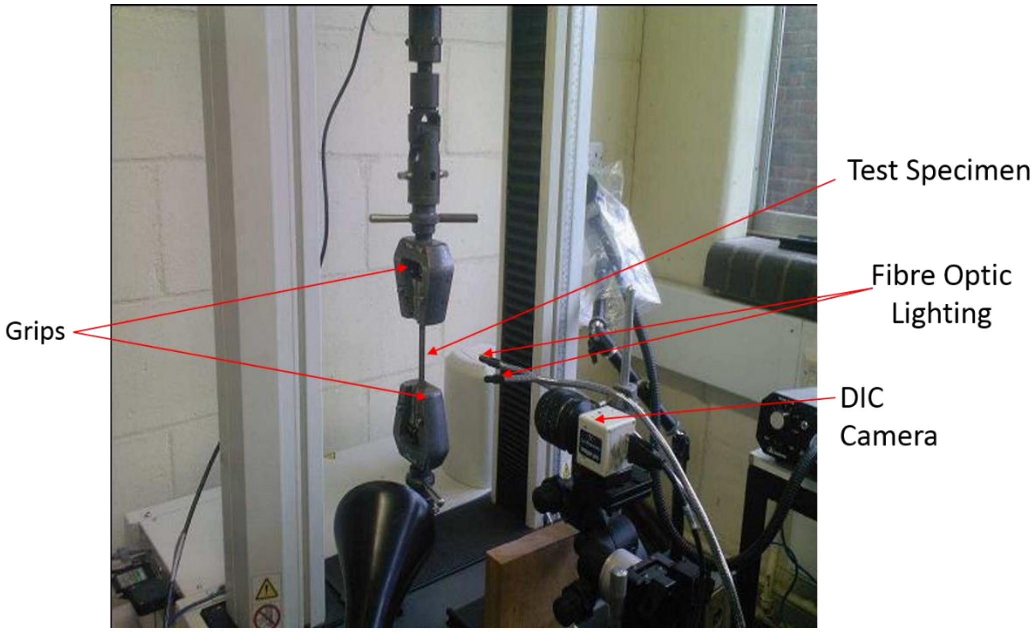

Figure 2-21: Optical image of 2D DIC acquisition system.

Figure 2-21 shows a typical setup that is used for 2D DIC. The specimen surface has a random speckle pattern that deforms along with the substrate and carries information about the surface deformation. This speckle pattern can be “natural” texture, obtained using spray paint, or in the case of this dissertation by the addition of tiny gold surface markers (this will be discussed later in Section 3.3). Imaging is done continuously throughout the deformation onto the camera sensor. The optical axis of the camera is kept normal to the surface of the specimen. The following considerations should be kept in mind to get accurate displacement measurements

- The specimen should remain flat and remain in a plane parallel to the camera sensor (backscatter electron detector in this dissertation) throughout the loading [115], [118].

- The imaging system should not give rise to any geometric distortions. If there are any geometric distortion that cannot be avoided, then correction techniques can be used to remove them [119]–[122].

In DIC, care is required to maintain constant light intensity acting on the surface features throughout the test duration. This is performed in the SEM by maintaining consistent contrast and count intensity, whilst imaging during the deformation process.

2.8.4.2 Region of Interest

The region of interest is defined prior to making the correlation between the reference and deformed images. Correlation is achieved by tracking of surface features, so that displacements before and after deformation can be identified. However, matching of surface features at the single pixel level is very difficult due to limitations of the imaging systems and hence the images of the surface are divided into evenly spaced grids as shown in the Figure 2-22 (a). A square subset is used in place of a single pixel for matching. This is because a square subset has a wider variation in grey levels that helps to uniquely identify it in the deformed image. The displacements are computed for each point of the virtual grid to get the full field deformation Figure 2-22 (b).

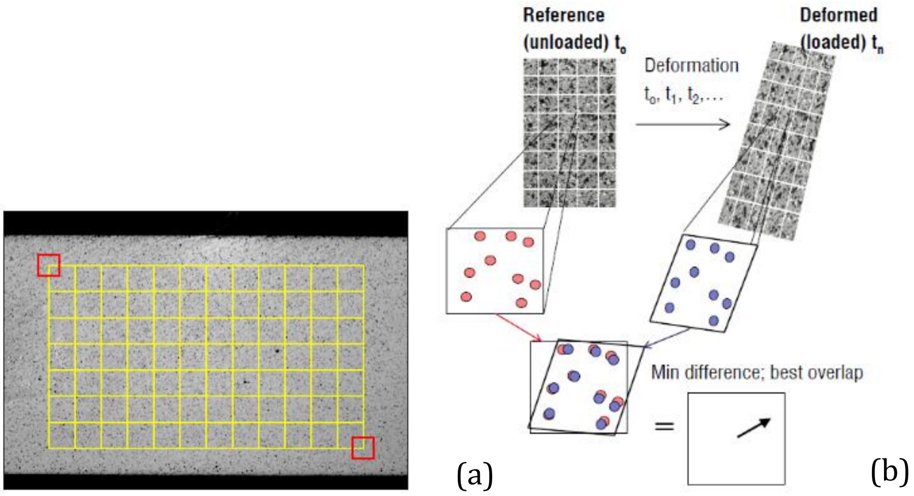

Figure 2-22: (a) Reference image, subdivided into subsets (b) subset tracking [117].

Usually, a square subset (a unit subset within the virtual grid) of (2M+1) x (2M+1) pixels is used from the reference image to track its corresponding location during the deformation of the image, where M is the midpoint of the subset.

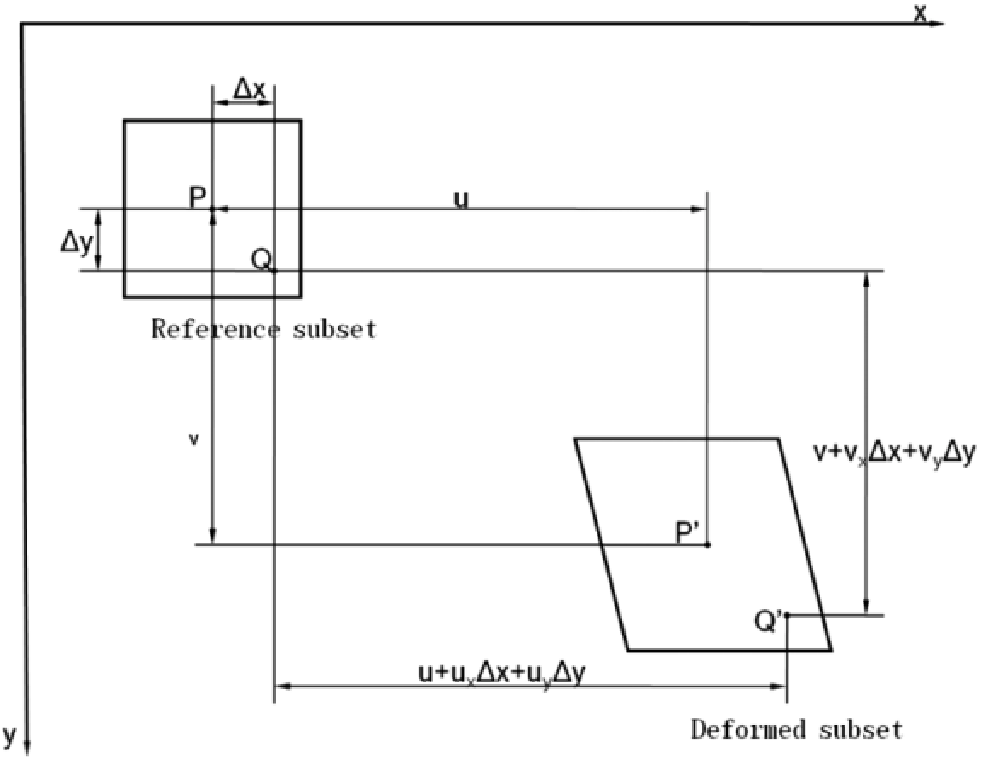

Figure 2-23: Schematic relationship between reference and deformed subset [123] .

2.8.4.3 Correlation Functions and Displacement Field Measurements

During material deformation it is quite possible that the subset (speckle pattern) deforms along with the substrate (see Figure 2-23 and Figure 2-24). However, the set of neighbouring points, within a sub-region, will remain a set of neighbouring points even in the deformed image. Here, the sampling region is moved and distorted in the deformed image in order to precisely match the reference and deformed images (see Figure 2-24). Thus, the schematic illustration in Figure 2-23 shows how the point Q around the subset centre P can be mapped in the deformed image subset using a correlation function.

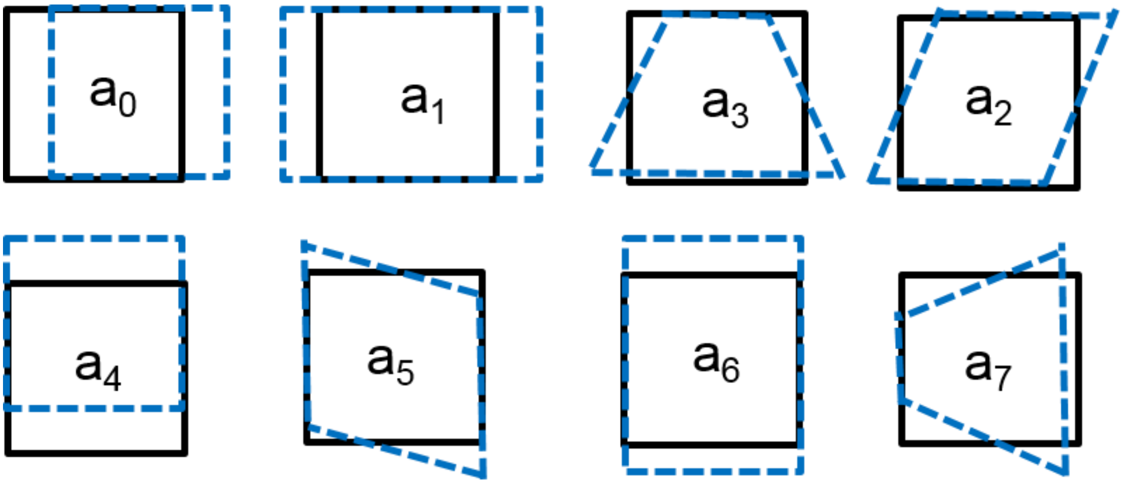

Figure 2-24. A schematic of change in shape of the subset, i.e. translation, stretch, shear and distortion is represented. Adapted from reference [124].

A cross-correlation function or sum-squared difference (SSD) function, can be used to help evaluate the degree of similarity between the reference and deformed subsets. Matching of the images is achieved by SSD of the grey level within an individual subset. The peak position of the distribution of correlation coefficient helps in completing this matching procedure. The position of the deformed subset is determined when the correlation coefficient extremum is detected (ideal scenario). In practice, a number of threshold parameters are defined. When any of these are reached (or in some cases a maximum number of iterations are completed), then this is taken as the answer. The reference and deformed images are matched by means of commonly-used correlation functions [116].

- Sum-squared difference (SSD)

$$C_{SSD} = \min_{a_0 \ldots, a_7} \Sigma \left(I_1(x, y) - I_2(a_0 + a_1 x + a_2 y + a_3 xy, a_4 + a_5 x + a_6 y + a_7 xy) \right)^2$$

Equation 30

For a given experiment, finding the minimum of the correlation function gives the best match between subsets at different strain increments (refer Figure 2-24 and the above equation). C_{SSD} is the correlation coefficient. The terms a_0 and a_4 indicate the x and y components of displacement vector of the subset being tracked (see Figure 2-24) and a_1, a_2, a_3, a_5, a_6 and a_7, are the affine transforms (see Figure 2-24).

2.8.4.4 Precision Errors in Digital Image Correlation

There may be certain errors in implementing 2D DIC that adversely affect its precision. These errors have been grouped by Pan *et al.* [117] into the following two groups.

1. Errors related to specimen, loading and imaging
    - Speckle pattern: The speckle pattern quality demonstrating various grey scales, such as different image contrasts or speckle sizes, can have an effect on the quality of the DIC measurements. It directly affects the selection of the subset size.

- Nonparallelism of the sensors and target and the object surface and out-of-plane displacement, *i.e.* surface of the specimen should be flat and parallel to the sensor.
- Imaging distortion: Optical imaging lenses may suffer from lens distortion. In this PhD project, as the SEM is to be used there may be errors due to both spatial and drift distortions, due to the electron beam rastering over the area of interest.
- Noise during acquisition and digitizing: Various sources of noise, such as shot noise, thermal noise and cut-off noise are unavoidable while recording images for DIC.

2. Errors related to the correlation algorithm
    - Subset size: The subset size should be large enough to have distinct intensity patterns, enabling it to be uniquely identified, still a small subset size is preferable.
    - Correlation function: Some correlation functions maybe more reliable and robust than others in the face of variable lighting.
    - Shape function: Second order shape yields a lower systematic error compared to a linear shape function when the random error is similar.

Thus, the quality of 2D DIC measurements depends both on the performance of the hardware as well as the correlation algorithm. The accuracy of 2D DIC, considering the above mentioned error sources, makes it challenging to evaluate.

2.8.4.5 Limits to resolution

Speckle pattern: The speckle pattern should be free of preferred orientation, be non-periodic and of a suitable size to resolve strain at a given length scale [116]. Typically the speckle patterns adhere to the surface and deform with it. Therefore, even under large translations and deformations, there is no loss of correlation. Further, pattern matching may be done throughout the entire surface when a suitable speckle pattern is applied. This allows for smaller subsets to be used for pattern matching throughout the deformation process. The limiting condition here is that within a subset there needs to be sufficient information (speckle-clusters of grey pixels within an image) available for it to be uniquely identified [116].

Lighting and Camera Resolution: There are always differences between the intensity of the image recorded at the different stages of the deformation process, even close to ideal conditions [116]. At times, these changes are localised and may not affect the entire sample. Now if the imaging sensor is kept at an angle, this may lead to localised brightness and contrast differences [116]. Therefore, pattern matching algorithms need to be developed that are able to precisely measure the correct correspondence between subsets throughout the deformation process, even when there is a significant change in the intensity values [116].

Surface preparation: Surface preparation is critical to getting good strain resolution in DIC. For 2D DIC, the surface needs to only move in plane throughout the deformation process and ideally should be free from surface irregularities or out of plane distortions. Details for the surface preparation used in this dissertation can be found in Section 3.2.1.

2.8.4.6 Application of 2D DIC

There are various applications of 2D DIC found in literature and Pan *et al*. [117] classified them into the following three groups

- When materials (e.g. metals, composites, polymer, biological materials) are mechanically or thermally loaded 2D DIC may be used for the quantitatively determination of the deformation field and for characterization of various deformation mechanisms [125]–[128].
- It can be applied to identify mechanical properties of material such as Young's modulus and Poison's ratio [119], [129], [130], residual stress and stress intensity factor [131]–[133] and thermal coefficient of expansion [134], [135].
- Deformation fields computed may be used to bridge the gaps between experiment, simulation and theory.

2.8.4.7 DIC for microstructural strain measurements

As 2D DIC deals with digital images, the digital images acquired from various high spatial resolution image recording devices can be directly processed using the 2D DIC method [117]. Various studies have been carried out on 2D DIC coupled with optical microscopy [136], [137], laser scanning confocal microscopy[138], scanning electron microscopy [18], [121], [122], atomic force microscopy[130] and scanning tunnelling microscopy [139]–[141]. Thus, with the above-mentioned techniques it is possible to measure deformation strains at the micro and nano-scales.

The speckle size and pattern quality affects the selection of a suitable subset size. The size of the subset should be such that it has a sufficiently distinctive light intensity pattern on the surface that helps in its unique identification. In addition for the accurate measurement of strains at the microstructural length scale, it is essential to develop a suitable (near nano-sized for some techniques) speckle pattern that will give enough spatial resolution within the subset. This will enable accurate measurements of strains that occur due to the γ to α' transformation. Hence, in this PhD project the aim is to use scanning electron microscope (SEM) to obtain sufficient resolution at the individual austenite grain scale.

In order to achieve grain scale resolution, first a suitable speckle pattern must be prepared such that it can be both imaged in the SEM and be of the appropriate scale and frequency for strain measurements. Therefore, in this study, a gold remodelling technique will be employed, as gold is a conductive material and gives excellent contrast with the steel background. Gioacchino *et al.* [18] developed this method in which a speckle pattern made of tiny gold particles is used for the measurement of strains on a similar scale to those produced by martensitic transformation.

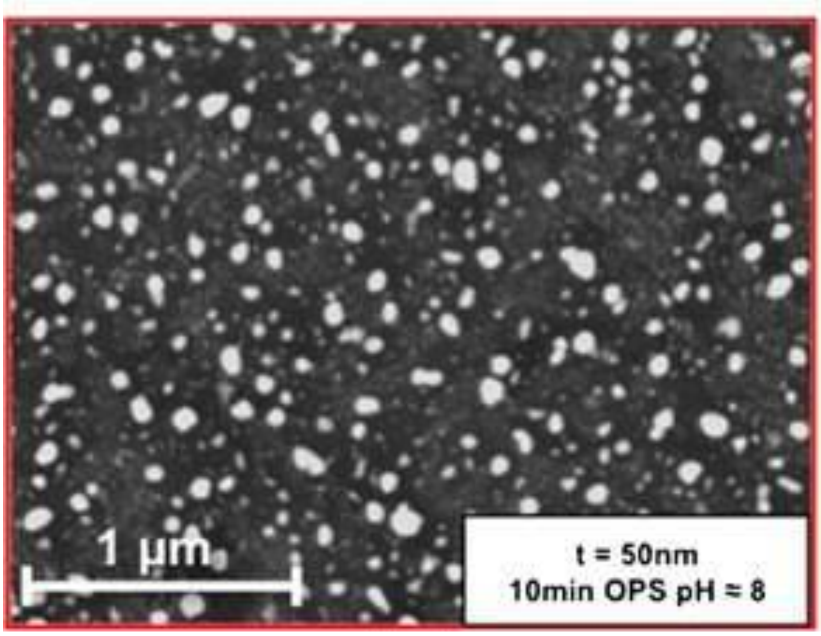

Figure 2-25: Speckle pattern formed after 1 hour exposure at 280 °C [18]

Figure 2-25 shows one of the gold remodelled surfaces from the work by Di Gioacchino and Fonseca [18], displaying high contrast between the gold speckles (white) and the steel background (dark). On account of very good contrast and small speckle size (in the nanometre range), very good strain resolution (tens of nanometres) is obtained using digital image correlation. Further details on the speckle pattern preparation for the measurement in this dissertation are given in the experimental work section 3.3.

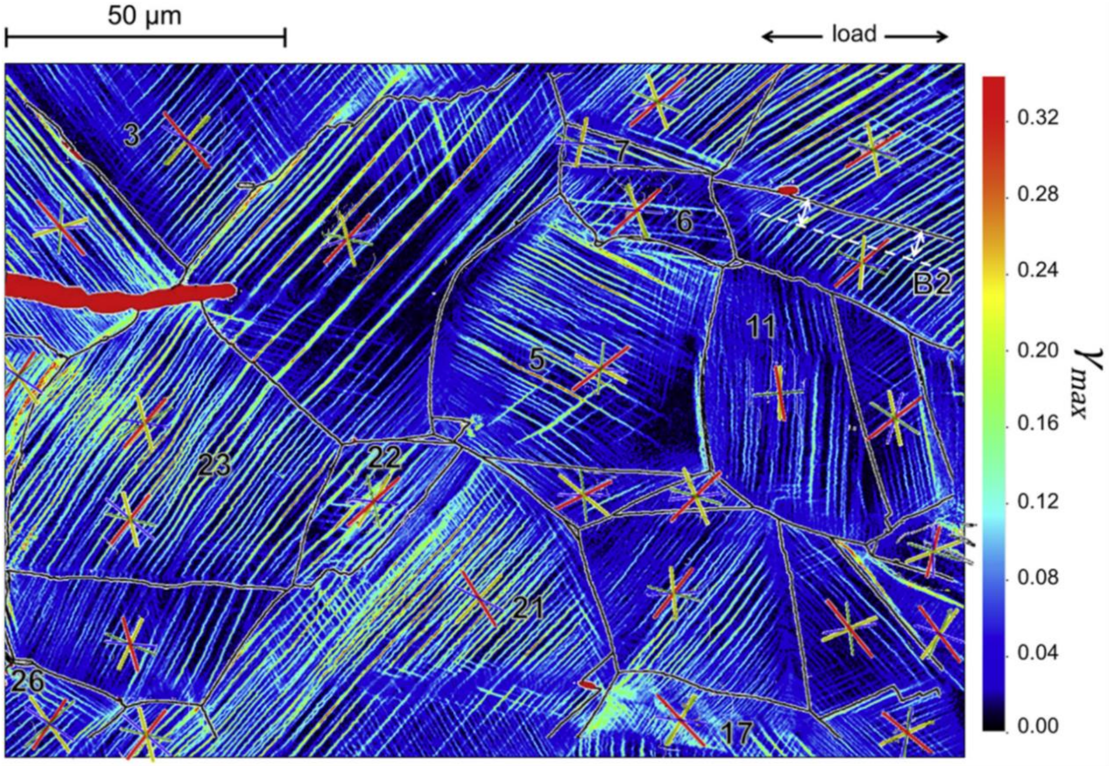

Figure 2-26. EBSD grain boundary maps overlaid on maximum shear strain maps at 6% strain. With the {111} slip plane traces overlaid, which are coloured (blue, green, yellow, red) according to increase in Schmid factor [22].

Using the above-mentioned speckle pattern, Di Gioacchino and Fonseca probed the plastic deformation of austenitic stainless steel, using the combination of HRDIC and EBSD [18], [22]. Figure 2-26 shows the EBSD grain boundary map overlaid onto the strain map, allowing for the deformation to be correlated with the microstructure. From the map it is clear that within individual austenite grains there may be different deformation domains active. Here, also bands are aligned towards a highly stressed {111} <110> slip system. Their imaging setup was such that the sample surface was very close to the detector, so that the most possible backscattered electrons get back to the detector. This results in excellent speckle contrast, which provides good correlation. This leads to good strain resolution, where strains from individual slip planes are clearly resolved.

It is significant to note that these experiments were carried *ex situ* and there was cumulative plastic straining of the microstructure.

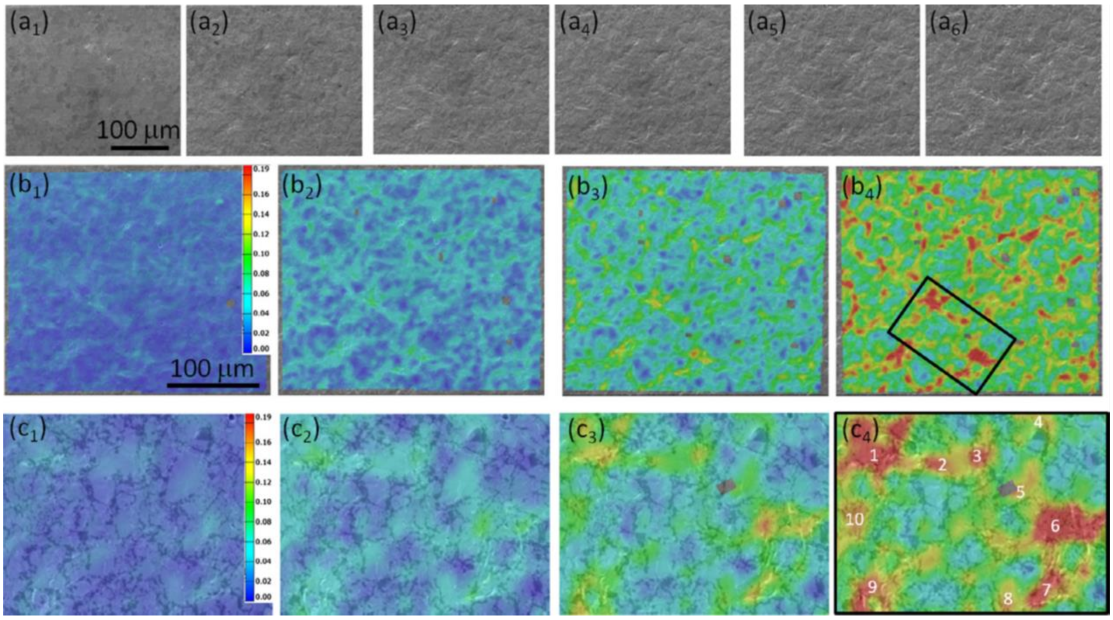

Figure 2-27. The secondary electron imaging carried out during the in-situ biaxial tension deformation experiment: (a) SE images, (b) local strain maps obtained by post-processing the SE images, (c) zoom-in region from these maps (location indicated by rectangular block in (b4)) [20].

Subsequently, other research groups have also applied EBSD and HRDIC technique, in order to associate the plastic deformation of a material to its microstructure. The work by Tasan *et al.*, probed the strain localisation and damage of a dual phase steel using HRDIC and crystal plasticity simulations [20]. Imaging was achieved using secondary electrons on etched surfaces (see Figure 2-27). Here it was not clearly stated how the overlapping of the EBSD and HRDIC data sets was done.

Carroll *et al.*, investigated experimentally the effects of grain orientation and neighbours on the elastic-plastic strain accumulation, on bcc tantalum using HRDIC and EBSD [142]. They matched DIC strain fields with EBSD grain measurements of grain structure using fiducial markers outlining the area of interest (see Figure 2-28). They were able to show the large strain heterogeneity within the microstructure, but could not resolve strain due to individual slip planes within individual grains.

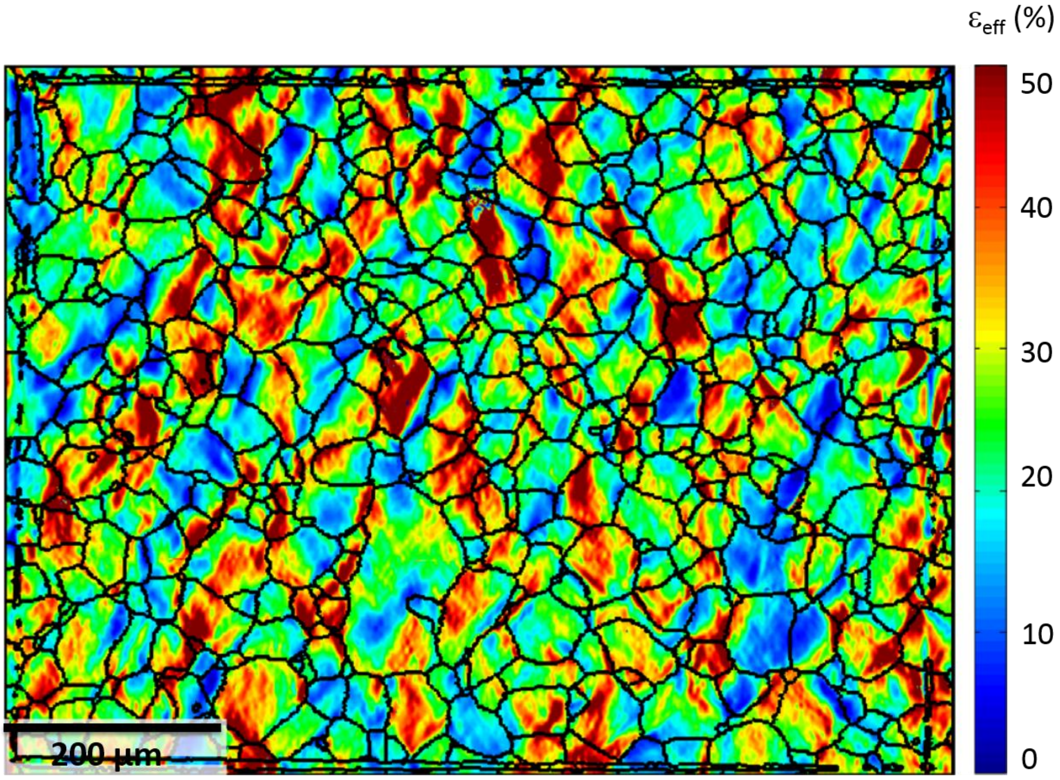

Figure 2-28. Effective strain field, ε_{eff}, in the polycrystals specimen at 25% applied strain [142].

Stinville *et al.* used an etched microstructure, to map full-field strain heterogeneity within a Ni based super alloy [143]. They showed very high-resolution strain fields and that the highest localised strains developed on {111} slip planes, which were parallel to and slightly offset from the annealing twins. However, there was no ideal technique presented to precisely overlay the EBSD grain boundaries over the full-field DIC strain maps. Furthermore, in their experiments, there was not clear indication to what imaging mode was used for image acquisition by in the SEM.

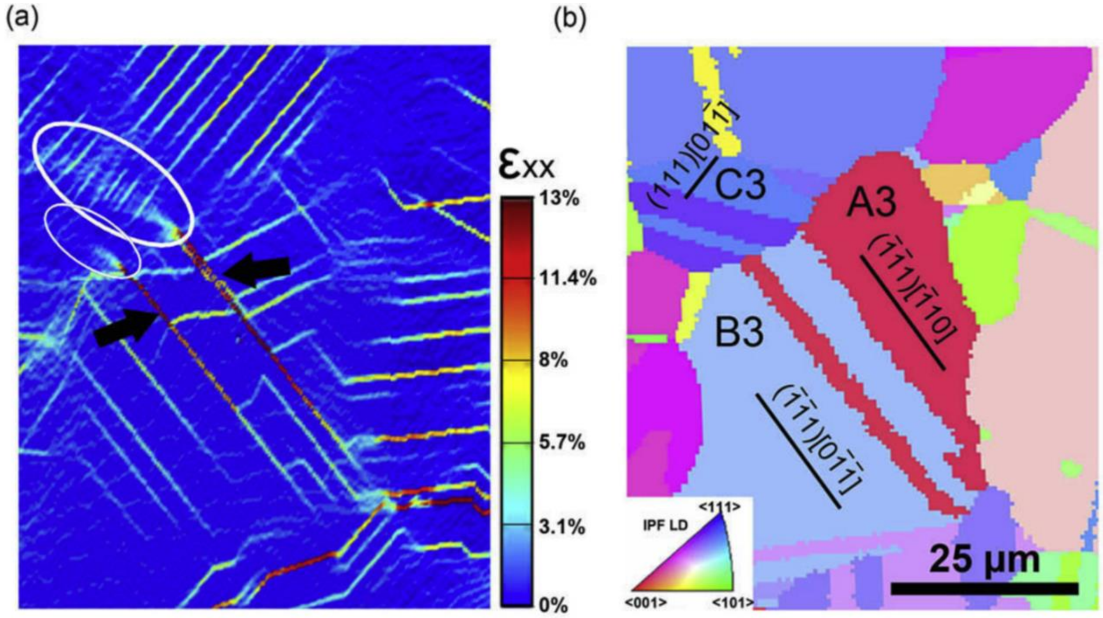

Figure 2-29. (a) Strain field ε_{xx} of a region of interest that was imaged under tensile loading; (b) associated EBSD map (before loading) [143].

In many of the experiments, in spite of the experiments being done *ex situ*, the strain resolution was not as clearly resolved as in the work reported by Di Gioacchino and Fonseca [22]. This is possibly due to the use of secondary imaging, imaging the region of interest far away from the detector, or on account of employing a standard scan speed in the SEM for their measurements. Further, the secondary electron dectector is positioned at an angle in the SEM and the resulting image is not fully flat, *i.e.* the surface markers on the specimen surface will be distorted. Due to the above mentioned reasons, the work presented in this dissertation follows the same approach as outlined by Di Gioacchino and Fonseca in reference [18], *i.e.* using backscatter electron imaging. The only major difference being that the experiments conducted in this dissertation were done *in situ* in an SEM.

2.9 Assessment of measurements in the literature

Very desirable mechanical properties may be obtained owing to the strain-induced martensitic transformation in metastable austenitic stainless steels and therefore these steels have been thoroughly investigated in various reports [4], [13], [14], [98], [144]–[148]. Usually, austenitic stainless steels are stable at room temperature and only form martensite when they are cooled to low temperatures below their M_s-temperature. However, as discussed in Section2.3.2, applying external stress may supply enough energy for the strain induced transformation to occur. Early studies looked at how plastic deformation of the austenite lattice usually preceded the martensitic transformation. These studies showed plastic deformation of the localised areas within the austenite lattice lead to the creation martensitic nucleation sites, which transform with further deformation. Olson and Cohen proposed that nucleation sites were at shear-band intersections [50], [60] and some of the more recent work by Talonen [144], using SEM and electron channelling contrast imaging confirmed this observation.

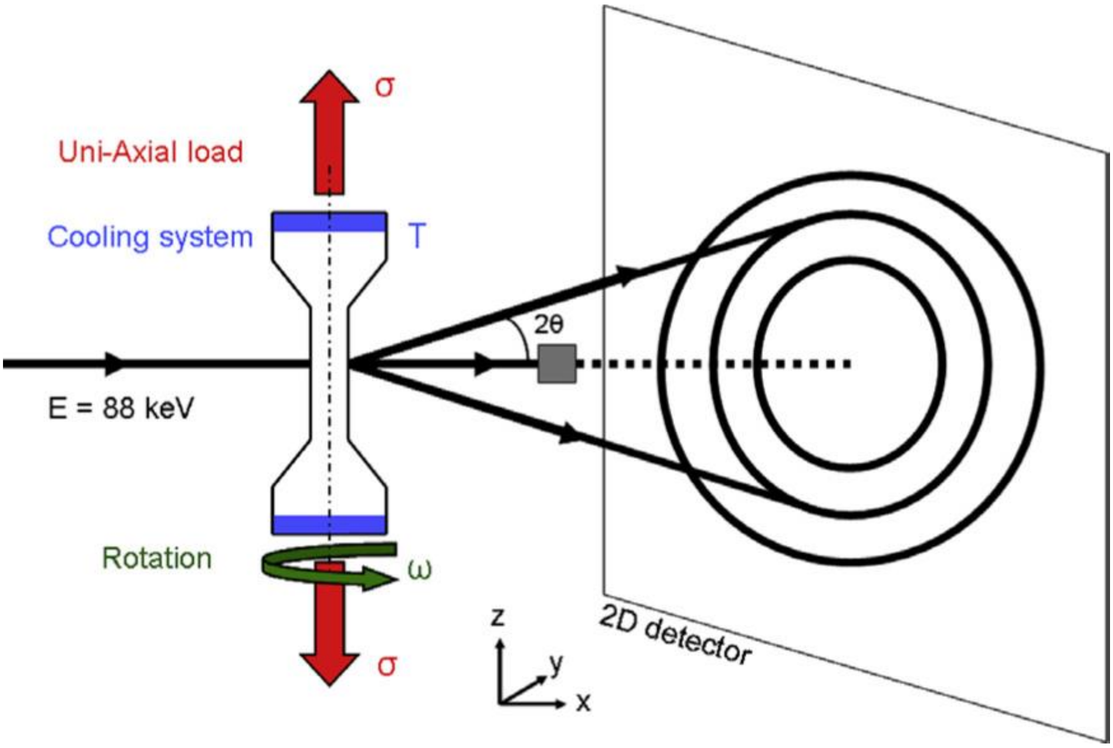

Figure 2-30. Schematic representation of the experimental setup used for the high-energy microbeam X-ray diffraction experiments on low-alloyed TRIP steels. The sample under tensile stress is cooled at both the ends. During exposure the sample was continuously rotated around the vertical axis [149].

Jimenez-Melero *et al*. and Blonde *et al*. investigated stability of individual austenite grains, using synchrotron X-ray diffraction experiments, when a low alloy TRIP steel was cooled down to form martensite [74], [149]. The schematic of the experimental setup is as shown in Figure 2-30. Here, as explained in the Section 2.5, the microstructure of TRIP steel comprised of metastable austenite (white grains), which was within a ferrite matrix (grey) and bainite phases (dark grey), see Figure 2-31. A schematic of the microstructure is given inset in Figure 2-31 and it indicates the location of the austenite, bainite and ferrite phases. Jimenez-Melero *et al*., measured the change in volume of individual austenite grains as cooling progressed [74]. In their measurements, there was a large variation of transformation behaviour of the individual grains measured, which showed how the grain stability variation between individual grains. In other words, some grains transformed completely, there was partial transformation in other grains and some very stable grains did not transform at all. Further, Jimenez-Melero *et al*. [74] and Blonde *et al*. [149] showed that grains with the lowest carbon content and the highest grain volume had the least stability and transformed at higher temperatures during the cooling process. Blonde *et al*. further showed that at the lower temperatures, there is enhanced tendency for a reduction in the intensity of the {220}, {200} and {311} austenite reflections, with increase in plastic deformation [149]. They further illustrated that there is a tendency martensite to form on the {200} austenite grains.

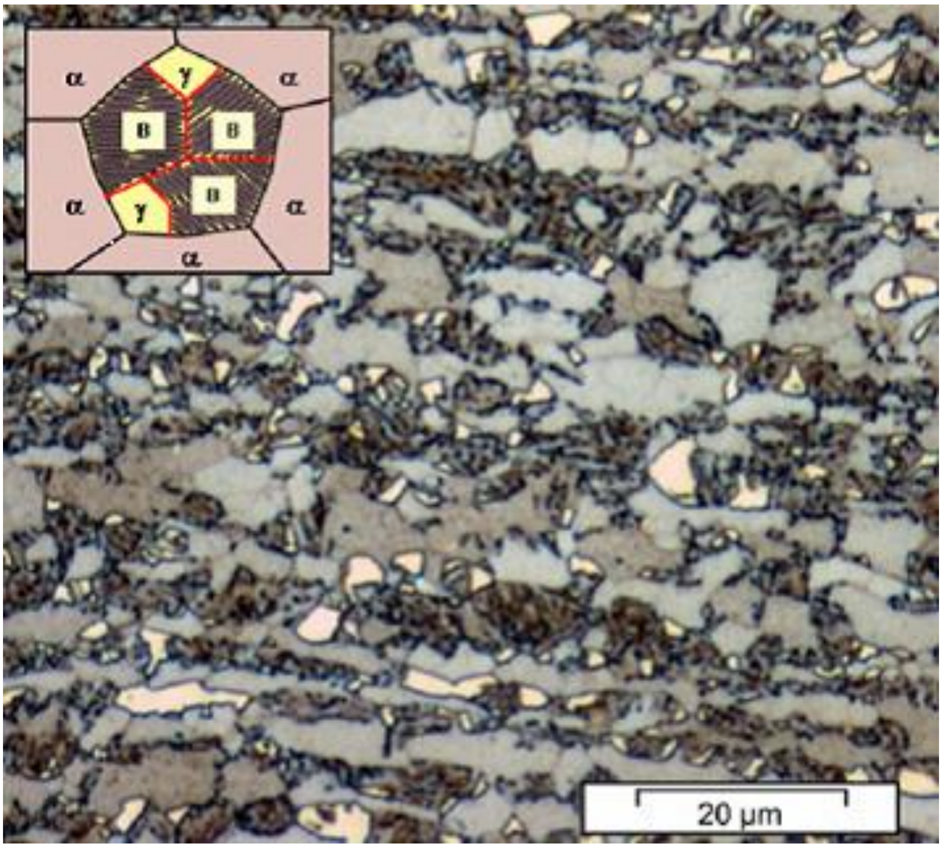

Figure 2-31. The optical photomicrograph of a TRIP steel [74].

Further, Hedstrom *et al.,* conducted various synchrotron diffraction studies to look at the effect of strain-induced transformation and found an autocatalytic sequence of transformations which were evidenced as bursts of strain induced α′ on loading [98]. They proposed that residual stress fields around such transformation lead to localised hardening, provide resistance to necking and ultimately improves the mechanical properties of the metastable austenite [98], [145] and these results supported the theory proposed by Zackay *et al*. [12]. They also observed that both the α′-martensite, ε-martensite formed on deformation of a 301 metastable austenitic stainless steel. Further, structural evolution of strain-induced α′ could be probed three-dimensionally in individual austenite grains using synchrotron X-rays [146]. They showed that large differences in lattice strain may be observed in grains having nearly identical crystallographic orientation, which may further be influenced by the local grain environment.

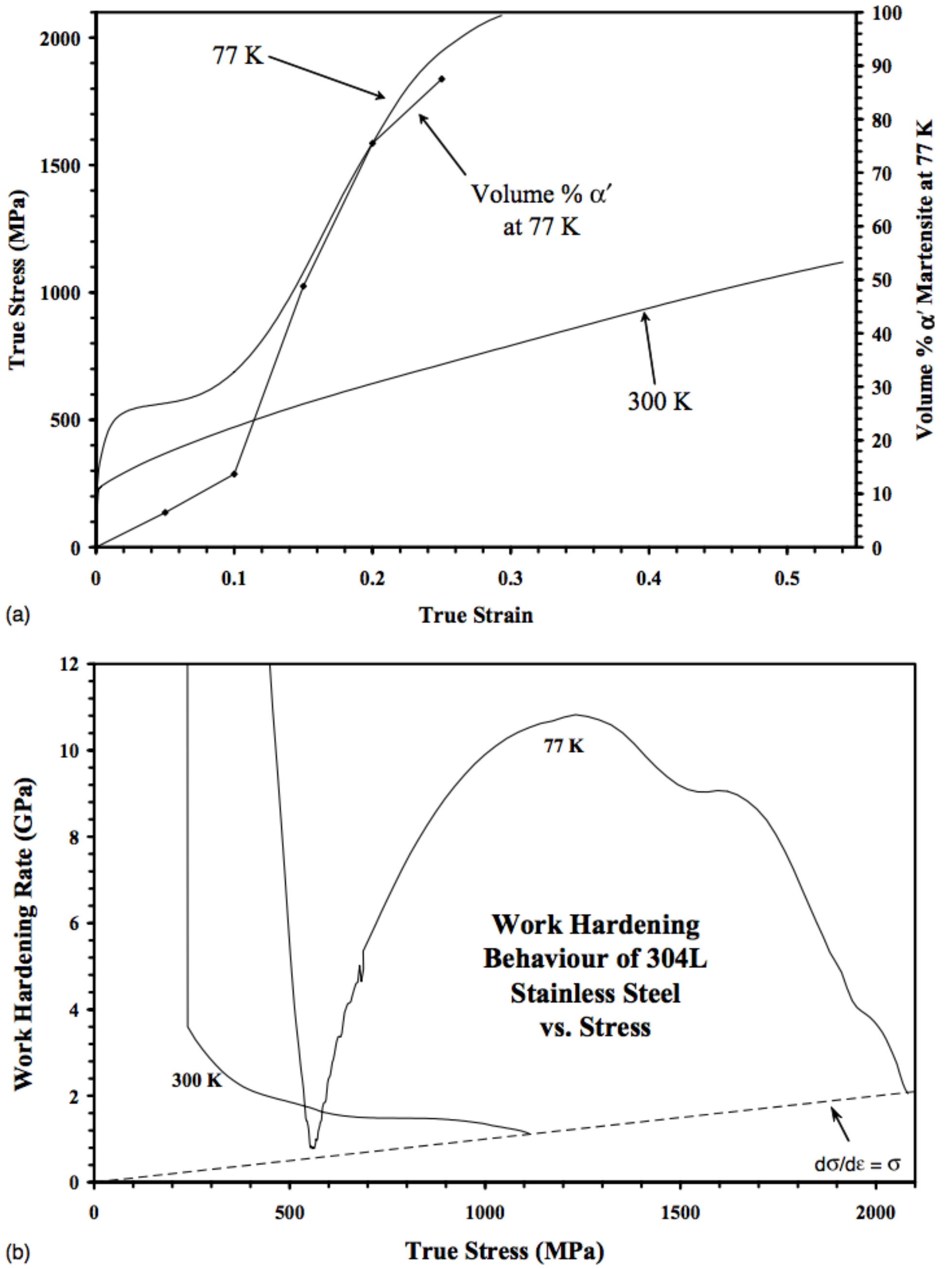

Figure 2-32. (a) Mechanical response at both 77 and 300K with volume fraction data superimposed and (b) work hardening rate at 77 and 300 K [150].

Neutron diffraction has been used for probing the nature of strain-induced martensitic transformations [2], [150]–[153]. The work by Spencer *et al.*, first showed that martensite acts as an elastic reinforcing phase, which supports higher stresses during the deformation process [150]. Their work further showed an approximate sigmoidal nature of the strain-induced martensitic transformation, which was also a function of plastic strain at 77 K (see Figure 2-32 (a)). Figure 2-32 (b) shows the work hardening rate plotted against the flow stress. At room temperature, it was observed that the work hardening rate decreases with increase in applied stress, whereas at 77 K, the work hardening rate decreases first and then with further applied stress, it increases sharply owing to the strain-induced martensite formation [150]. The measurements made by Ojima *et al.*, showed three stages of deformation in multi-layered steel, a fully elastic stage where both the austenite and martensite deform elastically, a partially plastic stage where the austenite lattice deforms in a plastic manner but martensite is still under elastic deformation and finally a plastic stage where both phases yield permanently [153]. Work done by Moat *et al.* was a representative study of the bulk behaviour of the material showing strain-induced transformation and results are shown in Figure 2-33 [2]. It shows the neutron diffraction profiles of the lattice planes that are normal to the tensile direction for samples prior to deformation, subject to low and high levels of deformation. They observed a decrease in the austenite peak intensity at both room temperature and at -50 °C after straining to 4% strain, while only observing a drop in peak intensity on straining to 0.5% at the -50 °C. They also measured the changes in peak positions of ferrite and austenite as the deformation process proceeded.

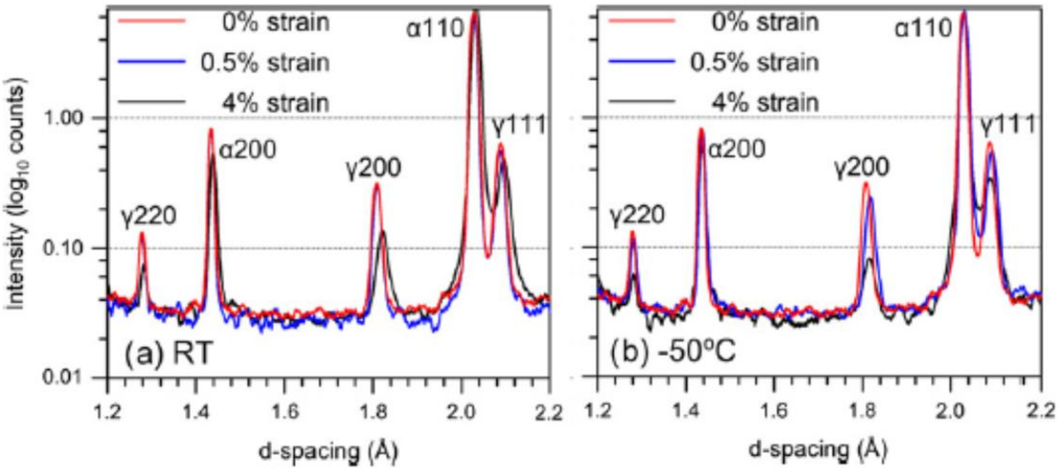

Figure 2-33. Example diffraction profiles for planes normal to the straining direction collected by neutron diffraction at (a) RT and (b) 50 °C for samples in theas-received condition and strained to 0.5% and 4% tensile plastic strain. Samples are in an unloaded condition (note log scale on intensities) [2].

The measurements made in this dissertation are similar to those given Figure 2-33 [2], where the austenite volume fraction is measured using the method outlined in the ASTM E 957-13, the standard for retained austenite measurements in steel [97]. The differing properties of neutrons in comparison to X-rays have been taken into consideration while making the retained austenite volume fraction calculations. Here comparison is made of relative peak intensities of the diffraction peaks of the individual phases. Further in their experiment, Moat *et al.* [2] prestrained samples to 2.3% strain at both RT and -50 °C, this was followed by subsequent deformation at the other temperature to measure the effect of strain-induced martensite on the work hardening rate. The experiment showed that the RT deformation on a prestrained sample at -50 ° C showed a much higher rate of work hardening, as compared to a specimen strained simply at RT. They proposed that it was due to strain-induced martensite formed during the prestraining at – 50 °C. The two factors responsible for change in stress / strain behaviour are (a) temperature dependence of flow stress and (b) a difference in the martensite volume fraction produced at the two different temperatures. It was further assumed that deformation to 2.3% strain at RT was due to normal plastic deformation (*i.e.* dislocation motion). When this prestrained sample was deformed at -50 °C, greater volume fraction of martensite was achieved within the elastic loading regime. A significant observation here was a substantial increase in the work hardening rate at -50 °C after RT prestraining, which was assumed to be caused by stress-induced martensite transformation. However, to simply investigate the $\gamma \rightarrow \alpha'$ transformation, the material used in reference [2] is complicated, on account of the multiple phases present. Therefore, in this dissertation, a type 301-metastable austenitic stainless steel showing the TRIP phenomenon is used. This material has a fully austenitic microstructure, which transforms into martensite under applied load.

Abreu *et al.*, measured the transformation texture of strain-induced martensite also using the 301 metastable austenitic stainless steel [14]. They made calculations using EBSD microtexture, based on the process of variant selection, itself based on the Patel and Cohen theory [16]. Measurements made in reference [14] were on samples strained directly to macroscopic strain values of ~ 10 and ~20% strain and were observed to be in good agreement with the theory in reference [16]. However, it is not clear how the EBSD measurements were made here, *i.e.* were the samples polished prior to the deformation process or post the deformation process. It has been observed during this project that polishing the sample post the deformation process can relieve the stresses and aid the formation of greater quantities of martensite. Therefore, measurements made in this dissertation were only on samples polished prior to the deformation process.

3 Experimental

3.1 Material

The material studied for this work was a 301 grade austenitic stainless steel. This material was provided in a fully annealed condition with a nominally fully austenitic microstructure (fcc crystal structure). A 301 stainless steel exhibits good oxidation and corrosion resistance properties and is generally used for decorative and structural applications. As mentioned earlier, this material has been selected because it has nearly 100 % austenitic starting material. This reduces the complications of analysis introduced by the plastic deformation of other bcc type phases, such as ferrite and bainite, which are often present in commercial TRIP steels. Previous studies have shown that this material readily transforms to martensite on application of stress [14], [144] and would therefore be ideal for this study. The material was supplied with a grain size of 15-20 μm and was relatively free from preferred orientation, as shown in Figure 3-1. The chemical composition is given in Table 3-1.

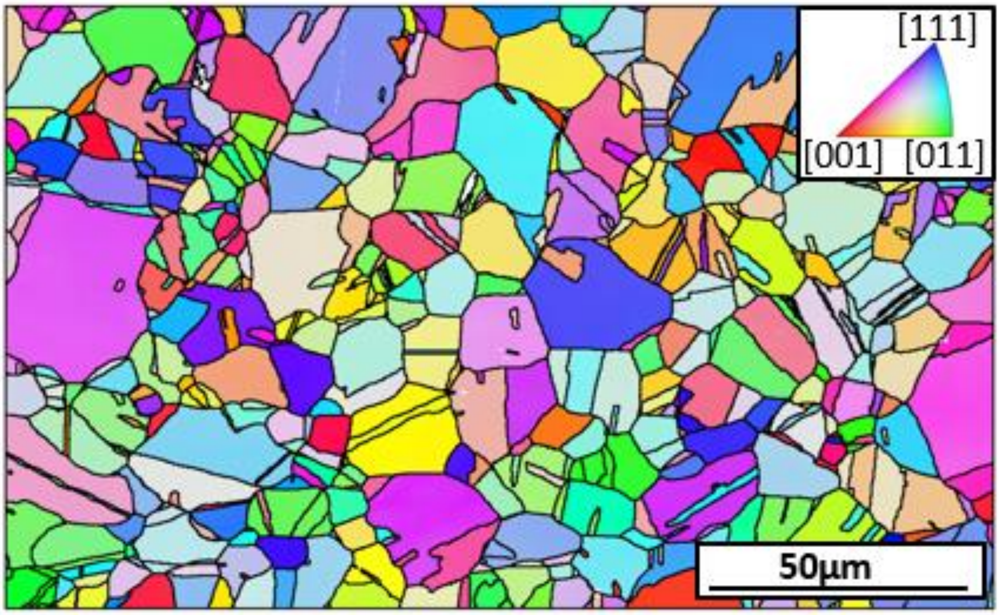

Figure 3-1.EBSD orientation map of the as received material having more than 99% austenite.

Table 3-1. The chemical composition of 301 austenitic stainless steel

Fe	C	Si	Mn	P	S	Cr	Ni	Cu	Mo
Bal.	0.001	0.48	1.057	0.043	0.001	16.98	7.12	0.381	0.311

3.2 Material characterisation using electron backscatter diffraction

3.2.1 Sample design and preparation

Each specimen was metallographically prepared by grinding on silicon carbide papers ranging from 220 grit (>60 µm), down to very fine papers of 4000 grit (5 µm). The grinding was done using a rotary grinding machine. For each subsequent step a finer paper was used and the grinding time was increased to remove scratches and near-surface deformation caused by the previous grinding step. This is followed by a polishing process using diamond suspension ranging from 6 µm down to 1 µm grain size, with a water based lubricant, to obtain a surface finish free from any observable scratches. Depending upon what characterization is required, a final stage may be employed. For optical microscopy, the sample is etched to reveal the grain structure using either chemical or electrolytic etching process. For electron backscatter diffraction (EBSD) for characterisation of the phases, on completion of the final polishing stage (1 μm diamond paste), the sample is polished using with colloidal silica (OPS) solution of 0.05 μm particle size. In this dissertation, after polishing with OPS, electrolytic polishing was carried out as the final stage before characterization using an electrolyte solution of 85% ethanol, 10% 2-butoxyethanol and 5% water (branded as Struers A2 electrolyte). The electropolishing parameters were voltage 22 V, flow rate 20 and time 60 seconds.

Reference indentations were made on the sample after electropolishing to effectively identify the region of interest after each intermediate stage of straining.

EBSD characterisation was done to investigate the microstructural evolution of the strain-induced martensitic transformation for a given set of grains. EBSD measurements were made using parameters as mentioned in Table 3-2. The working principles of EBSD are given Section 2.6.2.1. Phase maps were constructed for samples strained to different macroscopic strain values, using the crystallographic phase data for fcc-iron and bcc-iron phases, provided in EBSD acquisition software (provided by Oxford Instruments). The analysis of the EBSD data was conducted using the Matlab toolbox MTEX [154].

Table 3-2. List of the EBSD measurement parameters used.

Accelerating	Working	Tilt Angle	Mode	Aperture Size

voltage	distance			
20 kV	15 ± 0.1mm	70°	High current	120 µm

3.2.2 Macroscopic tensile strain measurements

All the deformation experiments were conducted at room temperature. Tests were carried out using an Instron 5569 load frame equipped with a 50 kN load cell. Uniaxial tensile tests were carried out with displacement rates of 0.2 mm/min. The dimensions of the subsize specimen as recommended in the ASTM E8/E8M standard [155] were used (see Figure 3-2).

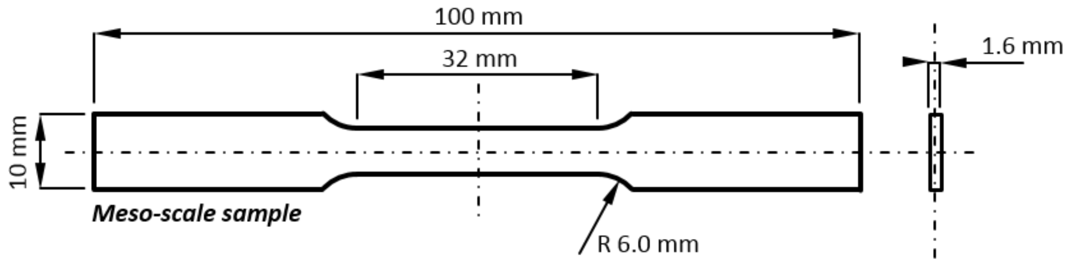

Figure 3-2. Engineering drawing of sub-size test specimen used for the ex situ experiments.

3.2.3 Data treatment

To make useful microtexture and strain-induced martensite measurements, it is important to look at the microstructural evolution of the same set of grains throughout the deformation process. In this PhD project, the microstructural evolution was studied using electron backscatter diffraction (EBSD), the principles of which are outlined in Section 2.6.2.1 . The steps involved in the EBSD data acquisition and data processing may be plotted using the flowchart (as shown in Figure 3-3). EBSD maps were acquired both prior to and post the deformation process at the region of interest. Here, as outlined in Section 2.6.3.2, at least 7 Kikuchu bands were identified to assign the crystal structure. This enhanced the confidence of the measurement. The austenite grain boundaries prior to deformation and the strain-induced martensite) phase boundaries were identified after deformation process. Each martensite variant is then assigned by comparing the observed habit plane, which closely matches one of the 24 KS variants as listed in Table 2-1.

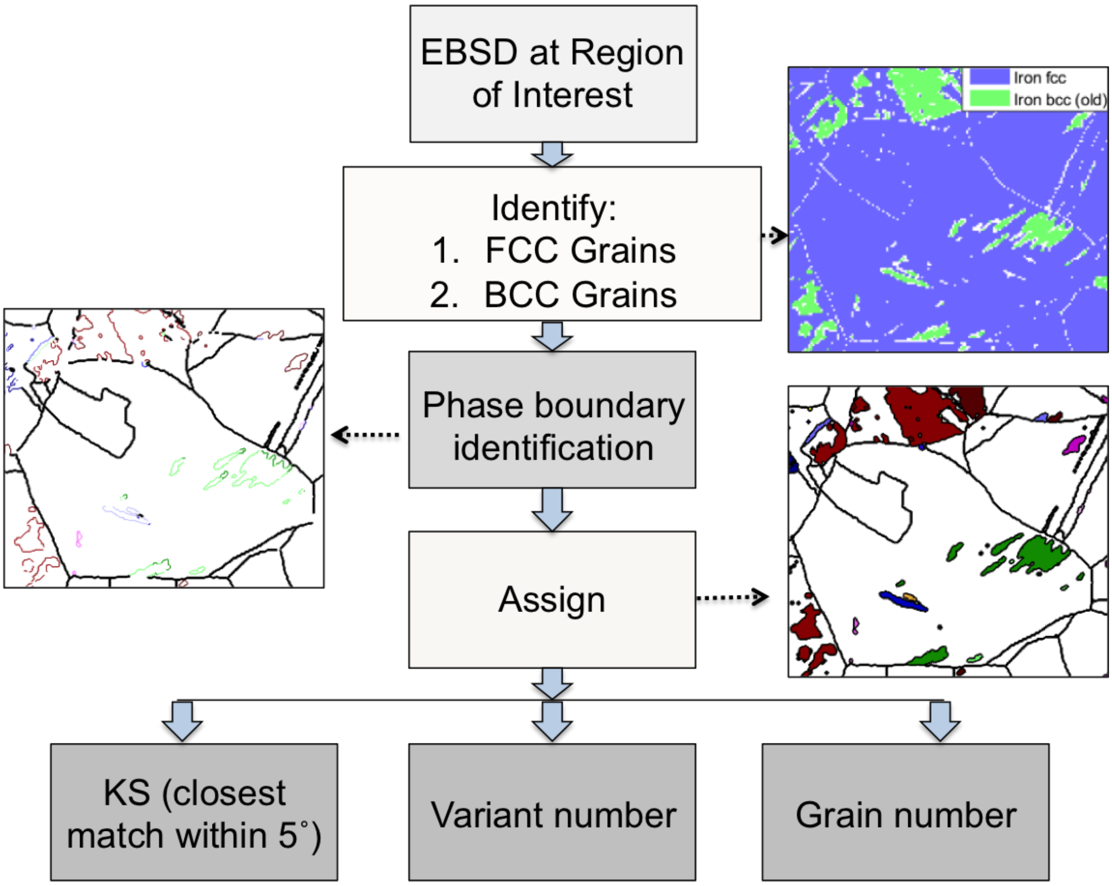

Figure 3-3. Flow chart of steps involved in the EBSD data processing.

In the experiments made here, the same set of grains were mapped both prior to and post the deformation process as shown in Figure 3-4. The matching was done based on the size of the prestrained austenite grain, *i.e.*, the biggest grain was marked ‘grain 1’ and then the subsequent grains marked in the decreasing order of size. After locating the biggest grain, the EBSD system probes the location of this grain in both the pre and post-deformation strain map. This is done simultaneously looking at the orientation change of the given grain in both the EBSD maps. In total twenty grains were mapped in this manner.

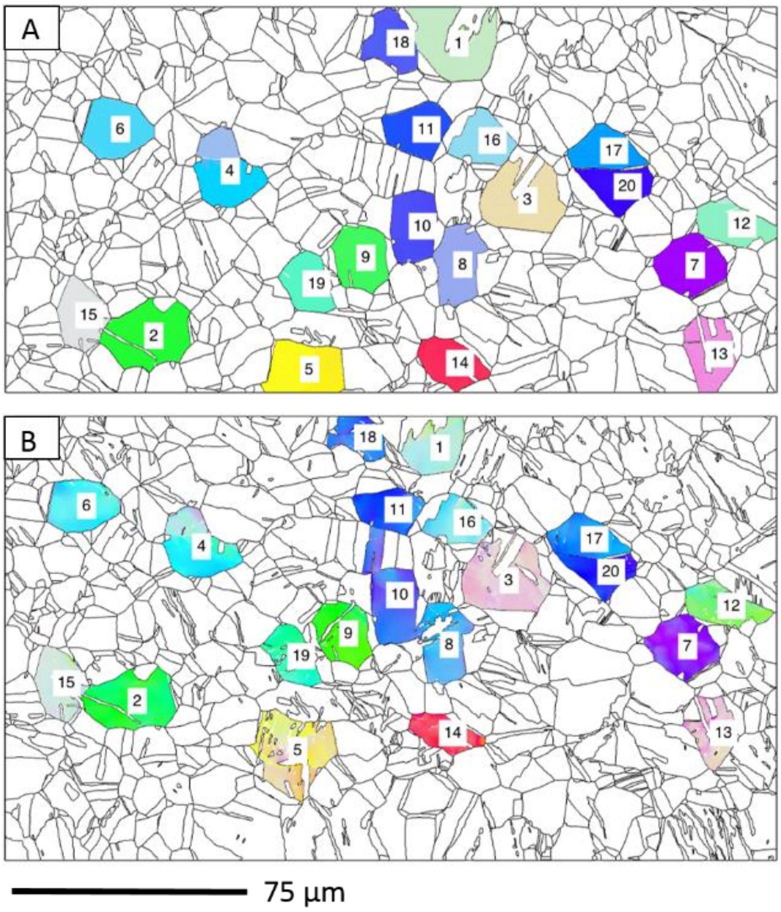

Figure 3-4 EBSD orientation maps showing grain matching throughout the deformation process. (a) Grain boundary map of the microstructure prior to deformation, (b) grain boundary map post deformation process.

Looking at the EBSD phase maps, it is possible to see whether there is any residual martensite present in the microstructure prior to deformation. This enables the residual martensite present in the microstructure (prior to deformation) to be accounted for precisely in the final martensite volume fraction calculated (after the deformation process). EBSD measurements on prestrained austenite grains confirmed that there was some residual martensite (Fe-bcc) present in the microstructure as shown in the Figure 3-5. This will be discussed in detail in Section 4.2. Figure 3-5 outlines the martensite variant boundaries in the prestrained (Figure 3-5 (A)) and post deformation (Figure 3-5 (B)), microstructures *i.e.* each martensite variant was coloured uniquely based on Table 2-1. Here, an example is given of a sample that was strained directly to a macroscopic strain of 10 percent. The encircled grain shows how the deformation induces the martensitic transformation in grains that did not contain martensite in the prestrained condition. The increase in the area fraction of strain-induced martensite maybe measured and the residual martensite accounted for with this approach. The grain within the square shows the residual martensite present in the material prior to deformation and maybe tracked in the deformed state also. If only the post-deformation mapping was done, these measurements would lead to inaccurate results. All results are explained in detail in the following chapter in Section 4.2.

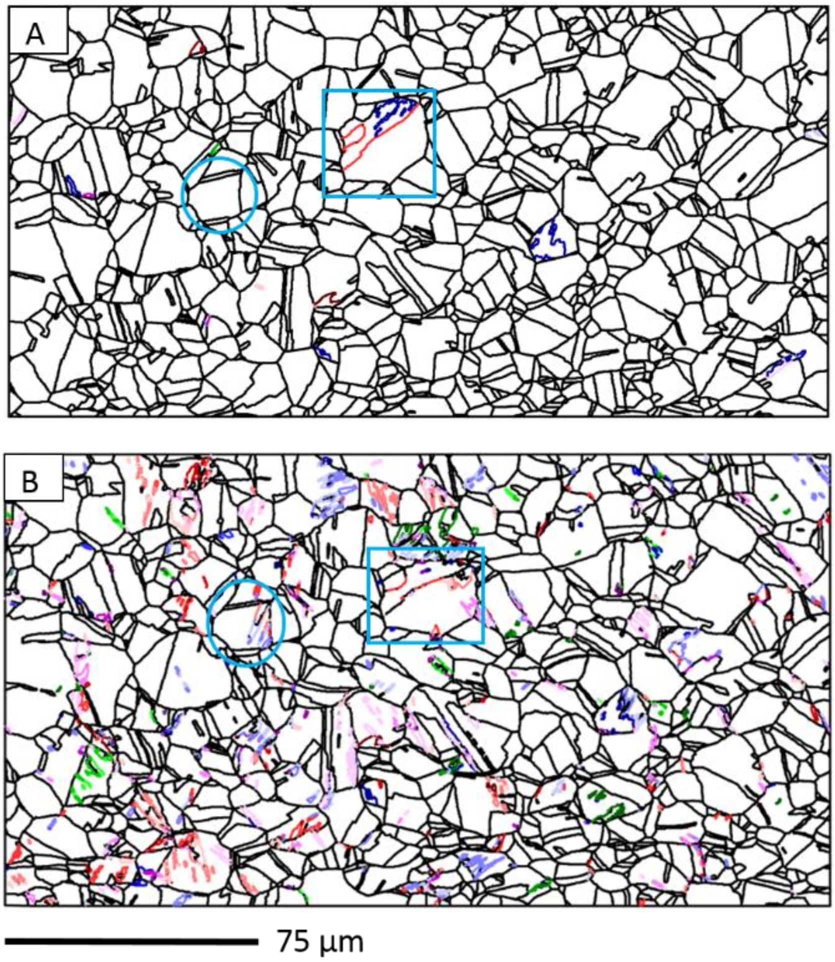

Figure 3-5. EBSD orientation maps showing strain induced martensite at 5% strain. (a) IPF orientation map of the microstructure prior to deformation, (b) residual K-S martensite variants present in the microstructure prior to deformation and (c) strain induced K-S variants at 5% macroscopic strain.

Figure 3-6 shows the microstructural evolution of strain-induced martensite grains strained to a global strain of ~ 10 percent. Part (a and c) is the inverse-pole-figure IPF orientation map of the microstructure prior to and post the deformation process, part (b) is the residual KS martensite variants present within prestrained austenite grain boundaries and part (d) shows strain-induced KS variants post deformation. The graphs show the increase in area fraction of KS martensite variants throughout the deformation process. The residual martensite present within the microstructure prior to the deformation process enables the identification of a unique set of grains that may be studied throughout the deformation process.

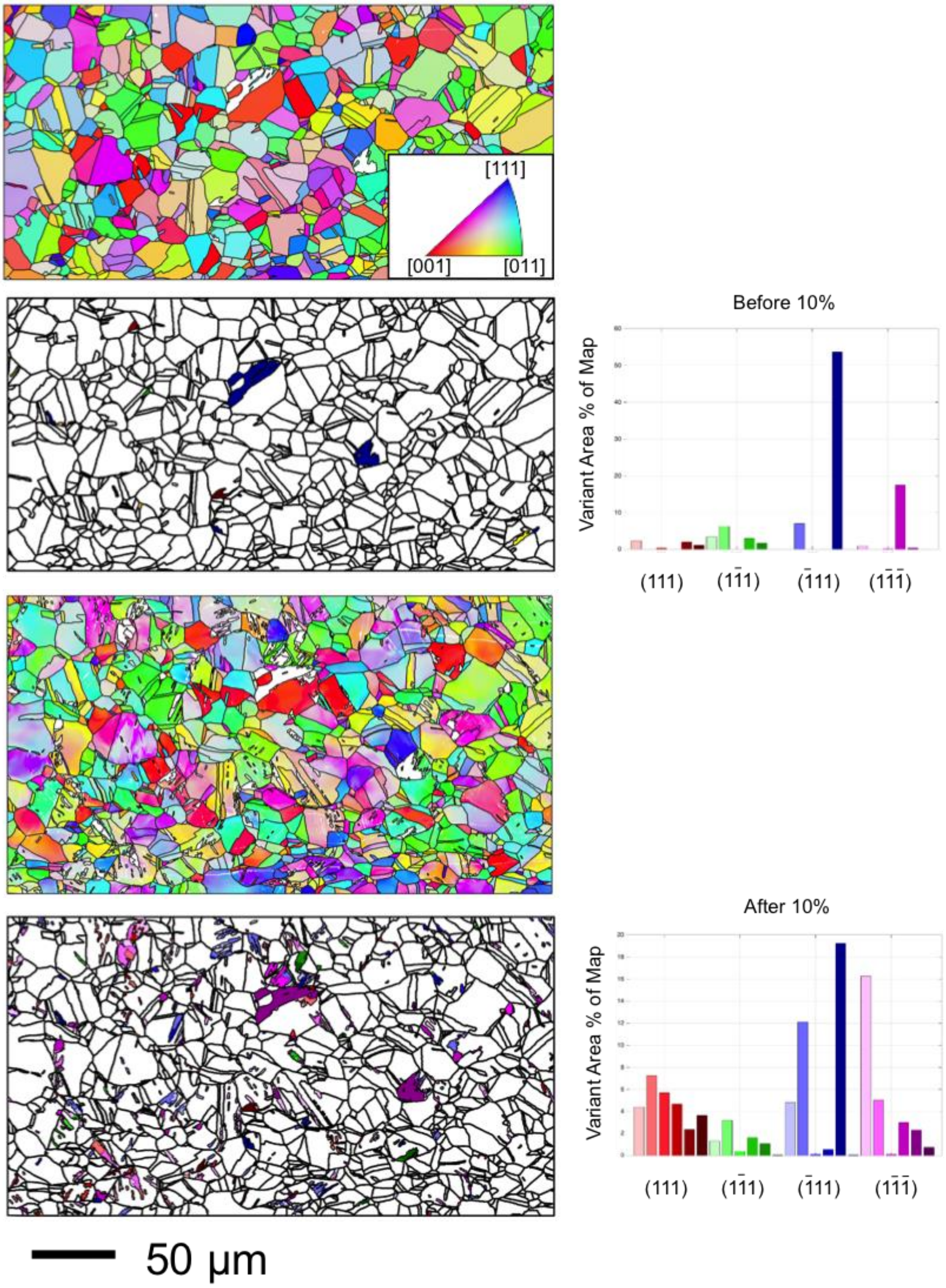

Figure 3-6. EBSD orientation maps showing strain induced martensite at 10% strain. (a) IPF orientation map of the microstructure prior to deformation, (b) residual K-S martensite variants present in the microstructure prior to deformation, (c) IPF orientation map of the microstructure post deformation and (d) strain induced K-S variants at 5% macroscopic strain.

For each measurement, grains were counted manually, both before and after the deformation process. The grains that contained some transformation product were only a small percentage of the total number of grains in the maps and this was calculated using the following formula

$$\text{Grains Transformed }(\%) = \frac{Grains\ transformed}{Total\ number\ of\ grains}\ x\ 100 \qquad \textit{Equation 31}$$

3.2.4 Plastic strain measurement from local misorientation

Kernel Average Misorientation (KAM), an EBSD parameter, was used to evaluate plastic strain for each deformation condition. For each condition, the spread of KAM distribution was considered as a measure of plastic strain accumulation within the sample. KAM considers the lattice curvature due to local change in geometrically necessary dislocation density in a localised region within an individual austenite grain and this calculation was done using a 3x3 kernel. The KAM of a point in the centre of a 3x3 kernel is defined as the numerical average misorientation of all its 8 neighbouring points and its values from range from 0 to 2^{o} were considered in this study.

3.3 Digital Image Correlation

3.3.1 Procedure

A 301 stainless steel sheet with a nominal thickness of 1.6 mm was machined into flat dog-bone shaped specimen having 20 mm gauge length and 3 mm width (see Figure 3-7, which schematically shows the testing regime). Stages I and II are explained in greater detail in the previous Section 3.2.1., whereas, stages III –

VI are discussed below. Stage III is discussed in detail in the following Section 3.3.2.

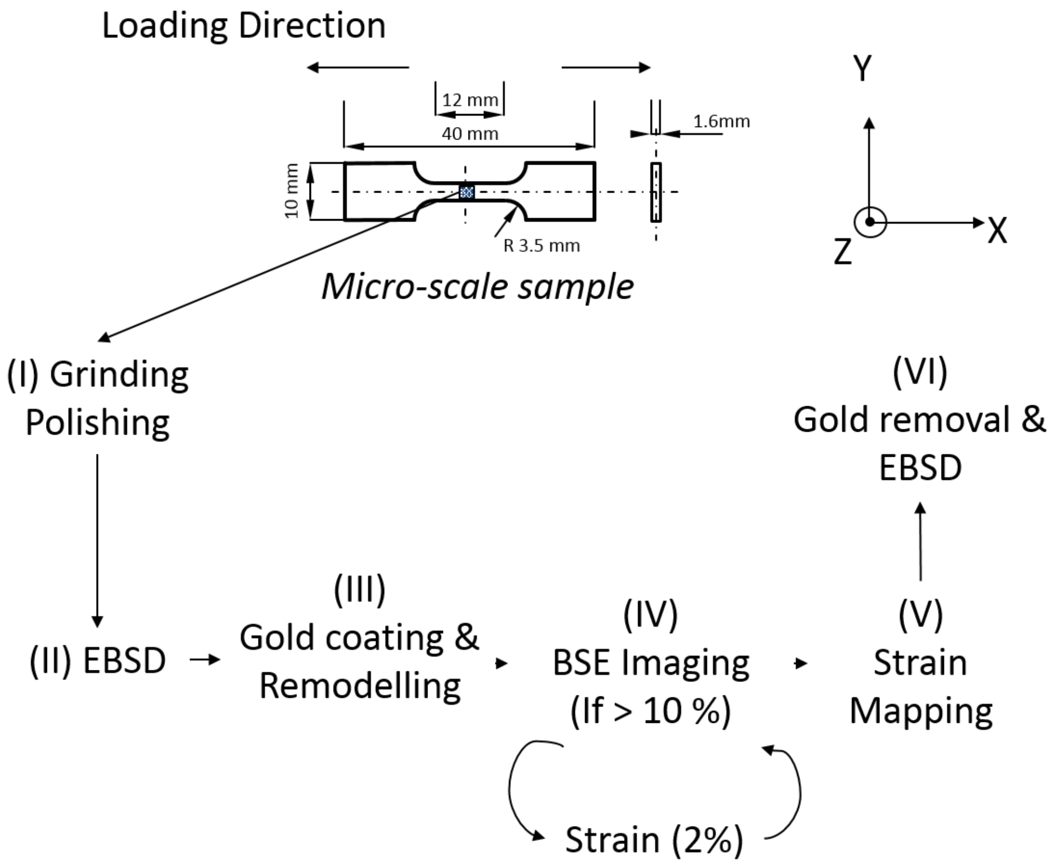

Figure 3-7: Engineering drawing of microscale specimen used for the in situ experiments and the schematic flowchart of experimental procedure.

During stage IV, the specimen was incrementally strained using a strain rate of $4x10^{-4}$ from 2 to 10 % strain with 2 % strain increments. The specimen was strained using *an in situ* 4.5 kN ADMET mini-tensile testing machine, inside a Zeiss Supra 55VP field emission gun scanning electron microscope (FEG SEM). At each macroscopic strain value, the test was interrupted to capture three backscattered electron (BSE) images at two different magnifications to be used for DIC analysis. The region of interest (ROI) for the high magnification images was contained within the lower magnification images. The parameters used for image capture are shown in Table 3-3.

Table 3-3 SEM Imaging parameters

Image	Imaging Mode	Accelerating Voltage	Working distance	Magnification	Image size (pixels)	Spatial resolution (nm)
Low mag	BSE	20	11.6 mm	2000X	2048 x 1536	92
Hi mag	BSE	20	11.6 mm	5000X	2048 x 1536	37

3.3.2 High resolution digital image correlation (HRDIC) data collection

After the initial EBSD scanning, the test specimen was coated with a thin film of gold (thinner than 50 nm) using a Polaron SC7640 gold sputter coater. It was difficult to determine a specific set of parameters for any particular gold sputter coater and some amount of trial and error was required to optimise the sputtering parameters. The surface with the gold layer was then held at 350 °C for 90 minutes in a humid atmosphere. The high-pressure steam penetrated the porous gold film and aided in the agglomeration of the gold layer into a fine speckle pattern (see Figure 3-8).

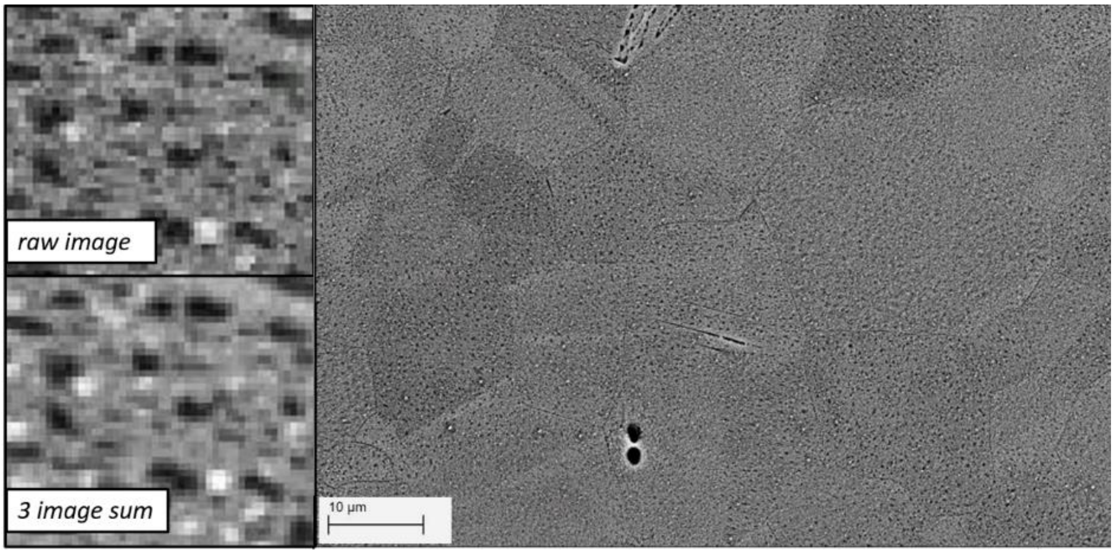

Figure 3-8. Backscatter image of gold remodelled speckle pattern used for digital image correlation. Raw image shows speckle pattern of a single image, 3-image sum is combination of three images actually used for correlation.

This method has been developed by Scrivens *et al.* [156] and further by Gioacchino *et al.* [18] and used by the same authors in their recent work [22] providing sub-pixel accuracy in strain measurements from SEM imaging. As a consequence of the wide separation in the atomic weight of gold and iron, the gold particles give an excellent contrast with the predominantly iron substrate in the BSE imaging mode. Moreover, the BSE mode is less sensitive to changes in topography throughout the straining process, which is critical for 2D digital image correlation (DIC).

3.3.3 HRDIC data treatment

Digital image correlation is a computational technique that tracks small regions throughout the deformation process. These regions on the surface are tracked throughout a series of digital images, producing a displacement vector. If this is performed at positions across the entire image then a vector field is produced. If the displacement of the sample occurs in the image plane, then this vector field will describe the displacement of the imaged sample. This vector field can then be differentiated to calculate strain difference in the sample between the two images. In addition to the assumption that the surface is moving in plane, there is also an implicit assumption that the pixels are square. This assumption is easily satisfied when using a standard camera sensor, but when using an SEM to produce the images this becomes more difficult to ensure, as described in the following paragraphs. For this reason, sets of three images were taken at each strain step so that any inconsistencies could be reduced by image summation.

Raster errors in images obtained by SEM may cause the violation of the square pixel assumption required in DIC analysis and lead to pseudo-strain in calculations. To alleviate this error, each set of three images, taken at a single strain step, was shift-corrected to sub-pixel accuracy by taking a DIC (in DaVis software using an FFT-based algorithm) measurement of the relative shifts for each image for a central 128 × 128 pixel region. The images were shifted to sub-pixel accuracy using bi-cubic spline interpolation and then summed together (see Figure 3-8). As well as reducing the raster error by improving the regularity of the pixel sample points, this step increases the effective bit depth of the images and improves the quantum efficiency of the imaging process so that the image stability is increased.

The DIC analysis of BSE images was carried out using commercial software DaVis 8.2 [157]. This software uses the least-squares approach to iteratively solve the sum of squared differences (SSD) correlation function [116]. The algorithm initially calculates the displacement of a specified seed point in the image via the Lucas-Kanade method [158] using the implementation of Bouguet [159]. Once the seed point displacement is established, a “region grow” approach is then used, assuming displacement continuity to limit the search area. The user-specific parameters for the DIC calculation are presented in Table 3-4.

Strain was calculated from the DIC displacement vectors using Matlab code that fits a plane to a square region containing 9 vectors: a “strain window” [160]. Strain is calculated for every vector position by overlapping the strain windows and is done separately for the x and y displacement fields. The gradients of the two planes, calculated from the x and y displacement fields, are taken as the average strain tensor for that vector position. By calculating strain in this way no further smoothing is required so the size of the smallest strain feature that can be resolved can be clearly established (*i.e.* the size of the strain window plus the size of the DIC subregion, a total of 26 pixels in this case). This method also has the advantage that strain is calculated at the same point for all parts of the strain tensor. However, in this case this makes little difference as the strain result is linearly interpolated onto the EBSD measurement points for plotting grain boundaries.

In this dissertation, the average strain in a grain is calculated in a similar manner to the local strain. In this case displacement vectors for a single grain are fitted to a plane. An outlier filter is then applied to remove any displacement vectors that are more than 3 standard deviations from the plane. The filtered data is fitted a second time to calculate the average strain for the grain. A sliding strain window containing 9 vectors (3 × 3) was used for this work.

Table 3-4 DIC Parameters used for displacement vector calculation

Subregion size	Step size	Pyramid Levels	Epsilon	Correlation threshold	Threshold confidence margin	Subregion weighting	Sub-pixel interpolation
11×11 pixels	5 pixels	1	0.01	0.2 pixels	0.01	Round Gaussian	Bi-cubic spline

3.4 Neutron diffraction

All the neutron diffraction studies in this dissertation have been conducted at the ENGIN-X beam line at the ISIS facility. As detailed below, ENGIN-X has the unique capability of performing *in situ* loading at cryogenic temperatures, while collecting many diffraction peaks simultaneously. Therefore, it was an ideal instrument and was capable of performing the desired measurements for this dissertation.

3.4.1 ENGIN-X instrument at ISIS

The neutron diffraction measurements in this dissertation were made using the ENGIN-X instrument at ISIS, Rutherford Appleton Laboratory. As explained earlier (refer Section 2.7.2), ISIS is a pulsed neutron diffraction facility and ENGIN-X enables simultaneous investigation of the entire spectrum of {hkl} lattice planes (diffracting peaks). Although ENGIN-X has been designed to make engineering strain measurements, *i.e.* the accurate measurement of lattice parameters at precise locations [103], it has been successfully used for investigating phase transformations by Oliver *et al.* [161] and more recently Moat *et al.* [2].

3.4.2 Flight path

The flight path of ENGIN-X is 50 m and it sits outside the main ISIS experimental hall on target station 1. Methane moderators (moderators slow down the speed of the incoming fast neutrons to levels of interest for any given instrument) with a narrow pulse width and high flux are used and the resulting wavelength of neutrons is in the 1-3 A° range, which is suitable for most engineering materials [103] (refer Section 2.7.2). A curved 'supermirror' neutron guide transports the neutrons from the moderators onto the sample. The curvature improves the signal-to-noise ratio and removes the higher energy neutrons and gamma rays; however, it limits the minimum wavelength at the sample position to about 0.5 A° [103]. With increases in the flight path length the wavelength resolution can be improved. This is because the time required for neutrons of different wavelengths to reach the detector will vary depending on their flight paths. However, it is not beneficial to increase the flight path indefinitely as there may be losses, or the faster neutrons in a given pulse may overlap the slower neutrons from the previous pulses.

3.4.3 Beam Collimation

There are two types of collimators at ENGIN-X, incident collimators and detector collimators. The neutrons travel from the moderators to the sample horizontally. Before interacting with the sample, the neutron beam is collimated with a pair of interchangeable, orthogonal slits made from sintered boron carbide [99]. The slits range from 0.5 to 25mm thickness and are 30mm long, allowing for a wide range of rectangular or square beams to be used for experiments. These slits ultimately define the gauge volume of the neutrons in the horizontal and vertical geometries (refer Figure 3-10).

The instrument gauge volume (IGV) of the material diffracting corresponds to the intersection of the incident neutron beam (using slits) and the diffracted neutron beams (using radial collimators), as shown in the Figure 2-16. The actual diffraction from the sample constitutes the sample gauge volume or simple gauge volume. At ENGIN-X there are four sets of radial collimators available of, 0.5, 1, 2 and 4 mm gauge width options [103]. These radial collimators are made of thin absorbing blades and are used to collimate the diffracted beam and ensure all the detectors are looking at the same volume from the sample [162]. The position of these radial collimators is in front of the detectors horizontally making angles ± 90° to the incident neutron beam. Placing the radial collimator this way allows for a near cuboidal gauge volume.

Different gauge volumes may be achieved by changing either the size of the slits or the radial collimator used.

3.4.4 Detector banks

As schematically shown in Figure 2-16, EnginX has two fixed angle detector banks each centred on a Bragg angle 2θ of ±90°, at about 1.5m from the instrument gauge volume, just behind the radial collimators. This allows for the measurement of diffraction data from two orthogonal directions of crystal planes simultaneously. The fixed geometry proves advantageous for the measurement of intergranular and interphase strains, as the scattering vector remains the same for each reflection. The elastic scattering vector is the bisector of the incident and diffracted beams and lies normal to the reflecting planes (refer Figure 3-10). Each detector bank has 1200 ZnS/^{6}Li scintillator detector elements, arranged in five horizontal rows stacked vertically, each of 240 detector elements horizontally stacked [163]. The detectors cover an angular range of 81.4 - 98.6° in 2θ on either side of the incident beam [99]. As discussed earlier in Section 2.6.1, variation in sin θ is small as θ approaches 90°, minimizing the errors in the measurement.

3.4.5 ENGIN-X stress rig with cryogenic environment

ENGIN-X is equipped with two uniaxial hydraulic loading rigs to enable online or offline mechanical or fatigue testing of materials, with various sample environments available. Both these rigs were custom built by Instron to avoid having parts that impinge on the incident or diffracted beams and have load capacities of 50 kN and 100 kN [163]. In this dissertation the effect of temperature on the nature of martensite transformation kinetics was investigated. For such experiments, a cryogenic chamber was required that could be mounted on the stress rigs (see Figure 3-9). This newly commissioned cryogenic chamber was mounted on the 100 kN stress rig as shown in Figure 3-9. Moreover, results presented here were the first measurements made on this newly-developed state-of-the-art cryogenic chamber.

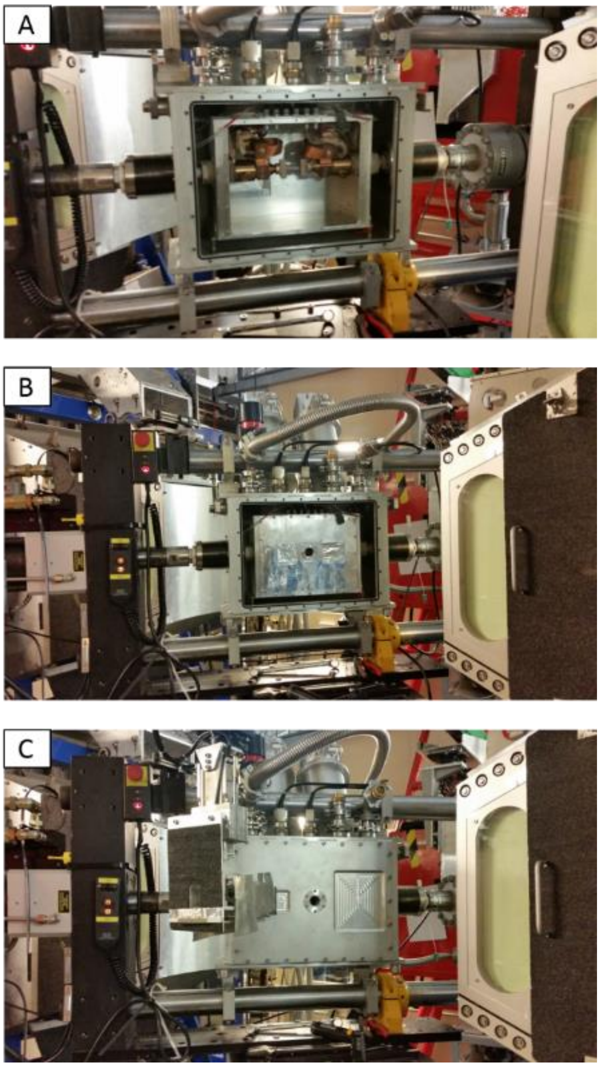

Figure 3-9. Cryogenic rig at ENGIN-X. (A) Shows the sample gripped inside the chamber, (B) shows the inner chamber of the cryogenic-rig and (C) shows the outer chamber sealed up and slits brought in for the start of the experiment.

This cryogenic chamber enabled deformation induced martensitic phase transformation measurements to be made between room temperature and temperatures well below 100K. The experiments were conducted at room temperature (~ 300 K), 263 K, 223 K, 173 K and 100 K respectively. It is known that plastic deformation due to dislocation motion is suppressed with decreasing temperatures. To experimentally ascertain this and to distinguish between the stress-assisted and strain-induced martensite transformations, various low temperatures were explored. The new sample environment allowed for faster cooling and heating times compared to the older versions, thereby improving sample change-over times (20 minutes to cool to 100K compared to 120 minutes with the previous system).

3.4.6 Test procedure

The stress rig with the cryogenic chamber (Figure 3-9) is placed at 45° to the incident beam. Because ENGIN-X is set up with each detector at 90° to the incident beam, positioning the sample at 45° ensures that the directions of strain measurement align along the loading and transverse directions, this is schematically presented in Figure 3-10.

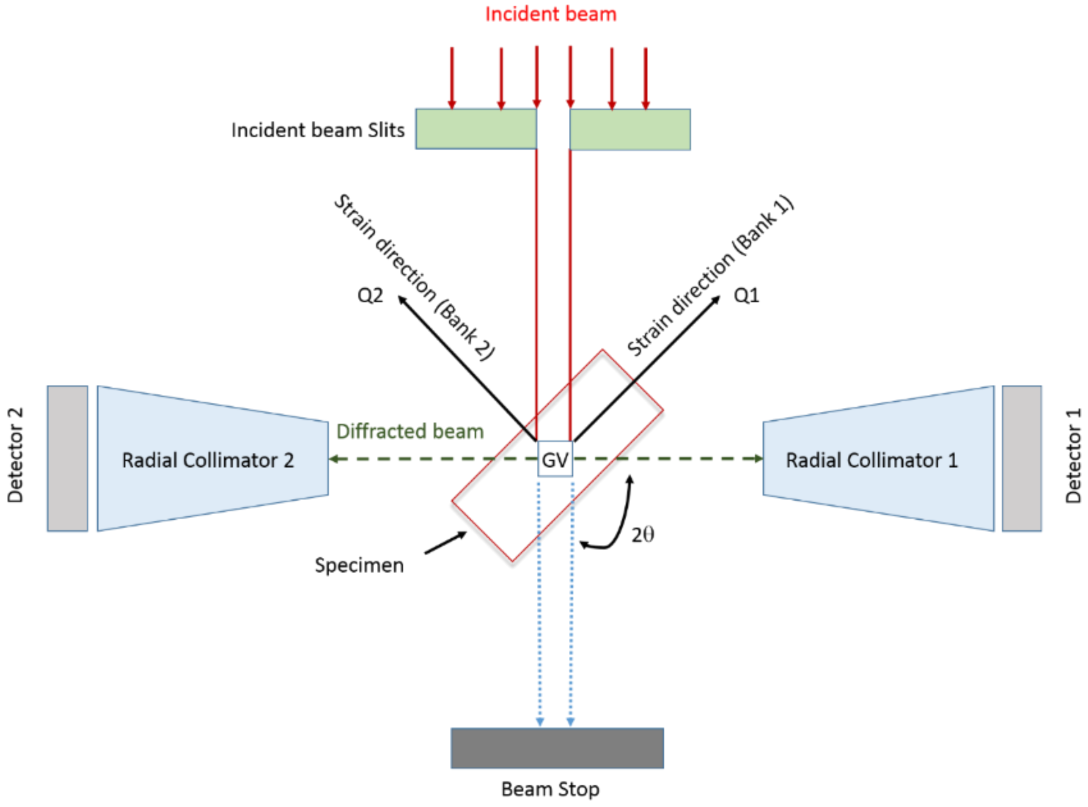

Figure 3-10. Schematic of ENGIN-X diffractometer.

Flat "dog-bone" shaped test specimens were electro-discharge machined from a 1.6 mm thick 301 austenitic stainless steel plate. The sample dimensions were similar to the sample dimensions of a standard ASTM E8M sub-size specimen (width 6 mm and gauge length 25 mm), however, with shorter grip sections, as shown in Figure 3-11. Specially designed aluminium grips were needed because the test temperatures used were below the brittle transition temperature of standard steel grips and aluminium has a good thermal conductivity to minimise the time needed to reach a stable temperature.

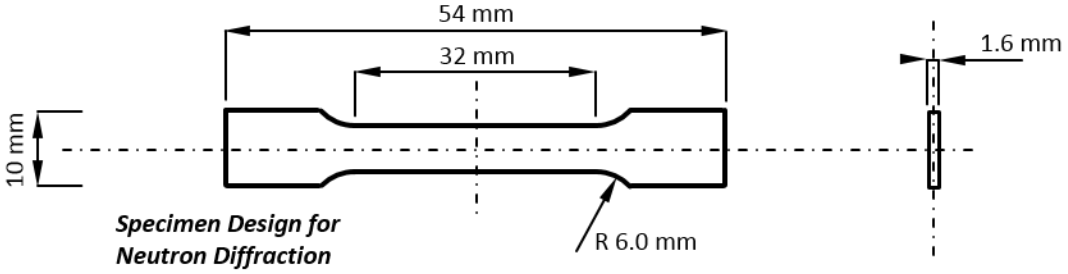

Figure 3-11. Engineering drawing of test specimen used for the neutron diffraction experiments.

As shown in Figure 3-10, the samples were aligned nominally at angles of ±45° to the direction of the incident beam using a positioner and optical theodolite. The positioner table is motorized and programmed for movements in x, y, z and ω directions, it can hold samples that weigh up to 1.5 tonnes making possible the positioning of a servo-hydraulic tensile rig to the sub millimetre precision required [164]. When set this way, measurements in Detector 1 (Bank 1 in Figure 3-10) are from the sample axial direction (loading direction) and the measurements in Detector 2 (Bank 2) are in the transverse direction see Figure 3-12.

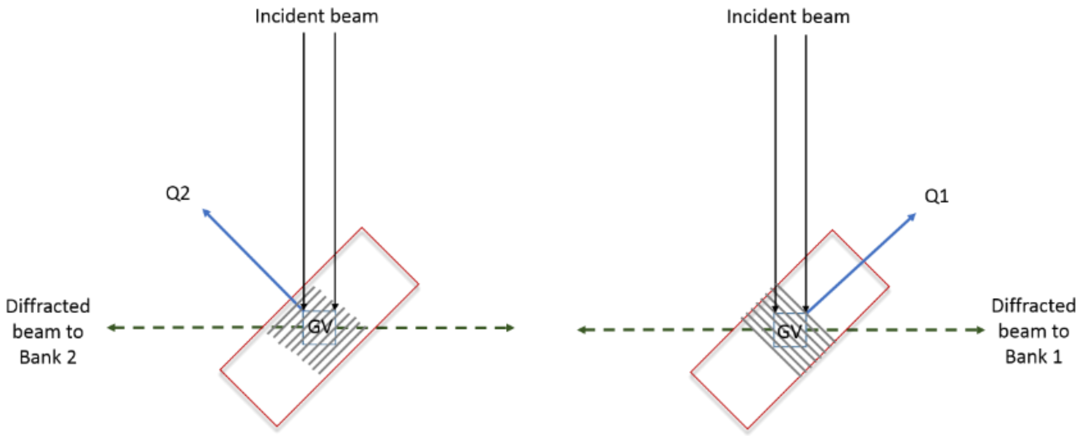

Figure 3-12. Schematic of scattering vectors Q1 and Q2.

Each test was performed first in load control when the material was in the elastic regime and then changed to position control after the material yielded. In load control, each sample was loaded from 50 MPa to 400 MPa, with 50 MPa load increments. After the sample was loaded to 400 MPa, it was strained in 0.3 mm increments or ~ 1.2 % strain increments. For each measurement point, the count time was 20 minutes.

As discussed earlier (see Section 2.7.2), the wavelength of neutrons used at ENGIN-X ranges between 0.5-6 A°. They travel a distance of 50 m in the neutron guides. The time required for the travel can be measured and therefore the velocity and wavelength calculated (refer Table 2-3). This enabled for measurements to be made from the individual austenite and martensite phases as explained in Section 2.6.1.

To make volume fraction measurements, diffraction spectra (individual {hkl} peaks} from both the axial and transverse directions were recorded. The intensity of each phase peak/spectrum was then summed together as outlined in Section 2.6.4.

4 Material characterisation and microstructural mapping of strain induced martensite: An electron backscatter diffraction study

4.1 Introduction

As mentioned in Section 3.2.3, there are three main results chapters in this dissertation. The first is an EBSD study, mapping martensitic phase transformations both prior to and post the deformation process. It is common to observe ~1-3% residual ferrite present in commercially available austenitic stainless steel. As discussed in Section 3.2.3, this may skew the volume fraction, texture and strain-induced martensite variant measurement if not properly accounted for.

As mentioned earlier (Section 3.2.3), each experiment involved directly straining the as-received samples and the stress strain curves are shown in the Figure 4-1. Here, a total of 6 specimens were uniaxially deformed directly to 5%, 6%, 7%, 8%, 9% and 10% macroscopic strain respectively. A further 2 samples were incrementally loaded to 5% and 10% strain with 1% strain increments to determine the effect unloading has on the martensite transformation.

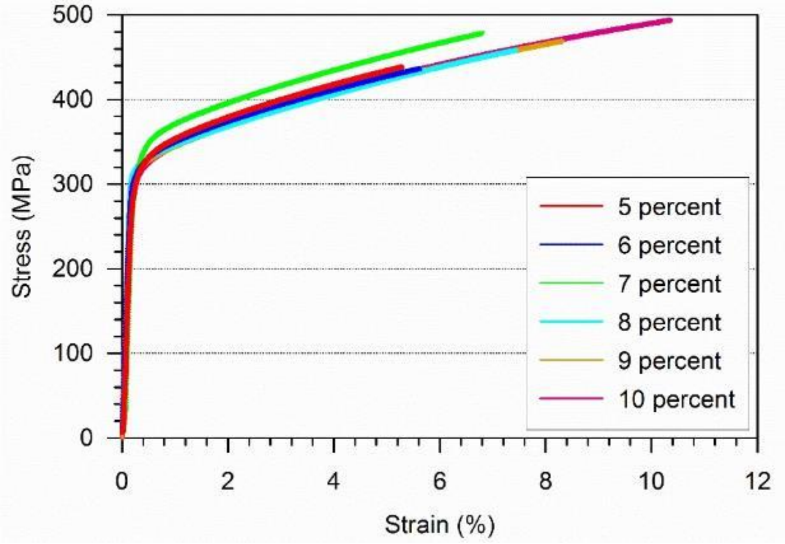

Figure 4-1. Stress-strain curves of samples strained for EBSD measurements.

4.2 Results (EBSD)

4.2.1 Direct loading

For each test (shown in Figure 4-1), EBSD mapping was carried out both prior to and post the deformation process. All the tensile strain experiments have similar yield points (~320 MPa), with the exception of the specimen deformed to 7% macroscopic strain (~350 MPa). This was possibly due to a slight variation in the experimental set-up, for *e.g.*, a slight variation in the cross sectional area of under load, or perhaps owing to a slight chemical variation within the batch of the as-received material.

Figure 4-2, shows the EBSD data for the sample deformed to 5% macroscopic strain. Figure 4-2, comprises of the prestrained IPF color map and the pre- and post-deformation maps of austenite grain boundaries, which have the ferrite phase colored. The pre- and post-deformation maps further indicate the location of the residual delta ferrite and the strain-induced martensite. The residual delta ferrite aides in the identification of a given area prior to and post the deformation process. In Figure 4-2 the increase in area-fraction of martensite was calculated to be approximately 0.63 percent at macroscopic strain of 5%. Further, it was also evident that at 5% macroscopic strain only ~ 2% of the austenite grains are seen to contain some transformation product.

Figure 4-3 and Figure 4-4 are EBSD orientation maps from the specimens deformed to 6% and 7% macroscopic strain respectively. Here, although there was not a substantial increase in the area fraction of the martensite, there was an increase in the overall plasticity (discussed later in the Section 4.2.4). The martensite fraction increased only slightly when the sample was deformed up to 7% macroscopic strain with a fraction of ~ 0.51% calculated for this sample (Figure 4-4).

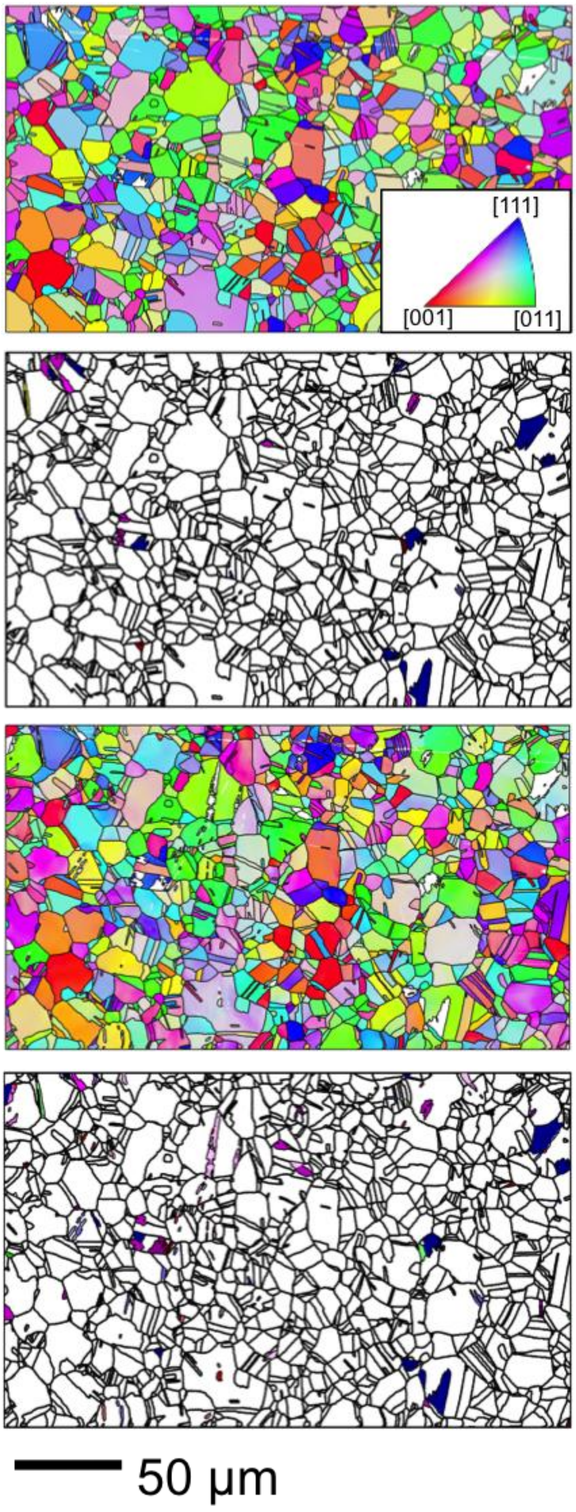

Figure 4-2. EBSD orientation maps showing strain-induced martensite at 5% strain. (a) IPF orientation map of the microstructure prior to deformation, (b) residual K-S martensite variants present in the microstructure prior to deformation, (c) IPF orientation map of the microstructure post deformation and (d) strain induced K-S variants at 5% macroscopic strain.

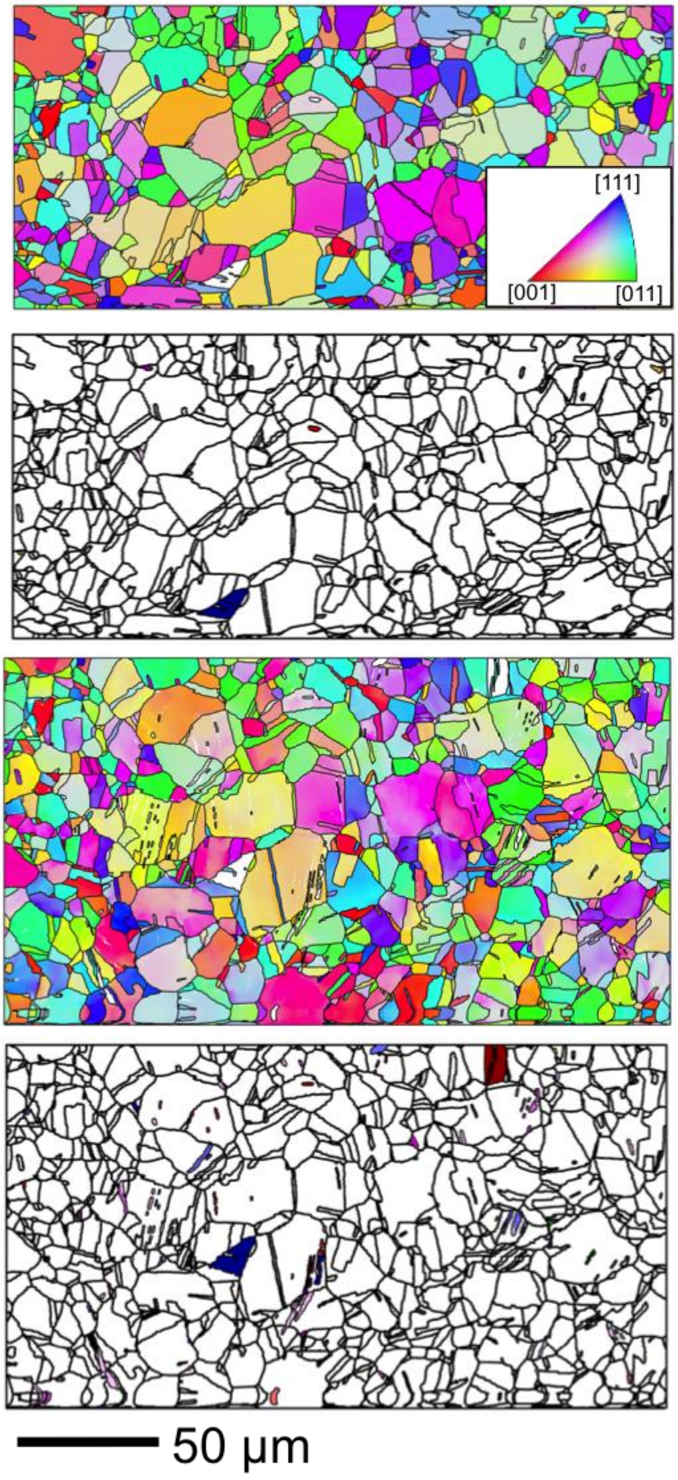

Figure 4-3. EBSD orientation maps showing strain-induced martensite at 6% strain. (a) IPF orientation map of the microstructure prior to deformation, (b) residual K-S martensite variants present in the microstructure prior to deformation, (c) IPF orientation map of the microstructure post deformation and (d) strain induced K-S variants at 6% macroscopic strain.

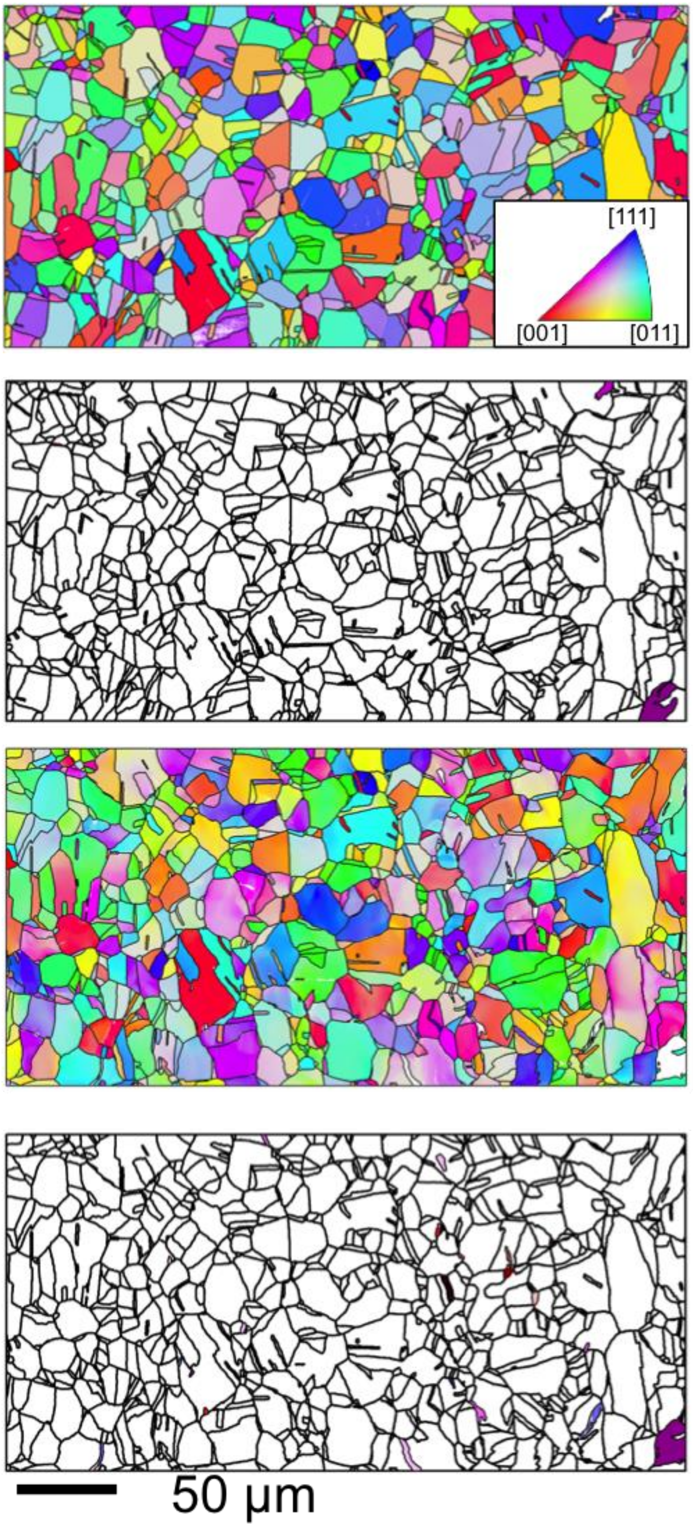

Figure 4-4. EBSD orientation maps showing strain-induced martensite at 7% strain. (a) IPF orientation map of the microstructure prior to deformation, (b) residual K-S martensite variants present in the microstructure prior to deformation, (c) IPF orientation map of the microstructure post deformation and (d) strain induced K-S variants at 7% macroscopic strain.

Beyond macroscopic strains of 7% greater fractions of strain-induced martensite were observed compared to smaller macroscopic strain increments. At 8% macroscopic strain (see Figure 4-5) the amount of strain-induced transformation is ~0.8%; whereas, it increased to 2.6 and 4.2 percent at 9% (see Figure 4-6) and 10% (see Figure 4-7) macroscopic strain respectively.

With an increase in the amount of transformation there was also an increase in the number of austenite grains containing transformation product. From ~ 2 percent grains showing the transformation at 5% macroscopic strain, to ~ 14 percent grains transforming at 10% macroscopic strain. Figure 4-9 (a) and (b) show the martensite phase fraction and fraction of grains containing transformation product.

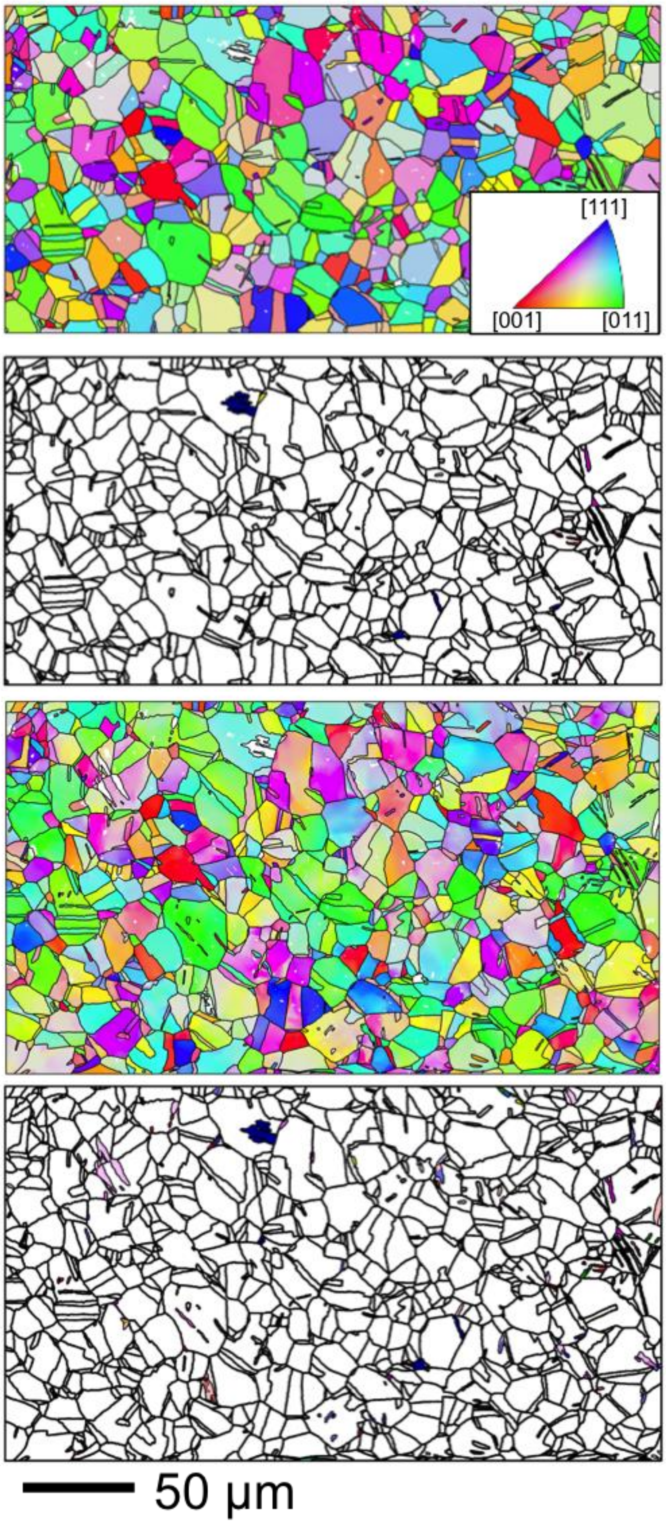

Figure 4-5. EBSD orientation maps showing strain-induced martensite at 8% strain. (a) IPF orientation map of the microstructure prior to deformation, (b) residual K-S martensite variants present in the microstructure prior to deformation, (c) IPF orientation map of the microstructure post deformation and (d) strain induced K-S variants at 8% macroscopic strain.

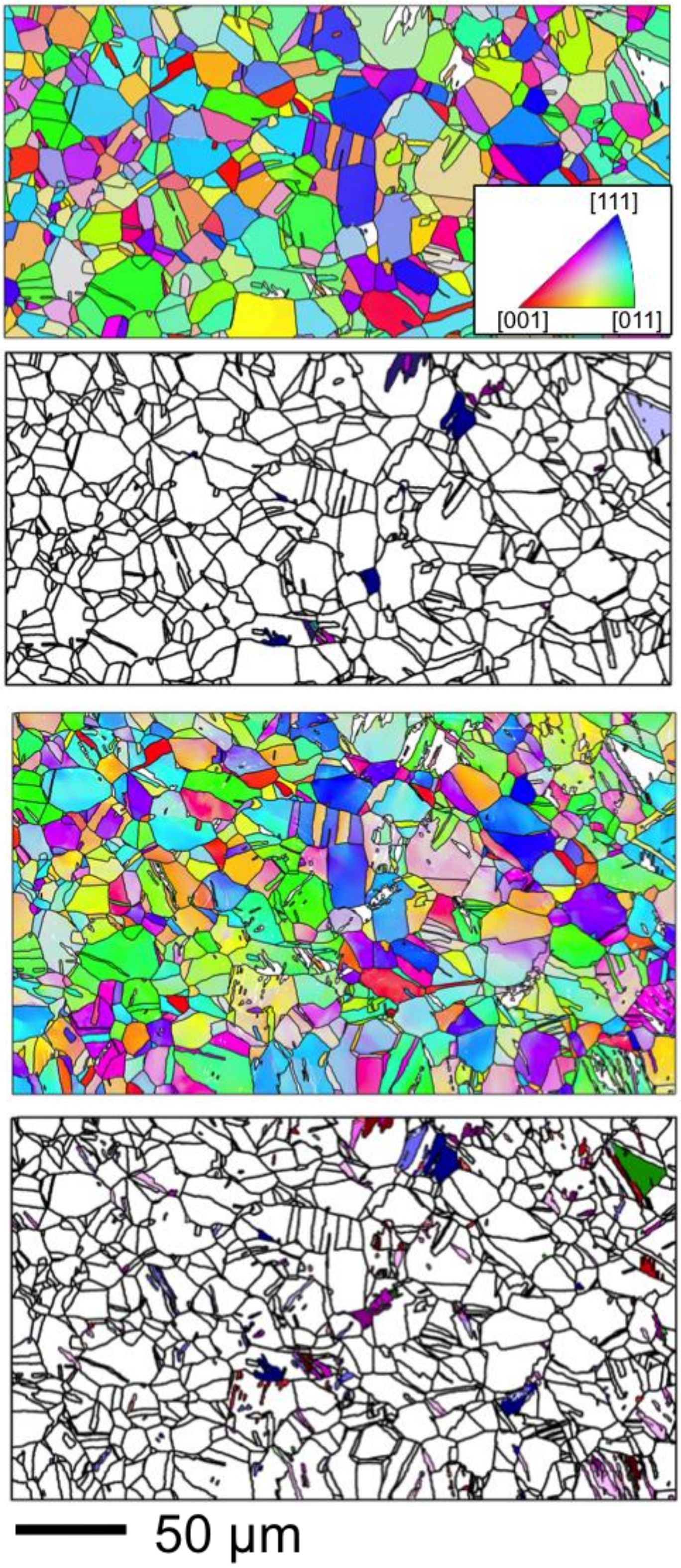

Figure 4-6. EBSD orientation maps showing strain-induced martensite at 9% strain. (a) IPF orientation map of the microstructure prior to deformation, (b) residual K-S martensite variants present in the microstructure prior to deformation, (c) IPF orientation map of the microstructure post deformation and (d) strain induced K-S variants at 9% macroscopic strain.

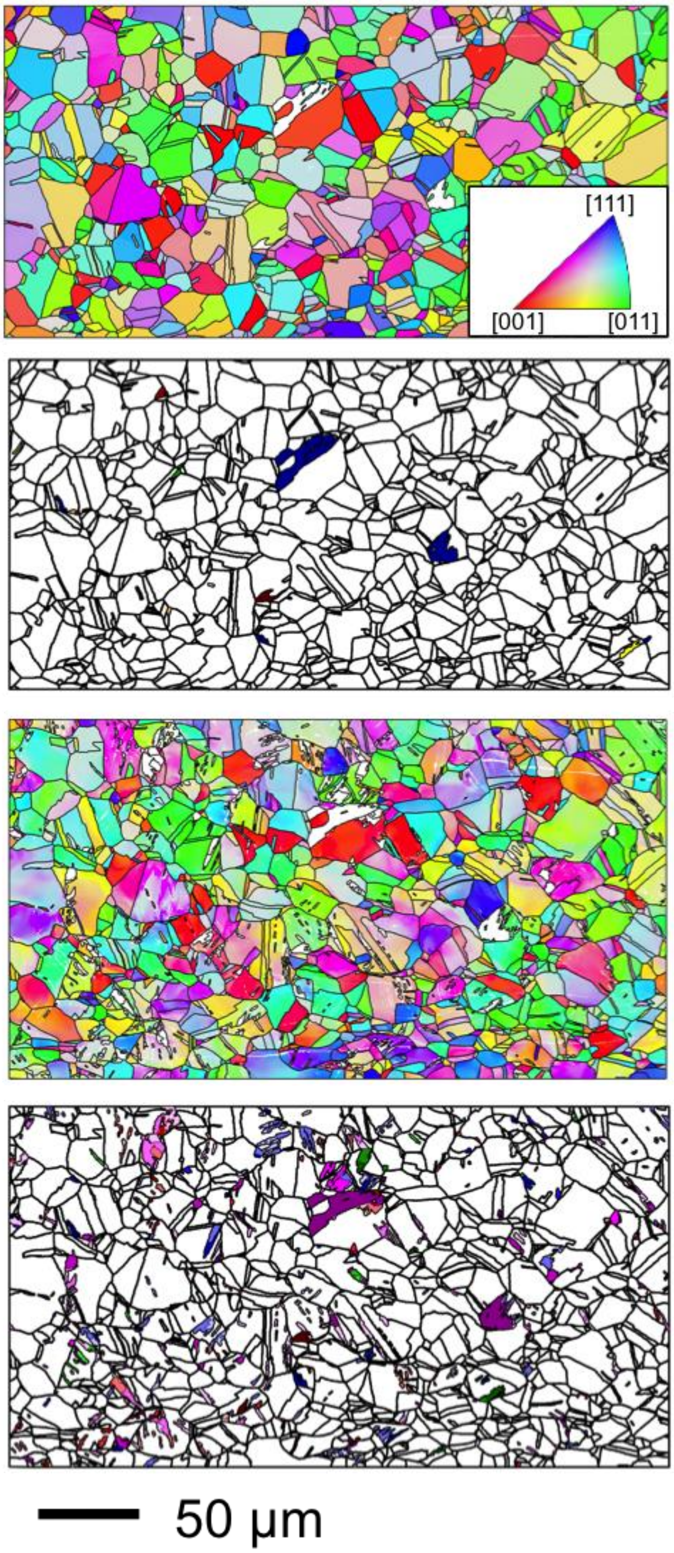

Figure 4-7. EBSD orientation maps showing strain-induced martensite at 10% strain. (a) IPF orientation map of the microstructure prior to deformation, (b) residual K-S martensite variants present in the microstructure prior to deformation, (c) IPF orientation map of the microstructure post deformation and (d) strain induced K-S variants at 10% macroscopic strain.

The strain-induced martensite for each of the measurements (see Figure 4-9) was further analysed in the form of individual martensite variants (based on the K-S orientation relationships [41]). Here, the total area-fraction of each martensite variant (every colour indicates one of the 24 KS relationships) is summed together and plotted both prior to and post, straining. The total amount of deformation-induced martensite depends on various parameters such as the amount of plastic deformation, stress state of the material, temperature and the strain rate [11], [14], [147]. It is also greatly influenced by the steel composition and stacking fault energy [3], [5], [50], [165], [166]. The samples used in this dissertation are austenitic stainless steel which have relatively low stacking fault energy [144]. These austenitic stainless steels were deformed at room temperature to induce martensite at a fixed strain rate of $4\times10^{-4}s^{-1}$, similar to the strain rate employed in reference [11]. As the deformation progresses, there is an increase in the strain-induced martensite (refer Figure 4-2 to Figure 4-7) and consequently the area fraction of the other favoured variants increase in comparison to residual variants present prior to deformation (refer Figure 4-8). Variant selection for strain-induced martensitic transformations depends on the interaction of applied stress, with the habit plane of the martensite, *i.e.*, the interphase between the parent (austenite) and product (martensite) lattices and the shape deformation associated with the martensite [17].

Figure 4-8 shows the above-mentioned microstructural evolution of the strain-induced martensite variants. Here, each variant is assigned by looking at the habit plane orientation (relation between the parent austenite and product martensite) which is the closest match with 24 KS orientations given in Table 2-1.

Initially, in all the prestrained measurements, the residual martensite contained >35% area fraction of variant number 17 (refer to Table 2-1) and this was as high as 65% in the strained sample 6. It was observed that on application of strain, variant number 19 had the highest area fraction (> 16% at 5% strain, which was followed by variant number 14. It is clear from Figure 4-8 that application of stress promotes the formation of certain variants.

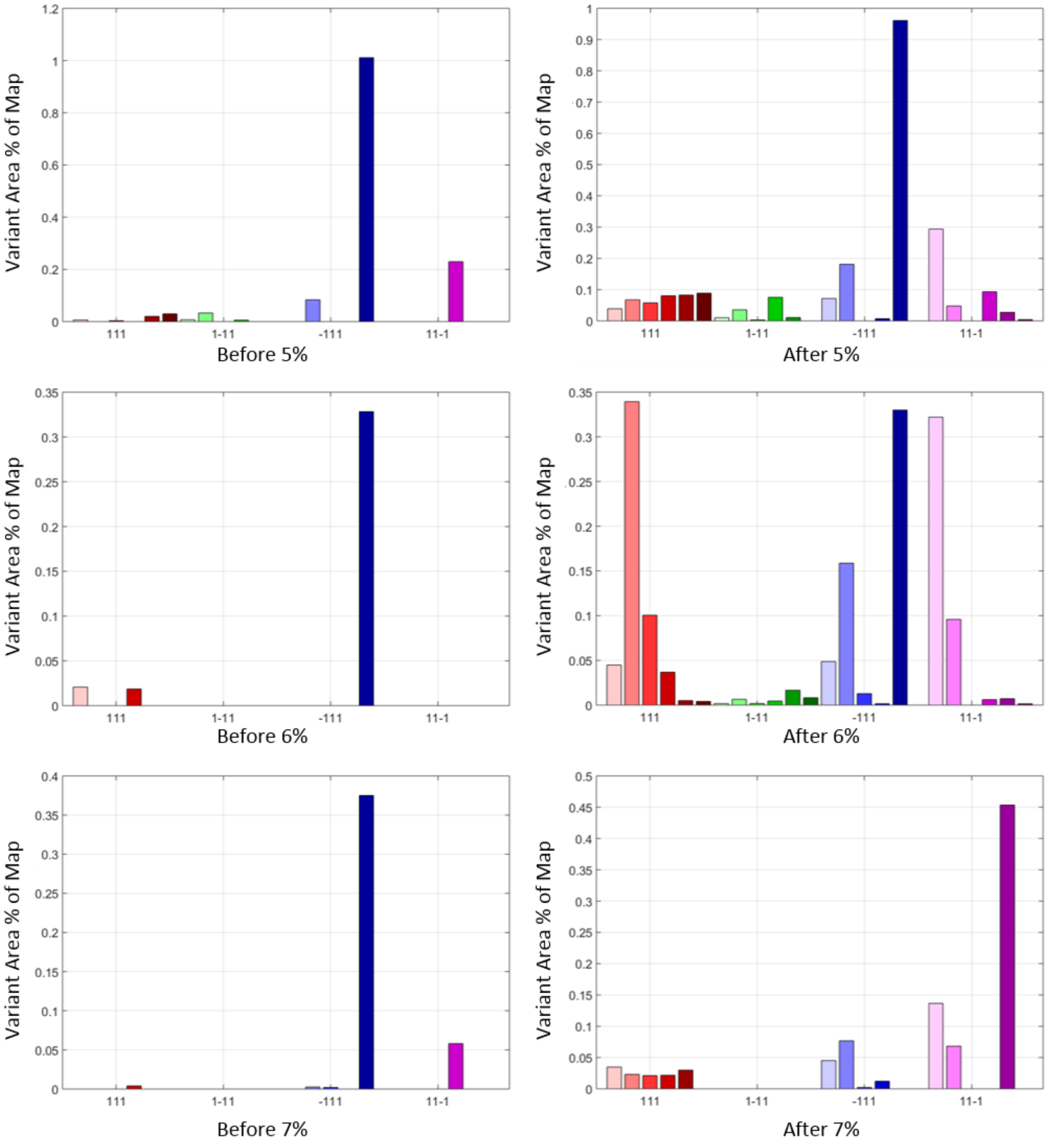

Before 5%

After 5%

Before 6%

After 6%

Before 7%

After 7%

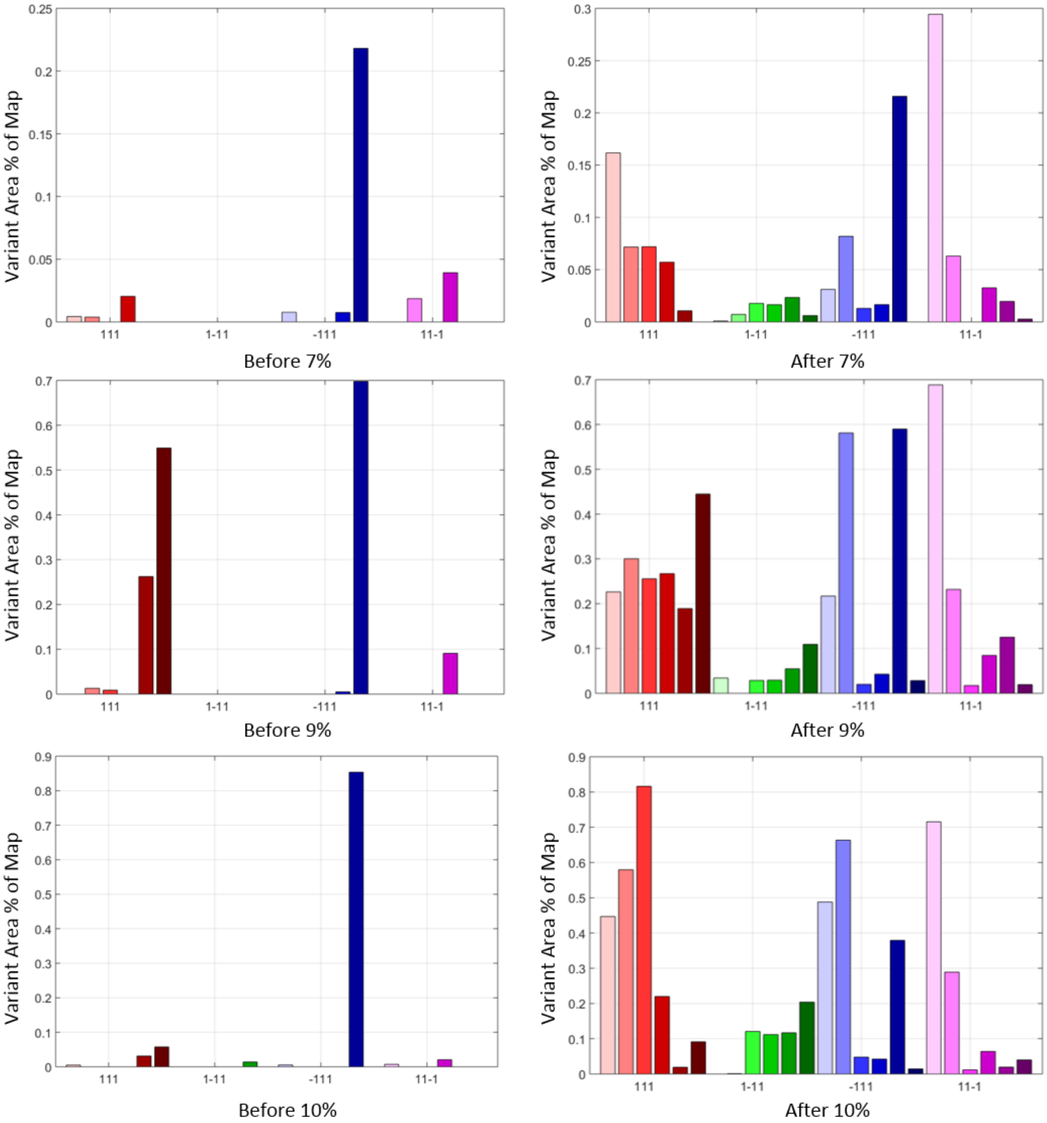

Figure 4-8. Strain-induced martensite variants (area % of the EBSD map) during deformation process.

It is clear from Figure 4-8 that certain variants form more than others, as these maps are variant area fractions for the entire EBSD maps. Variant selection may be further probed on an austenite grain-by-grain basis of known orientations, with respect to the loading axis (this point is argued in detail in the final discussion, Section 7.1.2). On the other hand, there are some austenite grains, which do not undergo strain-induced γ→α′ transformation. The total amount of increase in strain-induced martensite is plotted in Figure 4-9 (A), whereas the percentage of austenite grains transforming is plotted in Figure 4-9 (B). Small fluctuations in the amount of strain-induced martensite (~ 0.5 - 1 % transformation) were observed on straining the material up to ~ 8% macroscopic strain. Further, as each test was conducted on a different specimen such a small scatter is very possible. Here, it is believed that plastic deformation predominantly leads to the distortion of the austenite crystal lattice and creation of martensite embryos. Thereafter, a significant increase in martensite volume fractions was observed upon deforming the material to strains greater than 9%. The increase in strain induced martensite at 10% macroscopic strain was measured as ~ 4.2%. Although the martensite volume fraction measured increases with application of strain, there was a subsequent decrease in the indexing. The percentage of non-indexed points was as high as ~ 6.58 percent for sample incrementally loaded to 10 percent macroscopic strain. This may be due to increase in plastic deformation of the austenite lattice, *i.e.*, formation and accumulation of dislocations within the crystal structure.

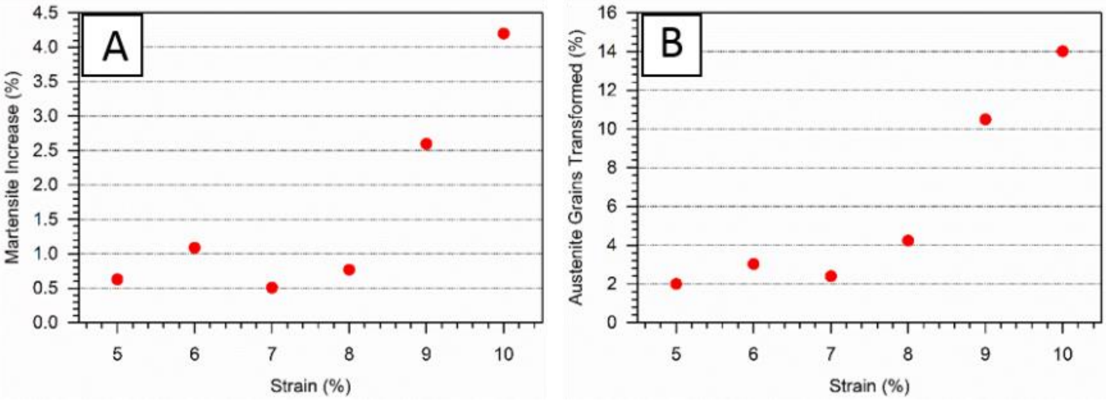

Figure 4-9. (A) Strain induced martensite fraction measured using EBSD vs applied macroscopic strain. (B) Percentage of austenite grains transformed versus applied macroscopic strain.

4.2.2 Incremental loading

Further EBSD measurements were carried out on samples incrementally strained to 5% and 10% macroscopic strains respectively (see Figure 4-10). Here, each specimen was loaded and unloaded in 1% strain increments up to maximum values of 5 and 10% macroscopic strain. Straining the material in this manner resulted in a greater volume fraction of martensite, ~ 0.98% and ~ 7.3% strain-induced martensite at 5 and 10% macroscopic strain respectively (see Figure 4-11 (A)).

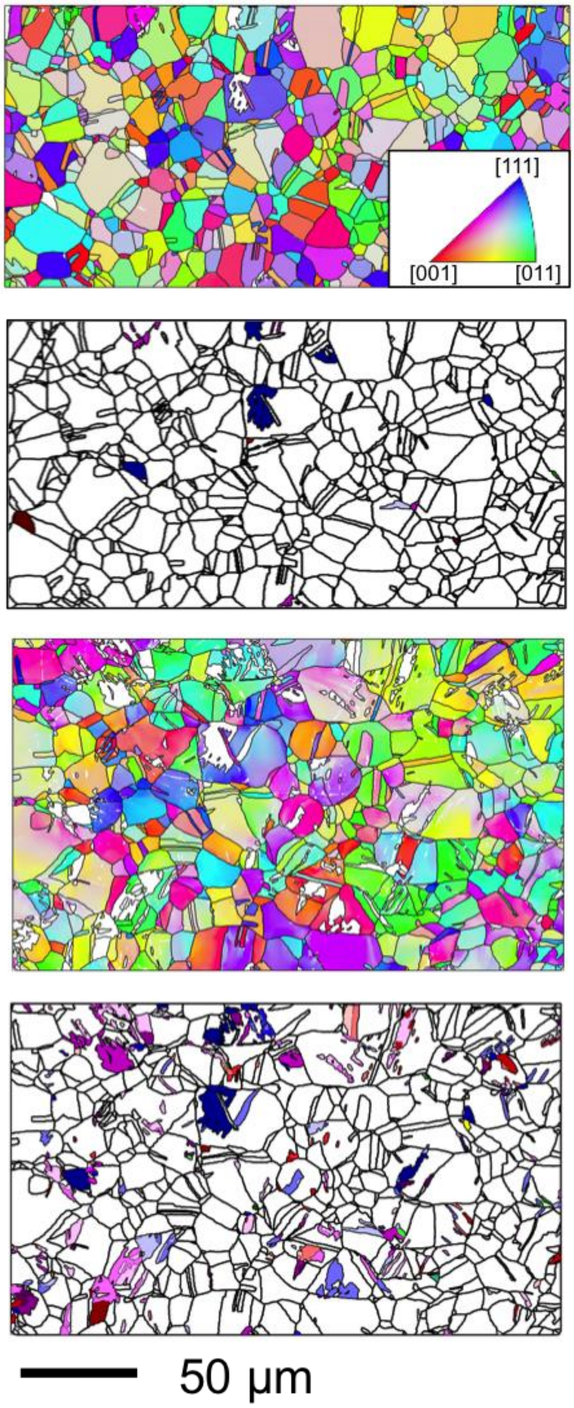

Figure 4-10. EBSD orientation maps showing strain-induced martensite at 10% incremental strain. (a) IPF orientation map of the microstructure prior to deformation, (b) residual K-S martensite variants present in the microstructure prior to deformation, (c) IPF orientation map of the microstructure post deformation and (d) strain induced K-S variants at 10% incremental macroscopic strain.

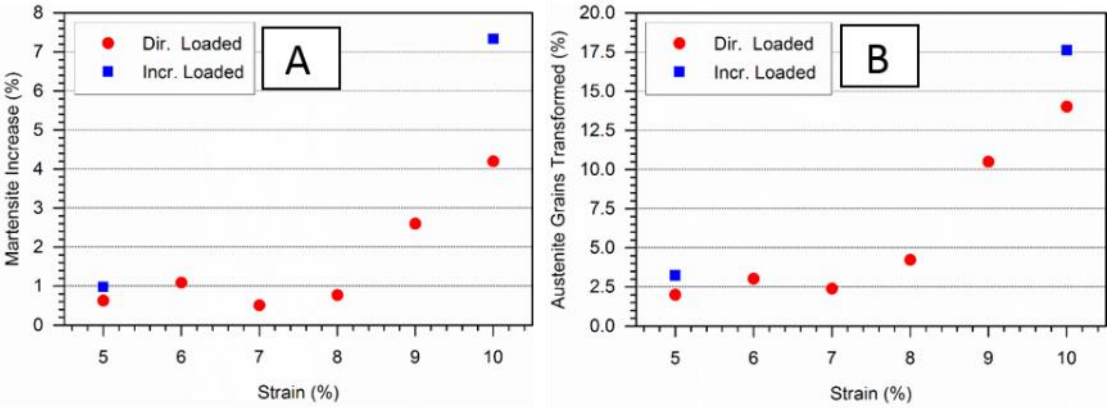

Figure 4-11. (A) Strain-induced martensite fraction measured using EBSD vs applied macroscopic strain. (B) Percentage of austenite grains transformed versus applied macroscopic strain. For samples deformed both directly (coloured red) and incrementally (coloured blue).

Figure 4-11 (B) shows an increase in the number of grains transforming with increasing applied macroscopic strain. It shows that incremental loading-unloading increases the total amount of strain-induced martensite to a greater extent, than it does the number of grains transforming. This indicates that once the transformation progresses, it creates potential nucleation sites for further strain-induced transformation to occur within the same grain.

4.2.3 Transformation in preferred austenite orientation

Observation of the grain maps in Figure 4-2 to Figure 4-7 indicate that grains orientated in a {110} orientation (*i.e.* grains coloured green in the IPF maps) show a preferential transformation tendency. Orientation distribution functions (ODF at 45° section) maps of the same austenite grains prior to and post the deformation process (refer Figure 4-12) corroborate these results. The ODFs calculated from the same tested to 5% strain show little change in intensities, with only a little smoothing noticed because of an increase in mosaicity resulting from plasticity (also evident in the post deformation grain maps. In both the samples tested to 7% and 10% show a distinct drop in intensity at the {110}<001> position.

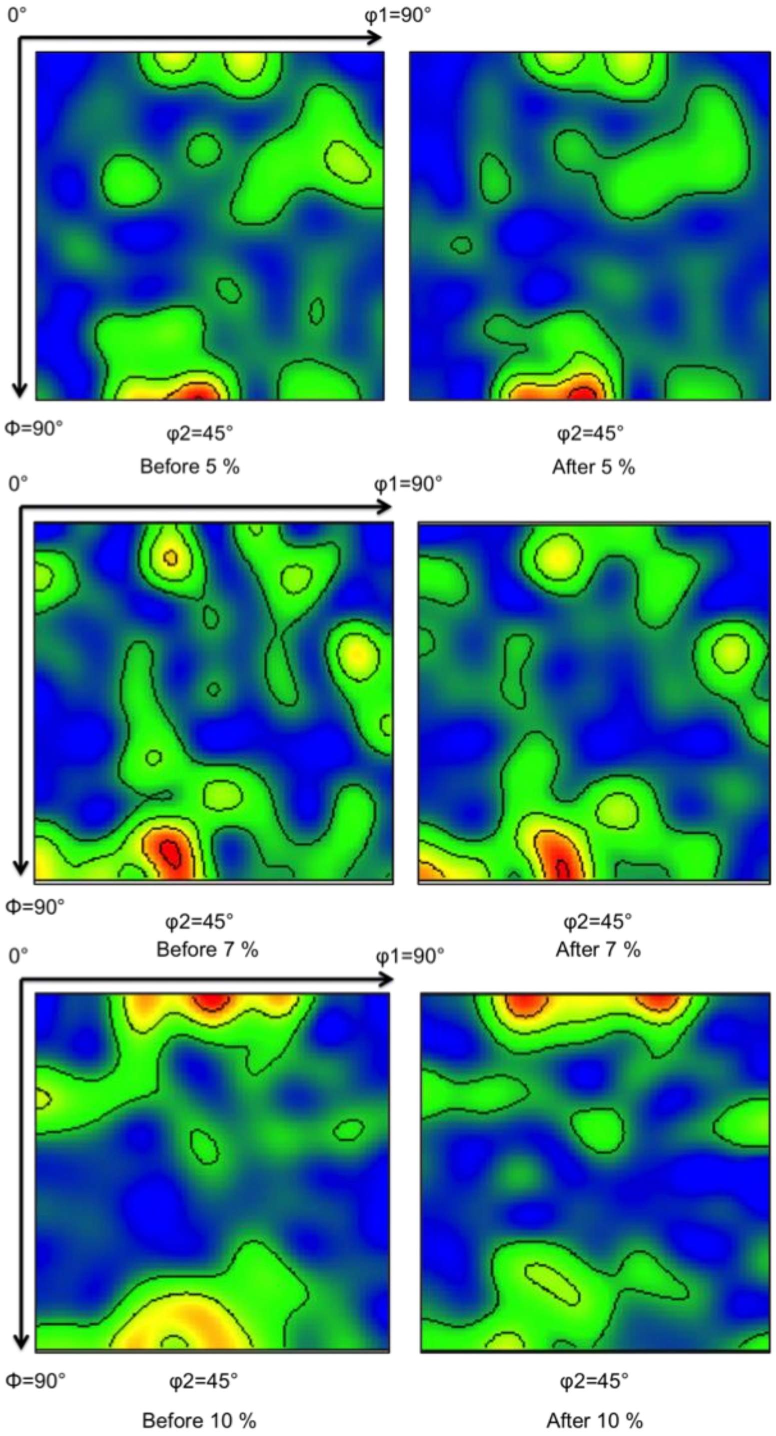

Figure 4-12. The 45° ODF sections of the microtexture evolution of austenite phase during its plastic deformation.

4.2.4 Plastic strain accumulation

Because deformations were conducted at room temperature and martensite transformation occurs at strains beyond the yield point, deformation due to dislocation generation, movement and accumulation was a competing mechanism in the material. The dislocations produced from this deformation lead to local changes in lattice orientation and the degree of plastic strain in the material was measured by plots of misorientation mapping similar to the approaches in Brewer *et al.* [167] and more recently Githinji *et al.* [168] and Unnikrishnan *et al.* [169]. The plastic strain leads to degradation in quality of the Kikuchi diffraction patterns [170]; however, the main drawback here was that other factors affecting the quality of pattern and result in erroneous measurements such as surface preparation and contamination, pattern overlapping close to the grain boundaries and particular crystallographic planes contributing to an individual pattern [171], were not factored. The approach taken here is similar to [168], [169], where small lattice rotations (local misorientation) due to the accumulation of geometrically necessary dislocation (GNDs) between adjacent measurement points gives the measure of deformation. Here, using EBSD grain data, boundaries are defined as regions surrounded by austenite grains having crystallographic misorientation greater than 15°. Figure 4-13 shows the Kernel average misorientation (KAM) map of samples both prior to and post the deformation process. These misorientations are localized near the grain boundaries, along slip line traces, near and around strain-induced martensite and where sub-grains are formed (see Figure 4-13).

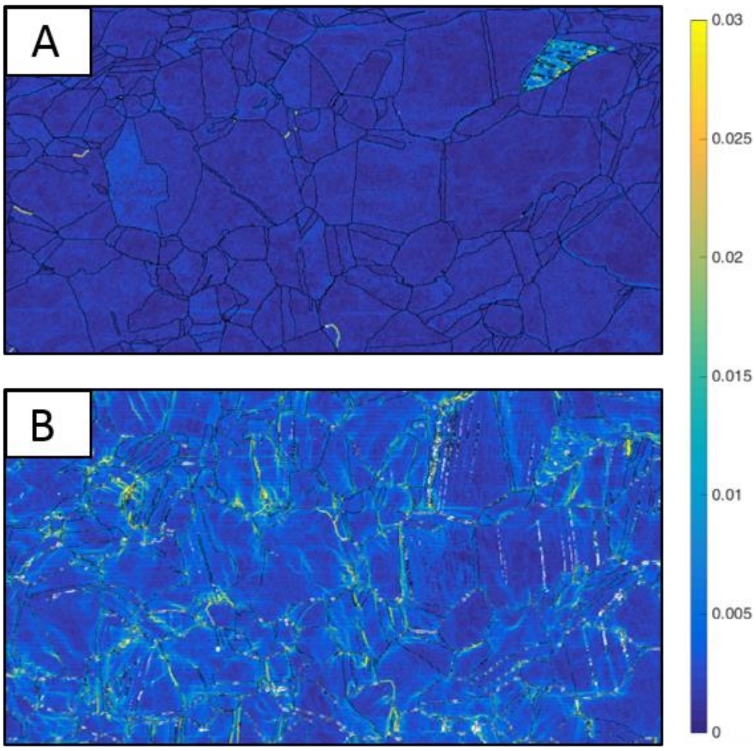

Figure 4-13. The Kernel average misorientation (KAM) maps of (A) before deformation and (B) post deformation process.

Figure 4-14 shows the frequency of the local misorientation (KAM plots here are similar to those plotted in [168], [169]) values of samples strained to different macroscopic strains as discussed earlier for samples strained to 5 to 10% macroscopic strain. KAM considers misorientation less than 2°, here the KAM values increased as the total macroscopic strain increased. These KAM values do not give an absolute measure of plastic strain, as they are dependent on the step size [168]; however, they can be used to measure geometrically necessary dislocation density [172]. It was seen that each strain increment resulted in an increase in amount of plastic deformation of crystal lattice, which was picked up by the KAM plots and peaks shifted to higher values of misorientation. This trend showed the increase in GND with strain at each macroscopic strain value.

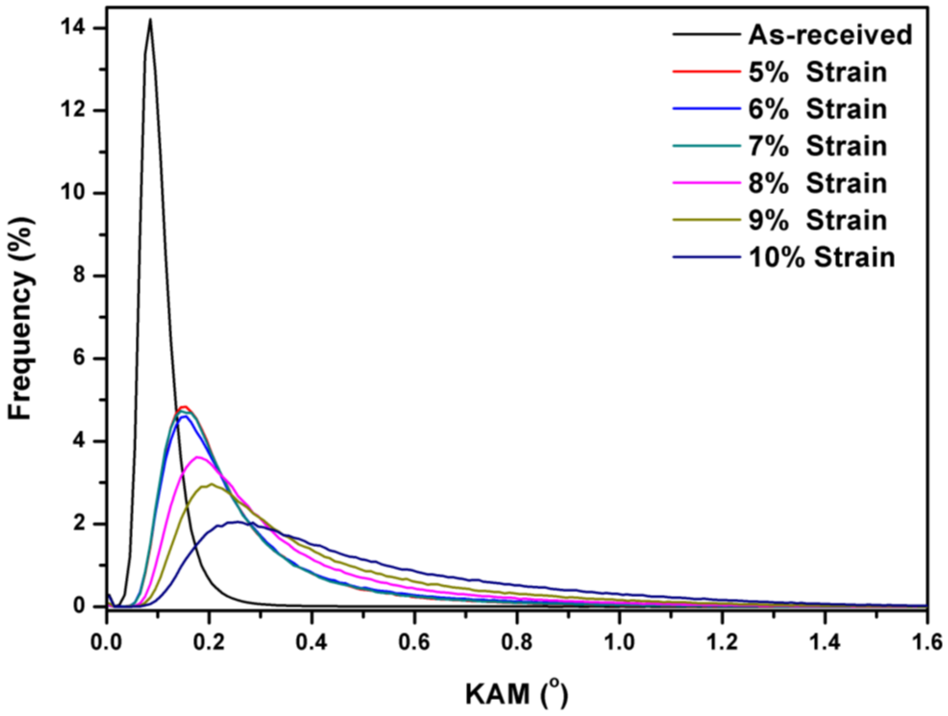

Figure 4-14. Kernel Average Misorientation (KAM) plots of samples directly strained.

Figure 4-15 shows KAM plots of the samples strained to directly and incrementally to global macroscopic strains of 5 and 10% strain. There was a slight decrease in the peak height and increase in peak width at 5% strain. In the 10% sample any difference is less visible, however a similar trend is observed. These KAM plots show an increase in geometrically necessary dislocations with increase in applied macroscopic strain. Although this is observed in samples loaded, unloaded and reloaded, this effect is not as profound as changes in KAM observed when a sample is simply deformed to a higher macroscopic strain increment (see Figure 4-15).

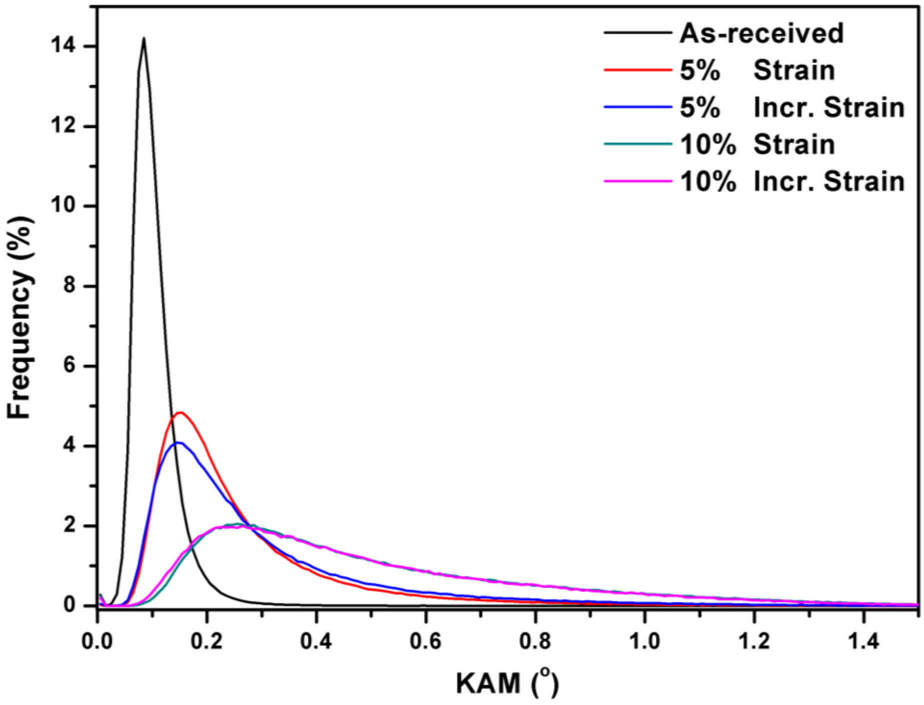

Figure 4-15. Kernel average misorientation (KAM) plots of samples strained directly and incrementally.

In comparison to the directly strained samples, the incrementally strained samples did not show an increase in geometrically necessary dislocations to a great extent (refer Figure 4-14). However, there is a significant increase in the amount of strain-induced martensite as measured in Figure 4-8. To investigate further, a closer look at stress-strain curves for the incrementally and directly loaded, deformed samples are required. Figure 4-16 (A) shows the comparison between both the incrementally and directly loaded samples to 10% macroscopic strain. Figure 4-16 (B) is the magnified curve showing an increase in the width of the hysteresis on unloading and subsequent re-loading. These back stresses seem to affect the amount of strain-induced martensitic transformation, especially in the grains showing tendency to transform (refer Section 4.2.2).

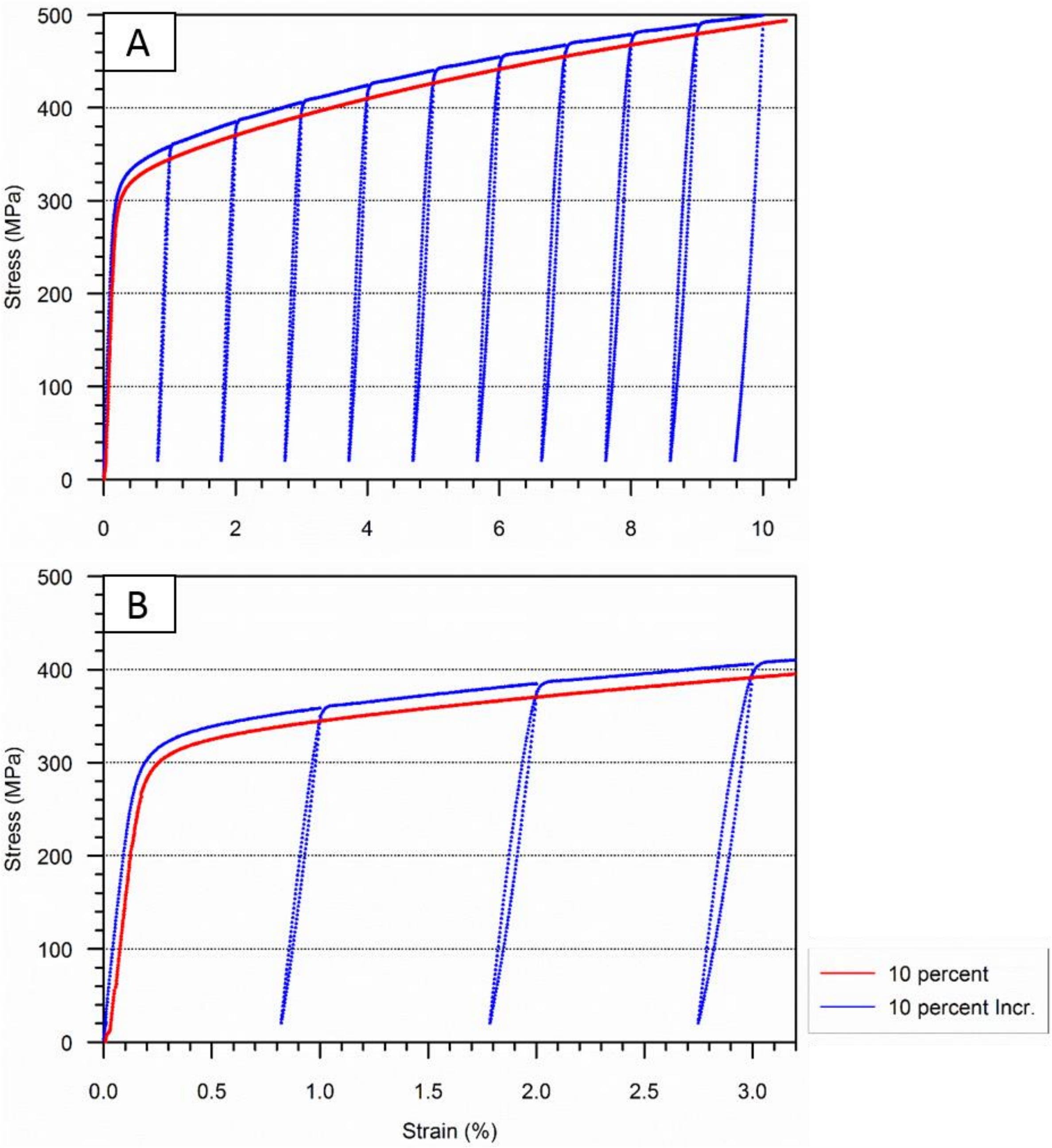

Figure 4-16. Stress-strain curves for samples directly and incrementally loaded to 10 percent strain. (A) Complete curves and (B) magnified curve up to 3.2% total strain.

4.3 Discussion

4.3.1 Effect of normal vs. incremental loading on strain-induced martensite formation

An increase in the amount of plastic deformation is measured with KAM maps (see Figure 4-14 and Figure 4-15). The effect is distinct when the samples are strained to different global macroscopic strain increments in comparison to the samples loaded, unloaded and reloaded. Further, it was observed that with this increase in applied strain, a higher volume fraction of martensite was formed. Here, less than 1% transformation was observed up to ~8% macroscopic, whereas ~4.2% transformation observed at 10% applied macroscopic strain (see Figure 4-9 and Figure 4-11). With the increase in strain, there is lattice deformation leading to formation of potential nucleation sites (martensite embryos), which transform to strain-induced martensite on still greater deformation or application of stress [3], [4], [60]. The formation of martensite nucleation sites and strain-induced martensite transformation is explained in greater detail in the Section 5.3.

Observations on the incremental loading, unloading and reloading experiments showed that still a higher volume fraction of strain-induced martensite was formed, when material was deformed in this manner (see Figure 4-11). This is obtained owing to the back stresses in the unloading cycle, as well a greater cummulative loading effect, which trigger transformation in the newly formed martensite embryos.

Further, there is a considerable difference in the KAM plots of materials deformed directly or incrementally to 5% macroscopic strain, where the incremental KAM plot is slightly lower and broader in comparison to the directly strained specimen. Here it is possible that dislocation density around phase transformation sites causes the peak to broaden slightly. However, for samples deformed to relatively higher strain increments to 10% strain, the KAM distribution is very similar. Here, owing to the massive lattice distortion it is not possible to detect KAM changes in the material due to plastic strain build up and strain built up, around transformation sites (see Figure 4-15). This level of macro strain has essentially saturates the KAM.

With increase in strain and strain-induced martensitic transformation, a greater number of austenite grains undergo strain-induced transformation (see Figure 4-9). However, when the samples are incrementally loaded, although the percentage of strain-induced transformation increases by over 50%, there is not a similar trend in the increase in the number of grains transforming. It is therefore thought that the grains most affected by strain, *i.e.* the grains that deform and form martensite embryos, are the most likely sites for the formation of strain-induced martensite on further deformation. It is unlikely that at room temperature, strain-induced transformation can progress without some plastic deformation, within individual austenite grains. This is further discussed in Section 6.3.

4.3.2 Crystallography

For the austenite (fcc) grains, slip occurs on the {111} slip planes and along the <110> directions [173]. When the highly deformed austenite grains are further deformed, the plastic deformation of the austenite lattice leads to formation of nucleation sites for the strain-induced transformations to occur. On still further deformation of the material, strain-induced martensite occurs on these {111} slip planes [144]. Details of the transformation mechanism and transformation sequence are explained in the final discussion chapter combining results from all three-measurement techniques (refer Section 7.1.2).

The variant plots (see Figure 4-8) show the transformation behaviour for the entire EBSD map and for all grains within it. This technique is not ideal, as at the grain boundaries it is difficult to predict the true habit plane with respect to any given grain. However, this technique gives a good indication of preferential variant selection in the overall microstructure. A more detailed insight into variant selection may be obtained by probing individual grains within a larger EBSD map. This analysis is done in the following chapter on two individual austenite grains (refer Section 7.1.2).

4.4 Summary

Deformation in the materials is due to both a combination of dislocation generation and accumulation and due to strain-induced martensitic transformation.

Incremental deformation greatly affected the total amount of strain-induced transformation. This is evident from Figure 1-20 (A) and appears to be the reason for the broadening of the hysteresis (Figure 1-24 (B)), during the loading, unloading and reloading cycles.

Grains that underwent strain-induced martensitic transformation formed potential nucleation sites for further transformation to occur. In the incrementally strained experimental specimens, the load-unload cycles activated greater transformation in those grains.

There was not a clear distinction or difference in the KAM plots of samples strained directly or incrementally to given strains, implying that overall deformation due to geometrically necessary dislocations were the same.

Therefore, in the following chapter, in order to eliminate the effect of these back-stresses on the amount of transformation, all the high-resolution digital image correlation measurements (HR-DIC) were made *in situ* SEM.

5 *In situ* observation of strain and phase transformation in plastically deformed stainless steel using DIC

5.1 Introduction

This chapter discusses the combination of EBSD and DIC data with the aim of drawing insights into the martensitic phase transformations. Further experimental details may be found in Chapter 3. In short, DIC data is overlaid on EBSD grain boundaries to look at the strain heterogeneity within the microstructure and around potential transformation sites. EBSD measurements were made both prior to and post the deformation process as explained in Chapters 3 and 4.

Figure 5-1 shows high-resolution EBSD orientation maps before and after the strain-induced martensitic phase transformation. Figure 5-1 (a) is the pre-strained EBSD grain boundary map of the as-received 301 austenitic stainless steel. It does not have any strain-induced martensite present and has an austenite volume fraction greater than 99%. Figure 5-1 (b) is the post deformation EBSD grain boundary map showing strain-induced martensite locations within the same set of grains at 10% applied strain.

In this figure the orientation relationship between the parent austenite (γ) grain and the product martensite (α') plate used is that of Kurdjumov-Sachs (KS) [41], where $(111)_{\gamma}$ is parallel to $(011)_{\alpha'}$ and $[011]_{\gamma}$ is parallel to $[111]_{\alpha'}$. However, it is now known that the true orientation relationship between γ/α' is irrational [15], [45], [47], reported as $(111)_{\gamma}$ parallel to $(0.012886\ 0.981915\ 0.978457)_{\alpha'}$ and the $[110]_{\gamma}$ direction parallel $[0.927033\ 1.055684\ -1.071623]_{\alpha'}$ [15]. Still, the KS orientation relation is found to be a good approximation. In Figure 5-1 (b), each variant of strain-induced martensite plates is coloured distinctly and the grains labelled 1 and 2 are analysed in the following sections. Since only the martensite variant most favourable to the direction of the applied stress nucleates [61], post-straining EBSD results (Figure 5-1(b)) will help in identifying the conditions for martensitic transformations, when combined with the strain maps obtained with DIC analysis. The dominance of variants 5 and 6 is interesting and may be due to the driving force from either chemical or mechanical origins being higher for these variants [44].

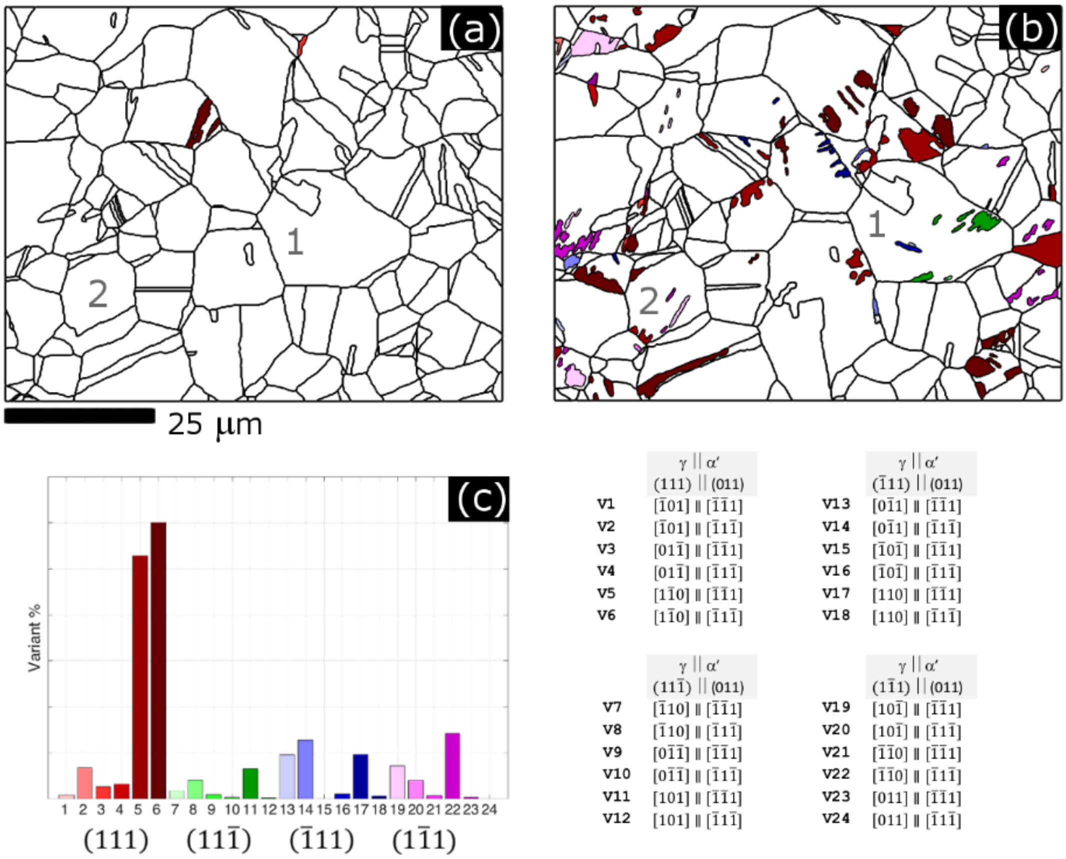

	$\gamma \parallel \alpha'$ $(111) \parallel (011)$		$\gamma \parallel \alpha'$ $(\bar{1}11) \parallel (011)$
V1	$[\bar{1}01] \parallel [\bar{1}\bar{1}1]$	**V13**	$[0\bar{1}1] \parallel [\bar{1}\bar{1}1]$
V2	$[\bar{1}01] \parallel [\bar{1}1\bar{1}]$	**V14**	$[0\bar{1}1] \parallel [\bar{1}1\bar{1}]$
V3	$[01\bar{1}] \parallel [\bar{1}\bar{1}1]$	**V15**	$[\bar{1}0\bar{1}] \parallel [\bar{1}\bar{1}1]$
V4	$[01\bar{1}] \parallel [\bar{1}1\bar{1}]$	**V16**	$[\bar{1}0\bar{1}] \parallel [\bar{1}1\bar{1}]$
V5	$[1\bar{1}0] \parallel [\bar{1}\bar{1}1]$	**V17**	$[110] \parallel [\bar{1}\bar{1}1]$
V6	$[1\bar{1}0] \parallel [\bar{1}1\bar{1}]$	**V18**	$[110] \parallel [\bar{1}1\bar{1}]$

	$\gamma \parallel \alpha'$ $(11\bar{1}) \parallel (011)$		$\gamma \parallel \alpha'$ $(1\bar{1}1) \parallel (011)$
V7	$[\bar{1}10] \parallel [\bar{1}\bar{1}1]$	**V19**	$[10\bar{1}] \parallel [\bar{1}\bar{1}1]$
V8	$[\bar{1}10] \parallel [\bar{1}1\bar{1}]$	**V20**	$[10\bar{1}] \parallel [\bar{1}1\bar{1}]$
V9	$[0\bar{1}\bar{1}] \parallel [\bar{1}\bar{1}1]$	**V21**	$[\bar{1}\bar{1}0] \parallel [\bar{1}\bar{1}1]$
V10	$[0\bar{1}\bar{1}] \parallel [\bar{1}1\bar{1}]$	**V22**	$[\bar{1}\bar{1}0] \parallel [\bar{1}1\bar{1}]$
V11	$[101] \parallel [\bar{1}\bar{1}1]$	**V23**	$[011] \parallel [\bar{1}\bar{1}1]$
V12	$[101] \parallel [\bar{1}1\bar{1}]$	**V24**	$[011] \parallel [\bar{1}1\bar{1}]$

Figure 5-1. EBSD orientation maps of strain-induced martensitic phase transformation in the same set of grains. (a) Prior to straining having more than 99% austenite and (b) after 10% applied strain in horizontal direction. A histogram of the frequency of different variants (by number of individual martensite grains using the lower magnification EBSD scan) is shown in (c). The details of the 24 K-S variants and the planes and directions that are parallel in the austenite and martensite are displayed. The martensite variants are coloured based on which of these 24 variants they represent.

Figure 5-2 shows the lower-magnification DIC strain maps overlaid over the pre-strained EBSD grain boundary map. Figure 5-2 (a) & (b) are the ε_{xx} strain maps at 5 and 10 % strain respectively. They clearly show the heterogeneous nature of strain accommodation in the different grains. At 10 % global strain, some grains are experiencing close to 20 % strain whilst there are nearby grains exhibiting little or no strain. We have developed a Matlab graphical user interface (GUI) for combining the EBSD and DIC data sets, which uses the MTEX toolbox [174]. The toolbox enables partitioning of DIC data with respect to individual grains calculated from EBSD grain boundary measurements. To get a representative average strain measurement, the displacement outliers observed within grains are removed, before strain calculation. However, some of the high displacements close to some grain boundaries are still taken into account (Figure 5-2 (d)). Thus average ε_{xx} within individual austenite grains can be plotted (Figure 5-2 (d) shows data for a macro strain of 10%). This allows for the least square average for each individual grain to be measured for each strain increment, which enables the determination of the average ε_{xx} distribution within the different grains, at each strain increment (Figure 5-2 (c)). The histogram plot (Figure 5-2 (c)) shows the distribution of average strain within grains as the global strain increases (Figure 5-2 (c)), providing a useful indication of how strain heterogeneity develops during deformation. It is observed that application of strain does not simply shift the histogram plot to the right, but it is accompanied by a change in shape of the profile.

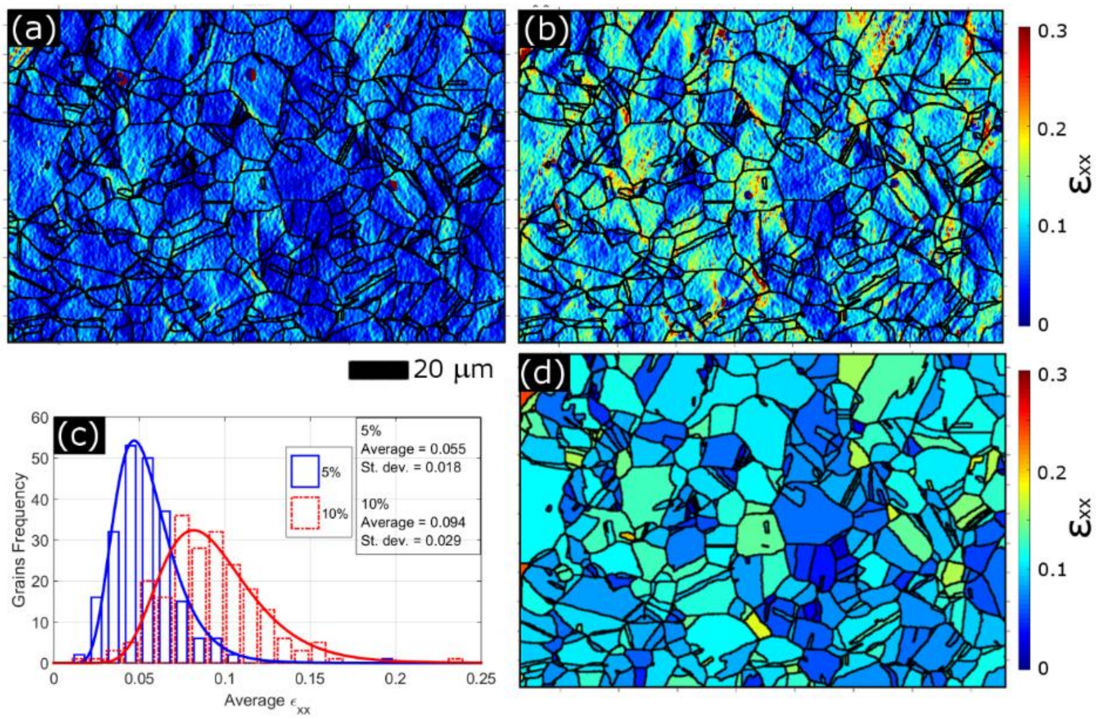

Figure 5-2: Low magnification strain maps overlaid with the EBSD grain boundary map, showing the heterogeneous nature of strain accommodation within individual grains. (a) & (b) show ε_{xx} at 5% and 10% strain respectively. (c) Histogram plot of ε_{xx} at 5% and 10% macroscopic global strain values. (d) Map of the average ε_{xx} within grains at 10% strain used for producing (c).

To obtain greater resolution in strain, a fraction of the area was analysed at a magnification of 5000X. Figure 5-3 shows the HRDIC ε_{xx} strain map at 10 % elongation. This ε_{xx} strain map is overlaid on the post-strain EBSD map of austenite grain boundaries and the strain-induced martensite phase boundaries. In this material slip occurs on the {111} slip-lines and these are visible as shear bands that are a few microns thick. These shear bands occur at about ±45° to the loading direction and along the direction of maximum resolved shear stress. It can be seen that on deforming the material, the strain-induced martensite forms and is parallel to these {111} slip planes.

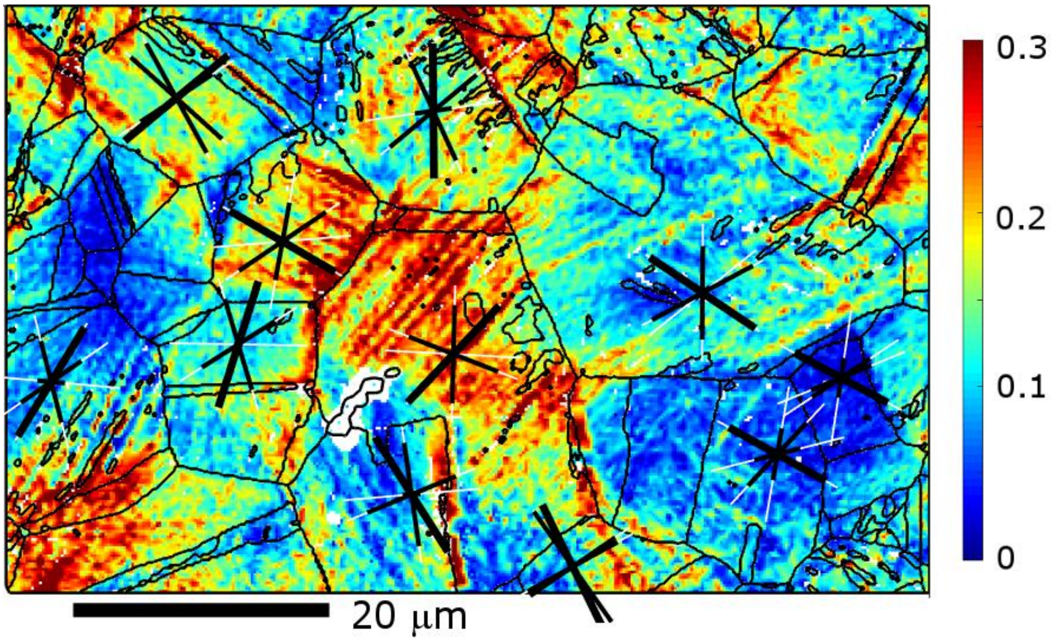

Figure 5-3: High magnification ε_{xx} strain maps overlaid on the EBSD grain boundary map at 10% strain. The EBSD grain boundary map has phase transformation boundaries as well. The lines represent the different {111} slip traces; the length of the black lines is proportional to the Schmid factor and the plane with the highest Schmid factor is thicker.

5.2 Results (DIC strain analysis)

Two DIC and EBSD measurements were made to look at the repeatability of the technique. Both these measurements were made at two different magnifications, *i.e.* at slightly different length scales, as explained in Section 3.3.1.

5.2.1 Microscale strain measurement 1

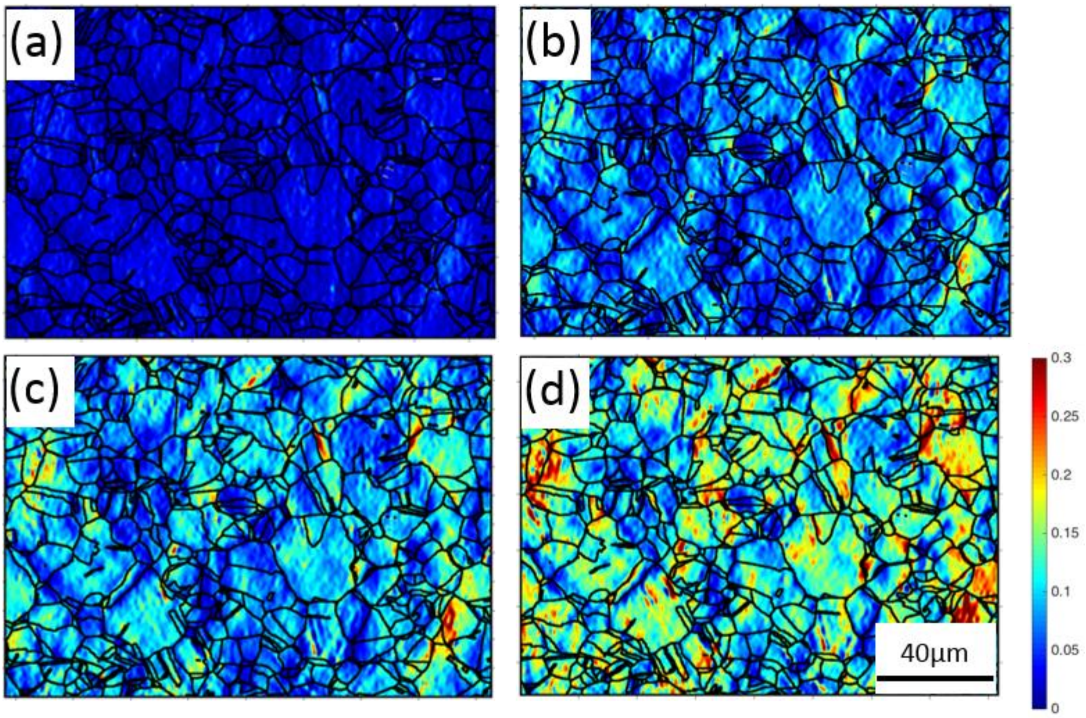

Figure 5-4. Low magnification strain maps overlaid with the EBSD grain boundary maps, showing the heterogeneous nature of deformation within grains for measurement 1. (a) - (d) Are ε_{xx} *measurements made at approximately 2%, 6.5%, 9% and 12.5% strain respectively.*

Figure 5-4 shows the low magnification strain maps, which display the heterogeneous nature of deformation from the very onset of the deformation process. As discussed earlier, at this magnification strain measurements may be used to quantify the amount of plastic deformation within grains. However, at this magnification it is not possible distinguish strain due to individual shear bands, but average deformation within individual grains may still be measured.

These maps are a good measure of the increase in strain heterogeneity, with increase in overall plastic deformation. However, to characterize and locate deformation owing to individual slip planes, higher magnification strain mapping is required.

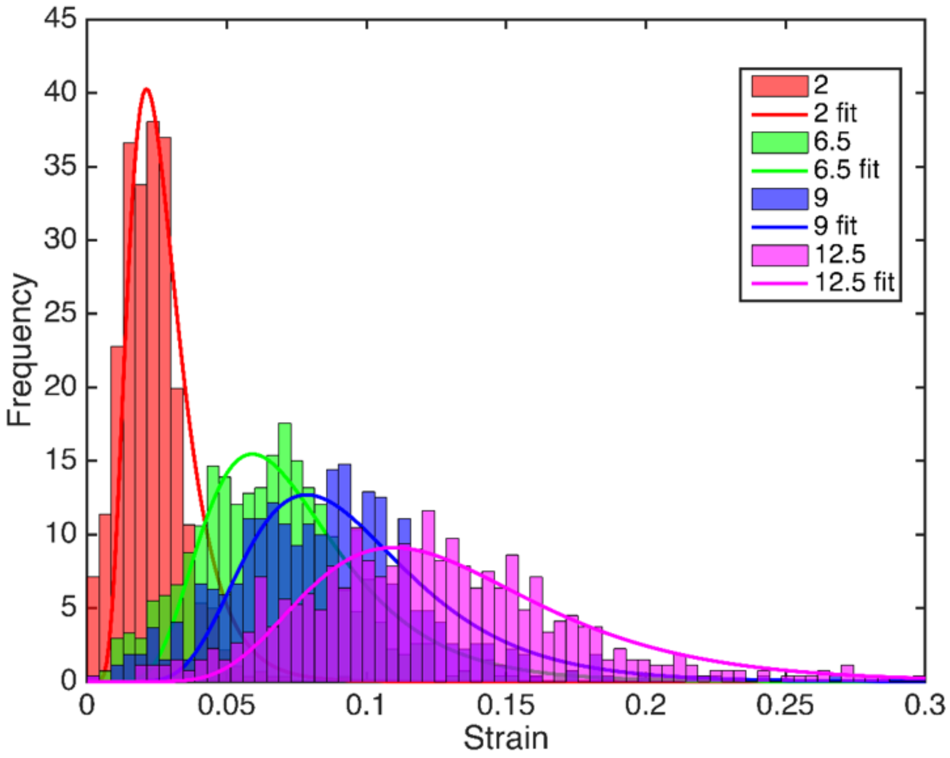

Figure 5-5. Histogram plot showing distribution of strain within individual austenite grains at each applied macroscopic strain increment.

Data from Figure 5-4 can be interpreted as shown in Figure 5-5. Here the x-axis represents the applied global macroscopic strain and the y-axis the frequency of grains. The details of the plotting may be found in Section 5.1. As applied macroscopic strain increases there is an increase in the asymmetry of the curve, *i.e.*, it is not a perfectly Gaussian distribution. Here the positive deviation increases with increase in overall macroscopic strain is as shown in Figure 5-6.

Figure 5-6 is the full width at half maximum of each measurement shown in Figure 5-5 and shows the deviation on either side of the modal strain of the fit.

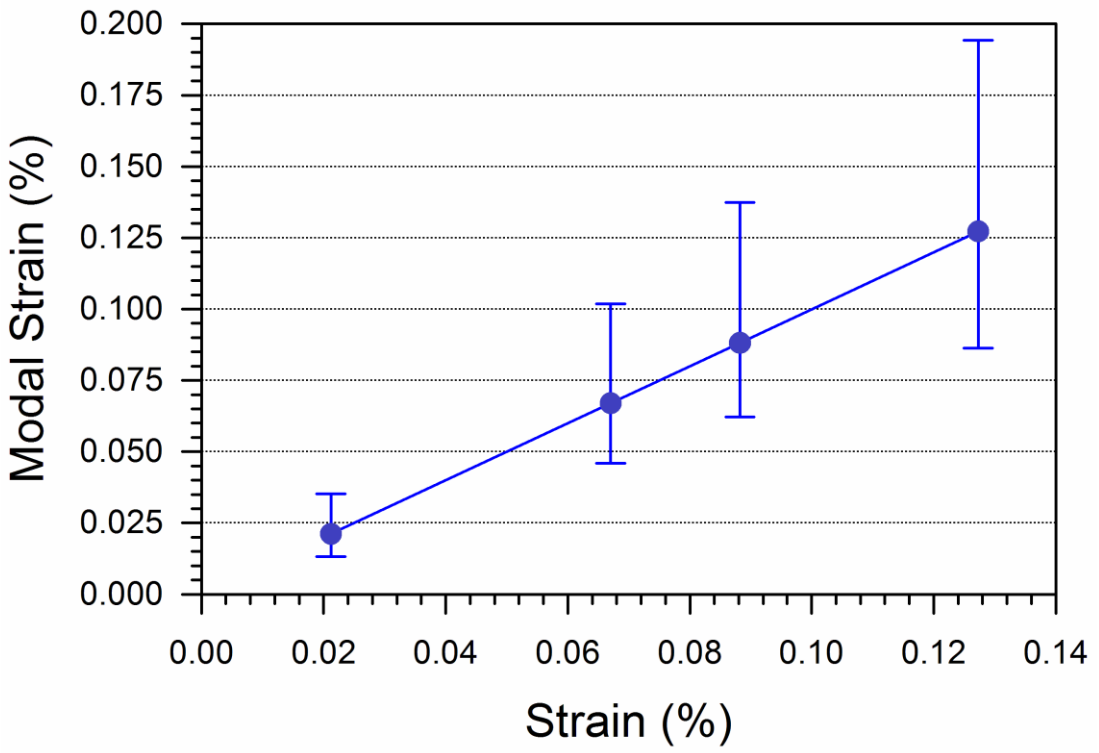

Figure 5-6. Modal strain broadening for grains at each measurement for experiment 1.

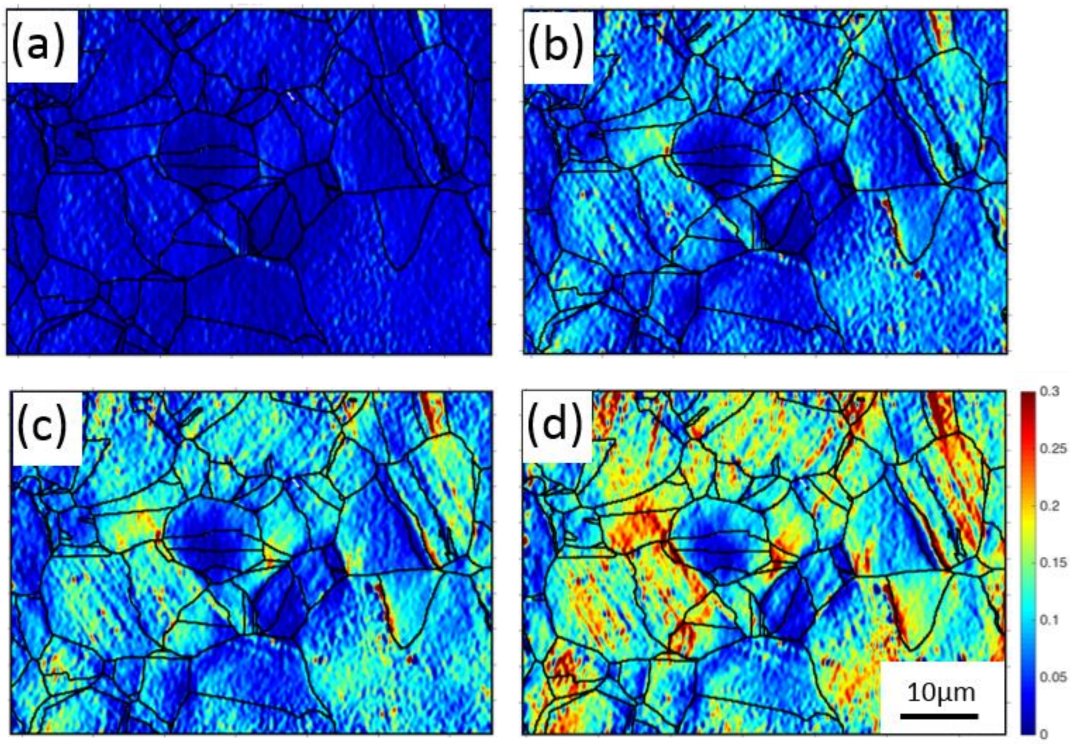

Figure 5-7. High magnification strain maps overlaid with the EBSD grain boundary maps, showing the heterogeneous nature of deformation within grains for measurement 1. (a) - (d) Are ε_{xx} *measurements made at approximately 2%, 6.5%, 9% and 12.5% strain respectively.*

As explained above, an area fraction of Figure 5-4 is probed at still a higher magnification enabling greater strain resolution strain maps to be created, as shown in Figure 5-7. Strain resolution at this length scale enables pinpointing the strain heterogeneity within individual grains, throughout the deformation process, as well as distinguishing strain owing to individual shear planes. All of the strain maps are overlaid on the pre-strain EBSD grain boundary maps.

5.2.2 Microscale strain measurement 2

To show the repeatability of the techniques, a second measurement was made. As with the previous experiment, here measurements were also made at two different length scales. Figure 5-8 shows the low magnification strain maps, which depict the strain heterogeneity with increase in applied macroscopic strain. In this experiment measurements were made at ~2% strain increments. The resulting of modal strain distribution within individual grains is as shown in Figure 5-9.

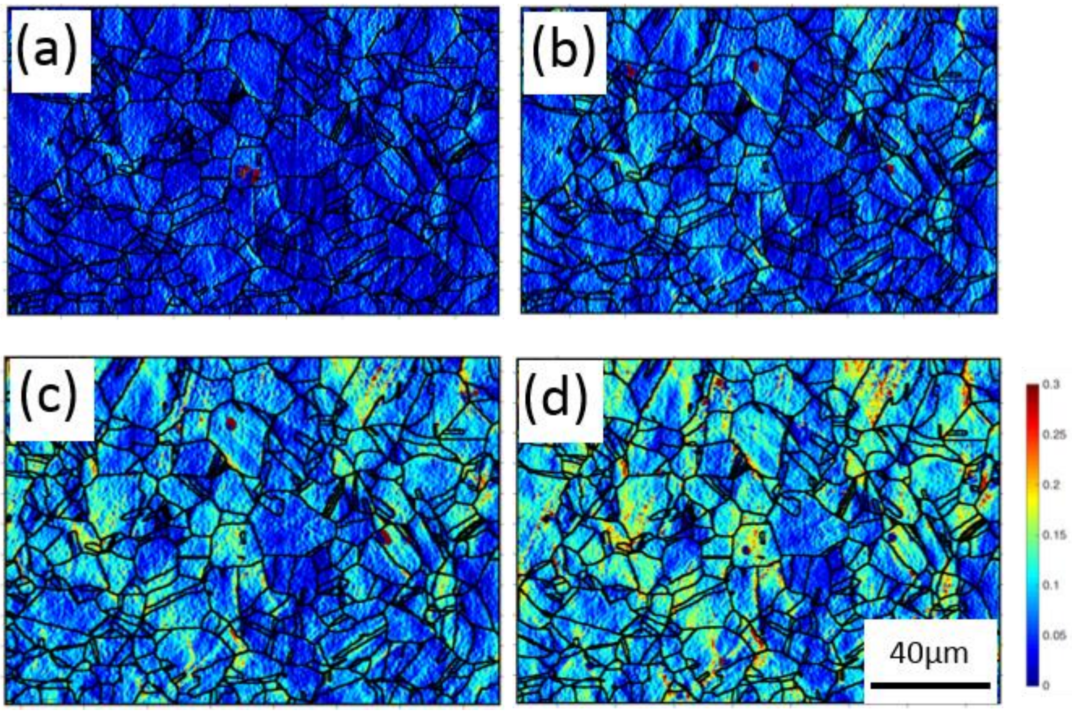

Figure 5-8. Low magnification strain maps overlaid with the EBSD grain boundary maps, showing the heterogeneous nature of deformation within grains for measurement 1. (a) - (d)Are ε_{xx} *measurements made at approximately 4%, 6%, 8% and 10% strain respectively.*

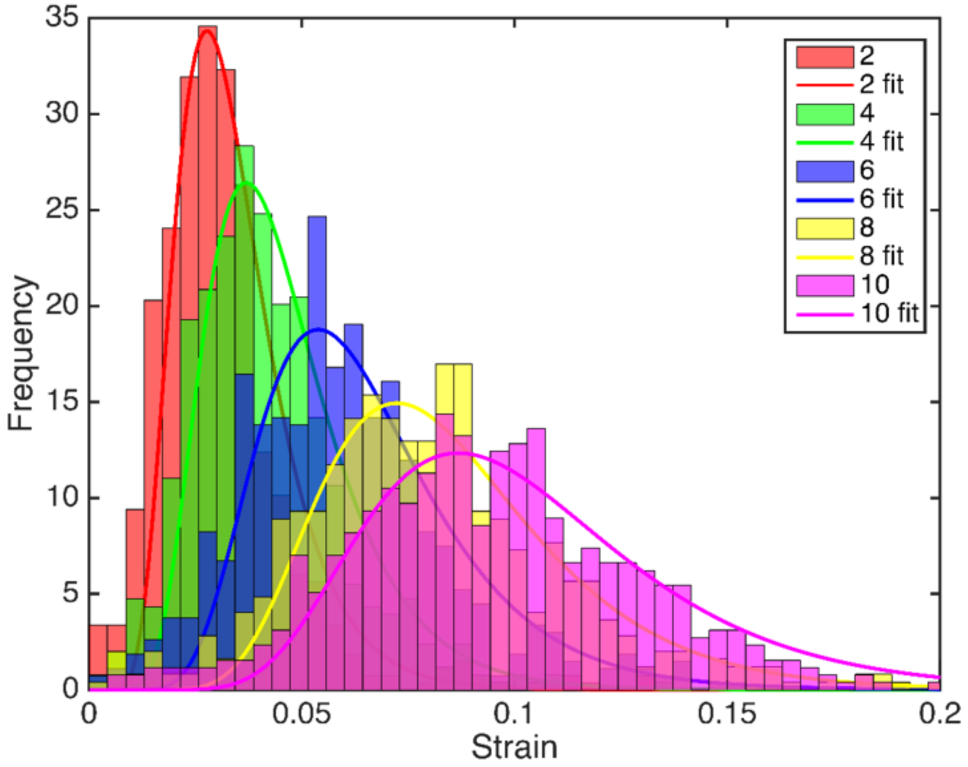

Figure 5-9. Histogram plot showing distribution of strain within individual austenite grains at each applied macroscopic strain increment.

From Figure 5-9, it is clear that similar to measurement 1, asymmetry of the strain increases with every strain increment, as shown in Figure 5-10. It shows deviation on either side of the peak strain of the distribution, *i.e.* where the perpendicular to the peak strain intersects the full width at half maximum in Figure 5-9.

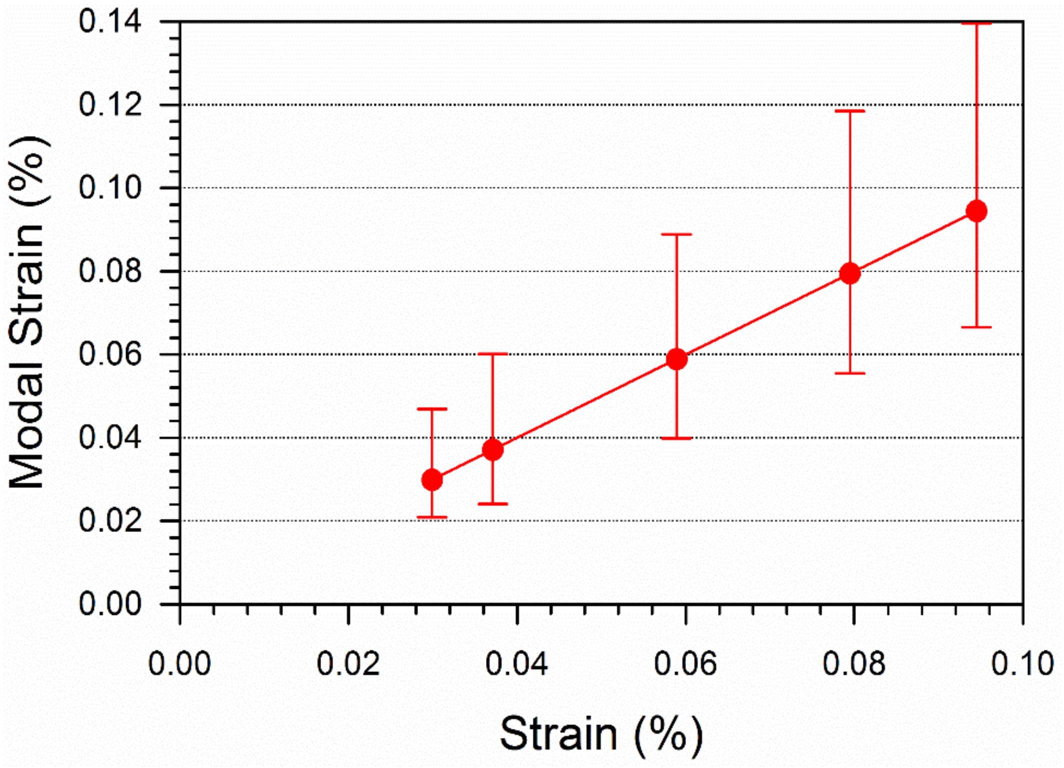

Figure 5-10. Modal strain broadening for grains at each measurement for experiment 2.

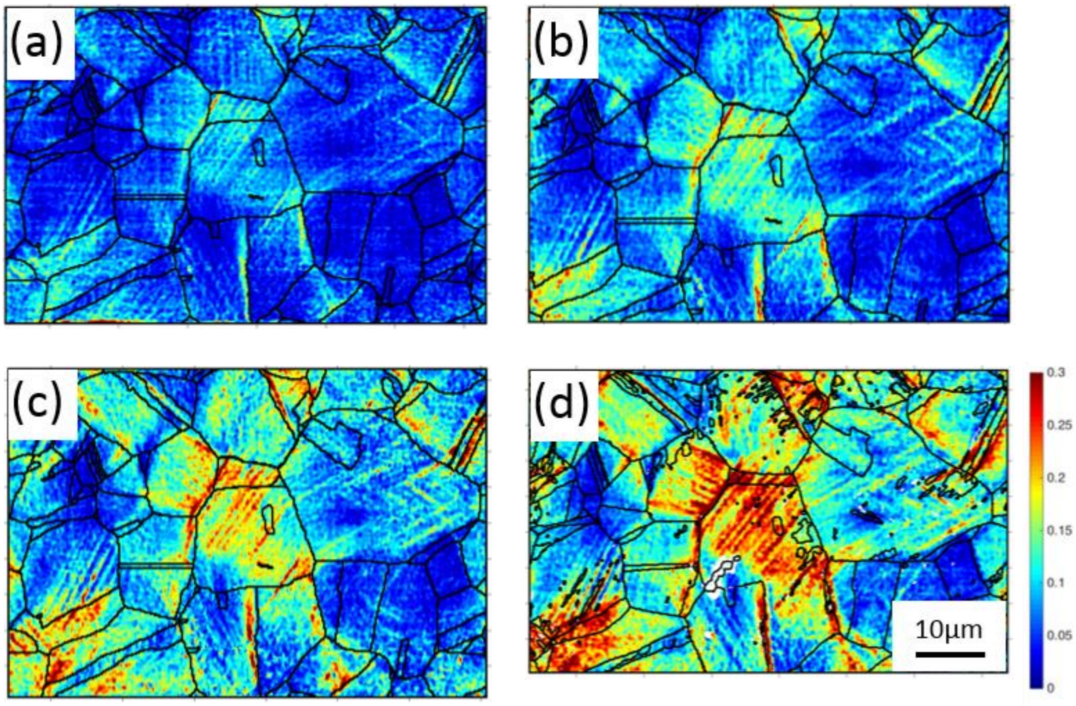

Figure 5-11. High magnification strain maps overlaid with the EBSD grain boundary maps, showing the heterogeneous nature of deformation within grains for measurement 1. (a) - (d) Are ε_{xx} measurements made at approximately 4%, 6%, 8% and 10% strain respectively.(a)-(c) strain maps are overlaid on the prestrained EBSD map, whereas (d) is overlaid on post-deformation EBSD map.

Figure 5-11 is a higher magnification probe of the same are as shown in Figure 5-8. The first three maps (Figure 5-11 (a) - (c)) show strain maps overlaid on the pre-strain EBSD grain boundary maps, whereas Figure 5-11 (d) is a strain map at ~10 % strain overlaid on the post-deformation EBSD grain boundary maps. Further, Figure 5-11 (d) shows the boundaries around α′ transformation sites.

5.3 Discussion

Acquisition of the images was performed *in situ* to eliminate the possibility of transformation or plasticity owing to back-stresses [175], which builds up during the unloading stage. It is worth noting here, that in preliminary studies of this material, higher fractions of transformation product were observed in samples that had undergone unloading cycles compared to those strained directly to the same final macro strain. Moreover, optimal contrast and resolution in BSE images is obtained at low working distance; however owing to the bulkiness of the *in situ* equipment it was not possible to obtain a working distance lower than 11.5 mm.

Due to the necessity of *in situ* testing and the higher working distance the resolution was limited compared to that obtained by Di Gioacchino *et al.* [22]. However, by performing additional processing the quality of the strain results was improved. Averaging of SEM images increased the number of vectors the DIC obtained from a given set of data. Moreover, introducing this step also reduced the number of vectors being removed at the grain averaging stage, indicating fewer spurious vectors. This indicates that there is significant benefit from taking multiple images at each increment of these quasi-static tests, with little detriment to the test efficacy or duration. From the comparison of a single image to the summed image in Figure 3-8, it is evident that the summing process reduces the high-spatial-frequency stochastic noise present in the single images. Summing the images both reduces the effect of the image noise and increases the effective contrast of the speckles by summing the sensitivity depth of the images (see Figure 3-8). This approach also mitigates the effect of step changes in e-beam position during the scanning process, as the step positions are random [121]. This dramatically improves the consistency of strains measured perpendicular to the scanning direction (the y direction in this case).

Due to the two different magnifications of imaging being used on the same region, a compromise in speckle pattern size was required. The speckle pattern size was optimised for the low magnification images, where the gold-remodelled surface produced a speckle size of approximately 2 pixels, which is optimal for DIC [116]. In the high-resolution images speckle size is compromised, but sufficient speckle detail was still found to enable DIC to work successfully at a similar sub-region size. The gold-remodelled surface, imaged using BSE, was found to contain sufficient detail to allow DIC to be performed over a range of length-scales and so reducing the requirement for extensive speckle optimisation investigations.

Strain localisation is observed within some grains and more evidently at certain grain boundaries. This is mainly caused by the incompatibility between grains, since they would rotate in different ways if no boundary was present [22]. However, there can be secondary effects such as the build-up or transfer of dislocations at grain boundaries (see Figure 5-2 (a) & (b)) [176]. The low magnification data allow for a larger number of grains to be collected and provide a more representative sample of the bulk, improving the reliability of microstructural plasticity models such as the Taylor model or crystal plasticity finite element model. However, at this magnification it is difficult to resolve the strain owing to individual slip planes. This is possibly due to a small grain size of the material and lower magnification (2000X) used in these measurements compared to the higher magnification measurements at (5000X) as shown in Figure 5-3.

The plastic deformation observed in these tests shows a periodic and discontinuous variation in shear strain. This creates regularly-spaced micro shear bands which are similar to but sharper than that observed in aluminium [177], in duplex steel [20] and in Fe-Cr alloy [178], but less than those measured in austenitic stainless steel [22]. The characteristic of these bands is that they form in groups and are a few microns apart from each other (see Figure 5-3, Figure 5-7 and Figure 5-11). At higher strain values most of these shear bands become more intense. As the deformation progresses new bands form at the boundary of the existing ones. The heterogeneous nature of plastic deformation is evident from the start of the uniaxial tensile straining in all the high-resolution strain maps as shown in Figure 5-2.

The variation in modal strain plots has been combined for both the experiments in Figure 5-6 (Experiment 1- blue line) and Figure 5-10 (Experiment 2 – red line) to form Figure 5-12. Figure 5-12 shows the data from two independent experiments, *i.e.* two different test specimens of nominally similar material (same sheet of material) match in the modal strain of each grain and the level of asymmetry. Future work may be carried out to incorporate for this variation in material models, *i.e.* to assign strain heterogeneity for samples deformed plastically on a larger scale (differences in strain between different grains) and for a greater number of grains.

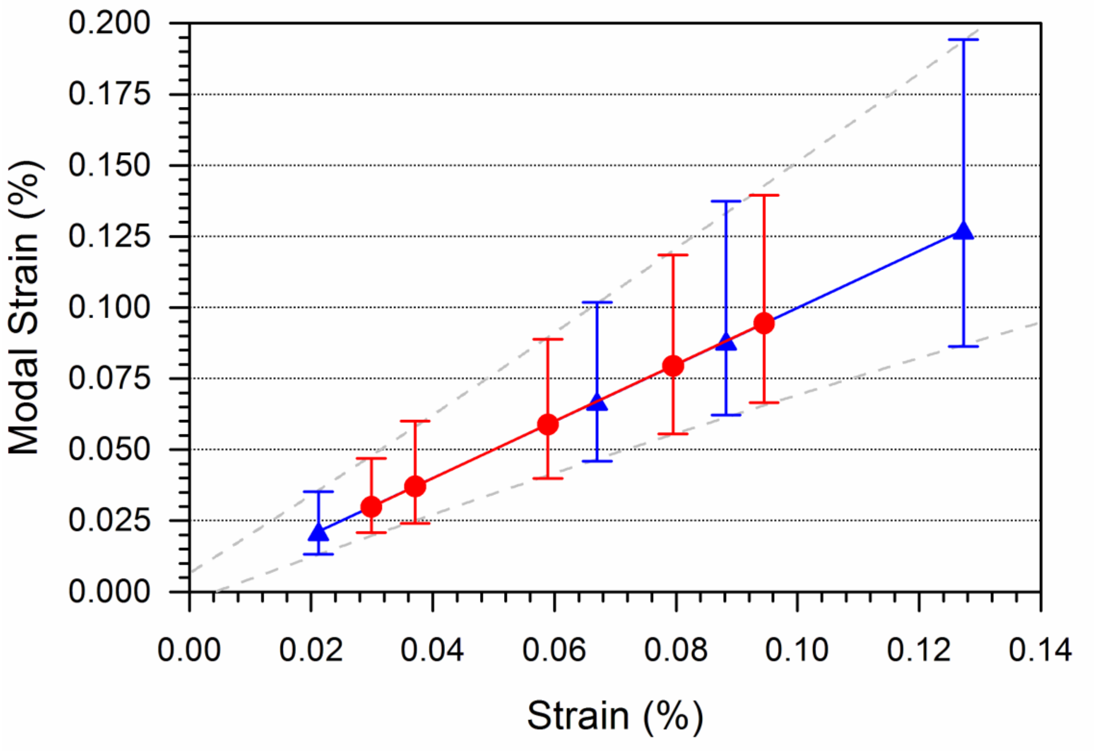

Figure 5-12. Modal strain broadening within for grains, at each measurement, for both experiment 1 and 2.

In this dissertation looking at the experimental scope of the project only a simple Schmid factor plot was used. In order to improve the ability to predict martensitic transformations in each austenite grain, further work is needed to explore plasticity prior to transformation using more complicated plasticity models, e.g. crystal plasticity modelling or improving the Kundu model by incorporating for various active slip systems present.

Advanced modelling work could involve investigations at various length scales and from a few grains to many hundreds of grains. Modelling techniques such as the Sachs model and the Taylor model could be used, however, it was observed that a large variation of average strain across each grain is present, as shown in Figure 5-12. Further, it was also observed that within an individual austenite grain, there are often multiple slip systems active, neither effect would be considered using the Sachs model [179]. In this model the stress state of each grain is assumed to be the same and the active slip system is the one with the maximum Schmid factor. A good first approximation to account for this is to assume all grains have the same strain, as used in the Taylor model [180], [181]; however with the data we now have available by combining local strain measurements with EBSD, this is also an unreasonable assumption. For the meantime, using Schmid factor as a first approximation is felt to be the most reasonable method considering the experimental, rather than modelling scope of this project work.

5.4 Conclusion

In this work, strain-induced martensitic transformations in TRIP steel have been studied by *in situ* EBSD and high-resolution digital image correlation to better understand the mechanisms and conditions of the strain-induced martensitic transformations. The main conclusions of this work are as follows:

- The combination of EBSD and HRDIC data displayed an increase in strain heterogeneity when strains were observed at the grain level (2000x magnification). When probed at still higher magnifications (5000x magnification), an increase in heterogeneity even within individual austenite grain was noticed. At the individual grain level, factors such as grain orientation, localised stresses acting on the grain (actual load acting on the grain) and the surrounding constraints all need to be factored in to existing materials models.

- Combining high-resolution DIC (HR-DIC) with EBSD has provided invaluable understanding for the crystallographic origins of local strains owing to plastic deformation and phase transformations in polycrystalline steel, which is further discussed in detail in Section 7.1.2.
- The modal strain variation of the full width at half max appears to fit well between fixed ranges for plastically deformed stainless steel.

6 The influence of temperature on the martensite transformation – An *in situ* neutron diffraction study

6.1 Background

In bulk polycrystalline materials internal phases and their lattice parameters may be uniquely measured using diffraction techniques involving X-rays, electrons or neutrons [73]. As explained in section 2.6, diffraction techniques generate information specific to individual phases and grain families. They can be used for research into intergranular and interphase stress developments, or for the investigation of phase transformations. Electromagnetic waves with wavelengths of dimensions smaller than the lattice spacing of the material to be measured may be used. Of such waves, neutrons have the greatest penetration depth due to their lack of charge. Whilst laboratory X-rays and electron diffraction techniques can only penetrate a few micrometers and therefore limit measurement to the near surface [108], neutron diffraction allows for the bulk sampling of most engineering materials. The ability for neutrons to penetrate into the bulk of engineering materials is particularly important when stress or the influence of stress is of concern because the surface stress state may significantly differ from that in the bulk. A further benefit of using neutrons for studying engineering material is that, in general, larger gauge volumes are possible compared to X-ray and electron techniques. This, coupled with the relatively non-parallel nature of most neutron beam sources, means a significant number of grains may contribute to the diffraction signal (due to a wider acceptance angle of Bragg's law).

Due to these advantages the martensitic phase transformations studied in this dissertation were measured using neutron diffraction during *in situ* loading of austenitic stainless steels. The principles of the method and the instrument used for the experiments are explained in the literature review (section 2.6.4) and experimental methods (section 3.4) sections.

6.2 Raw results

Figure 6-1 and Figure 6-2 show the raw diffraction spectra of samples deformed at room temperature and at 100 K, to different macroscopic strain increments. These temperature measurements are shown as they are representative of the two distinct transformation mechanism presented and discussed in this dissertation. These raw data were converted to volume fraction measurements of austenite and martensite phases, as explained in 2.6.4.

From Figure 6-1, it is clear that not much change is observed in the diffraction spectra for the room temperature measurements even at relatively large strains of ~ 10%. A comparable amount of transformation occurs at ~2.5% strain, on deformation at 100 K see Figure 6-2.

Further, in this section each set of results is plotted with respect to stress and strain. These are the same data, however plotting against stress increases the resolution in the early load control stages (*i.e.* during the elastic portion of the test) and plotting against strain (position control) gives the best resolution towards the end of the test.

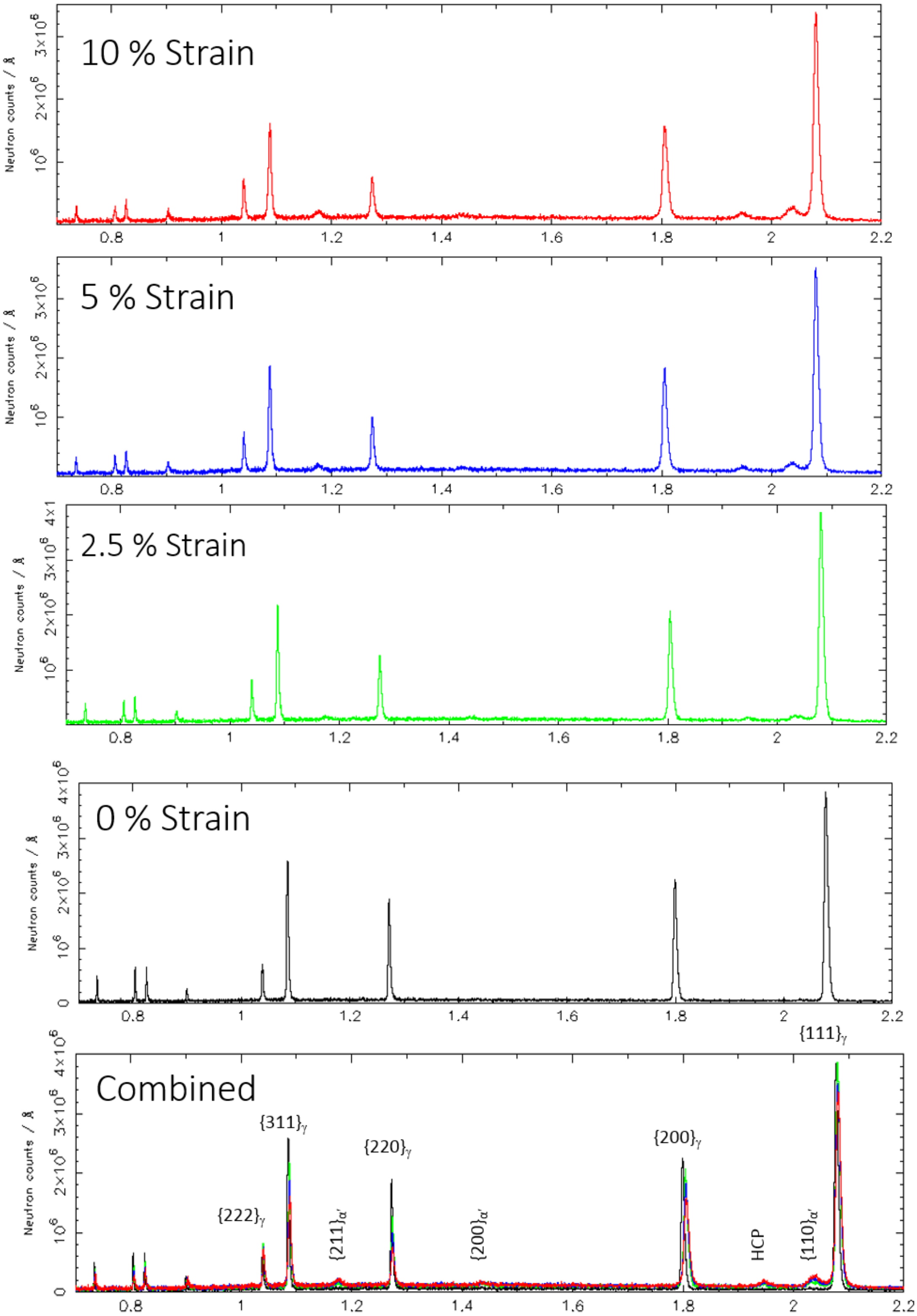

Figure 6-1. Diffraction spectra for measurement at room temperature.

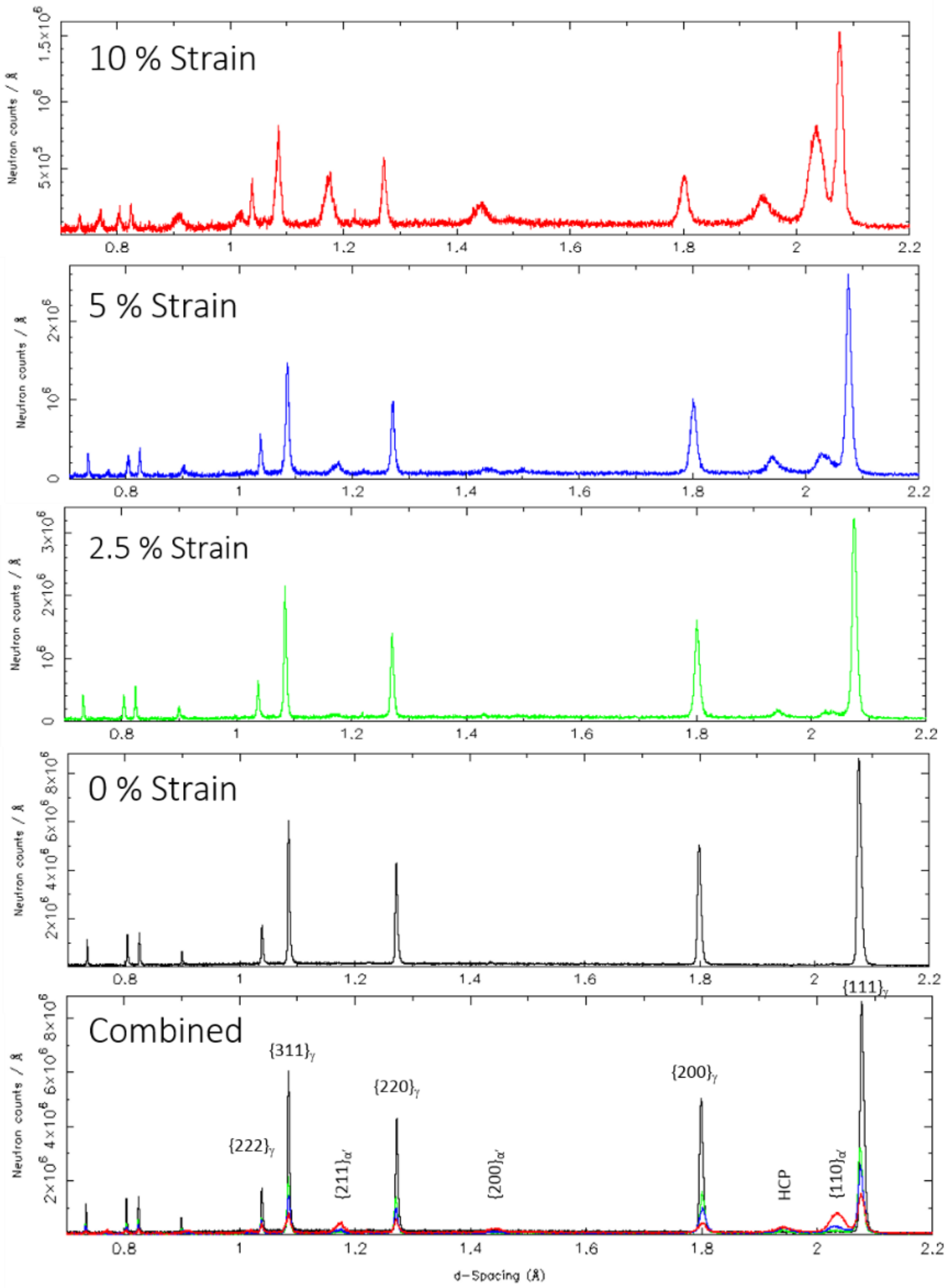

Figure 6-2. Diffraction spectra for measurement at 100 K.

Figure 6-3 shows plots of the typical raw intensities calculated from each diffraction peak made during the experiment at ENGIN-X. This plot was for the measurements made at 100 K; similar measurements made at all the test temperatures have been omitted, as the purpose of this figure is to illustrate the types of data collected and little difference can be observed until further analysis is performed. Figure 6-3(A) and (C) show data collected from the longitudinal (Bank 1) and transverse (Bank 2) peak intensities of the face centered cubic austenite (γ), body centered cubic martensite (α′) and hexagonal martensite (ε) peaks with respect to stress. Figure 6-3 (B) and (D) are the same peak intensities with respect to strain.

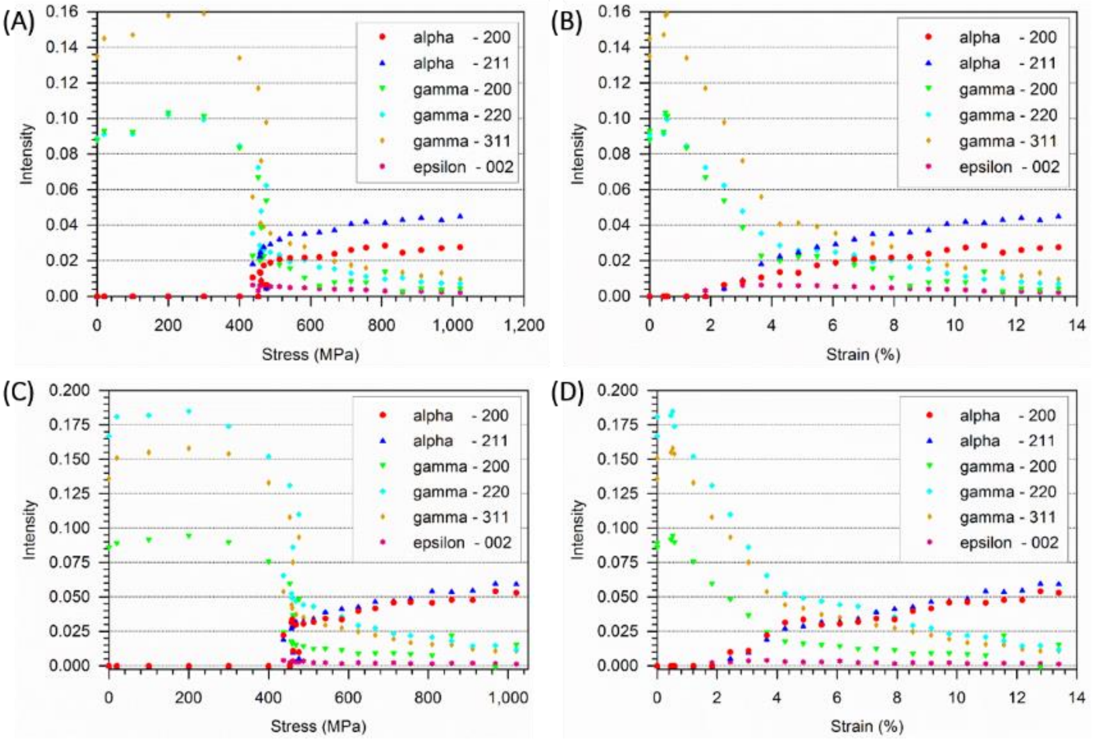

Figure 6-3. Intensity versus stress/strain plots of measurement at 100 K. (A) & (B) are measurements made in the longitudinal (parallel to loading) direction and (C) & (D) are measurements in the transverse (perpendicular to loading) direction.

As shown in Figure 6-3, the early stages of the experiment, up to the end of the elastic portion of the test, are best observed with respect to stress, where a small increase in austenite peak intensity was observed. It is possible that the γ peak intensities increase owing to a greater number of austenite grains fulfilling the

Bragg condition and contributing to the diffraction spectrum. After a slight increase in peak intensities of austenite (possibly due to a larger number of grains diffracting) up to 300-400 MPa stress, the γ peaks continuously drop in intensity with further increase in strain. However, no increase in the peak intensities from either of the transformation products (α′, ε martensite phases) was observed at 100 K until a stress of ~ 430 MPa, indicating this variation in intensity is probably due to increases in dislocation density and not due to a reduction in austenite volume fractions. Above a stress of ~ 430 MPa the initial rate of α′ and ε transformation was fast with respect to stress. Therefore, beyond this stress level the transformation is best studied with respect to strain.

Up to a strain of approximately 4%, the rate of reduction in austenite intensity for both directions and for all reflections is relatively constant. This was combined with a relatively rapid intensity increase in both α′ and ε martensite phases. Above 4% strain, the transformation rate reduces and stays approximately constant until the completion of the test. For epsilon martensite the transformation rate above ~ 6 % strain is negative *i.e.* the fraction of epsilon phase decreases.

It must also be noted that the initial intensities of each austenite reflection are not equal in the two detector banks. For the longitudinal direction the $\{311\}_\gamma$ is the most intense, while in the transverse direction the $\{220\}_\gamma$ is the most intense. This is as a result of a slight crystallographic texture in the starting samples. As discussed in the earlier section (section 2.6.4), by analysing the intensities of the several individual peaks, volume fraction calculations using the modified formula used by Moat et *al*. [2], become less sensitive to texture. This enabled the volume fraction measurement to be made of individual γ austenite, α′ and ε martensite phases. This said, studying the changes of individual peaks during transformation gives information on how differently orientated grains may be transforming at a different rate.

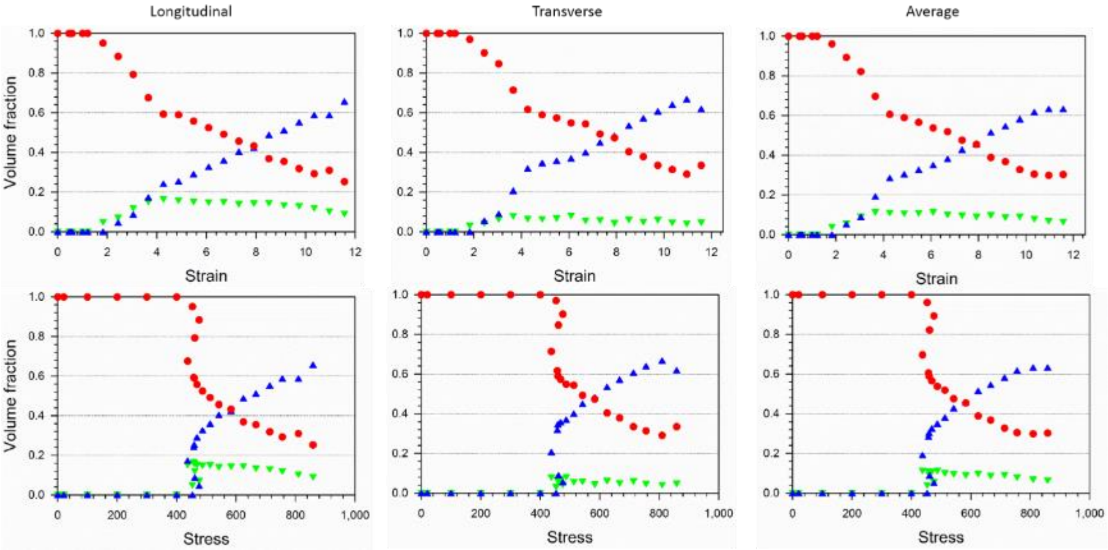

Figure 6-4. Volume fraction of γ - austenite (red), α′ - martensite (blue) and ε - martensite (green) martensite with respect to both strain and stress, in the longitudinal, transverse and average of the two directions at 100 K.

Figure 6-4 shows the calculated volume fractions of γ, α′ and ε phases measured in the longitudinal, transverse and in the average of the two directions. From Figure 6-4 (100K), it is observed that the ε martensite phase nucleates before α′ martensite phase. In the longitudinal direction, the volume fraction of ε martensite is almost twice the fraction compared to ε martensite in the transverse direction. The volume fraction of α′ martensite increases alongside the decrease in γ fractions and increase in ε martensite fractions until ~ 4% strain. Beyond 4% strain, α′ volume fraction continues to increases, while the other phases γ and ε decrease in volume fractions beyond this strain.

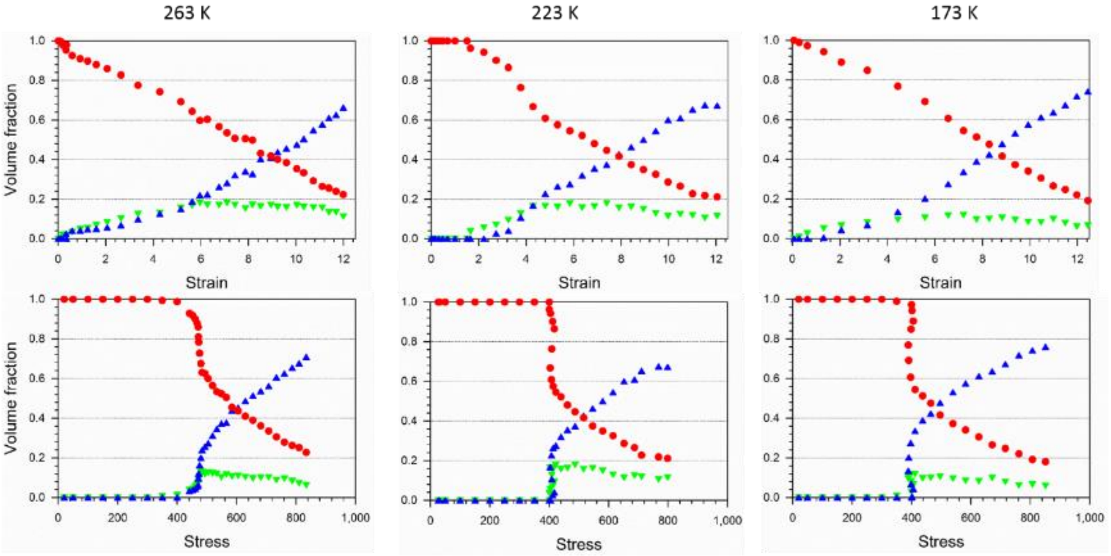

Figure 6-5. Volume fraction γ (red), α′ (blue) and ε (green) phases measured along the longitudinal and transverse directions, at 263 K, 223 K and 173 K, with respect to strain and stress respectively.

As seen in the 100K example in Figure 6-4, in all other low temperature tests (see Figure 6-5), the volume fraction of ε martensite phase initially increases at strains below 2% , accompanied by a decrease in volume fractions of austenite (γ). This is followed by subsequent increase in the volume fractions of α′ martensite phase at less than 1% strain after the start of ε transformation. Again, in a similar fashion to the 100K test, at strain values greater than 4% the volume fraction of α′ martensite increases in transformation rate and is accompanied by a drop in the volume fraction of the other two γ and ε phases. In all the tests it was observed that the volume fraction of the ε martensite phase in the longitudinal direction is almost twice that in the transverse direction.

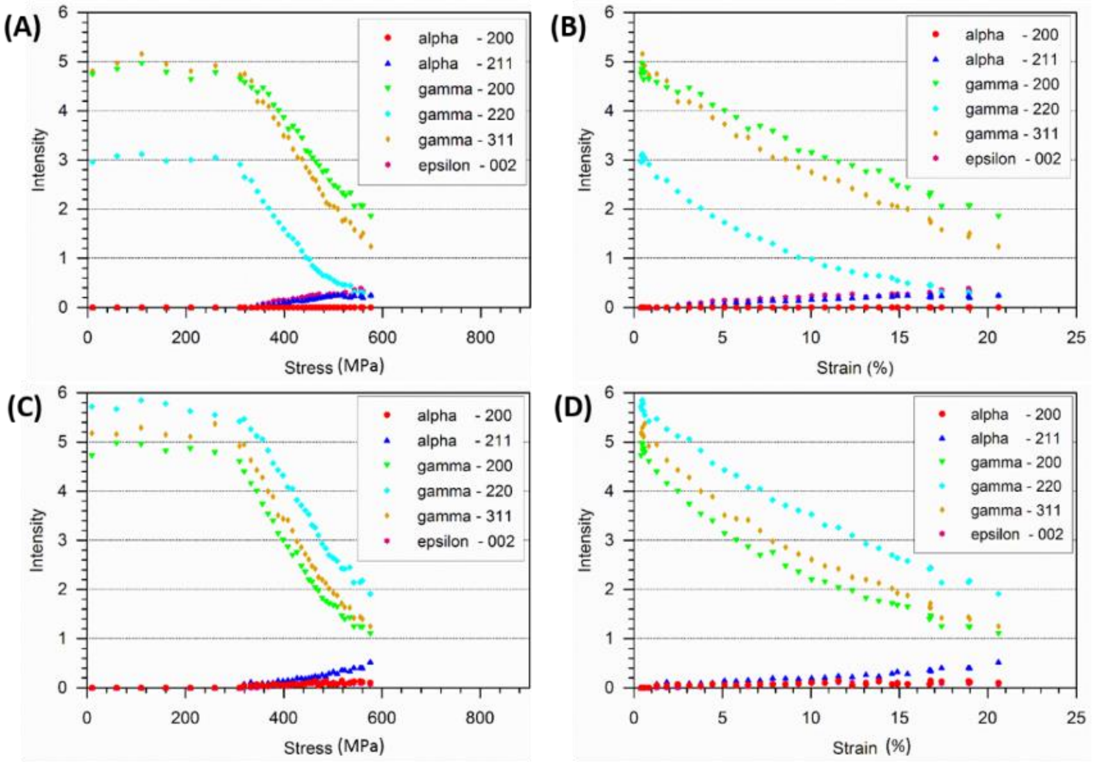

Figure 6-6. Intensity versus stress/strain plots of measurement at 300 K. (A) & (B) are measurements made in the longitudinal (parallel to loading) direction and (C) & (D) are measurements in the transverse (perpendicular to loading) direction. (Note: At room temperature the sample strained to greater total strain).

Figure 6-7 displays results from room temperature (300 K) testing, comparable to those in Figure 6-6. In a similar fashion, the initial intensities of each austenite reflection were not equal and furthermore, different in each of the two measurement directions. For the longitudinal direction the $\{311\}_\gamma$ and $\{200\}_\gamma$ are more intense as compared to the $\{220\}_\gamma$, while in the transverse direction the $\{220\}_\gamma$ is the most intense and $\{200\}_\gamma$ the least intense peak. Such variations were observed in all the measurements and as stated before, a result of some crystallographic texture in the virgin material. In data collected from both the directions, the peak intensities $\{200\}_\gamma$ and $\{311\}_\gamma$ remain higher than the peak intensities of the martensite peaks. However, the peak intensity of $\{220\}_\gamma$ decreases below martensite peak intensities in the longitudinal direction at higher than 17 % strain. The intensity of $\{200\}_\alpha$ is absent in the longitudinal direction and only contributes very slightly in the transverse direction. Therefore, $\{211\}_\alpha$ peak intensities contribute predominantly in the martensite volume fraction measurement. The epsilon martensite intensities are similar to the $\{211\}_\alpha$ peak intensity in the longitudinal direction, however it drops off in the transverse direction. From these peak intensities the individual phase fraction is as given in Figure 6-7.

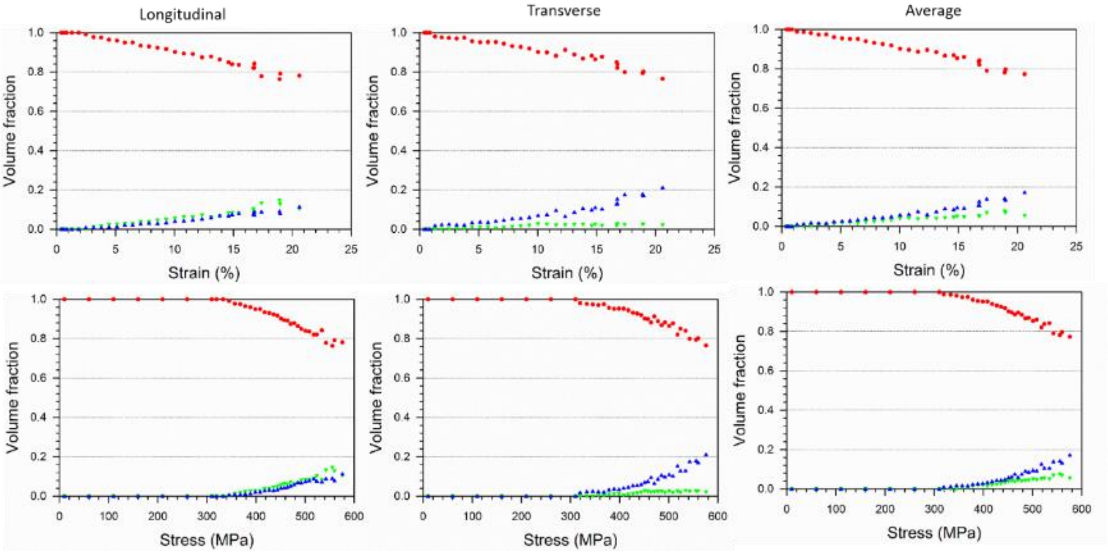

Figure 6-7. Volume fraction measurements of γ - austenite (red), α′ - martensite (blue) and ε - martensite (green) martensite with respect to both strain and stress, in the longitudinal, transverse and average of the two directions at 300 K.

From Figure 6-7 it is clear that, in the longitudinal direction, epsilon martensite nucleates first (below 5% strain). On further deformation, the volume fraction of both α′ and ε martensite increased at about the same rate in the longitudinal direction. However, in the transverse direction, α′ phase nucleates first and the volume fraction increase was greater. This shows the difference in the ε phase transformation behaviour in the longitudinal and transverse directions, which may mean that the longitudinal stresses are more favourable to induce ε transformation as compared to the compressive ones. At room temperature, the transformation seems to initiate at stresses above 350MPa. The total volume fraction of α′ and ε martensite phases combined is close to ~ 25% at over 20% macroscopic strain.

The calculated phase fractions at the different temperatures with respect to strain for all test temperatures are shown in Figure 6-8. This reveals a transition in transformation behaviour, with the RT transformation differing significantly from all the low temperature behaviour. All the cryogenic/low temperature measurements had a similar trend. However, the volume fraction of α′ and ε phases varies slightly at the different measurement temperatures with respect to either the applied strain (Figure 6-8) or applied stress (Figure 6-9). From Figure 6-9, the γ volume fraction reduced by ~10% at 2.5% strain for all the cryogenic temperatures, whereas at room temperature it reduced by less than 5%. At 5% strain the γ phase fraction reduced by 30% for 263K, 173K and – 40% for 223K, 100K. By 10% strain over 65% of the austenite has transformed for all the low temperature tests. However, at room temperature only ~10% transformation is observed at 10% applied macroscopic strain and the decrease in γ volume fractions corresponds with increase in α′ and ε volume fractions. For all temperatures, α′ martensite volume fraction increased continuously throughout the deformation process. For the low temperature measurements, the ε martensite volume fraction peaked to over 11% at 6% macroscopic strain. Beyond 6% strain, further deformation led to decrease in the ε martensite volume fraction. For the room temperature measurement ε martensite volume fraction increased throughout the deformation process, which may be because the point at which the fraction starts to decrease has not yet been reached.

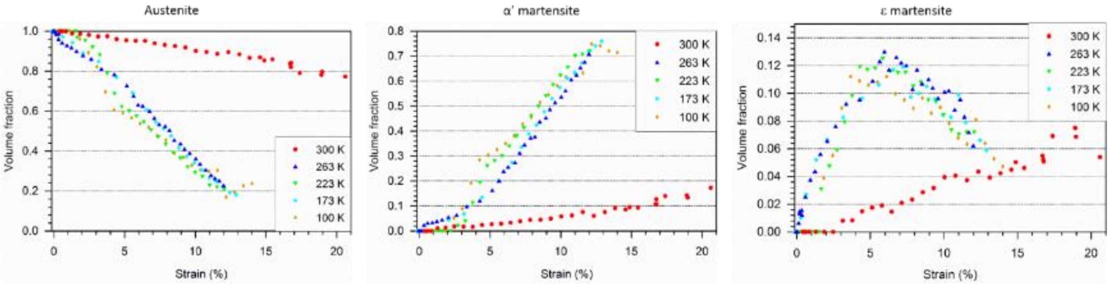

Figure 6-8. γ, α' and ε volume fraction vs strain, at the different measurement temperatures.

Figure 6-9 shows (γ , α′ and ε) volume fractions with respect to the macroscopic applied stress at each of the test temperatures. For the low temperature measurements, γ and α′ volume fractions began transforming close to 400 MPa, *i.e.* the γ fraction decreased with stress increments above 400 MPa and corresponding α′ volume fraction increased. Here, ε volume fraction was measured at slightly lower stress values close to about 350 MPa, where it first began transformation, *i.e.* the α′ martensite nucleates after the ε martensite. The volume fraction of the ε phase peaked at ~ 480 MPa for the low temperature measurements, thereafter it decreased with further increase in applied stress.

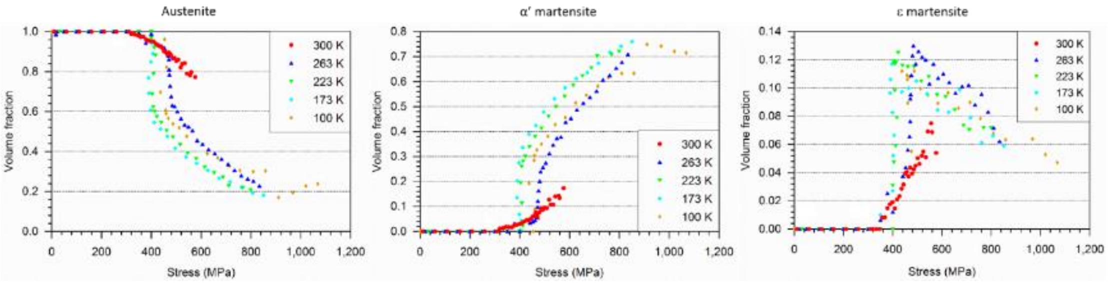

Figure 6-9. γ, α' and ε phase intensity vs stress, at the different measurement temperatures.

Although at room temperature the sample was strained to over 20% strain (Figure 6-8), it only reached a maximum stress of ~575 MPa (Figure 6-9). The volume fraction of γ decreased at stresses above 320 MPa, with corresponding increase in the volume fraction of α′ martensite. The volume fraction of ε martensite increased at stresses above ~350 MPa, *i.e.* α′ phase nucleated before the ε martensite phase.

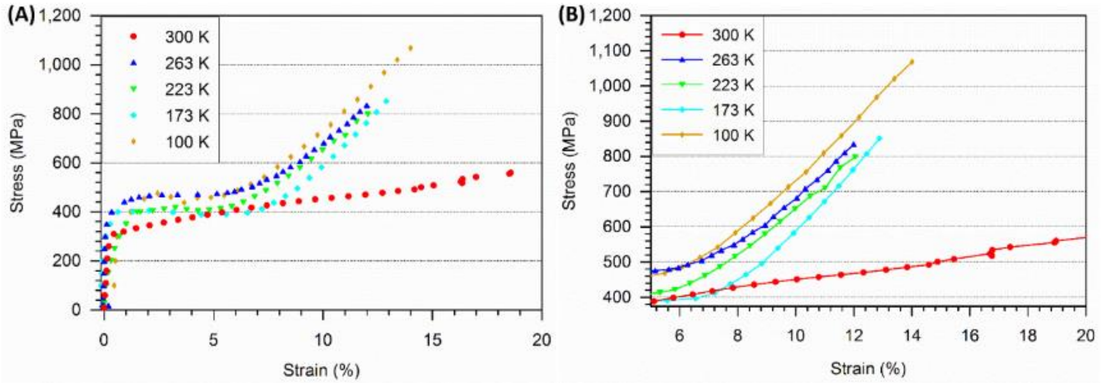

Figure 6-10. Stress-strain curve for tensile loading at RT, 263 K, 223 K, 173 K and 100 K. (A) Entire plot and (B) plot showing divergence in room temperature and cryogenic temperature behaviour.

Figure 6-10(A) shows the entire stress-strain curves for all the 5 measurements temperatures, whereas Figure 6-10(B) shows magnified line plots above 5% strain and above 375 MPa load. Similar to the observations of Datta *et al.*, for the lower temperature experiments, it is evident from Figure 6-10(A) that there is an initial softening trough observed beyond the yielding of the material [182]. This softening is observed in the elongation range of 1% to 5% strain. Further, from the stress-strain curves of the low temperature measurements, the work hardening phenomenon becomes evident at macroscopic strain increments above 5% strain, similar to the measurement by Spencer *et al.* [150]. Beyond 6% strain the load increased significantly on further deformation in comparison to the room temperature measurement. This increase in the work hardening rate at the low temperatures is due to the formation of the strain-induced α′ and ε martensite phases. Detailed explanation is given in the following discussion section. However, for the room temperature measurement, significant hardening is absent possibly due to the relative low volume fractions of strain induced α′ and ε martensite. It is probable here that the stress and strain leads to the deformation of only the soft austenite matrix and no significant load transfer has occurred even up to 20% macroscopic strain.

6.3 Discussion

As explained in the results section, samples have been tested at 5 different measurement temperatures to look at the effect of temperature on the nature of the martensitic transformations. This section discusses those results.

No martensite was observed to form upon cooling the austenitic stainless steel down to very low temperatures, a similar observation was made by Spencer *et al.* [150]. Therefore, it can be assumed that nucleation of martensite is not thermodynamically possible without the introduction of a further external driving force. For instance, energy in the form of stress, plastic deformation and formation of potential nucleation sites must play a key role in the phase transformation [183]. At low temperatures, the following transformation sequence was observed: FCC (γ) →HCP (ε) →BCC (α′). A similar transformation sequence has been reported in the literature [50], [66], [144], [150]. Here it seems that the application of stress or strain leads to local deformation of the austenite matrix (austenite has a low stacking fault energy [54], [144]). This austenite deformation is along the {111} slip plane and leads to formation of the ε martensite (HCP) [50], such that $(111)_\gamma || (0001)_\varepsilon$ [39] and forms at the shear band intersections [60], [144], [150], [184]. Further deformation of the microstructure leads to the formation of α′ martensite, where the nucleation site is the intersection of stacking faults or the HCP bands [50], [150]. In the room temperature measurement, no observable intermediate step is seen and the deformation of the austenitic material led to the direct transformation in the form of α′ martensite or ε martensite phases.

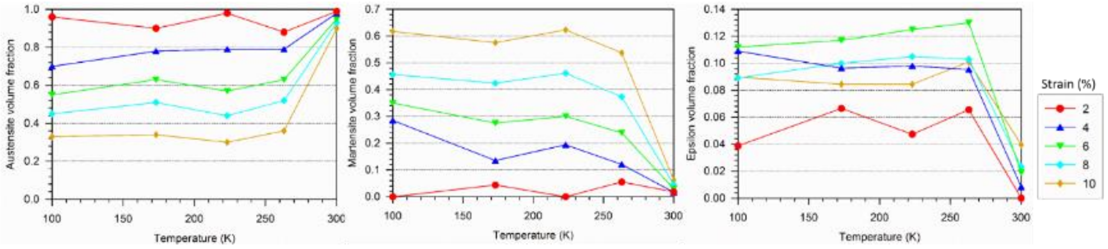

Figure 6-11. γ , α' and ε volume fractions as a function of applied macroscopic strain for all measurement temperatures.

The transform of the individual γ, α′ and ε phases is summarized in Figure 6-11. For all the measurement temperatures, the volume fraction of the γ phase continuously decreased with increase in the applied macroscopic strain, whereas the α′ phase fraction increased with every strain increment. However, for the low temperature measurements, the ε volume fraction increased and peaked (14% volume fraction) at about 6% applied macroscopic strain and further deformation led to decrease in their volume fraction. From this it seems that at applied macroscopic strain increments the transformation sequence is ε → α′ martensite. For the room temperature measurement, the ε phase increased with every strain increment and was measured as ~ 4% volume fraction at 10% applied macroscopic strain.

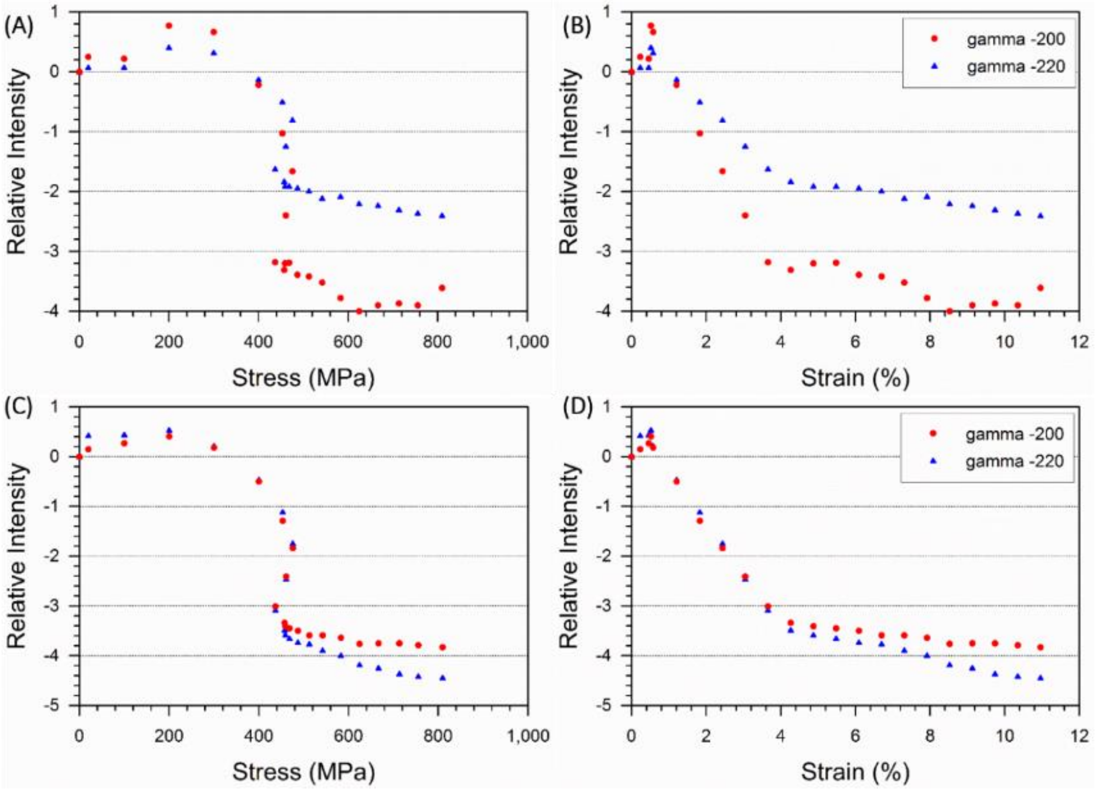

Figure 6-12. Relative γ austenite peak intensities at 100 K. Red markers are for {200} and blue for {220}. (A) & (B) are for measurements in the longitudinal direction and (B) & (D) are for measurements in the transverse directions.

The relative peak intensities of the measurements made at 100 K are as shown in Figure 6-12. From Figure 6-12, it is observed that the peak intensities decrease more in the transverse direction in comparison to the loading direction. In the loading direction, the peak intensity of $\{220\}_{\gamma}$ decreases less in comparison to $\{200\}_{\gamma}$ peak. In fact, the $\{200\}_{\gamma}$ decreases rapidly up to macroscopic strain of ~ 4% strain compared to $\{220\}_{\gamma}$. Beyond 4% strain both the peaks decrease at about the same rate; whereas, in the transverse direction $\{220\}_{\gamma}$ decreases slightly to a greater extent compared to $\{200\}_{\gamma}$ peak above 4% macroscopic strain.

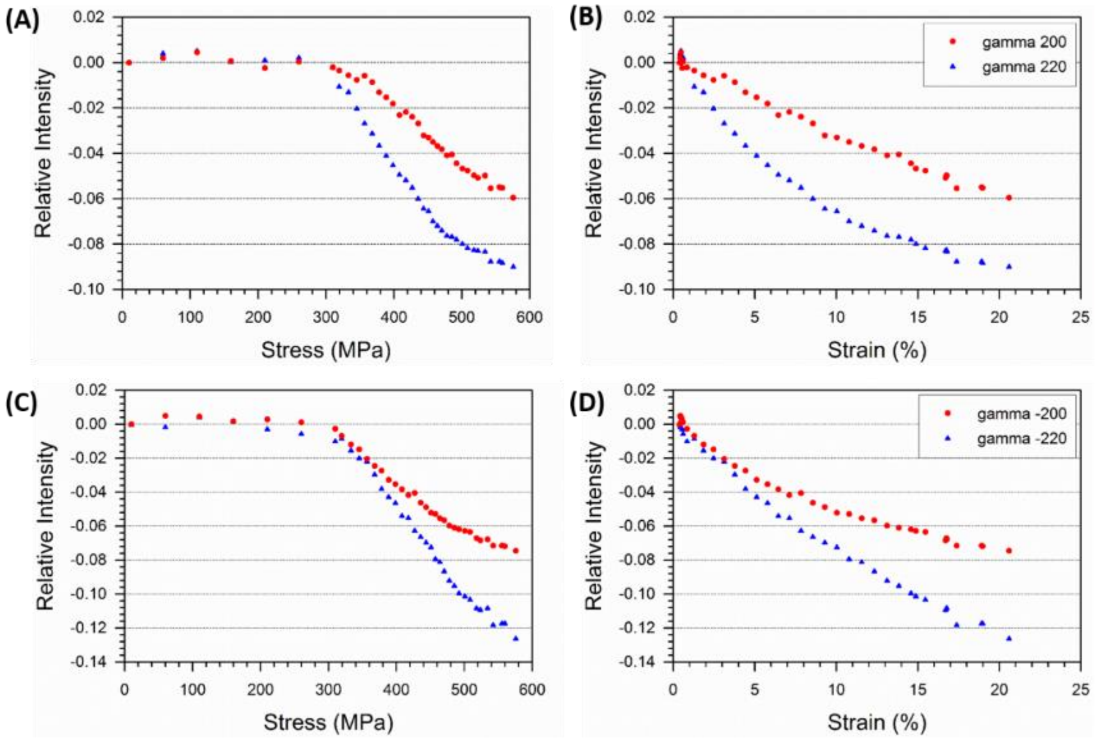

Figure 6-13. Relative γ austenite peak intensities at 300 K. Red markers are for {200} and blue for {220}. (A) & (B) are for measurements in the longitudinal direction and (B) & (D) are for measurements in the transverse directions.

The relative austenite peak intensities for the measurement made at ambient temperature are shown Figure 6-13. From Figure 6-13, it is clear that the peak intensities decrease more in the transverse direction than they do in the longitudinal direction. Moreover, the $\{220\}_\gamma$ peak intensity decreases rapidly in comparison to the $\{200\}_\gamma$ peak intensity in both directions. This is possibly owing to the fact that plastic deformation is needed at room temperature prior to $\gamma \rightarrow \alpha'$ phase transformation. Furthermore, initially in the longitudinal direction (see Figure 6-13 (A) & (B)), the $\{220\}_\gamma$ decreases slightly more in comparison to the $\{311\}_\gamma$. In the transverse direction the decrease in peak intensities of $\{220\}_\gamma$ and $\{311\}_\gamma$ is very similar. Therefore, it seems that the strain-induced α' transformation commences in the $\{220\}_\gamma$ and $\{311\}_\gamma$ first and then at higher applied macroscopic stress/strain increment it occurs in the $\{200\}_\gamma$. The differences in peak intensities may be lead to formation of transformation texture.

6.4 Conclusion

The following conclusions may be drawn from the neutron diffraction studies presented in this dissertation:

- The rate and sequence of transformation is different at room temperature and low temperature. At room temperature the transformation sequence is $\gamma \rightarrow \alpha'$, or $\gamma \rightarrow \varepsilon$. At low temperatures, the transformation sequence appears to be $\gamma \rightarrow \varepsilon \rightarrow \alpha'$. Moreover, there appears to be a difference in the transformation behaviour measured in the two directions, possibly due to presence of texture.
- Grain families whose peak intensities decrease to a greater extent as compared to other grain families imply they transform to a greater extent. The intensity of the $\{220\}_\gamma$ austenite peaks decreases most for room temperature deformation. When deforming the samples at lower temperature the intensity of the $\{200\}_\gamma$ peaks decreases the most. Grain families whose peak intensities decrease to a greater extent as compared to other grain families imply they transform to a greater extent.
- At the same macroscopic strain increment, the low temperature measurements show greater volume fractions of deformation-induced martensitic transformation and enhanced work hardening. In the low

temperature deformation regimes it seems that the enhanced work hardening of the austenitic stainless steel is due to the load transfer taking place from the soft austenite matrix to the harder martensite phase, as well as the work hardening of the austenite matrix.

7 Discussion

7.1 Introduction

The aim of this PhD project was to gain insight into the local stresses and strains occurring due to the strain-induced martensite transformation. This was achieved by developing the high-resolution digital image correlation (HRDIC) technique for the first time at The Open University. In order to isolate the strain occurring due to the martensite transformations, it was essential to remove as many variables as possible. Therefore, the material used in this dissertation was a 301 austenitic stainless steel, which had a nominally fully austenitic starting microstructure and one that show the TRIP phenomenon at room temperature. This material, proved to be an ideal material to investigate the micromechanics of the plastic deformation (deformation of the austenite crystal lattice) and the strain-induced martensitic transformations, owing to the fully austenitic microstructure at the start of the experiments.

Besides developing the HRDIC technique employed to probe high-resolution strain maps of the strain-induced martensite, EBSD and neutron diffraction experiments were done to characterise the transformation mechanism. The EBSD and HRDIC experiments gave insights into the plastic deformation of the austenite crystal lattice, crystallography and micromechanics of the martensite transformation at the surface; whereas the neutron diffraction probed the transformation characteristics within the bulk of the material. This chapter recaps the entire major findings, critiques the techniques and discusses how significant information may be obtained by probing the materials using these different techniques. It concludes with an explanation of the transformation mechanism of strain-induced martensite.

7.1.1 EBSD, high-resolution DIC and neutron diffraction - a recap

The EBSD results in this dissertation showed that there was only a small increase in the amount of strain-induced martensite up to about 8% applied strain (~0.8% transformation observed at 8% applied macroscopic strain). However, at macroscopic strain increments of 9% strain (2.6% transformation was observed) and above, there was a marked increase in the amount of strain-induced martensite (4.2% transformation at 10% macroscopic strain) (refer Section 4.2.1). Further, investigating the same set of grains throughout the deformation process enabled for the residual bcc phase present in the microstructure (bcc phase was randomly distributed within the microstructure) to be correctly accounted for in the final volume fraction calculations.

The incremental loading, unloading and reloading experiments showed that still greater volume fractions of strain-induced martensite formed (7.34% transformation observed, for incrementally loaded sample at 10%), when compared to the directly loaded samples (4.2% transformation at 10% macroscopic strain) (refer Section 4.2.2). This was due to the cumulative plastic strain effect, which triggers the formation of martensite embryos with every strain increment and results in the formation of higher volume fractions of strain-induced martensite. If these newly formed martensite embryos transform within the elastic range of the next loading cycle, it may be reasonable to assume this is due to the stress-assisted martensitic transformation [60]. Incremental loading produces a different volume fraction of strain-induced martensite in comparison to the directly loaded specimens. Therefore, incrementally deforming samples outside the SEM when performing HRDIC would add a further complication to understanding the strains that form making de-convolution of local direct stresses and back stresses difficult. In order to mitigate the aforementioned effect, data acquisition for DIC in Chapter 5 was done *in situ* SEM to avoid the influences of cumulative plastic deformation. Moreover, in the EBSD chapter using the approach outlined by Githinji *et al.* [168] and Unnikrishnan *et al.* [169] the accompanying plastic strain were quantified. These maps showed an increase in the accumulated plastic strain when directly strained to different macroscopic strain increments. However, misorientation maps of incrementally loaded unloaded and reloaded specimens could not distinguish the changes in accumulated strains in comparison to directly loaded materials, especially at higher values of plastic deformation. Furthermore, there was evidence that applied stress favoured the formations of certain strain-induced martensite variants over others, *i.e.* it gave a good indication of preferential variant selection for the entire set of grains under investigation. However, as discussed below, to accurately predict the strain-induced variants, it is important to consider the strain heterogeneity in between grains and even within individual austenite grains.

In order to obtain this strain heterogeneity, an ideal speckle pattern was required. This was done by agglomerating a porous gold film, which was a few nano-metres thick using the technique outlined by Gioacchino and Fonseca [18]. Here high temperature steam vapour was then able to enter this porous film and aides in the gold hillock formation, which were ultimately used as the speckle pattern for the microscale strain mapping. The speckle pattern developed here was able to analyse into strain fields over two different magnifications of interest and consisted of gold speckles ~ 100-200 nm range. In the high-resolution and lower-resolution strain maps, each pixel equated to about ~ 37nm and ~ 92nm respectively. Further as the data acquisition was done *in situ* SEM, there was slight loss in signal coming to the detector from the sample owing to the reduced mobility on attaching a micro tensile tester. However, was overcome this to some extent by averaging over three images at each magnification and at every strain increment. The added advantage of averaging of the images was that it reduced the "non-square" pixel shape errors due to the rastering of the electron beam.

Here, on plastic deformation the is strain heterogeneity within the parent austenite material was quantified at two distinct length scales. These observations were similar to the work presented by Gioacchino and Fonseca [18], [22] and made it evident that the applied macroscopic load may not be an ideal assumption (direction of applied stress) at the microstructural length scale (refer Section 5.2) It showed that due to plastic deformation-induced anisotropy, the macroscopic applied stress does not match at the individual austenite grain level. Therefore, in order to enhance the reliability of material models such as the Kundu model [17] it is essential to factor this stress/strain heterogeneity. This will enable these material models to more precisely predict either the plastic deformation of the crystal lattice or the strain-induced transformations.

A significant aim of the project was to quantify strain fields around transformation sites within individual austenite grains. However, strain fields measured here, were saturated by the effect of plastic deformation on the {111} slip/shear bands (refer Section 7.1.2) and it is therefore difficult to resolve the strain induced by martensite. These shear or slip band intersections provide the nucleation sites for the transformation to occur, when the material is loaded to still higher strains [4], [50], [60], [185]. This mechanism is discussed later in the chapter (refer Section 7.1.2).

The EBSD and HRDIC experiments only revealed the micromechanics of the deformation process at the surface of the material (Chapters 4 and 5). From these experiments and literature it is known that plastic deformation of the parent austenite matrix supplies the necessary energy for the material to overcome the energy barrier for strain-induced transformation to occur [40]. These measurements were then compared with the bulk transformation behaviour using neutron diffraction experiments (Chapter 6). These measurements at the ENGIN-X diffractometer were the average transformation behaviour of a large number of diffracting grains.

The neutron diffraction results showed distinct transformation behaviours one at the ambient and another in the lower temperature regime (refer Section 6.3). At room temperature plastic deformation precedes the transformation [186], which is discussed in detail below (refer Section 7.1.2). Whereas, deforming in the lower temperature regime, on account of deformation by slip being suppressed, the plastic deformation of the crystal lattice is believed to be due to the deformation-induced martensitic transformation. This is because the driving energy required for the transformation to occur at the lower temperatures is less in comparison to samples deformed at room temperature (refer Equation 3) [40], [50], [60], [187]. Further, there was no observable transition temperature range and there simply appears to be a step change in the transformation behaviour (300 K to 263K). Moreover, at ambient temperature, it was shown that the intensity of those diffraction peaks from austenite grain families most affected by plastic deformation, decreased most due to martensitic transformation. At ambient temperature, this was the {220} austenite peak. Whereas, at the lower temperature regimes, slip is suppressed, this is not the case and the {200} austenite peak loses intensity the most, similar to the observations have been made by Blonde *et al*. [149]. Another distinction between the two transformation regimes was transformation sequence, at ambient temperature it was $\gamma \rightarrow \alpha'$ and/or $\gamma \rightarrow \varepsilon$ and at low temperatures regimes it was $\gamma \rightarrow \varepsilon \rightarrow \alpha'$. Such transformation sequences have been reported in literature [66], [186], [188].

7.1.2 Transformation mechanism

For the room temperature experiments, at early stages in the deformation process, plasticity does not seem to be due to the martensitic phase transformation and is possibly due to slip occurring in the material. However, martensite adds to total plasticity and only occurs at higher global strain values at the shear band intersections, grain boundaries, or from other nucleation sites [50]. Here, initially plastic deformation of the parent austenite grains leads to formation of stacking faults, which are two-dimensional planar defects [176]. For a regularly stacked austenite material (fcc crystal structure) the stacking sequence is ABCABCABC. However, when there is irregularity in the stacking sequence, *e.g.* ABCABCBCABC it is termed as a stacking fault (refer Figure 7-1). Stacking faults occur on the closed packed planes, which are the {111} planes for fcc crystals. These stacking faults play an important role in the deformation of the austenite lattice and ultimately in the formation of strain-induced martensite [186] and an important role in the determination of the critical driving force required for the transformation [182]. On room temperature straining of a fcc crystal structure the deformation mode is initially by the formation of stacking faults on the closed packed {111} planes and in the <011> direction. This deformation in tern creates nucleation sites or martensite embryos. Therefore, at room temperature where there is deformation of the parent austenite matrix, prior to the the γ→α′ transformation, it may be considered to be strain-induced transformation [50], [60].

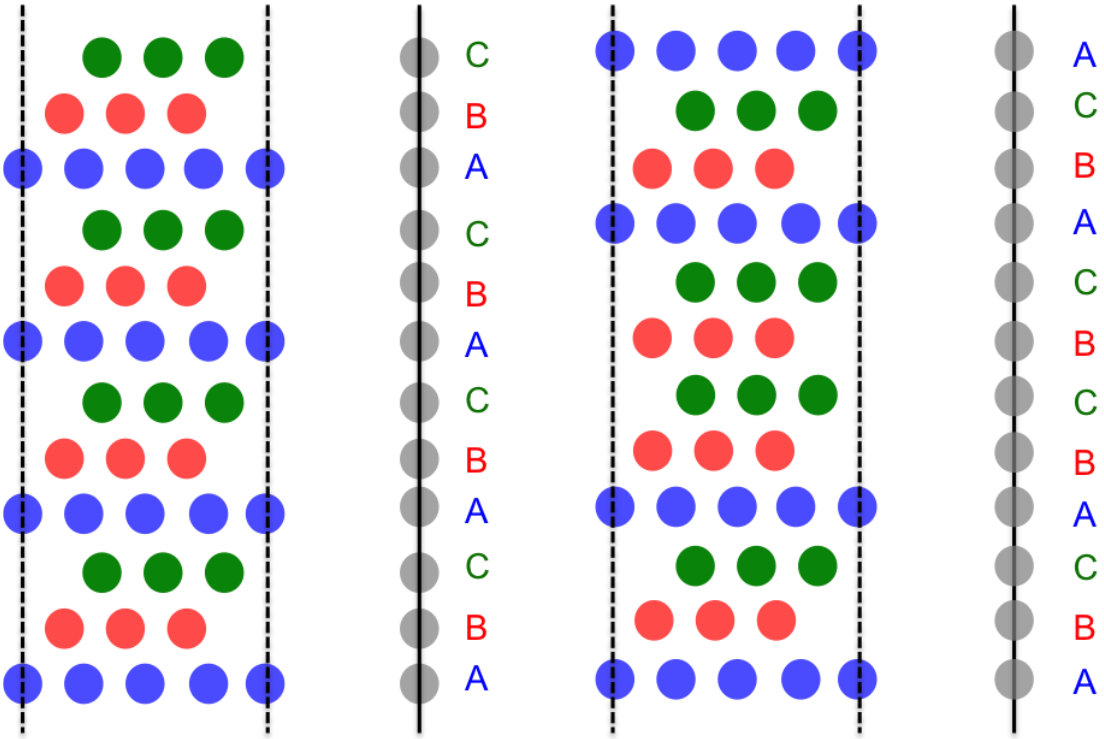

Figure 7-1: Schematic of stacking fault arrangement of (111) closed packed plane in fcc crystalline materials. (a, b) show a perfect fcc stacking sequence and (c, d) show a stacking fault. Adapted from Ref. [186].

Therefore, it can be said that stacking faults are the atomic scale mismatches which lead to formation of nucleation sites for strain-induced martensite to occur on. It is challenging to identify a single stacking fault and microstructural features originating owing to a bunch of stacking faults constitute what may be called as a shear/slip bands [182], [186]. To probe the strains at this length scales would require the use of high-resolution transmission electron microscope (HRTEM), which is beyond the scope of the present dissertation.

Here, using EBSD and HRDIC it has not been possible to separate the strains associated with slip and martensitic transformation. This could be improved if the gaps between strain increments were reduced, or if the formation of the martensite could be observed, which is not possible because of the gold coating. However, these changes were impractical for the current *in situ* EBSD and DIC experiments.

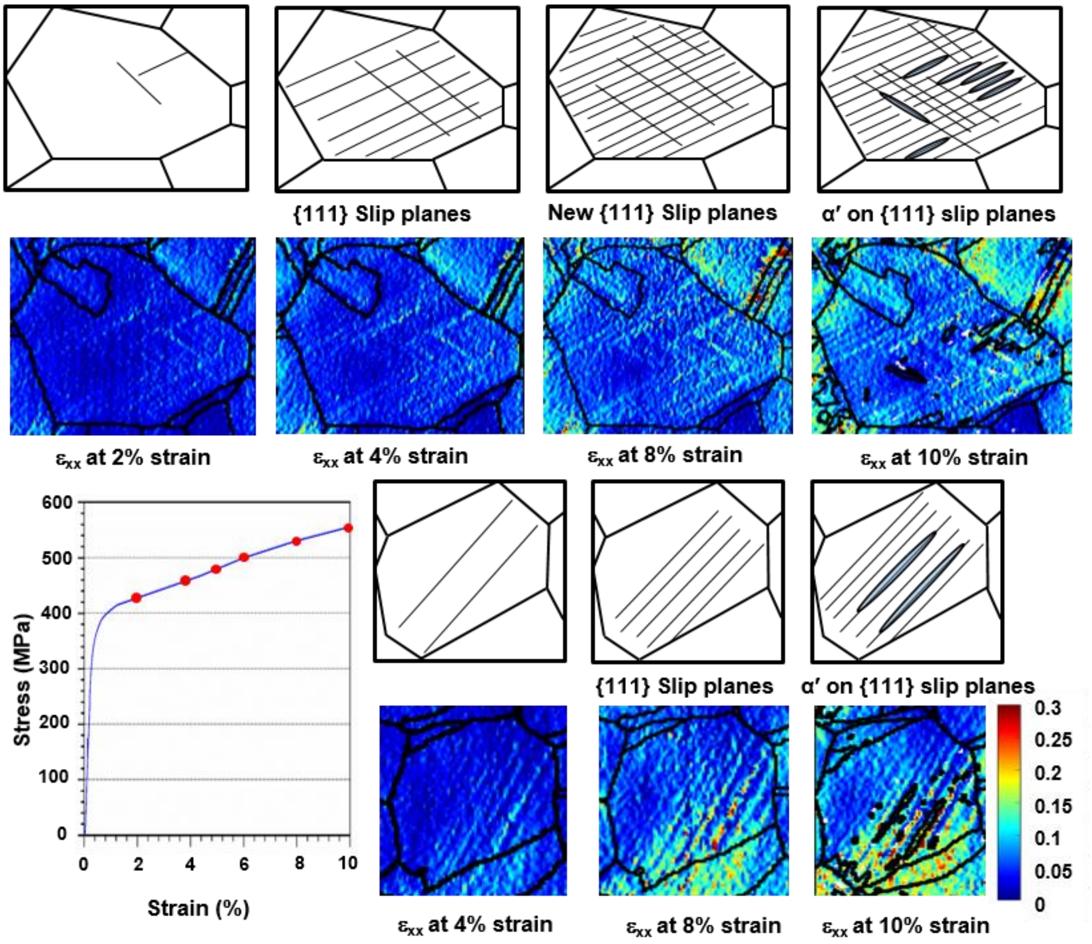

Figure 7-2: Mechanisms for martensitic phase transformation in fully austenitic grains. Grain 1 (top) and grain 2 (bottom) are shown with the corresponding DIC strain maps, made at various strain increments represented by dots on the stress strain curve.

Figure 7-2 explains the two-step nature of the strain-induced martensitic phase transformation mechanisms at room temperature for Grains 1 and 2 (refer to Figure 5-1). Grain 1 shows two active slip systems and four martensite variants;

whilst in grain 2, a single dominant slip system and three unique martensite variants are found (see Figure 7-3). In Grain 1 there are two {111} slip planes which appear to dominate the deformation process (the green and blue lines approximately equal length), both activated when the critically-resolved shear stress is reached for that slip plane (see Figure 7-2 - grain 1). Other slip systems may be active; however, they do not seem to be as localised along their slip plane as the dominant ones. That is why no additional slip lines appear in either the DIC and EBSD data sets. Initially, when the stress exceeds the critically-resolved shear stress threshold, plasticity occurs due to shear band formation on the {111} slip planes of the austenite grains [144]. Even at relatively low strain values of ~ 2% strain a second slip system may be activated. Intersection of the slip/shear bands within these highly-strained grains leads to potential nucleation sites for martensitic transformation [50]. The grain now contains significant overlapping of stacking faults and if further strained, these martensite (α') nucleation sites become activated leading to α' transformation [144]. In Grain 2 (Figure 7-2 – grain 2), only one {111} slip system is activated upon straining of the austenite grain (the pink slip plane in Figure 7-3 is dominant). Here, additional straining of the grain leads to activating $\gamma \rightarrow \alpha'$ on the very same shear bands, where the potential nucleation site may be a region with a high density and overlapping of stacking faults. The specimen was only strained to 10% strain, at which a small fraction (~10%) of austenite transformed into martensite.

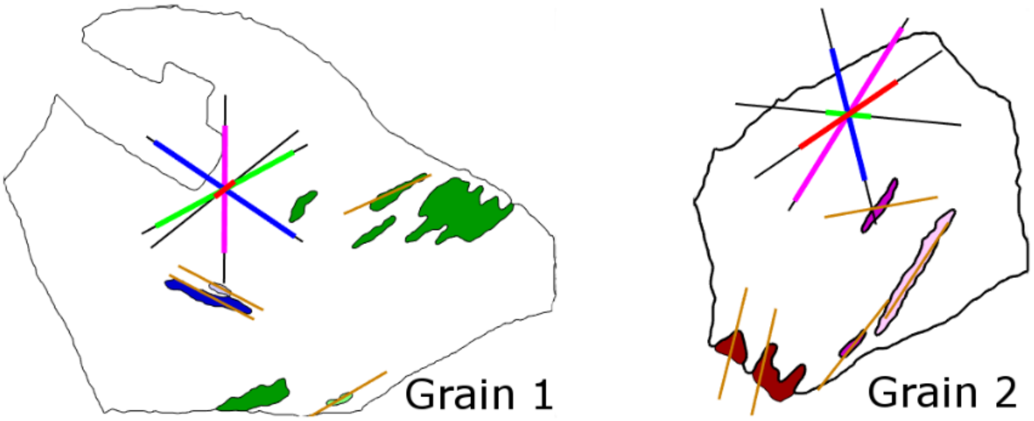

Figure 7-3: EBSD maps of the two grains studied. The martensite is coloured to represent the different K-S variants (see Figure 4). The {111} austenite slip traces of these different variants are shown, where the length of the coloured line is proportional to the Schmid factor. The strain-induced martensite plates display the (110) slip line trace, indicating that the K-S orientation relationship is approximately observed.

It is observed that the orientation relationship between austenite and strain-induced martensite approximately follows the K-S relationship. These martensite plates form in austenite grains along the {111} slip planes with higher Schmid factors. In Grain 1, it is seen that the martensite forms along the corresponding slip line traces and these seem to be the dominant slip systems active within the grain. In Grain 2, although the pink coloured martensite variant occurs along the active slip plane, the red coloured variants do not have an ideal match. This mismatch may be due to the constraints provided by the surrounding grains. Kundu *et al.* [17] modelled transformation texture in austenite grains having Goss and Cube components of texture that showed martensite variant selection. As explained earlier (Section 2.4.1), the model was based on the interaction of the applied stress with the shape deformation associated with the martensitic phase change and interaction energy calculated in accordance with Patel *et al.* [16]. We have applied this model to our data as shown in Figure 7-4.

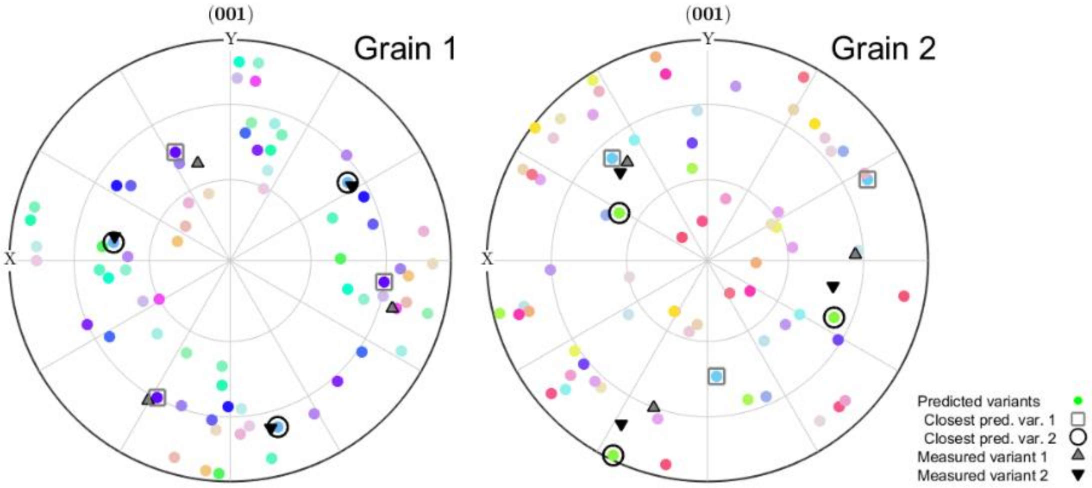

Figure 7-4: Pole figure plots of the spread of 24 possible martensite variants predicted for grain 1 and grain 2. The coloured circle shows predictions, the triangles are the measured variants and the circle encircling the predictions shows the closest match for a given grain.

In Figure 7-4 all the predicted martensite variants based on the above model for grain 1 and grain 2 are shown. In grain 1, the measured variant 2 was the closest to the predicted variants, which was ranked third in the list of 24 possible variants based on interaction energy [16], [17]. Hence, for this variant there is a good agreement between the predicted and measured variants. However, the same was not true for grain 2; the agreement between the predicted and measured variants was poor and the closest to the measured variant was variant 13, which was ranked eighth out of 24 possible variants. In grain 2, martensite transformation occurs on the {111} slip plane with the highest critically-resolved shear stress (highest Schmid factor). Here, as explained above in the section, it was believed that the nucleation sites were on highly deformed shear bands, which were locations of planar defects arising from the overlapping of stacking faults on the {111} austenite slip planes [144].

From Figure 7-5 it was shown that there was also a correlation between the maximum Schmid factor and the number of strain-induced martensite variants formed within a single grain. As shown earlier, slip bands mostly form on {111} slip systems with the highest Schmid factor. Furthermore, the martensite also tends to form along these slip bands. An example of this is shown in Figure 7-3, but this is also found in several more grains (see Figure 7-5 (B)). For an austenite grain having a single dominant slip system, slip was limited to a single slip plane and direction and strain-induced martensite appeared to form mainly along this plane (Grain 2 and 4). Whereas, if a single dominant slip system was not observed and there were two slip systems having a similar critically-resolved shear stress, martensite nucleation could occur on both the slip planes (grain 1 and 3). This meant that a greater number of martensite orientations were present in that particular grain. It was thought that the sequence of transformation has the following steps [50], [66], [144]:

- Dislocation generation, accumulation and glide along the {111} slip systems with highest critically-resolved shear stress. Slip lines occurred when critically-resolved shear stress crossed its threshold, enabling the slip system to get activated.
- Formation of nucleation sites (martensite embryos) – *i.e.* locations of planar defects – arose from overlapping of stacking faults [186]; also they may have formed at the intersection of shear bands.
- Further deformation of the austenite grains with nucleation sites lead to formation of strain induced α′ martensite.

Even if the above assumptions were correct, the use of the Schmid factor (see Figure 7-5 (A)) to predict the number of variants forming within a single austenite grain offered little insight, as can be seen from Figure 7-5 (B). For example, grains with very low Schmid factor (numbered 5 and 6) had little transformation present and grains with moderate to high Schmid factors (numbered 1 to 4) had up to 8 variants present. However, because some grains with moderate Schmid factor had 2 active slip systems, there was opportunity for many more variants to form. Further, as in some grains with the highest Schmid factor there was no sign of transformation, so it could be said that the Schmid factor alone did not give the full picture. This could be due to the 2 dimensional cross-section of a 3 dimensional system. The summarized data for the 6 sampled grains from Figure 7-5 (B) is restated in Table 7-1.

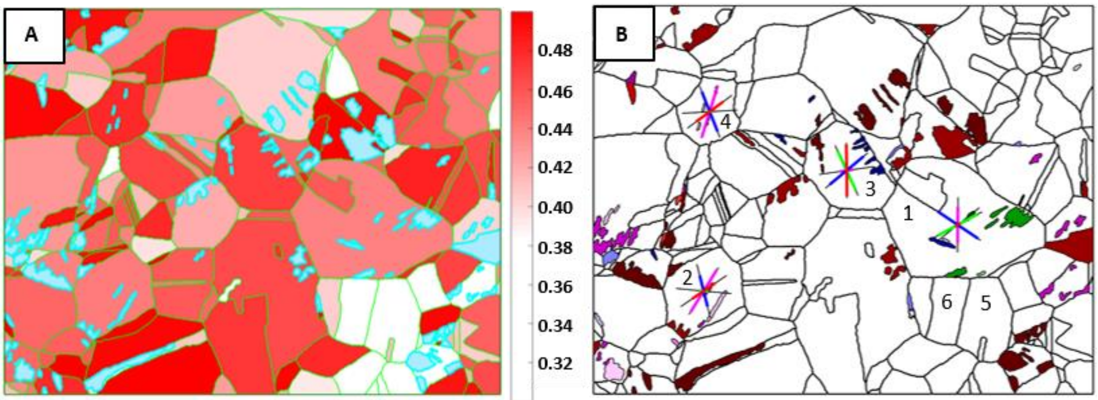

Figure 7-5: Figure (A) Schmid factor map of austenite grains at 10 % strain with the martensite phase shown in blue (B) Strain-induced martensite variants at 10 % global strain within each of these austenite grains. The {111} austenite slip traces of these different variants are shown for Grains 1 to Grain 4, where the length of the colored line is proportional to the critically-resolved shear stress on that plane.

Table 7-1. List of Schmid factor, number of active slip systems and number of strain induced martensite variants

Grain number	Schmid factor	No. of active slip systems	No. of variants
1	0.44	2	8
2	0.45	1	5
3	0.47	2	8
4	0.48	1	4
5	0.38	0	0
6	0.37	0	0

It will be interesting to conduct the EBSD and HRDIC experiments for the low temperature deformation of these steels. It is known that at the lower temperatures, the driving force required for the transformation is much lower and the application of stress results in the formation of stress-assisted transformation [50], [60]. Further, the low temperature experiments here showed a considerable volume fraction of deformation-induced martensite, even at relatively small strain increments. Therefore, a low temperature experiment would aid in probing transformation strain field, which will be around individual transformation sites. As discussed above, at sufficiently low temperatures and small strain increments, the plastic deformation due to slip is highly suppressed. In other words, straining (as per the procedure outlined in Section 3.3.1) the samples ex situ to ~ 2.5 % strain increment at say -50°C and subsequently mapping deformation strain fields.

7.1.3 Effect on work hardening

Work hardening rate can be visualised by differentiating the stress-strain curves (Figure 6-10(A)), *i.e.* the slope of the curve gives Figure 7-6. From Figure 7-6, it is clear that the material begins to work harden as the amount of strain induced martensite increases, this is above ~ 5% macroscopic strain at the low temperature measurements. The strain hardening mechanisms and phase transformations in materials at low and ambient temperatures are non-trivial [3], [5], [56], [60], [66], [165], [166], owing to the composite nature of the microstructure as discussed earlier in Section 2.5. It is possible that the high work hardening is due to load transfer occurring from the soft γ phase to the much stiffer α′ phase. This is because the stiffer product α′ phase is able to carry much higher loads when it forms in comparison to the parent γ phase [184]. Additionally, these martensite plates have a higher dislocation density and act as reinforcing phase within the softer austenite matrix [75]. With an increase in the volume fraction of deformation-induced martensite, there is a significant reduction in the grain size as the martensite plates divide the austenite grains, *i.e.* the Hall-Petch effect is triggered (refer Equation 1) [28], [29]. Moreover, these martensite plates provide a barrier for dislocation motion and much higher loads are required to further the deformation to higher strain increments.

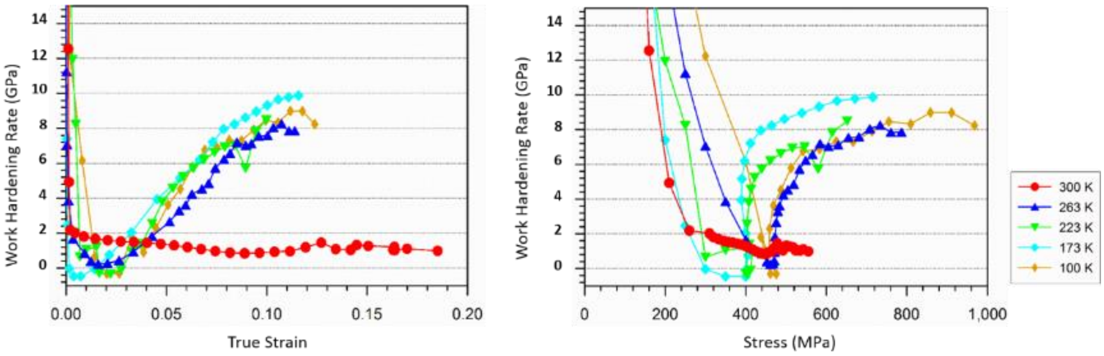

Figure 7-6. Slope of the stress-strain curves giving the work hardening rate plotted with respect to the applied macroscopic True Strain and Stress.

Moreover, the experimental results also show volume fraction of deformation-induced martensite affects the subsequent work hardening rate of the material, as there appears to be a direct correlation between the increase in volume fraction of the transformation and work hardening of the steel (refer Figure 7-7). Figure 7-7 shows the broadly linear trend observed between work hardening rate and the deformation-induced martensite volume fraction. The test conducted at 300K, where comparatively little transformation has occurred and slip is relatively easy show negligible work hardening. While the tests conducted at low temperature where slip is highly suppressed show relatively high levels of work hardening. This is possible when sufficient amount of the product phase is formed and load transfer takes place from the softer austenite matrix to the harder martensite phase. Spencer *et al.* [150] and Hedstrom *et al.* [184] showed the load in the α′ phase was almost twice as much as in the γ phase. As detailed above, the work hardening mechanisms are relatively complicated and probably dependent on many interlaced phenomena, therefore the scatter seen in Figure 7-7 is expected.

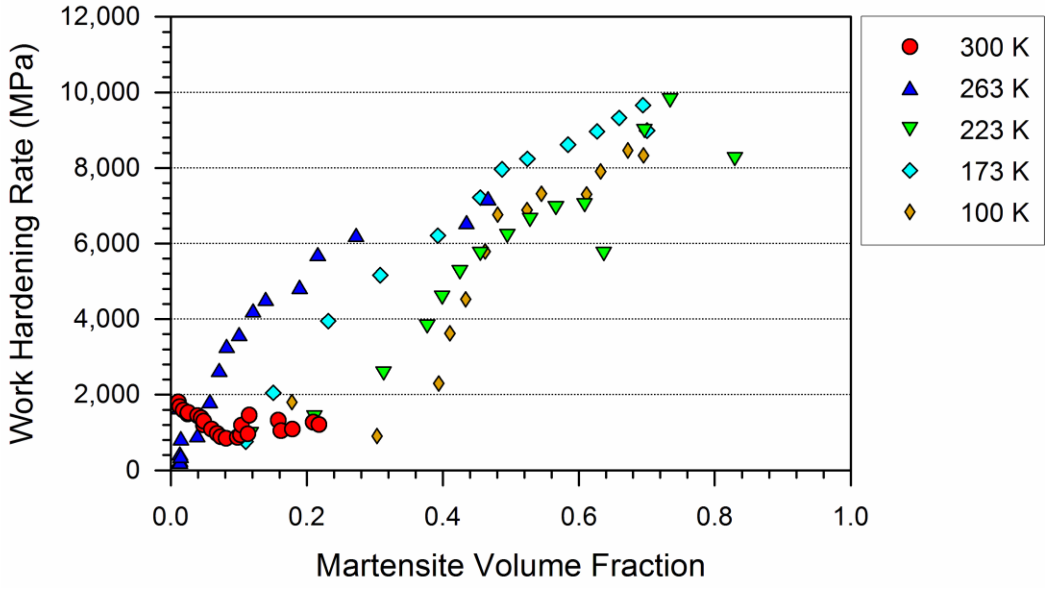

Figure 7-7. The work hardening response of the steel plotted with the corresponding increase in volume fraction of the deformation-induced martensite.

Thus, the measurements made in this research project focus on the quantification of the volume fraction of deformation-induced martensitic transformation with respect to temperature and applied macroscopic strain and their subsequent effect on the work hardening of the material.

8 Conclusions and further work

8.1 Conclusions

Probing the TRIP phenomenon by combining of the various EBSD, HRDIC and neutron diffraction techniques has enabled a deeper insight into micromechanics of the deformation-induced martensitic transformation. Further, the combination of the three experimental techniques illustrated that at ambient temperature, the strain-induced martensitic transformation was preceded by plastic deformation of the austenite crystal lattice and formation of nucleation sites within it. This plastically deformation austenite (with martensite nucleation sites) led to the formation of strain-induced transformation when it was still further deformed.

The key findings can be summarized as follows:

- EBSD results revealed that analysing the same set of grains throughout the deformation process enabled for the accurate measurement of the area fractions of strain-induced martensite. Further, the results showed that incrementally loading, unloading and reloading the samples lead to higher volume fractions of strain-induced transformations, in comparison to samples directly strained to same macroscopic strain.
- The combination of EBSD and HRDIC data displayed an increase in strain heterogeneity when strains were observed at the grain level (2000x magnification). When probed at still higher magnifications (5000x magnification), an increase in heterogeneity even within individual austenite grain was noticed. At the individual grain level, factors such as

grain orientation, localised stresses acting on the grain (actual load acting on the grain) and the surrounding constraints all need to be factored in to existing materials models.

- Upon straining, plastic deformation occurs due to the formation of {111} slip bands. Subsequent deformation of the austenite leads to strain-induced martensitic phase transformation. These martensite plates form along the {111} slip planes in the deformed austenite grains with the $(111)_\gamma$ parallel to $(0.012886\ 0.981915\ 0.978457)_{\alpha'}$ and the $[110]_\gamma$ direction parallel $[0.927033\ 1.055684\ -1.071623]_{\alpha'}$ [15]; however, the KS orientation relationship is found to be a good approximation.
- The variant selection model of Kundu *et al.* predicts the transformation only in some grains. Where it fails is possibly due to the constraints provided by the surrounding material. A more robust technique needs to be developed that can incorporate these effects.
- The Schmid factor has been shown to be a method to predict whether transformation will occur in a particular grain, but is limited in predicting the number of variants due to not taking into account slip on multiple slip systems. This is as combining DIC examination with EBSD has confirmed that grains containing two slip systems with high and similar Schmid factors show slip in two directions and independently corroborates the conclusion that transformation occurs along these slip lines.
- Neutron diffraction results showed two distinct transformation modes; one at the room temperature and another at low temperature. It is believed that deformation at room temperature was first due to formation of slip or shear bands [186]. Plastic deformation of the crystal lattice in

this way leads to creation of martensite embryos (at the shear band intersections) and ultimately strain-induced martensite on further deformation. Whereas, in the low temperature measurements, as plastic deformation due slip was suppressed and the application of external load results in the formation of deformation-induced martensite. This may be considered as stress-assisted transformation.

8.2 Further work

- The main scope of this project was experimental investigations of martensitic transformations, which were done using EBSD, HRDIC and neutron diffraction. Therefore a bulk of the further work could be based around modelling both plastic deformation preceding and post the deformation-induced martensitic transformations. This will enable the greater insights into TRIP behaviour and the strengthening mechanism associated with the transformation.
    - This may be accomplished by precisely accounting for the local strain heterogeneity in existing models, e.g. the Kundu model, which can be done on a grain-by-grain basis.
    - Further, crystal plasticity models may use these data sets to more reliably predict and compare the measurements (See section 5.3)
- In terms of short term experimental advances further work could include
    - Experiment-1: An investigation of the transformation behaviour at the transition temperature, *i.e.* between room temperature and the low temperature measurements using neutron diffraction (e.g. at the ENGIN-X beamline). This will give insights into the

    - transformation behaviour for application in various real world scenarios.
    - Experiment-2: Device an experiment that combines all the experimental techniques used in this project together, *i.e.* EBSD, HRDIC and neutron diffraction. For a given specimen, this would enable surface measurements made using the EBSD and HRDIC to be directly correlated with the bulk behaviour of the materials measured using neutrons. Beam time has been allocated for conducting this experiment to characterise plastic deformation due to the transformation and its effect on the subsequent work hardening rate. This will be done for all transformation regimes.
- On a longer scale,
    - There is still scope to further improve the software package, which incorporates the EBSD and DIC datasets together. Furthermore, HRIDC technique can be applied to characterise plastic deformation at the microscale in other metallic alloys of commercial significance, e.g. Ni-super alloys, Ti-alloys, Zr-alloys, etc.
    - The advances in combining EBSD and HRDIC data could pave the way to allow much more targeted TEM studies, *i.e.* investigating dislocation density in highly deformed grains, or around martensitic transformation sites. This would improve the understanding of structure property relationships during the deformation process.

9 References

[1] M. Takahashi, “Development of high strength steels for automobiles,” *Shinnittetsu Giho*, no. 88, pp. 2–7, 2003.

[2] R. J. Moat, S. Y. Zhang, J. Kelleher, a. F. Mark, T. Mori, and P. J. Withers, “Work hardening induced by martensite during transformation-induced plasticity in plain carbon steel,” *Acta Mater.*, vol. 60, no. 20, pp. 6931–6939, Dec. 2012.

[3] G. Olson and M. Cohen, “Stress-assisted isothermal martensitic transformation: application to TRIP steels,” *Metall. Trans. A*, vol. 13, no. November, pp. 1907–1914, 1982.

[4] J. Talonen, “Effect Strain-Induced α’-Martensite Transformation on Mechanical Properties of Metastable Austenitic Stainless Steels,” Helsinki University of Technology, 2007.

[5] F. Lecroisey and A. Pineau, “Martensitic transformations induced by plastic deformation in the Fe-Ni-Cr-C system,” *Metall. Trans.*, vol. 3, no. 2, pp. 391–400, 1972.

[6] Y. Tomita and T. Iwamoto, “Constitutive modeling of TRIP steel and its application to the improvement of mechanical properties,” *Int. J. Mech. Sci.*, vol. 37, no. 12, 1995.

[7] E. C. Bain and N. Y. Dunkirk, “The nature of martensite,” *trans. AIME*, vol. 70, no. 1, pp. 25–47, 1924.

[8] F. . Frank, “Martensite,” *Acta Metall.*, vol. 1, no. 1, pp. 15–21, 1953.

[9] G. F. Bolling and R. H. Richman, “The plastic deformation of ferromagnetic

face-centred cubic Fe-Ni-C alloys," *Philos. Mag.*, vol. 19, no. 158, pp. 247–264, 1969.

[10] F. Delogu, "A few details of the austenite to martensite phase transformation in 304 stainless steel powders under mechanical processing," *Acta Mater.*, vol. 59, no. 5, pp. 2069–2074, 2011.

[11] N. Tsuchida, Y. Yamaguchi, Y. Morimoto, T. Tonan, and Y. Takagi, "Effects of Temperature and Strain Rate on TRIP Effect in SUS301L Metastable Austenitic Stainless Steel," *ISIJ Int.*, vol. 53, no. 10, pp. 1881–1887, 2013.

[12] V. Zackay, E. Parker, D. Fahr, and R. Busch, "The enhancement of ductility in high-strength steels," *ASM Trans Quart*, 1967.

[13] H. Ferreira, G. De Abreu, S. Santana, D. Carvalho, P. Maria, D. O. Silva, S. Souto, and M. Tavares, "Deformation Induced Martensite in an AISI 301LN Stainless Steel : Characterization and Influence on Pitting Corrosion Resistance," vol. 10, no. 4, pp. 359–366, 2007.

[14] H. F. G. De Abreu, M. J. G. Da Silva, L. F. G. Herculano, and H. Bhadeshia, "Texture analysis of deformation induced martensite in an AISI 301L stainless steel: microtexture and macrotexture aspects," *Mater. Res.*, vol. 12, no. 3, pp. 291–297, 2009.

[15] H. Bhadeshia, "Worked Examples in the Geometry of Crystals', 1987," *London, Inst. Met. UK.*

[16] J. R. Patel and M. Cohen, "Criterion for the action of applied stress in the martensitic transformation," *Acta Metall.*, vol. 1, no. 5, pp. 531–538, 1953.

[17] S. Kundu and H. K. D. H. Bhadeshia, "Transformation texture in deformed stainless steel," *Scr. Mater.*, vol. 55, no. 9, pp. 779–781, 2006.

[18] F. Gioacchino and J. Quinta da Fonseca, “Plastic Strain Mapping with Sub-micron Resolution Using Digital Image Correlation,” *Exp. Mech.*, vol. 53, no. 5, pp. 743–754, 2012.

[19] M. D. McMurtrey, G. S. Was, B. Cui, I. Robertson, L. Smith, and D. Farkas, “Strain localization at dislocation channel-grain boundary intersections in irradiated stainless steel,” *Int. J. Plast.*, vol. 56, pp. 219–231, 2014.

[20] C. C. Tasan, J. P. M. Hoefnagels, M. Diehl, D. Yan, F. Roters, and D. Raabe, “Strain localization and damage in dual phase steels investigated by coupled in-situ deformation experiments and crystal plasticity simulations,” *Int. J. Plast.*, vol. 63, pp. 198–210, 2014.

[21] H. Lim, J. D. Carroll, C. C. Battaile, T. E. Buchheit, B. L. Boyce, and C. R. Weinberger, “Grain-scale experimental validation of crystal plasticity finite element simulations of tantalum oligocrystals,” *Int. J. Plast.*, vol. 60, pp. 1–18, 2014.

[22] F. Di Gioacchino and J. Q. da Fonseca, “An experimental study of the polycrystalline plasticity of austenitic stainless steel,” *Int. J. Plast.*, vol. 74, pp. 92-109, 2015.

[23] T. H. Simm, “The use of EBSD and Digital Image Correlation to understand the deformation of HCP alloys,” University of Manchester, Thesis, 2007.

[24] R. Abbaschian, L. Abbaschian, and R. E. Reed-Hill, *Physical Metallurgy Principles*, 4th ed., *Cengage Learning*, Stamford, CT, USA, 2009.

[25] R. E. Smallman and R. J. Bishop, “Modern Physical Metallurgy and Materials Engineering,” 6th ed., *Butterworth-Heinemann*, Oxford, UK, 1999.

[26] H. K. D. H. Bhadeshia and R. W. . Honeycombe, "Steels - Microstructure and

Properties", 3rd ed., *Butterworth-Heinemann*., Oxford, UK, 2006.

[27] W. D. C. Jr, "*Material Science and Engineering : An Introduction*" 7th ed., John Wiley & Sons, USA, 2006.

[28] E. O. Hall, "The deformation and ageing of mild steel III Discussion of results," *Proc. Phys. Soc. Sect. B*, vol. 64, no. 9, pp. 747, 1951.

[29] PETCH and N. J., "The Cleavage Strength of Polycrystals," *J. Iron Steel Inst.*, vol. 174, pp. 25–28, 1953.

[30] D. Hull and D. J. Bacon, "Introduction to Dislocations." 5th ed., *Butterworth-Heinemann*, Oxford, UK, 2011.

[31] N. Hansen, "Hall-petch relation and boundary strengthening," *Scr. Mater.*, vol. 51, no. 8 SPEC. ISS., pp. 801–806, 2004.

[32] H. K. D. H. Bhadeshia, "Properties of fine-grained steels generated by displacive transformation," *Mater. Sci. Eng. A*, vol. 481–482, pp. 36–39, 2008.

[33] M. F. Ashby, "Engineering Materials 2," *2nd ed.*, *Butterworth-Heinemann*, Oxford, UK, 1999.

[34] A. H. Cottrell and B. A. Bilby, "Dislocation Theory of Yielding and Strain Ageing of Iron," *Proc. Phys. Soc. Sect. A*, vol. 62, no. 1, pp. 49, 1949.

[35] J. G. Sevillano, "Flow Stress and Work Hardening," in *Materials Science and Technology*, Weinheim, Germany: Wiley-VCH Verlag GmbH & Co. KGaA, 2006.

[36] S. L. Kakani and A. Kakani, "Material Science." *New Age International*, New Delhi, India, 2004.

[37] M. Howes, T. Inoue, and G. E. Totten, "Handbook of Residual Stress and

Deformation of Steel." *ASM International*, Materials Park, OH, USA, 2002.

[38] B. S. Mitchell, "An Introduction to Materials Engineering and Science." *John Wiley & Sons,* New Jersey, USA, 2004.

[39] Z. Nishiyama, M. E. Fine, M. Meshii, and C. M. Wayman, “Martensitic transformation,” *Academic Press,* New York, USA, 1978.

[40] C. M. Wayman and H. K. D. H. Bhadeshia, "Physical Metallurgy," 4th ed., vol. II. *Elsevier Science BV*, pp. 1508-1554, 1996.

[41] G. Kurdjumov and G. Sachs, “Over the mechanisms of steel hardening,” *Z. Phys*, vol. 64, pp. 325–343, 1930.

[42] Z. Nishiyama, “X-ray Investigation of the Mechanism of the Transformation from Face-centered Cubic Lattice to Body-centered Cubic,” *Sci. Rep. Tohoku Univ*, vol. 23, pp. 637–664, 1934.

[43] A. Crosky, P. G. McDougall, and J. S. Bowles, “The crystallography of the precipitation of α rods from β Cu-Zn alloys,” *Acta Metall.*, vol. 28, no. 11, pp. 1495–1504, 1980.

[44] S. Kundu, “Transformation Strain and Crystallographic Texture in Steels,” University of Cambridge, PhD Thesis, 2007.

[45] J. Mackenzie and J. Bowles, “The crystallography of martensite transformations II,” *Acta Metall.*, vol. 2, no. 1, pp. 138–147, 1954.

[46] J. Bowles and J. Mackenzie, “The crystallography of martensite transformations III. Face-centred cubic to body-centred tetragonal transformations,” *Acta Metall.*, 1954.

[47] J. Bowles and J. Mackenzie, “The crystallography of martensite transformations I,” *Acta Metall.*, vol. 2, no. 1, pp. 129–137, 1954.

[48] J. D. Eshelby, “The Determination of the Elastic Field of an Ellipsoidal Inclusion, and Related Problems,” *Proc. R. Soc. A Math. Phys. Eng. Sci.*, vol. 241, no. 1226, pp. 376–396, 1957.

[49] J. Christian, “Discussion of ‘Comments on accommodation strains in martensite formation and the use of a dilatation parameter,’” *Acta Metallurgica*, vol. 7, no. 3. pp. 218–219, 1959.

[50] G. B. Olson and M. Cohen, “A mechanism for the strain-induced martensitic transformations,” *J. Less-Common Met.*, vol. 28, pp. 107–118, 1972.

[51] S. R. Pati and M. Cohen, “Kinetics of isothermal martensitic transformations in an iron-nickel-manganese alloy,” *Acta Metall.*, vol. 19, pp. 1327–1332, 1971.

[52] S. R. Pati and M. Cohen., “‘Nucleation of the isothermal martensitic transformation.,’” *Acta Metall.*, vol. 17, pp. 189–199, 1969.

[53] V. Raghavan and A. R. Entwiste, “No Title,” *Iron and Steel Institute Special Report No. 93*, pp. 20, 1965.

[54] J. Venables, “The martensite transformation in stainless steel,” *Philos. Mag.*, vol. 7, pp. 35–44, 1962.

[55] R. Lagneborgj, “The martensite transformation in 18% Cr-8% Ni steels,” *Acta Metall.*, vol. 12, no. 7, pp. 823–843, 1964.

[56] P. L. Mangonon and G. Thomas, “The martensite phases in 304 stainless steel,” *Metall. Trans.*, vol. 1, no. 6, pp. 1577–1586, 1970.

[57] G. F. Bolling and R. H. Richman, “The plastic deformation-transformation of paramagnetic f.c.c. Fe-Ni-C alloys,” *Acta Metall.*, vol. 18, no. 6, pp. 673–681, Jun. 1970.

[58] G. F. Bolling and R. H. Richman, “The influence of stress on martensite-start temperatures in Fe-Ni-C alloys,” *Scr. Metall.*, vol. 4, no. 7, pp. 539–543, 1970.

[59] R. H. Richman and G. F. Bolling, “Stress, deformation, and martensitic transformation,” *Metall. Trans.*, vol. 2, no. 9, pp. 2451–2462, 1971.

[60] G. Olson and M. Cohen, “Kinetics of strain-induced martensitic nucleation,” *Metall. Trans. A*, vol. 6A, pp. 791–795, 1975.

[61] S. Kundu, K. Hase, and H. K. D. H. Bhadeshia, “Crystallographic texture of stress-affected bainite,” *Proc. R. Soc. A Math. Phys. Eng. Sci.*, vol. 463, no. 2085, pp. 2309–2328, 2007.

[62] S. Kundu and H. K. D. H. Bhadeshia, “Crystallographic texture and intervening transformations,” *Scr. Mater.*, vol. 57, no. 9, pp. 869–872, 2007.

[63] J. C. Bokros and E. R. Parker, “The mechanism of the martensite burst transformation in Fe-Ni single crystals,” *Acta Metall.*, vol. 11, no. 12, pp. 1291–1301, 1963.

[64] P. Bate and B. Hutchinson, “The effect of elastic interactions between displacive transformations on textures in steels,” *Acta Mater.*, vol. 48, no. 12, pp. 3183–3192, 2000.

[65] V. Pancholi, M. Krishnan, I. S. Samajdar, V. Yadav, and N. B. Ballal, “Self-accommodation in the bainitic microstructure of ultra-high-strength steel,” *Acta Mater.*, vol. 56, no. 9, pp. 2037–2050, 2008.

[66] N. Gey, B. Petit, and M. Humbert, “Electron backscattered diffraction study of ε/α' martensitic variants induced by plastic deformation in 304 stainless steel,” *Metall. Mater. Trans. A*, vol. 36, pp. 3291-3299, 2005.

[67] N. J. Wittridge, J. J. Jonas, and J. H. Root, "A dislocation-based model for variant selection during the γ-to-α′ transformation," *Metall. Mater. Trans. A*, vol. 32, no. 4, pp. 889–901, 2001.

[68] S. Kundu, "Comments on 'Effects of stress on transformation plasticity and texture in a tool steel,'" *Scr. Mater.*, vol. 58, no. 10, pp. 934–936, 2008.

[69] S. Kundu, A. K. Verma, and V. Sharma, "Quantitative Analysis of Variant Selection for Displacive Transformations Under Stress," *Metall. Mater. Trans. A*, vol. 43, no. 7, pp. 2552–2565, 2012.

[70] H. N. Han, C. G. Lee, C.-S. Oh, T.-H. Lee, and S.-J. Kim, "A model for deformation behavior and mechanically induced martensitic transformation of metastable austenitic steel," *Acta Mater.*, vol. 52, no. 17, pp. 5203–5214, 2004.

[71] G. Wassermann, "Ueber den Mechanismus der [alpha]-[gamma]-Umwandlung des Eisens," *Mit. K.-With.-Inst. Eisenforsch*, vol. 17, pp. 149–155, 1935.

[72] G. Nolze, "Irrational orientation relationship derived from rational orientation relationships using EBSD data," *Cryst. Res. Technol.*, vol. 43, no. 1, pp. 61–73, 2008.

[73] E. C. Oliver, "The Generation of Internal Stresses in Single and Two Phase," University of Manchester, PhD Thesis, 2002.

[74] E. Jimenez-Melero, N. H. van Dijk, L. Zhao, J. Sietsma, S. E. Offerman, J. P. Wright, and S. van der Zwaag, "Martensitic transformation of individual grains in low-alloyed TRIP steels," *Scr. Mater.*, vol. 56, no. 5, pp. 421–424, 2007.

[75] H. K. D. H. Bhadeshia, "TRIP-Assisted Steels?," *ISIJ Int.*, vol. 42, no. 9, pp. 1059–1060, 2002.

[76] M. Cherkaoui, M. Berveiller, and X. Lemoine, "Couplings between plasticity and martensitic phase transformation: overall behavior of polycrystalline TRIP steels," *Int. J. Plast.*, vol. 16, no. 10–11, pp. 1215–1241, 2000.

[77] N. Tsuchida, Y. Morimoto, T. Tonan, Y. Shibata, K. Fukaura, and R. Ueji, "Stress-Induced Martensitic Transformation Behaviors at Various Temperatures and Their TRIP Effects in SUS304 Metastable Austenitic Stainless Steel," *ISIJ Int.*, vol. 51, no. 1, pp. 124–129, 2011.

[78] H. J. M. Geijselaers and E. S. Perdahcıoğlu, "Mechanically induced martensitic transformation as a stress-driven process," *Scr. Mater.*, vol. 60, no. 1, pp. 29–31, 2009.

[79] F. Roters, P. Eisenlohr, L. Hantcherli, D. D. Tjahjanto, T. R. Bieler, and D. Raabe, "Overview of constitutive laws, kinematics, homogenization and multiscale methods in crystal plasticity finite-element modeling: Theory, experiments, applications," *Acta Mater.*, vol. 58, no. 4, pp. 1152–1211, 2010.

[80] E. Cakmak, H. Choo, K. An, and Y. Ren, "A synchrotron X-ray diffraction study on the phase transformation kinetics and texture evolution of a TRIP steel subjected to torsional loading," *Acta Mater.*, vol. 60, no. 19, pp. 6703–6713, Nov. 2012.

[81] S. Chatterjee and H. K. D. H. Bhadeshia, "Transformation induced plasticity assisted steels: stress or strain affected martensitic transformation?," *Mater. Sci. Technol.*, vol. 23, no. 9, pp. 1101–1104, 2007.

[82] J. R. C. Guimarães, “Stress assisted martensite: Pre-strain, grain-size and strain-rate effects,” *Mater. Sci. Eng. A*, vol. 475, no. 1–2, pp. 343–347, 2008.

[83] H. K. Yeddu, A. Borgenstam, and J. Ågren, “Stress-assisted martensitic transformations in steels: A 3-D phase-field study,” *Acta Mater.*, vol. 61, no. 7, pp. 2595–2606, 2013.

[84] P. Jacques, Q. Furnémont, A. Mertens, and F. Delannay, “On the sources of work hardening in multiphase steels assisted by transformation-induced plasticity,” *Philos. Mag. A*, vol. 81, no. 7, pp. 1789–1812, 2001.

[85] S. Stock and B. Cullity, "Elements of X-RAY Diffraction." *Addison-Wesley,* USA, 1956.

[86] “Scanning electron microscope,” 2016. [Online]. Available: https://www.purdue.edu/ehps/rem/rs/sem.htm. [Accessed: 28-Jun-2016].

[87] D. Dingley, “Progressive steps in the development of electron backscatter diffraction and orientation imaging microscopy,” *J. Microsc.*, vol. 213, no. September 2003, pp. 214–224, 2004.

[88] V. Randle, “Electron backscatter diffraction: Strategies for reliable data acquisition and processing,” *Mater. Charact.*, vol. 60, no. 9, pp. 913–922, 2009.

[89] F. Humphreys, “Review grain and subgrain characterisation by electron backscatter diffraction,” *J. Mater. Sci.*, vol. 6, pp. 3833–3854, 2001.

[90] K. Z. BABA-KISHI, “Electron backscatter Kikuchi diffraction in the scanning electron microscope,” *J. Mater. Sci. …*, vol. 7, pp. 1715–1746, 2002.

[91] F. Humphreys, “Quantitative metallography by electron backscattered

diffraction.," *J. Microsc.*, vol. 195, no. 3, pp. 170–185, 1999.

[92] A. J. Schwartz, M. Kumar, B. L. Adams, and D. P. Field, "Electron Backscatter Diffraction in Materials Science." *Springer*, Boston, MA, USA, 2000.

[93] O. Engler and V. Randle, "Introduction to Texture Analysis, Macrotexture, Microtexture, and Orientation Mapping," CRC Press, USA, 2000.

[94] O. Engler and V. Randle, "*Introduction to Texture Analysis*, *Macrotexture, Microtexture, and Orientation Mapping," 2nd ed.*, CRC Press, USA, 2009.

[95] K. Z. Baba-Kishi and D. J. Dingley, "Backscatter Kikuchi diffraction in the SEM for identification of crystallographic point groups," *Scanning*, vol. 11, no. 6, pp. 305–312, 1989.

[96] D. J. Dingley and S. I. Wright, "Determination of crystal phase from an electron backscatter diffraction pattern," *J. Appl. Crystallogr.*, vol. 42, no. 2, pp. 234–241, 2009.

[97] ASTM, "Standard Practice for X-Ray Determination of Retained Austenite in Steel with Near Random Crystallographic Orientation 1," *ASTM*, vol. 3, no. Reapproved 2008, pp. 1–7, 2009.

[98] P. Hedström, U. Lienert, J. Almer, and M. Odén, "Stepwise transformation behavior of the strain-induced martensitic transformation in a metastable stainless steel," *Scr. Mater.*, vol. 56, no. 3, pp. 213–216, 2007.

[99] M. E. Fitzpatrick and A. Lodini, "Analysis of Residual Stress by Diffraction using Neutron and Synchrotron Radiation." *Taylor and Francis,* London, UK, 2003.

[100] M. T. Hutchings, Withers.P.J, T. M. Holden, and T. Lorentzen, "Introduction to characterization of residual stress by neutron diffraction," *Taylor and*

Francis, Boca Raton, FL, USA, 2005.

[101] T. Pirling, G. Bruno, and P. J. Withers, “SALSA-A new instrument for strain imaging in engineering materials and components,” *Mater. Sci. Eng. A*, vol. 437, no. 1, pp. 139–144, 2006.

[102] “How ISIS works.” [Online]. Available: http://www.isis.stfc.ac.uk/about/how-isis-works6313.html. [Date Accessed: 20-Jun-2016].

[103] J. R. Santisteban, M. R. Daymond, J. A. James, and L. Edwards, “ENGIN-X: A third-generation neutron strain scanner,” *J. Appl. Crystallogr.*, vol. 39, no. 6, pp. 812–825, 2006.

[104] MIT, “Chapter 29 : Kinetic Theory of Gases : Equipartition of Energy and the Ideal Gas Law Chapter.” Boston, USA.

[105] SUNY Stony Brook University, “Ideal Gasses and Equipartition.” Stony Brook, USA.

[106] H. M. Rietveld, “A profile refinement method for nuclear and magnetic structures,” *Journal of Applied Crystallography*, vol. 2, no. 2. pp. 65–71, 1969.

[107] W. N. Sharpe, Ed., "Springer Handbook of Experimental Solid Mechanics." *Springer,* Boston, US, 2008.

[108] P. J. Withers and H. K. D. H. Bhadeshia, “Residual stress Part 1 – Measurement techniques,” vol. 17, no. April, pp. 355–365, 2001.

[109] G. S. Schajer, "Practical Residual Stress Measurement Methods." *Wiley* Sussex, UK, 2013.

[110] S. I. Wright, M. M. Nowell, and D. P. Field, “A Review of Strain Analysis

Using Electron Backscatter Diffraction," *Microsc. Microanal.*, vol. 17, no. 3, pp. 316–329, 2011.

[111] D. Katrakova and F. Mücklick, "Specimen preparation for electron Backscatter Diffraction. Part I : Metals," *Prakt. Metallogr.*, vol. 38, no. 10, pp. 547–565, 2001.

[112] W. H. Peters, W. F. Ranson, M. A. Sutton, T. C. Chu, and J. Anderson, "Application of digital correlation methods to rigid body mechanics," *Opt. Eng.*, vol. 22, no. 6, pp. 213427, 1983.

[113] M. Sutton, C. Mingqi, W. Peters, Y. Chao, and S. McNeill, "Application of an optimized digital correlation method to planar deformation analysis," *Image Vis. Comput.*, vol. 4, no. 3, pp. 143–150, 1986.

[114] C. Lee, W. Peters, M. Sutton, and Y. Chao, "A study of plastic zone formation by digital image processing," *Int. J. Plast.*, vol. 3, no. 2, pp. 129–142, 1987.

[115] H. W. Schreier, "Investigation of two and three-dimensional image correlation techniques with applications in experimental mechanics," University of South Carolina, PhD Thesis, 2003.

[116] H. Schreier, J. J. Orteu, and M. A. Sutton, "Image Correlation for Shape, Motion and Deformation Measurements." Springer, Boston, MA, USA, 2009.

[117] B. Pan, K. Qian, H. Xie, and A. Asundi, "Two-dimensional digital image correlation for in-plane displacement and strain measurement: a review," *Meas. Sci. Technol.*, vol. 20, no. 6, p. 62001, 2009.

[118] M. A. Sutton, S. R. Mcneill, J. D. Helm, and Y. J. Chao, "Advances in Two-Dimensional and Three-Dimensional Computer Vision," vol. 372, pp. 323–372, 2000.

[119] M. Luo, “Displacement/strain measurements using an optical microscope and digital image correlation,” *Opt. Eng.*, vol. 45, no. 3, p. 33605, 2006.

[120] M. A. Sutton, N. Li, D. Garcia, N. Cornille, J. J. Orteu, S. R. McNeill, H. W. Schreier, and X. Li, “Metrology in a scanning electron microscope: theoretical developments and experimental validation,” *Meas. Sci. Technol.*, vol. 17, no. 10, pp. 2613–2622, 2006.

[121] M. A. Sutton, N. Li, D. C. Joy, a. P. Reynolds, and X. Li, “Scanning Electron Microscopy for Quantitative Small and Large Deformation Measurements Part I: SEM Imaging at Magnifications from 200 to 10,000,” *Exp. Mech.*, vol. 47, no. 6, pp. 775–787, 2007.

[122] M. A. Sutton, N. Li, D. Garcia, N. Cornille, J. J. Orteu, S. R. McNeill, H. W. Schreier, X. Li, and a. P. Reynolds, “Scanning Electron Microscopy for Quantitative Small and Large Deformation Measurements Part II: Experimental Validation for Magnifications from 200 to 10,000,” *Exp. Mech.*, vol. 47, no. 6, pp. 789–804, 2007.

[123] B. Peng, “Modified correlation criterion for digital image correlation considering the effect of lighting variations in deformation measurements,” *Opt. Eng.*, vol. 51, no. 1, p. 17004, 2012.

[124] M. Hagara, R. Hunady, and M. Stamborska, “Using of digital image correlation in experimental modal analysis of a horizontal stabilizer of the airplane model phoenix,” *Mod. Mech. Mechatr. Sys.*, 2011, pp. 151–159, 2011.

[125] A. Bastawros and A. G. Evans, “Experimental analysis of deformation mechanisms in a closed-cell aluminum alloy foam,” vol. 48, pp. 301–322,

2000.

[126] L. Chevalier, S. Calloch, F. Hild, and Y. Marco, “Digital image correlation used to analyze the multiaxial behavior of rubber-like materials,” *Eur. J. Mech. - A/Solids*, vol. 20, no. 2, pp. 169–187, 2001.

[127] J. Abanto-Bueno and J. Lambros, “Investigation of crack growth in functionally graded materials using digital image correlation,” *Eng. Fract. Mech.*, vol. 69, no. 14–16, pp. 1695–1711, 2002.

[128] B. Wattrisse, A. Chrysochoos, and J. Muracciole, “Analysis of Strain Localization during Tensile Tests by Digital Image Correlation,” pp. 29–39, 2000.

[129] D. Zhang, X. Zhang, and G. Cheng, “Compression strain measurement by digital speckle correlation,” *Exp. Mech.*, vol. 39, no. 1, pp. 62–65, 1999.

[130] I. Chasiotis and W. G. Knauss, “A New Microtensile Tester for the Study of MEMS Materials with the Aid of Atomic Force Microscopy,” pp. 51–57, 2001.

[131] S. R. McNeill, W. H. Peters, and M. A. Sutton, “Estimation of stress intensity factor by digital image correlation,” *Eng. Fract. Mech.*, vol. 28, no. 1, pp. 101–112, 1987.

[132] S. Roux and F. Hild, “Stress intensity factor measurements from digital image correlation: post-processing and integrated approaches,” *Int. J. Fract.*, vol. 140, no. 1–4, pp. 141–157, 2006.

[133] S. Yoneyama, Y. Morimoto, and M. Takashi, “Automatic Evaluation of Mixed-mode Stress Intensity Factors Utilizing Digital Image Correlation,” *Strain*, vol. 42, no. 1, pp. 21–29, 2006.

[134] B. M. B. Grant, H. J. Stone, P. J. Withers, and M. Preuss, “High-temperature strain field measurement using digital image correlation,” *J. Strain Anal. Eng. Des.*, vol. 44, no. 4, pp. 263–271, 2009.

[135] P. Bing, X. Hui-min, H. Tao, and A. Asundi, “Measurement of coefficient of thermal expansion of films using digital image correlation method,” *Polym. Test.*, vol. 28, no. 1, pp. 75–83, 2009.

[136] Z. Sun, J. S. Lyons, and S. R. McNeill, “Measuring Microscopic Deformations with Digital Image Correlation,” *Opt. Lasers Eng.*, vol. 27, no. 4, pp. 409–428, 1997.

[137] M. Pitter, C. See, J. Goh, and M. Somekh, “Focus errors and their correction in microscopic deformation analysis using correlation.,” *Opt. Express*, vol. 10, no. 23, pp. 1361–1367, 2002.

[138] T. a Berfield, J. K. Patel, R. G. Shimmin, P. V Braun, J. Lambros, and N. R. Sottos, “Fluorescent image correlation for nanoscale deformation measurements.,” *Small*, vol. 2, no. 5, pp. 631–5, 2006.

[139] G. Vendroux and W. G. Knauss, “Submicron deformation field measurements: Part 1. Developing a digital scanning tunneling microscope,” *Exp. Mech.*, vol. 38, no. 1, pp. 18–23, 1998.

[140] G. Vendroux and W. G. Knauss, “Submicron deformation field measurements: Part 2. Improved digital image correlation,” *Exp. Mech.*, vol. 38, no. 2, pp. 86–92, 1998.

[141] G. Vendroux, N. Schmidt, and W. G. Knauss, “Submicron Deformation Field Measurements : Part 3 . Demonstration of Deformation Determinations,” vol. 38, no. 3, 1998.

[142] J. D. Carroll, B. G. Clark, T. E. Buchheit, B. L. Boyce, and C. R. Weinberger, “An experimental statistical analysis of stress projection factors in BCC tantalum,” *Mater. Sci. Eng. A*, vol. 581, pp. 108–118, 2013.

[143] J. C. Stinville, N. Vanderesse, F. Bridier, P. Bocher, and T. M. Pollock, “High resolution mapping of strain localization near twin boundaries in a nickel-based superalloy,” *Acta Mater.*, vol. 98, pp. 29–42, 2015.

[144] J. Talonen and H. Hänninen, “Formation of shear bands and strain-induced martensite during plastic deformation of metastable austenitic stainless steels,” *Acta Mater.*, vol. 55, no. 18, pp. 6108–6118, 2007.

[145] P. Hedström, “Deformation and Martensitic Phase Transformation in Stainless Steels,” 2007.

[146] P. Hedström, T. S. Han, U. Lienert, J. Almer, and M. Odén, “Load partitioning between single bulk grains in a two-phase duplex stainless steel during tensile loading,” *Acta Mater.*, vol. 58, no. 2, pp. 734–744, 2010.

[147] P. Hedström, L. Lindgren, and M. Odén, “Stress State and Strain Rate Dependence of the Strain-induced Martensitic Transformation in a Metastable Austenitic Stainless Steel,” pp. 171–174, 2007.

[148] H. Bhadeshia, S. Kundu, and H. Abreu, “Mathematics of Crystallographic Texture in Martensitic and Related Transformations,” *Microstruct. Texture Steels*, pp. 19–32, 2009.

[149] R. Blondé, E. Jimenez-Melero, L. Zhao, J. P. Wright, E. Brück, S. van der Zwaag, and N. H. van Dijk, “High-energy X-ray diffraction study on the temperature-dependent mechanical stability of retained austenite in low-alloyed TRIP steels,” *Acta Mater.*, vol. 60, no. 2, pp. 565–577, 2012.

[150] K. Spencer, J. D. Embury, K. T. Conlon, M. Véron, and Y. Bréchet, “Strengthening via the formation of strain-induced martensite in stainless steels,” *Mater. Sci. Eng. A*, vol. 387–389, no. 1–2 SPEC. ISS., pp. 873–881, 2004.

[151] P. Haušild, V. Davydov, J. Drahokoupil, M. Landa, and P. Pilvin, “Characterization of strain-induced martensitic transformation in a metastable austenitic stainless steel,” *Mater. Des.*, vol. 31, no. 4, pp. 1821–1827, 2010.

[152] R. Woracek, D. Penumadu, N. Kardjilov, A. Hilger, M. Boin, J. Banhart, and I. Manke, “3D mapping of crystallographic phase distribution using energy-selective neutron tomography,” *Adv. Mater.*, vol. 26, no. 24, pp. 4069–4073, 2014.

[153] M. Ojima, J. Inoue, S. Nambu, P. Xu, K. Akita, H. Suzuki, and T. Koseki, “Stress partitioning behavior of multilayered steels during tensile deformation measured by in situ neutron diffraction,” *Scr. Mater.*, vol. 66, no. 3–4, pp. 139–142, 2012.

[154] F. Bachmann, R. Hielscher, and H. Schaeben, “Grain detection from 2d and 3d EBSD data-Specification of the MTEX algorithm,” *Ultramicroscopy*, vol. 111, no. 12, pp. 1720–1733, 2011.

[155] ASTM, “ASTM E8 / E8M - 13a Standard Test Methods for Tension Testing of Metallic Materials.” USA, 2015.

[156] W. a. Scrivens, Y. Luo, M. a. Sutton, S. a. Collette, M. L. Myrick, P. Miney, P. E. Colavita, a. P. Reynolds, and X. Li, “Development of patterns for digital image correlation measurements at reduced length scales,” *Exp. Mech.*, vol.

47, no. 1, pp. 63–77, 2007.

[157] LaVision, "StrainMaster 8.2." Göttingen, Germany, 2014.

[158] B. D. Lucas and T. Kanade, “An iterative image registration technique with an application to stereo vision,” *7th international joint conference on Artificial intelligence*, vol. 2. pp. 674–679, 1981.

[159] J.-Y. Bouguet, “Pyramidal implementation of the affine lucas kanade feature tracker—description of the algorithm,” *INTEL Corp. Microprocess. Res. LABS*, USA, 2001.

[160] W. F. Clocksin, K. F. Chivers, P. H. S. Torr, J. Quinta da Fonseca, and P. J. Withers, “Inspection of surface strain in materials using dense displacement fields,” *Proc. Int. Conf. New Challenges Mesomech. Aaalborg Univ. Denmark*, vol. 2, pp. 467–475, 2002.

[161] E. . Oliver, T. Mori, M. . Daymond, and P. . Withers, “Neutron diffraction study of stress-induced martensitic transformation and variant change in Fe–Pd,” *Acta Mater.*, vol. 51, no. 20, pp. 6453–6464, 2003.

[162] P. J. Withers, M. W. Johnson, and J. S. Wright, “Neutron strain scanning using a radially collimated diffracted beam,” *Phys. B Condens. Matter*, vol. 292, no. 3–4, pp. 273–285, 2000.

[163] E. Oliver and J. Santisteban, “ENGIN-X user manual,” *ISIS, Didcot,* UK, 2004.

[164] S. Paddea, “Stress and creep damage evolution in materials for ultra-supercritical power plants,” The Open University, PhD Thesis, 2013.

[165] E. Nagy, V. Mertinger, F. Tranta, and J. Sólyom, “Deformation induced martensitic transformation in stainless steels,” *Mater. Sci. Eng. A*, vol. 378, no. 1–2, pp. 308–313, 2004.

[166] J.-Y. Choi and W. Jin, “Strain induced martensite formation and its effect on strain hardening behavior in the cold drawn 304 austenitic stainless steels,” *Scr. Mater.*, vol. 36, no. 1, pp. 99–104, 1997.

[167] L. N. Brewer, M. A. Othon, L. M. Young, and T. M. Angeliu, “Misorientation Mapping for Visualization of Plastic Deformation via Electron Back-Scattered Diffraction,” *Microsc. Microanal.*, vol. 12, no. 1, pp. 85–91, 2006.

[168] D. N. Githinji, S. M. Northover, P. J. Bouchard, and M. A. Rist, “An EBSD study of the deformation of service-aged 316 austenitic steel,” *Metall. Mater. Trans. A Phys. Metall. Mater. Sci.*, vol. 44, no. 9, pp. 4150–4167, 2013.

[169] R. Unnikrishnan, S. M. Northover, H. Jazaeri, and P. J. Bouchard, “Investigatin plastic deformation around a reheat-crack in a 316H austenitic stainless steel weldment by misorientation mapping,” *21st Eur. Conf. Fract.*, pp. 20–24, 2016.

[170] P. J. Buchanan, V. Randle, and P. E. J. Flewitt, “A simple procedure for the assessment of plastic strain in electron back-scatter diffraction patterns,” *Scr. Mater.*, vol. 37, no. 10, pp. 1511–1518, 1997.

[171] M. F. Chisholm, “Scanning Microscopy for Nanotechnology,” *Scanning Microsc. Nanotechnol. Tech. Appl.*, pp. 152–191, 2006.

[172] K. Fujiyama, K. Mori, D. Kaneko, H. Kimachi, T. Saito, R. Ishii, and T. Hino, “Creep damage assessment of 10Cr-1Mo-1W-VNbN steel forging through EBSD observation,” *Int. J. Press. Vessel. Pip.*, vol. 86, no. 9, pp. 570–577, 2009.

[173] W. Callister and D. Rethwisch, "*Material Science and Engineering : An Introduction*" 7th ed., John Wiley & Sons, USA, 2007.

[174] F. Bachmann, R. Hielscher, and H. Schaeben, “Grain detection from 2d and 3d EBSD data-Specification of the MTEX algorithm,” *Ultramicroscopy*, vol. 111, no. 12, pp. 1720–1733, 2011.

[175] H. Kato, R. Moat, T. Mori, K. Sasaki, and P. Withers, “Back Stress Work Hardening Confirmed by Bauschinger Effect in a TRIP Steel Using Bending Tests,” vol. 54, no. 7, pp. 1715–1718, 2014.

[176] G. Dieter, “Mechanical metallurgy,” *McGraw-Hill Publishing*, London, 1988.

[177] A. D. Kammers and S. Daly, “Digital Image Correlation under Scanning Electron Microscopy: Methodology and Validation,” *Exp. Mech.*, vol. 53, no. 9, pp. 1743–1761, 2013.

[178] L. Patriarca, W. Abuzaid, H. Sehitoglu, and H. J. Maier, “Slip transmission in bcc FeCr polycrystal,” *Mater. Sci. Eng. A*, vol. 588, pp. 308–317, 2013.

[179] G. Sachs, “Zur Ableitung einer FlieBbedingung,” *Z. Ver. Deu. Ing*, vol. 72, no. 22, p. 734, 1928.

[180] H. J. Bunge, “Some applications of the Taylor theory of polycrystal plasticity,” *Krist. und Tech.*, vol. 5, no. 1, pp. 145–175, 1970.

[181] G. L. Taylor, “Plastic strain in metals,” *J. Inst. Met.*, vol. 62, pp. 307, 1938.

[182] K. Datta, R. Delhez, P. M. Bronsveld, J. Beyer, H. J. M. Geijselaers, and J. Post, “A low-temperature study to examine the role of martensite during strain-induced transformations in metastable austenitic stainless steels,” *Acta Mater.*, vol. 57, no. 11, pp. 3321–3326, 2009.

[183] R. P. Reed and A. F. Clark, “Materials at low temperatures.,” *Am. Soc. Met.*, pp. 590, 1983.

[184] P. Hedström, L. E. Lindgren, J. Almer, U. Lienert, J. Bernier, M. Terner, and

M. Odén, “Load partitioning and strain-induced martensite formation during tensile loading of a metastable austenitic stainless steel,” *Metall. Mater. Trans. A Phys. Metall. Mater. Sci.*, vol. 40, no. 5, pp. 1039–1048, 2009.

[185] I. Tamura, “Deformation-induced martensitic transformation and transformation-induced plasticity in steels,” *Met. Sci.*, vol. 16, no. 5, pp. 245–253, May 1982.

[186] A. Das, “Revisiting Stacking Fault Energy of Steels,” *Metall. Mater. Trans. A Phys. Metall. Mater. Sci.*, vol. 47, no. 2, pp. 748–768, 2016.

[187] G. B. Olson and M. Azrin, “Transformation Behavior of Trip Steels,” vol. 541, no. I, pp. 1893, 1978.

[188] A. Das, S. Tarafder, and P. C. Chakraborti, “Estimation of deformation induced martensite in austenitic stainless steels,” *Mater. Sci. Eng. A*, vol. 529, no. 1, pp. 9–20, 2011.

[189] P. Hedström, U. Lienert, J. Almer, and M. Odén, “Elastic strain evolution and ε-martensite formation in individual austenite grains during in situ loading of a metastable stainless steel,” *Mater. Lett.*, vol. 62, no. 2, pp. 338–340, 2008.